

**University of Strathclyde**



**Department of Mechanical Engineering**  
**Department of Electrical & Electronic Engineering**

“ Metering of Two-Phase  
Slug Flow”

Colin Stewart

PhD thesis

June 2002

The copyright of this thesis belongs to the author under the terms of the United Kingdom Copyright Acts as qualified by Strathclyde University Regulation 3.49. Due acknowledgement must always be made of the use of any material contained in, or derived from, this thesis.

## Abstract

This thesis describes the development of a novel system, for metering of two-phase (gas-water) slug flows. The approach combines a model for *stable slug flow*, a non-intrusive set of conductance sensors, and appropriate closure relationships. This system allows each of the parameters in the model to be determined.

The slug flow model is analysed, to determine the sensitivity of the phase flowrates to each measurement parameter. A metering system is then proposed which combines ring-shaped electrodes, electronic instrumentation, and processing software. The ring electrodes are optimised, for the measurement of the phase fraction and the translation velocity. New instrumentation is developed to activate the electrodes, with high measurement accuracy and a wide bandwidth. Analysis software is developed, to process the sensor data, provide suitable closure relations, and deliver the flowrates. A unique feature of this software is its ability to calculate *uncertainty margins* in the predicted flowrates.

The NEL multiphase facility is used, to obtain data for developed, horizontal, gas-water slug flow in a 4-inch pipe. The data span the range of liquid phase superficial velocities  $0.1 \text{ m s}^{-1}$  to  $1.0 \text{ m s}^{-1}$ , and gas phase superficial velocities  $0.6 \text{ m s}^{-1}$  to  $6.0 \text{ m s}^{-1}$ . The analysis software is used to obtain the flowrate predictions and estimates for the uncertainty margins. The stable slug flow model does not give good results. The relative error in the gas phase prediction is between 10% and 100%, and for the liquid phase prediction, between 50% and 500%. The uncertainty margins are also of comparable magnitude.

Proposals for improving the accuracy of the translation velocity measurement, and for directly measuring the local velocities in the slug body (using a pressure transducer) are presented. These proposals aim to reduce the uncertainty that is caused by the use of the empirical closure relationships in the model.

## Acknowledgements

The work that follows was carried out as part of the Postgraduate Training Partnership (PTP) scheme, between the University of Strathclyde in Glasgow, and the National Engineering Laboratory (NEL) in East Kilbride. I would like to thank a number of people at both locations for their support.

At Strathclyde University, I would like to thank my formal supervisor William Dempster, and my ‘informal’ supervisor Brian Stimpson, for their help in getting my project off the ground. There is no way I would have reached the end of this, without their assistance. I would also like to thank David Hamilton, Pat McGinnis and all his staff in the Mechanical Engineering workshop, and Bill Rooney in the Electrical Engineering workshop. It was their help that enabled me to create all the necessary sensor components and the electronic circuit boards.

A significant proportion of the research work, and the acquisition of the experimental data, was performed at NEL. Here, I would like to thank Andrew Hall for his advice, and my industrial supervisor Gregor Brown for helping me to ‘get things done’. Much thanks should also go to Patricia Hone and Richard Harvey, for helping me install the instrumentation within the NEL facility, and operating the loop.

I would particularly like to thank my parents, for putting up with me during the final year of my studies. They drove me insane, but I wouldn’t have completed the work that follows without a roof over my head.

It was at this point in an early version of my thesis, that I had some critical comments about the managers of the PTP scheme. Suffice to say here, “Make sure someone know what your PhD thesis is supposed to be about, make sure you have a source of income when your funding runs out, and don’t take nonsense from anyone.” Future PhD students, take note!

## Table of contents

<b><u>1. Introduction</u></b>	<b>24</b>
<b>1.1 Thesis overview</b>	<b>25</b>
<b>1.2 Thesis objectives</b>	<b>26</b>
<b>1.3 Thesis structure</b>	<b>26</b>
<b><u>2. The multiphase flow meter</u></b>	<b>29</b>
<b>2.1 Phase velocity measurement</b>	<b>30</b>
2.1.1 Differential pressure measurement	31
2.1.2 Signal cross-correlation	33
2.1.3 Positive displacement method	35
2.1.4 Nuclear magnetic resonance	36
<b>2.2 Phase fraction measurement</b>	<b>37</b>
2.2.1 Gamma-ray attenuation	37
2.2.2 Impedance electrodes	39
2.2.3 Tomographic measurement	43
<b>2.3 Phase density measurement</b>	<b>46</b>
<b>2.4 Processing software</b>	<b>47</b>
2.4.1 Flow pattern identification	47
2.4.2 Parameter extraction	48
2.4.3 The predictive model	48
<b>2.5 Meter performance</b>	<b>49</b>
2.5.1 Test conditions	49
2.4.2 Performance	51
2.4.3 Limitations	53
<b>2.6 Summary</b>	<b>54</b>
<b><u>3. Modelling of slug flow</u></b>	<b>55</b>
<b>3.1 Qualitative description of slug flow</b>	<b>56</b>
3.1.1 Slug flow initiation	56
3.1.2 The slug zone structure	58
3.1.3 The film zone structure	59
3.1.4 Inclination effects	60
<b>3.2 The phase flowrates</b>	<b>61</b>
3.2.1 Model parameters	61
3.2.2 Flowrate equations	62
3.2.3 Stable slug flow	63
<b>3.3 The slug body velocities</b>	<b>64</b>

3.3.1 Dukler & Hubbard model	64
3.3.2 Maron <i>et al</i> model	65
3.3.3 Bendiksen model	66
3.3.4 Drift-flux models	67
3.3.5 Woods & Hanratty model	68
3.3.6 Gas bubbles within the slug body	70
<b>3.4 Pressure drop models</b>	<b>71</b>
3.4.1 The slug zone pressure drop	71
3.4.2 The film zone pressure drop	75
3.4.3 Prediction of the film zone holdup profile	78
3.4.4 Closure relationships	79
<b>3.5 Pickup and shedding processes</b>	<b>82</b>
3.5.1 Liquid pickup and shedding	82
3.5.2 Gas entrainment	85
3.5.3 Developing slug flow	86
<b>3.6 Other correlations</b>	<b>89</b>
3.6.1 Slug frequency correlations	89
3.6.2 Slug holdup correlations	90
3.6.3 Slug length	91
<b>3.7 Multiphase slug flow model</b>	<b>93</b>
3.7.1 Flowrate equations	93
3.7.2 Homogeneous liquid model	93
3.7.3 Separated liquid model	95
<b>3.8 Summary</b>	<b>96</b>
<b><u>4. Metering approach</u></b>	<b>99</b>
<b>4.1 Parameter specification</b>	<b>100</b>
<b>4.2 Sensitivity analysis</b>	<b>102</b>
4.2.1 Background	102
4.2.2 Results	104
<b>4.3 Measurement techniques</b>	<b>109</b>
4.3.1 Phase fraction measurement	109
4.3.2 Translation velocity measurement	110
4.3.3 Local velocity measurement	111
4.3.4 Software specifications	113
<b>4.4 Summary</b>	<b>114</b>
<b><u>5. Conductance sensor design</u></b>	<b>116</b>
<b>5.1 Phase fraction sensor design</b>	<b>117</b>
5.1.1 Design Selection	117

5.1.2 Theory	117
5.1.3 The film holdup measurement	119
5.1.4 The slug holdup measurement	121
5.1.5 Spatial filtering between the electrodes	123
5.1.6 Conductivity calibration	125
<b>5.2 Cross-correlation sensor design</b>	<b>126</b>
5.2.1 Design Selection	126
5.2.2 Theory	127
5.2.3 Signal bandwidth	128
5.2.4 Sensor separation	131
5.2.5 Record duration	132
<b>5.3 Implementation</b>	<b>133</b>
5.3.1 Manufacture	133
5.3.2 Assembly	134
5.3.3 Crosstalk prevention	136
5.3.4 Guard electrode simulation	137
5.3.5 Design parameters	139
<b>5.4 Performance assessment</b>	<b>140</b>
5.4.1 Film zone measurement	140
5.4.2 Transition zone measurement	143
5.4.3 Slug holdup measurement	143
<b>5.5 Summary</b>	<b>143</b>
<b><u>6. Instrumentation design</u></b>	<b>146</b>
<b>6.1 Instrumentation specifications</b>	<b>147</b>
6.1.1 Functionality specifications	147
6.1.2 Performance specifications	148
<b>6.2 Design solution</b>	<b>150</b>
6.2.1 Limitations	152
6.2.2 Modified design	153
<b>6.3 Detailed design</b>	<b>155</b>
6.3.1 Channel structure	156
6.3.2 Operating frequency and operating current	158
6.3.3 Transfer functions $G(\omega)$ and $H(\omega)$	159
6.3.4 Demodulation method	162
6.3.5 The 'PI' controller	164
6.3.6 Performance simulation	165
6.3.7 Interference rejection	167
<b>6.4 Implementation</b>	<b>171</b>
6.4.1 Operating range settings	171

6.4.2	Signal distortion	172
6.4.3	D.C. performance errors	175
6.4.4	Electromagnetic compatibility	178
6.4.5	Manufacture	180
<b>6.5</b>	<b>Performance assessment</b>	<b>182</b>
<b>6.6</b>	<b>Summary</b>	<b>185</b>
<b><u>7.</u></b>	<b><u>Analysis system</u></b>	<b>186</b>
<b>7.1</b>	<b>Hardware system</b>	<b>187</b>
<b>7.2</b>	<b>Parameter extraction</b>	<b>188</b>
7.2.1	Threshold level subroutine	189
7.2.2	Cross-correlation subroutine	190
7.2.3	Signal bandwidth calculation	191
<b>7.3</b>	<b>Flowrate prediction</b>	<b>192</b>
7.3.1	Closure relations	193
7.3.2	Averaging techniques	196
<b>7.4</b>	<b>Uncertainty estimation</b>	<b>197</b>
7.4.1	The translation velocity uncertainty	197
7.4.2	The phase fraction uncertainty	198
7.4.3	The local velocity uncertainty	199
7.4.4	Data processing uncertainty	199
7.4.5	Flowrate uncertainty	200
<b>7.5</b>	<b>Summary</b>	<b>201</b>
<b><u>8.</u></b>	<b><u>Performance assessment</u></b>	<b>203</b>
<b>8.1</b>	<b>Data acquisition</b>	<b>204</b>
8.1.1	The NEL facility	204
8.1.2	The measurement system	206
8.1.2	System bench tests	207
8.1.3	The sensor data	207
<b>8.2</b>	<b>Data analysis</b>	<b>209</b>
8.2.1	The cross-correlation method	214
8.2.2	Parameter predictions	217
8.2.3	Flowrate predictions	224
8.2.4	Parameter uncertainty margins	226
8.2.5	Flowrate uncertainty margins	231
<b>8.3</b>	<b>Interpretation</b>	<b>234</b>
8.3.1	Validity of the slug flow model	234
8.3.2	The total superficial velocity ( $j$ )	236
8.2.3	The slip ratio ( $s$ )	236

<b>8.4 Summary</b>	<b>237</b>
<b><u>9. Conclusions</u></b>	<b>240</b>
<b>9.1 Future work</b>	<b>244</b>
9.1.1 The local velocity measurement	244
9.1.2 The translation velocity measurement	246
9.1.3 The phase fraction measurement	247
9.1.4 Unstable slug flow	248
<b>9.2 Final Summary</b>	<b>248</b>
<b><u>References</u></b>	<b>251</b>
<b>Appendix A: ANSYS modelling</b>	<b>262</b>
<b>Appendix B: Instrumentation design details</b>	<b>268</b>
<b>Appendix C: Processing software</b>	<b>279</b>

## List of figures

### **Chapter 2. The multiphase flowmeter**

<b>2.1:</b> Principal components of the multiphase flow meter.	29
<b>2.2:</b> Venturi meter for the measurement of the total flow velocity.	32
<b>2.3:</b> Typical 12-inch Venturi meter sections (Westfall Instruments)	32
<b>2.4:</b> Typical designs for the <i>flow homogeniser</i> and the <i>flow separator</i>	32
<b>2.5:</b> Cross-correlation velocity measurement. (a) system components; (b) the ideal sensor output and the normalised function $\rho_{xy}$ ; (c) the actual sensor output and function $\rho_{xy}$ , due to spatial filtering and flow evolution effects.	34
<b>2.6:</b> ‘Turbine’-type positive displacement flowmeter.	35
<b>2.7:</b> SRZ Series Geared positive displacement meters (AW Company) and FTM turbine flowmeter.	36
<b>2.8:</b> Two-phase NMR system (Sandia National Laboratory).	36
<b>2.9:</b> Principle of the multi-beam gamma-ray densitometer system. (a) system components; (b) calibration points for three-phase flow.	38
<b>2.10:</b> Single-beam and traversing-beam type gamma-ray densitometers (Imperial College).	39
<b>2.11:</b> Simplified model for the impedance of a fluid mixture, between impedance sensor electrodes.	40
<b>2.12:</b> Non-intrusive sensors, for making a global phase fraction measurement: (a) arc electrodes (Xie et al <sup>130</sup> , Lemmonier et al <sup>65</sup> ); (b) ring electrodes (Andreussi et al <sup>8</sup> ); (c) helical electrodes (Abouelwafa & Kendall <sup>1</sup> , Geraets & Borst <sup>37</sup> ); (d) rotating field electrodes (Merilo et al <sup>81</sup> , Snell et al <sup>109</sup> and Tournaire <sup>118</sup> ).	42
<b>2.13:</b> Example of a gamma-ray tomography system.	44
<b>2.14:</b> Three-phase X-ray tomography system (Imperial College).	44
<b>2.15:</b> Electrical impedance tomography (‘EIT’) system	45
<b>2.16:</b> Capacitance tomography system (Process Tomography Ltd).	46
<b>2.17:</b> ESMER multiphase flowmeter (Petroleum Software Ltd).	50
<b>2.18:</b> MPFM-400 multiphase flowmeter (Agar Inc.), for high gas volume fraction (GVF) flow measurement.	50
<b>2.19:</b> Typical range of test conditions, compared against flow pattern maps for horizontal flow (Mandhane et al <sup>74</sup> ) and vertical flow (Taitel et al <sup>114</sup> ).	51

### **Chapter 3. Modelling of slug flow**

<b>3.1:</b> The formation of a liquid slug by the Kelvin-Helmholtz instability mechanism. (a) A localised disturbance on the stratified film; (b) Pressure drop and wave growth; (c) Bridging of the pipe, acceleration of the blockage, and pickup of fluid	56
--	----

3.2: The relative motion of the liquid phase within the slug body, in a frame of reference translating with the slug front. (a) plug flow (low $j_g$ ); (b) slug flow ( $j_g \sim 3 \text{ m s}^{-1}$ ); (c) slug flow ( $3 < j_g < 7 \text{ m s}^{-1}$ ); (d) slug-annular flow ( $j_g > 7 \text{ m s}^{-1}$ ).	59
3.3: Simplified model of the slug unit.	62
3.4: Idealised velocity profiles throughout the slug zone, assuming a homogeneous mixture of fluids.	66
3.5: The correlation data of Woods & Hanratty <sup>127</sup> . (a) The translation velocity $V_t$ ( $C_B$ ), as a function of the total superficial velocity $j$ ( $U_{SG} + U_{SL}$ ); (b) Calculated values of the slip ratio $s$ , as a function of the total superficial velocity $j$ ( $U_{SG} + U_{SL}$ ).	70
3.6: Idealised pressure drop profile along the slug zone and the film zone, for the slug unit illustrated in figure 3.3.	72
3.7: Slug holdup and pressure profiles, in air-water slug flow (from Fan <i>et al</i> <sup>34</sup> ). (a) $j_f = 0.6 \text{ m s}^{-1}$ , $j_g = 1.1 \text{ m s}^{-1}$ ; (b) $j_f = 0.9 \text{ m s}^{-1}$ , $j_g = 2.96 \text{ m s}^{-1}$ ; (c) $j_f = 0.5 \text{ m s}^{-1}$ , $j_g = 4.06 \text{ m s}^{-1}$ ; (d) $j_f = 0.9 \text{ m s}^{-1}$ , $j_g = 7.03 \text{ m s}^{-1}$ ; (e) $j_f = 0.6 \text{ m s}^{-1}$ , $j_g = 9.09 \text{ m s}^{-1}$ .	74
3.8: Modelling of the film zone: (a) the forces acting on a differential film zone element $dx$ ; (b) the film zone geometry.	76
3.9: Iterative solution procedure for the local film velocities $V_{le}$ and $V_{ge}$ , using the ‘constant film’ equations.	78
3.10: The slug tracking model of Barnea & Taitel <sup>15</sup> . The evolution of a random pattern of slugs at the pipe inlet, for the flowrates $j_f = 0.1 \text{ m s}^{-1}$ , $j_g = 0.25 \text{ m s}^{-1}$ .	88
3.11: Slug holdup data of Andreussi & Bendiksen <sup>5</sup> . $\phi$ represents the pipe inclination.	91
3.12: Simplified ‘slug unit’ for three-phase (gas-oil-water) flow.	94
3.13: The effect of varying the in-situ water fraction $\lambda$ upon the <i>mixture viscosity</i> (oil-water flow).	95
3.14: Three-phase (gas-oil-water) stratified flow geometry	95
 <b>Chapter 4. Metering approach</b>	
4.1: Components of the proposed metering system.	100
4.2: Sensitivity parameters $S(V_t)$ , $S(V_{gs})$ , $S(V_{ls})$ and $S(V_{gs})$ , for the gas and liquid phases. (Calculated using the correlations in section 4.2.1).	106
4.3: Comparison of the sensitivities for each model parameter, for the two conditions $\{j_f = 0.1 \text{ m s}^{-1}; j_g = 1.0 \text{ m s}^{-1}\}$ and $\{j_f = 1.0 \text{ m s}^{-1}; j_g = 6.0 \text{ m s}^{-1}\}$ .	108
 <b>Chapter 5. Conductance sensor design</b>	
5.1: The analytic solution geometry of Coney <sup>27</sup> for a 2D liquid film above flat electrodes: (a) flat-liquid layer; (b) stepped layer.	118

5.2: Simplified models for representig the fluid within each slug unit.	118
5.3: The effect of the electrode seperation ratio $D_e/D$ on the conductance predictions for stratified flow: (a) $a_f$ versus $G/G^*$ ; (b) $\Delta a_f$ versus $G/G^*$ (separation ratio $s/D=0.05$ )	120
5.4: The effect of moving from a stratified to an annular geometry upon the measurement uncertainty $\Delta a_f$ ( $D_e/D=3.0$ ; $s/D=0.05$ )	121
5.5: Comparision of the Coney-Andreussi predictions for annular flow geometry, with the ANSYS simulations described in appendix A. (a) $G$ versus $G/G^*$ ; (b) $\Delta a_f$ versus $G/G^*$ ( $D_e/D=3.0$ ; $s/D=0.05$ ).	122
5.6: The effect of the flow geometry upon the conductance predictions for the slug body: (a) $a_s$ versus $G/G^*$ ; (b) $\Delta a_s$ versus $G/G^*$ ( $D_e/D=3.0$ ; $s/D=0.05$ )	124
5.7: Simulated response to a step change in holdup passing between the sensor electrodes. (a) Simulation geometry ( $D_e/D=3.0$ ; $s/D=0.05$ ); (b) Calculated conductance ratio $G/G^*$ , for $a_s=1$ and $a_{fe}=0.1, 0.2, 0.5$ respectively.	125
5.8: The effect of the input to the sensing volume sensing volume upon the signal bandwith $B$ . (a) Flow impulse; (b) ‘simplified’ slug flow; (c) ‘real’ slug flow.	130
5.9: Conductance predictions, for different geometries between the cross-correlation sensor electrodes ( $D_e/D=0.05$ ; $s/D=0.05$ ).	131
5.10: Manufacture diagrams: (a) the block section face view; (b) a single embedded electrode (holdup sensor); (c) a double embedded electrode (correlation sensor); (d) the flange plates used for pipeline installation.	134
5.11: Changes to the <i>sensor field</i> and the <i>leakage current</i> due to the presence of grounded pipework.	135
5.12: Assembly diagrams: (a) the holdup sensor unit; (b) the cross-correlation sensor unit.	135
5.13: Crosstalk current between the cross-correlation and holdup sensors, for a full-pipe of liquid. (a) the ideal situation; (b) the crosstalk current, without a guard electrode; (c) the crosstalk current, with a guard electrode.	136
5.14: The effect of the guard electrode length $X$ upon the crosstalk current rejection. (Cell voltage ratio $V_H/V_{cc}=10$ ).	138
5.15: Assembly diagram	139
5.16: The system of sensor units, within the NEL facility.	141
5.17: Performance assessment. Comparison of the experimental measurements, the prediction obtained using ANSYS simulation and the Coney-Andreussi theoretical model, for a stratified flow geometry: (a) the phase fraction sensor; (b) the cross-correlation sensors.	142

## Chapter 6. Instrumentation design

6.1: Schematic diagram of the user interface.	148
---	-----

<b>6.2:</b> Constant-voltage system for conductance measurement, developed by Coney <sup>27</sup> and Brown <i>et al</i> <sup>23</sup>	151
<b>6.3:</b> Circuit used to perform amplitude demodulation of the carrier, and its performance in the time- and frequency domains.	152
<b>6.4:</b> Model illustrating the network of impedances surrounding the cell. (a) ‘Top level’ diagram. (b) Coaxial cable impedance.	154
<b>6.5:</b> Deterioration of the demodulator output, with increasing carrier-to-multiplexing frequency ratio: (a) $\omega_c/\omega_m=20$ ; (b) $\omega_c/\omega_m=5$ ; (c) $\omega_c/\omega_m=2$ .	154
<b>6.6:</b> Schematic diagram of the proposed design solution	155
<b>6.7:</b> Structure of a single measurement channel.	157
<b>6.8:</b> Bode plots of the system open-loop gain $A\beta$ . The demodulator filter provides -60dB attenuation at 60kHz.	163
<b>6.9:</b> Effect of the PI controller upon the open-loop gain and phase.	164
<b>6.10:</b> Circuit diagram of the PI controller.	165
<b>6.11:</b> Block diagram of the Simulink model.	166
<b>6.12:</b> Simulation results. Response to a periodic step change in the transfer function $G(\omega)$ ( $ G(\omega) =1$ to $ G(\omega) =0.5$ ), at various locations within the system.	168
<b>6.13:</b> The effect of increasing the d.c. gain upon the system stability: (a) the open-loop gain $A\beta$ ; (b) the system output $i(t)$ .	169
<b>6.14:</b> The effect of different 8 <sup>th</sup> order Bessel bandpass filters upon the system performance. (a) Open-loop gain $A\beta$ ; (b) System output $i(t)$ .	170
<b>6.15:</b> System of logic used to set the gains $A$ , $\beta$ , the reference voltage $V_{ref}$ and the transimpedance gain $C$ , for each operating range.	173
<b>6.16:</b> Ideal and actual performance, for (a) the system demodulator; (b) the system modulator.	174
<b>6.17:</b> D.C. error in the demodulator output, as a function of the input signal amplitude.	176
<b>6.18:</b> Effect of the analogue switch properties upon a $\times 10$ gain stage: (a) ideal circuit; (b) actual circuit.	177
<b>6.19:</b> Sources of external interference: (a) ground currents between the output and input stages; (b) magnetic flux acting upon the cell.	179
<b>6.20:</b> Photograph of the user interface.	181
<b>6.21:</b> Photographs of the PCB boards: (a) the display module; (b) a single measurement channel.	181
<b>6.22:</b> Typical performance of a system channel. (a) $2\Omega^{-1}$ to $0.08\Omega^{-1}$ operating ranges; (b) $0.04\Omega^{-1}$ to $0.002\Omega^{-1}$ ranges.	183
<b>6.23:</b> Experimental results. The response to a periodic step change in the transfer function $G(\omega)$ ( $ G(\omega) =1$ to $ G(\omega) =0.5$ ), at various locations within the system. Note the level of agreement with figure 6.12.	184

## Chapter 7: Analysis system

7.1: Data acquisition and processing software components (schematic diagram).	187
7.2: Computer system used to acquire data from the conductance sensors.	188
7.3: Use of the <i>threshold level subroutine</i> to process a section of experimental data. (a) $\theta=0.7$ is used to identify the ‘slug’ and ‘film’ zones. (b) $t_{film}=1$ s is used, to eliminate sections of data less than 1 s long from the film zone.	189
7.4: Cross-correlation of a 15 s long ‘slug unit’. (a) Good continuity between the beginning and end of the sample. (b) Poor continuity between the beginning and the end.	191
7.5: Peak width of the normalised cross-correlation function $\rho_{xy}(\tau)$	192
7.6: Total superficial velocity correlation of Woods & Hanratty <sup>123</sup> .	195
7.7: Correlation for the total superficial velocity $j$ , developed using the experimental data from Chapter 8.	195
7.8: Correlation for the slip ratio $s$ , using the experimental data of Woods & Hanratty <sup>127</sup> .	196

## Chapter 8: Performance assessment

8.1: Schematic diagram of the NEL flow facility.	205
8.2: The NEL 4-inch test section.	205
8.3: The conductance sensors and the NEL test section.	206
8.4: The experimental test matrix, and the gas-water flow map for the NEL facility developed by Hall <sup>44</sup> .	211
8.5: Normalised cross-correlation sensor and holdup sensor data, for the test points $a$ to $m$ in figure 8.4.	211
8.6: Detailed structure within some selected slugs, for low total flowrate conditions.	214
8.7: Spectral content of the cross-correlation sensor data, for the four test points $a, d, j$ and $n$ .	215
8.8: Comparison of ‘individual slug’ and ‘entire trace’ cross-correlation functions, for the four test points test points $a, d, j$ and $n$ .	216
8.9: Comparison of the translation velocity $V_t$ and the uncertainty $\Delta V_t$ obtained using the ‘unit-by-unit’ cross-correlation and the ‘entire record’ cross- correlation techniques.	218
8.10: The signal bandwidth $B$ , as a function of the total superficial velocity $j$ (calculated using equation [7.4]).	218
8.11: Comparison of the cross-correlation sensor data against the additive noise signal $n(t)$ , for the test points $a, d, j$ and $n$ respectively.	219
8.12: Mean parameter values, and the standard deviation, as a function of the total superficial velocity $j$ : (a) the unit translation velocity $V_t$ ; (b) the phase fractions $a_f$ and $a_s$ ; (c) the slug frequency $\nu$ , (d) the film and slug lengths $l_f$ and $l_s$ .	221

<b>8.13:</b> Superficial velocity predictions, calculated using the closure relations 1, 2 and 3 (equations [8.6] to [8.8]). (a) liquid phase; (b) gas phase.	228
<b>8.14:</b> The effect of different techniques for <i>averaging</i> the sensor data and calculating the <i>translation velocity techniques</i> upon the superficial velocities $j_l$ and $j_g$ .	229
<b>8.15</b> Relative errors in the superficial velocities, using closure models 1, 2, and 3 (equations [8.6] to [8.8]). (a) liquid phase; (b) gas phase	230
<b>8.16:</b> Comparison of the sensitivities for each model parameter, for the two conditions $\{j_l=0.1 \text{ m s}^{-1}; j_g=1.0 \text{ m s}^{-1}\}$ and $\{j_l=1.0 \text{ m s}^{-1}; j_g=6.0 \text{ m s}^{-1}\}$	233
<b>8.17:</b> Comparison of the predictions errors $\delta j_l/j_l$ and $\delta j_g/j_g$ (shown in grey) against the cumulative uncertainty margins $\Delta j_l/j_l$ and $\Delta j_g/j_g$ (various colours). (a) liquid phase comparison; (b) gas phase comparison.	235
<b>Appendix A: ANSYS modelling</b>	
<b>A1:</b> The ANSYS command code ‘re $l_{sim}$ ’, used for obtaining conductance predictions between electrode pairs.	265
<b>A2:</b> The simulation geometry used by the command code ‘re $l_{sim}$ ’. (Illustrating the keypoint numbers, the line numbers, and the user-defined distances $X_l, z_{1a}, D_{es}, z_{2a}, X, z_{1b}, h, h_1, h_2,$ and $x$ ).	265
<b>A3:</b> Calibration experiments: simulation of a 2D ‘flat liquid layer’ geometry for a range of film thickness: (a) conductance predictions; (b) the relative error $\Delta G/G$ in the simulation, by comparison with the analytical solution of Coney <sup>27</sup> .	266
<b>Appendix B: Instrumentation design details</b>	
<b>B1:</b> Measurement board schematic diagram: generation of the control voltage $V_{ref}$ and the control logic for setting system gains $A, \beta$ and $C$ .	269
<b>B2:</b> Measurement board schematic diagram: feedback loop ( $\beta$ ) components.	270
<b>B3:</b> Measurement board schematic diagram: forward-loop ( $A$ ) components.	271
<b>B4:</b> Measurement board schematic diagram: transimpedance stage ( $C$ ) and channel output components.	272
<b>B5:</b> Display module schematic diagram: Generation of the 30kHz carrier signal waveform, and system backplane connections.	273
<b>B6:</b> Display module schematic diagram: routing of signals to the local output port and digital display.	274
<b>B7:</b> PCB layout diagram (individual measurement channel)	275
<b>B8:</b> PCB layout diagram: display channel.	276

## Appendix C: Processing software

C1: Computer code 'flvxtr', used for processing the raw data and calculation of the flow parameters ( $V_t$ ,  $a_s$ ,  $\overline{a_f}$ ,  $l_f$ ,  $l_u$  and  $\nu$ ), the phase superficial velocities ( $j_l$  and  $j_g$ ), and the superficial velocity uncertainty components ( $\Delta j_l/j_l$  and  $\Delta j_g/j_g$ )

282

## List of tables

### **Chapter 2. The multiphase flowmeter**

- 2.1:** Electrical properties of the oil, water and gas phases 41
- 2.2:** List of commercial multiphase flow meter manufacturers, the technology incorporated and the reference for further information (adapted from Thorn *et al*<sup>113</sup>) 52

### **Chapter 3. Modelling of slug flow**

- 3.1:** Summary of the most important closure relationships defined between Sections 3.3 and Section 3.6. 98

### **Chapter 4. Metering approach**

- 4.1:** Table of the sensitivity parameters  $S_j(x)$ , defined by equation [4.5]. (Obtained by the partial differentiation of equations [4.4a] and [4.4b]). 103
- 4.2:** The maximum permissible error in each parameter, for 5% relative accuracy in the flowrates over the test range. 109

### **Chapter 6. Instrumentation design**

- 6.1:** Settings for the parameters  $V_{ref}$ ,  $A$ ,  $\beta$ , and  $C$ , the control logic and the cell voltage, for each operating range. 172
- 6.2:** Cumulative effect of each d.c. error source upon the of the error sources upon the relative error  $\Delta G/G$ , for each operating range. 177

### **Chapter 7: Analysis system**

- 7.1.** Sets of closure relationships used to calculate the superficial velocities in Chapter 8. 194
- 7.2.** Sensitivity parameters used to calculate the flowrate uncertainties. 200

### **Chapter 8: Performance assessment**

- 8.1:** Data acquisition and processing parameters for each test point. 208
- 8.2:** Data processing results. The start time  $t$ , the translation velocity  $V_t$ , the phase fractions  $\bar{a}_f$  and  $a_s$ , the film length ratio  $l_f/l_d$  and the slug frequency  $\nu$ , for each slug unit. 223
- 8.3:** Superficial velocity predictions, using the closure models 1, 2 and 3 listed in Table 7.1. 227

<b>8.4:</b> The superficial velocities, absolute errors, and relative errors, expressed as percentages. These data are obtained using ‘entire record’ cross-correlation, ‘parameter-averaging’, and the closure models 1, 2 and 3 listed in table 7.1.	227
<b>8.5:</b> Relative uncertainties in the measurement of the parameters $V_i$ , $a_f$ and $a_s$ , and the estimates for $V_{ls}$ and $V_{gs}$ , $\theta$ and $t_{film}$ , expressed as percentages.	231
<b>8.6:</b> Relative uncertainty in the flowrates due to the uncertainties listed in Table 8.5: (a) liquid phase $\Delta j_l/j_l$ ; (b) gas phase $\Delta j_g/j_g$ .	232
 <b>Appendix A: ANSYS modelling</b>	
<b>A1:</b> Summary table of the parameter values used for each simulation in Chapter 5. ( $X_I=100\text{mm}$ and $z_{Ib}=100\text{mm}$ for all experiments)	267
 <b>Appendix B: Instrumentation design details</b>	
<b>B1:</b> Bill of materials: Measurement board components.	277
<b>B2:</b> Bill of materials: Display board components.	278
<b>B3:</b> Bill of materials: Casing, power supplies and miscellaneous parts not listed above.	279

## Key Symbols

### Modelling of slug flow:

<u>Symbol</u>	<u>Denotes</u>	<u>Units</u>
$A$	pipe cross-section area	$m^2$
$a_f(x)$	film zone liquid holdup profile	-
$\bar{a}_f$	mean film zone liquid holdup	-
$a_{fe}$	local holdup at end of film zone	-
$a_o$ $a_{os}$	oil component fractions (multiphase flow)	-
$a_s$	slug body liquid holdup	-
$a_w$ $a_{ws}$	water component fractions (multiphase flow)	-
$C$	distribution parameter (unaerated slug body)	-
$C_o$	distribution parameter (aerated slug body)	-
$D$	pipe diameter	m
$D_g$ $D_l$	gas / liquid phase hydraulic diameters (equation [3.52])	m
$Fr$	slug Froude number (unaerated slug body)	-
$Fr_l$	slug Froude number (aerated slug body)	-
$f_i$	interfacial friction factor	-
$f_g$ $f_l$	gas / liquid phase friction factors	-
$g$	gravitational acceleration	$m\ s^{-2}$
$H$	channel height (2D slug flow model)	m
$h_f(x)$	dimensionless film interface height profile	-
$h_{fe}$	interface height at the end of the film zone (equation [3.58])	-
$h_s$	slug holdup (2D slug flow model, equation [3.64])	-
$j$	total superficial velocity	$m\ s^{-1}$
$j_g$ $j_l$	gas / liquid phase superficial velocities	$m\ s^{-1}$
$j_o$ $j_w$	oil / water component superficial velocities (multiphase flow)	$m\ s^{-1}$
$k$	proportionality constant for gas release (equation [3.41])	$m\ s^{-1}$
$l_d$	slug body development length	m
$l_f$	film zone length	m
$l_m$	slug mixing zone length	m
$l_u$	total slug unit length	m
$m_g$ $m_l$	gas / liquid phase mass flowrates	$kg\ s^{-1}$
$m_o$ $m_w$	oil / water component mass flowrates (multiphase flow)	$kg\ s^{-1}$
$q_{gf}$ $q_{gt}$	gas pickup / gas shedding flux velocities	$m\ s^{-1}$
$q_{lf}$ $q_{lt}$	liquid pickup / liquid shedding flux velocities	$m\ s^{-1}$
$Re_s$	slug body homogeneous Reynolds number (equation [3.12])	-
$r_f(x)$	local holdup profile within the liquid film	-
$S_g$ $S_l$	gas / liquid phase wetted perimeters	m

<u>Symbol</u>	<u>Denotes</u>	<u>Units</u>
$S_i$	film interface wetted perimeter	m
$s$	slug body slip ratio	-
$t_f$	film zone duration, passing a fixed reference point	s
$t_s$	slug zone duration, passing a fixed reference point	s
$t_u$	total slug unit duration ( $t_f+t_s$ )	s
$V_d$	dispersed gas bubble rise velocity (equation [3.26])	$\text{m s}^{-1}$
$V_g(x)$	local gas velocity profile (film zone)	$\text{m s}^{-1}$
$V_{ge}$	local gas velocity, at end of film zone	$\text{m s}^{-1}$
$V_{gs}$	local gas velocity (slug body)	$\text{m s}^{-1}$
$V_l(x)$	local liquid velocity profile (film zone)	$\text{m s}^{-1}$
$V_{ls}$	local liquid velocity (slug body)	$\text{m s}^{-1}$
$V_{le}$	local liquid velocity, at end of film zone	$\text{m s}^{-1}$
$V_{mf}$	limiting film inlet velocity (equation [3.66])	$\text{m s}^{-1}$
$V_o$	slug flow drift velocity	$\text{m s}^{-1}$
$V_{of} V_{os}$	local oil component velocities (multiphase flow)	$\text{m s}^{-1}$
$V_t$	slug unit translation velocity	$\text{m s}^{-1}$
$V_{tl}$	liquid velocity in the slug tail (equation [3.64])	$\text{m s}^{-1}$
$V_{tt}$	slug tail translation velocity (equation [3.73])	$\text{m s}^{-1}$
$V_{ws} V_{ws}$	local water component velocities (multiphase flow)	$\text{m s}^{-1}$
$x$	distance parallel to flow axis (upstream direction)	m
$y$	distance normal to flow axis (inward from pipe wall)	m
$\beta$	pipe inclination	rad
$\Delta j_l \Delta j_g$	superficial velocity uncertainty (section 8.2.5)	$\text{m s}^{-1}$
$\Delta P_{film}$	total film zone pressure drop (figure 3.6)	Pa
$\Delta P_{slug}$	total slug body pressure drop (figure 3.6)	Pa
$\Delta P_f$	slug body frictional pressure drop	Pa
$\Delta P_m$	slug body mixing zone pressure drop	Pa
$\Delta P_r$	slug body rear pressure drop	Pa
$\delta(x)$	boundary layer development profile	m
$\delta j_l \delta j_g$	superficial velocity error (section 8.2.3)	$\text{m s}^{-1}$
$\phi$	phase inversion point (multiphase flow)	-
$\lambda$	in-situ water fraction (multiphase flow)	-
$\mu_g \mu_l$	gas phase / liquid phase viscosities	$\text{N m}^{-2}$
$\mu_o \mu_w$	oil / water component viscosities (multiphase flow)	$\text{N m}^{-2}$
$\nu$	slug frequency	Hz
$\theta$	angle subtended by liquid film	rad
$\rho_g \rho_l$	gas / liquid phase densities	$\text{kg m}^{-3}$
$\rho_o \rho_w$	oil / water component densities	$\text{kg m}^{-3}$
$\sigma$	liquid phase surface tension (equation [3.26])	$\text{N m}^{-1}$

$\tau_g$	$\tau_l$	gas phase / liquid phase shear stress	$\text{N m}^{-2}$
$\tau_i$		film interface shear stress	$\text{N m}^{-2}$
$\xi$		hydrostatic head pressure centroid	-

### Sensing instrumentation:

<u>Symbol</u>	<u>Denotes</u>	<u>Units</u>
$A$	system forward-loop gain (section 6.3.1)	-
$A_V$	operational amplifier open-loop gain	-
$a(t)$	cell buffer input waveform	V
$B$	cross-correlation signal bandwidth	Hz
$B_s$	sensor bandwidth	Hz
$b(t)$	waveform across the cell terminals	V
$C$	system transimpedance stage gain	$\Omega$
$C_c$	cross-correlation sensor cell constant	$\Omega^{-1}$
$C_h$	holdup sensor cell constant	$\Omega^{-1}$
$C_W$	cable capacitance per unit length (section 6.3.3)	$\text{F m}^{-1}$
$c(t)$	cell voltage carrier waveform, before demodulation	V
$D$	pipe diameter	m
$D_e$	conductance sensor ring electrode separation	m
$d(t)$	demodulated cell voltage waveform	V
$e(t)$	feedback junction output waveform	V
$f(t)$	PI controller output waveform	V
$G(\omega)$	cell voltage transfer function (section 6.3.3)	-
$G^*$	full-pipe conductance (chapter 5)	$\Omega^{-1}$
$G_{cell}$	cell conductance	$\Omega^{-1}$
$G_{FS}$	instrumentation full-scale conductance	$\Omega^{-1}$
$g(t)$	transimpedance amplifier output waveform	V
$H(\omega)$	cell current transfer function (section 6.3.3)	-
$h$	equivalent liquid layer thickness (equation [5.4])	m
$h(t)$	demodulated transimpedance stage waveform	V
$I_{cell}$	cell current	A
$I_{leak}$	leakage current (section 5.3.5)	A
$i(t)$	channel output signal	V
$L_W$	coaxial cable inductance per unit length	$\text{H m}^{-1}$
$l$	coaxial cable length (section 6.3.3)	m
$l$	effective liquid layer contact distance (equation [5.4])	m
$n(t)$	additive noise signal	-
$P(\omega)$	PI controller transfer function	-
$R_{cell}$	cell resistance	$\Omega$

<u>Symbol</u>	<u>Denotes</u>	<u>Units</u>
$R_{con}$	connection resistance (section 6.3.3)	$\Omega$
$R_f$	transimpedance amplifier feedback resistance	$\Omega$
$R_{leak}$	cell leakage resistance (section 5.3.5)	$\Omega$
$R_{xx}(\tau)$	upstream signal autocorrelation function	-
$R_{xy}(\tau)$	cross-correlation function	-
$R_{yy}(\tau)$	downstream signal autocorrelation function	-
$r$	pipe radius	m
$s$	sensor ring electrode width	m
$T$	cross-correlation record duration	s
$t$	time	s
$V_d$	cell driving voltage amplitude (equation [6.10])	V
$V_o$	output voltage signal amplitude (equation [6.10])	V
$V_{ref}$	feedback loop d.c. reference voltage	V
$X$	guard electrode length (figure 5.13)	m
$x$	position of step change in film thickness (figure 5.1b)	m
$x(t)$	upstream cross-correlation sensor signal	-
$y(t)$	downstream cross-correlation sensor signal	-
$Z_I$	instrumentation amplifier internal impedance	$\Omega$
$Z_D$	driving (buffer) amplifier internal impedance	$\Omega$
$Z_T$	transimpedance amplifier internal impedance	$\Omega$
$Z_{WC}$	coaxial cable capacitive impedance (figure 6.4)	$\Omega$
$Z_{WL}$	coaxial cable inductive impedance (figure 6.4)	$\Omega$
$z_1 z_2$	sensor unit insulation distances (figure 5.12)	m
$\beta$	system feedback gain	-
$\epsilon$	fluid permittivity	$F m^{-1}$
$\mu_x \mu_y$	signal mean values (upstream/downstream sensors)	m
$\theta$	angle subtended at the pipe perimeter (section 5.1.1)	rad
$\rho_{xy}(\tau)$	normalised cross-correlation function	-
$\sigma$	fluid conductivity	$\Omega^{-1} m^{-1}$
$\tau^*$	cross-correlation function principal delay	s
$\omega_c$	carrier signal frequency	$rad s^{-1}$
$\omega_m$	multiplexing frequency	$rad s^{-1}$

(blank page)

## 1. Introduction

The mixture of fluid that emerges from an offshore oilwell needs to be continuously monitored. This monitoring is essential to ensure that production quotas are met, and also to ensure that the pipelines can be safely operated. These two requirements have led to the development of the *multiphase flow meter*.

As larger oilfields are used up, it becomes necessary to drill *satellite wells* around the main production zone. The contents of these wells are mixed at a manifold, and then they are transported to the surface via a trunk pipeline. However, because of the varying contents of each well (and because some wells may be owned by different companies) it is essential to meter the flowrates *before* the mixing at the manifold. Traditionally, this metering required the installation of sampling pipelines between each satellite well and the production platform. Such a solution is expensive and difficult to maintain, and occupies a lot of space on the production platform. The installation of multiphase flow meters at each well head is a preferable alternative, because the sampling pipelines become redundant.

The typical multiphase flow meter is a ‘technology-intensive’ system. It requires sensors that measure the fluid velocities, the fluid fractions and fluid densities, which must then be linked to software that analyses the data and calculates the flowrates. The system should also satisfy the following criteria:

- *Versatility*. (Ability to measure a wide range of flow phenomena in different offshore fields).
- *Durability*. (The amount of maintenance should be minimal, because of high installation costs).
- *Non-intrusiveness to flow*. (Intrusions into the pipeline complicate the design and inhibit the flow production).
- *Low cost*.

Despite the great cost of manufacturing and operating a multiphase meter (typically in the region of £100,000), considerable savings can be made over the lifetime of a well. However, to realise these savings it is important that the multiphase flow meter has *good measurement accuracy*. Uncertainties of less than about 5% in the mass flowrate measurement, and less than 2% in the ‘water-cut’ measurement, are considered necessary by the offshore industry for viability (Slijkerman *et al*<sup>108</sup>). Because there are many possible patterns in which the oil,

water and gas can be transported, these requirements are hard to achieve. The difficulty becomes particularly acute when one is trying to meter three-phase oil-water-gas *slug flow*.

## 1.1 Thesis overview

Multiphase flow can arrange itself as a variety of *flow patterns*, depending on the individual phase flowrates. Some commonly encountered patterns are ‘bubble flow’, ‘annular flow’, ‘stratified flow’ (horizontal pipes only), ‘churn flow’ (vertical pipes only), and *slug flow*. Slug flow often occurs in offshore pipelines, because of the high temperatures in the reservoir and the well head (around 120°C), which cause much of the liquid phase to evaporate. This flow pattern is damaging to pipework and it is particularly difficult to measure, due to large fluctuations in the local phase flowrates.

In this thesis, an attempt will be made to meter slug flow by measuring its *local characteristics*. The approach will be to measure the ‘slug zone’ and the ‘film zone’ in each slug unit, and combine these with a model taken from the literature. Two-phase (gas-water) slug flow shall be studied as opposed to three-phase (gas-water-oil) flow, for the following reasons:

- A three-phase flow meter is very expensive to develop, because of the difficulty in distinguishing between the oil and water components. By studying two-phase (gas-water) flow, the cost of the instrumentation is greatly reduced.
- Multiphase meters need to calculate the total liquid flowrate, before the individual oil phase and water phase flowrates can be determined. Therefore, accurate measurement of two-phase slug flow is a fundamental problem that must be addressed before an accurate measurement of a three-phase slug flow can be made.

As shall be discussed in Chapter 2 that follows, most commercial meters will make *global* measurements for the phase velocities and the phase fractions. By adopting a more sophisticated approach where the ‘slug zone’ and the ‘film zone’ are separately considered, an improvement in the metering accuracy is to be expected.

## 1.2 Thesis objectives

In this thesis, slug flow shall be generated using the NEL multiphase flow facility and shall then be metered using a set of non-intrusive sensors, a predictive model, and a set of empirical closure relationships. The predicted flowrates shall then be compared against the reference flowrates for the facility, and used to judge the effectiveness of the approach. This work is divided into four main objectives:

- A literature review, where the components of the multiphase meter and models for the slug flow process will be described.
- An assessment of the metering approach. The parameters within the slug flow that need to be measured will be identified, and the sensitivity of the model to these parameters and the most suitable measurement instrumentation will be discussed.
- Development of the metering system. A low-cost, non-intrusive set of electrodes, novel electronic instrumentation, and new software for the analysis of the sensor data will be created.
- Assessment of the system, using the NEL 4-inch multiphase flow facility. A series of horizontal slug flow will be generated and metered with the sensors, covering the range of liquid phase superficial velocities from  $0.1 \text{ m s}^{-1}$  to  $1 \text{ m s}^{-1}$  and the range of gas phase superficial velocities from  $0.6 \text{ m s}^{-1}$  to  $6 \text{ m s}^{-1}$  respectively.

A unique, and very important feature of the system will be its ability to calculate the *uncertainty margins* in the phase flowrates. These uncertainty margins will be compared against the flowrate errors (i.e. the difference between the calculated and the actual flowrates), and will then be used to determine whether or not the slug flow model is valid. As a result, it will be possible to conclude whether either the *model* or the *parameter measurements* need to be improved.

## 1.3 Thesis structure

The rest of this thesis is divided into eight chapters. The four objectives presented above are addressed in Chapters 2 to 3, Chapter 4, Chapters 5 to 7 and in Chapter 8 respectively, while Chapter 9 contains conclusions and suggestions for future work. In greater detail, their content is as follows:

- Chapter 2 will describe the components of the multiphase meter. The instrumentation for measuring the phase velocities, the phase fractions, the phase densities, and software for delivering the phase flowrates will be discussed. The performance of a typical flow meter, and the major limitations in this performance, will be summarised.
- Chapter 3 reviews the modelling of slug flow. The ‘slug flow’ process will be verbally described, and a model for the gas and the liquid flowrates will be presented. Various ‘sub-models’, defining the local velocities, the pressure drop, and the ‘slug pickup’ and ‘slug shedding’ processes will then be described, and some empirical correlations will then be presented. A model for three-phase (oil-water-gas) slug flow will then briefly be discussed.
- Chapter 4 discusses the approach that will be used to meter the gas-water slug flow. The parameters that will be measured are established, by analysing the *stable slug flow* model. The accuracy required in each measurement will then be established, by conducting a *sensitivity analysis*. The appropriate instrumentation for measuring each parameter is selected from Chapter 2. The need for new measurement techniques, or to use the ‘closure relationships’ described in Chapter 3, will be highlighted.
- Chapter 5 describes the design of conductance electrodes, for the measurement of the slug phase fractions and the translation velocity. The goal here is to minimise the measurement uncertainty. In each design, the separation between the electrodes will be carefully chosen, to compromise between conflicting factors. The measurement uncertainty will then be assessed, using simple geometric models and numerical simulation. Finally, the manufacture of the ‘sensor units’ and the prevention of crosstalk between the adjacent sensors will be discussed.
- Chapter 6 describes the design of an electronic instrument to measure the conductance between the electrode pairs. This instrument must be able to measure a large cell conductance, with a *wide bandwidth* and *high accuracy*. A novel analogue solution, which maintains a constant voltage across the conductance electrodes will be developed. The principle and the detail of this solution will be presented, the implementation using real components will be discussed, and then the performance will be verified by simple experiments.
- Chapter 7 describes the computer system for acquiring the sensor data and delivering the phase flowrates. The software will extract the phase fractions and the velocity for each ‘slug unit’, calculate the local velocities using closure

relationships, ‘average’ the ensemble data, and then deliver the phase flowrates. The computer hardware, the computer software, and the equations used to estimate the uncertainty margins, will each be discussed.

- Chapter 8 describes the assessment of the metering system, using gas-water slug flow data gathered from the NEL facility. The flow loop will be described, and the ‘raw’ experimental data will be presented. These data will be processed to obtain the *model parameters*, the predictions for the phase *flowrates*, and the *uncertainty* in the predictions. The prediction error and the prediction uncertainty will be compared. This comparison will be used to define the limitations of the system.

Chapter 9 will summarise the work done in this thesis, and will highlight the areas where future work is required. The four objectives of the thesis will be restated, and success in achieving each one shall be judged. It will be shown that the system is unable to meter the phase flowrates, particularly at low liquid velocities, with this inability largely due to uncertainties in the closure relationships used to estimate the local velocities. Finally, the nature of these closure relationships shall be discussed in some detail. Some proposals for improving the measurement of the translation velocity and the local film velocities in each slug shall be presented.

## 2. The multiphase flowmeter

In this chapter, some of the (many) techniques that can be used to meter multiphase flow shall be described. This description is separated into two parts. First of all, some common methods that are used for sensing the flow and processing the sensor data will be explained. The respective contents of Section 2.1 to Section 2.4 sections are as follows:

- Section 2.1 will describe differential pressure, cross-correlation, positive displacement and NMR techniques that can be used to measure the *phase velocities*, as well as instruments for homogenisation and separation of the flow.
- Section 2.2 will describe gamma-ray attenuation and electrical impedance techniques for measuring the *phase fractions*, and the further development of these techniques to provide *tomographic imaging* (i.e., reconstruction of the phase fraction distribution inside the pipe section).
- Section 2.3 will describe a standard technique for *density measurement*, which uses measurements of pressure and temperature and periodic sampling of the fluids at the pipe outlet.
- Section 2.4 will describe the *processing software*, which converts data from the sensors into phase flowrates. This software must identify the flow regime, evaluate the most suitable predictive model, and be able to provide suitable closure relationships where direct measurements of the model parameters cannot be obtained.

The components that are described in these four sections are summarised in Figure 2.1, on the following page.

Secondly, section 2.5 will discuss the performance of a commercial multiphase flow meter. Here the range of flowrate conditions that needs to be metered, possible combinations of the sensing instrumentation, and the accuracy that is necessary in the measurement shall be discussed. The main trends in the performance, and some reasons why there is poor performance when slug flow is being metered will be highlighted.

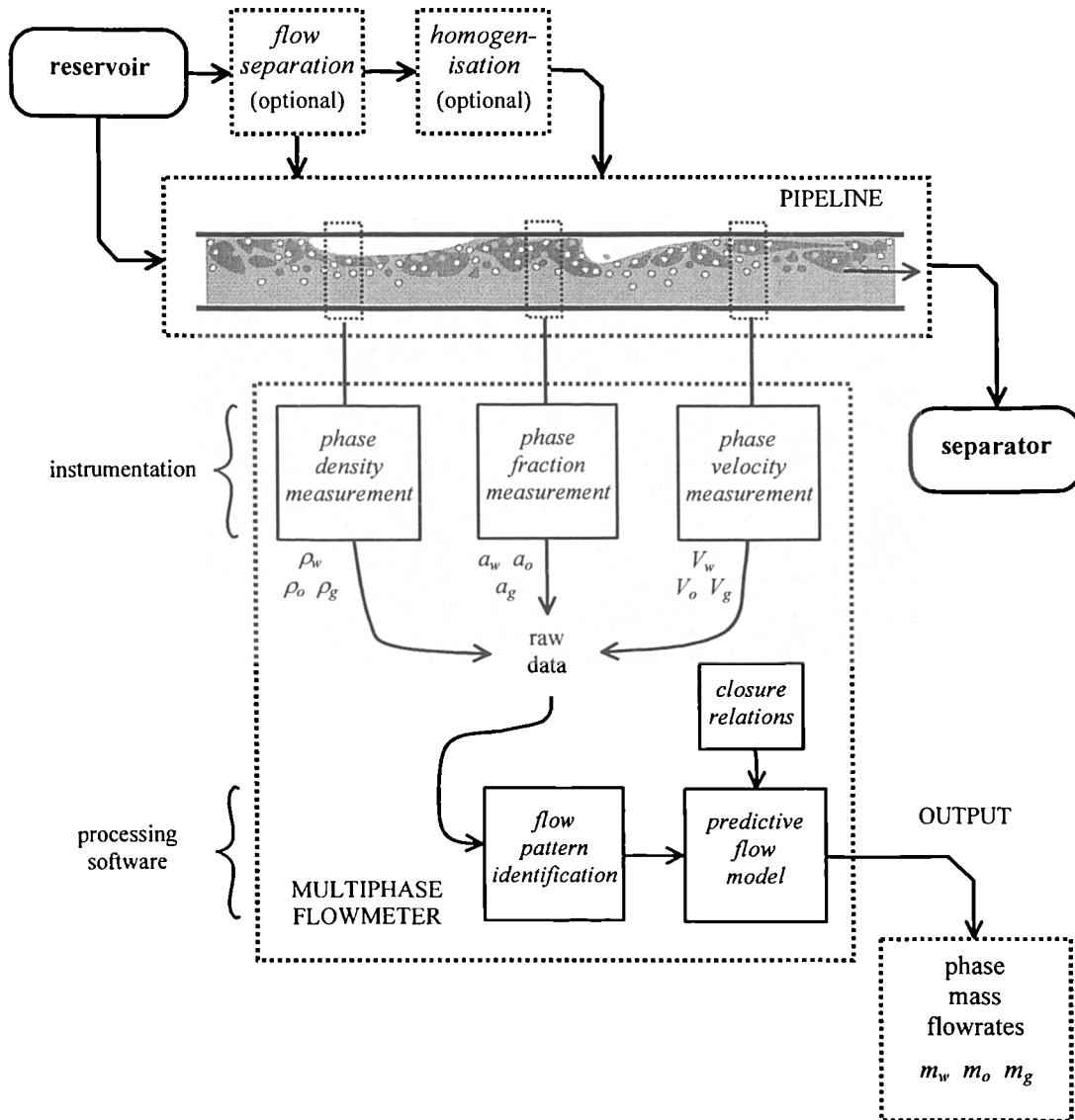


Figure 2.1: Principal components of the multiphase flow meter.

## 2.1 Phase velocity measurement

Of the various techniques available for making the phase velocity measurement, the differential pressure, cross-correlation, positive displacement and nuclear magnetic resonance (NMR) methods will be described in this section. The limitations and the frequency of use of each technique will be discussed. It should be noted that some of the material in this section is not developed in the rest of this thesis, but is included for completeness.

### 2.1.1 Differential pressure measurement

The mean flow velocity can be measured using a Venturi meter, an example of which is illustrated in figure 2.2 below. The meter throat restricts the flow, and thus produces a measurable pressure drop  $\Delta P$  that is similar to that obtained in single-phase flow. Assuming that the amount of fluid coming into the Venturi meter is steady, the mixture velocity is given by:

$$V = C_d \sqrt{\frac{2\Delta P - \rho gh}{\rho(1 - \beta^4)}} \quad [2.1]$$

where  $\rho$  is fluid density,  $C_d$  is the meter discharge coefficient,  $\beta$  is the ratio of throat to pipe diameter, and  $\rho gh$  is the meter hydrostatic head (zero for a horizontal inclination). As the Venturi method is relatively inexpensive, and as it can deliver a measurement accuracy of better than 1% for ‘well homogenised’ single-phase flow, it is frequently used within a multiphase system.

In general, the components in multiphase flow travel at different velocities, so that the measurement uncertainty increases. For approximately uniform flow, e.g. a wet-gas flow or an oil-in-water dispersion, it is possible to make empirical corrections to the discharge coefficient  $C_d$ . For example, Pal<sup>95</sup> describes an adjustment to the coefficient  $C_d$  for use in oil-water mixtures. However, for true multiphase flow, it is necessary to develop a *pressure drop correlation*. Several workers (for example, Lockhart & Martinelli<sup>68</sup>, Chisholm<sup>26</sup> and Hall<sup>45</sup>) have measured the pressure drop in straight pipe sections, and have found that this is strongly dependent upon the flow regime. This situation also arises for flow passing through a Venturi meter. Therefore, the relationship between the pressure drop and the phase velocities is not unique.

To achieve a more uniform flow profile, it may be necessary to mix or separate the flow upstream of the metering point. This is normally achieved by using the instruments illustrated in figure 2.4. The *flow homogeniser* (figure 2.4a) forces the gas phase to disperse into the liquid because of pressure build-up, while the *flow separator* (figure 2.4b) allows the gas to settle naturally above the liquid phases. These two types of instrument have a limited range, however, and their performance is optimised when:

- The gas fraction in the flow is small, less than 30% by volume (for the flow homogeniser).
- The gas fraction and the chamber size are both large, and the velocity of the incoming mixture is low (for the flow separator).

In general, it is difficult to design a homogenisation or a separation system that will operate effectively over a wide range of flowrates. It may be necessary to have several different chambers (and divert the flow accordingly), in order to guarantee accurate metering of the flowrates.

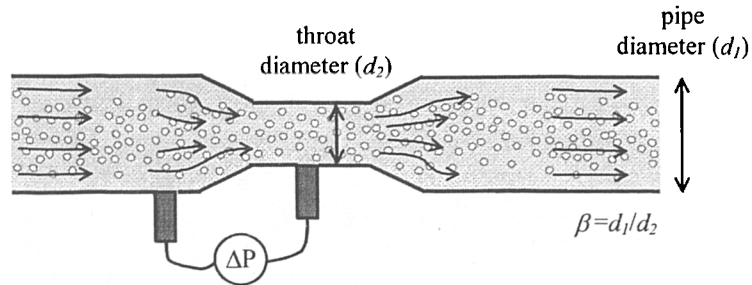


Figure 2.2: Venturi meter for total velocity measurement

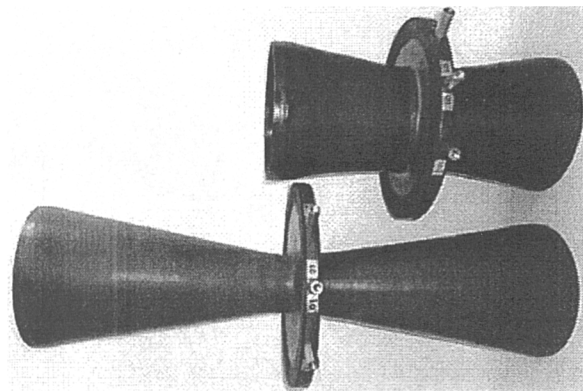


Figure 2.3: Typical 12-inch Venturi meter sections (Westfall Instruments).

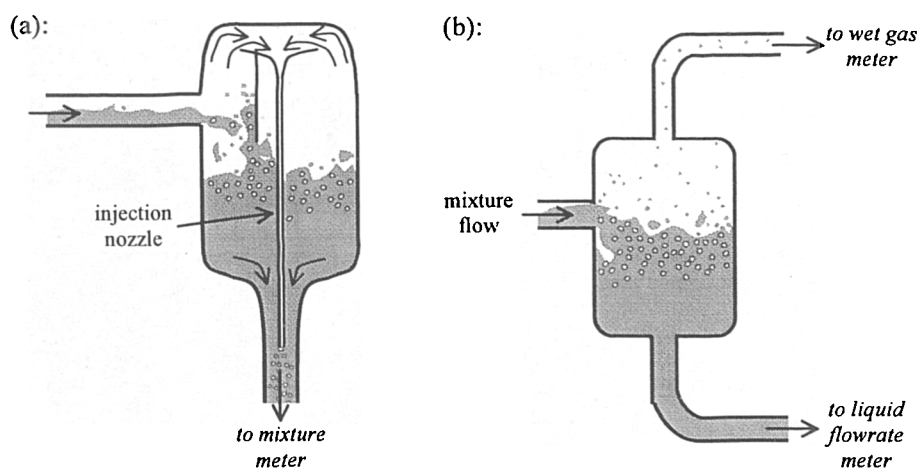


Figure 2.4: Typical designs for the flow homogeniser and the flow separator.

### 2.1.2 Signal cross-correlation

The individual velocities in multiphase flow can be determined, by *cross-correlating* the signals produced by a set of sensors. This principle is illustrated in figure 2.5. Two (or more) identical sensors are mounted at a distance  $x$  apart, so that the flow signals  $x(t)$  and  $y(t)$  are respectively produced (moving in the downstream direction). The cross-correlation of these signals is then defined by the function:

$$R_{xy}(\tau) = \lim_{T \rightarrow \infty} \frac{1}{T} \int_0^T x(t)y(t-\tau) dt \quad [2.2]$$

where  $T$  is the duration of the data being correlated. The function  $R_{xy}$  is often *normalised* so that its value always lies between +1 (perfect correlation) and -1 (anti-correlation); this process is discussed in detail in Chapter 7. Ideally,  $R_{xy}$  will have a distinctive peak at the time delay  $\tau = \tau^*$  (figure 2.5b). From this peak, the flow velocity is given by:

$$V = \frac{x}{\tau^*} \quad [2.4]$$

Often, however, there is evolution in the flow between the sensors. This causes the cross-correlation peak to reduce in height and broaden (figure 2.5c), and introduces uncertainty into the velocity measurement.

Because there is no limitation placed upon the sensing technology, the cross-correlation technique is very easy to incorporate into a multiphase flow meter. For example, Ong & Beck<sup>94</sup> and Xu *et al*<sup>131</sup> have used ultrasonic sensors, Roach & Watt<sup>102</sup> have used gamma-ray sensors, Økland & Berentsen<sup>90</sup> have used microwave sensors; Xie *et al*<sup>130</sup>, Lucas & Walton<sup>72</sup> and Manfield<sup>75</sup> used impedance sensors, and Lin & Hanratty<sup>67</sup> have used pressure transducers for the measurement of multiphase velocities. However, each type of sensor should satisfy the following criteria, in order to ensure accurate results:

- The sensors should have a wide bandwidth, in order to capture the *turbulent noise* within the flow. This wide bandwidth will result in a ‘narrow peak’ in the function  $R_{xy}$ .
- The sensor separation  $x$  should be optimised, to minimise the evolution of the flow between the signals, but also to minimise sensor crosstalk and the separation uncertainty ( $\Delta x/x$ ). This optimum separation will result in a ‘tall peak’ in the function  $R_{xy}$ .

In practice, the sensors should be as small as possible, and should be separated by about a few pipe diameters, to satisfy these criteria (see Beck & Plaskowski<sup>17</sup>). For well-homogenised flow, a relative accuracy of about 1% can then be achieved.

As discussed in the previous subsection, the individual phases will normally travel at different velocities. Under these conditions the measurement uncertainty increases. It may be also difficult to determine *which* phase velocity is actually being measured. To get round this difficulty, sensors have been developed which can simultaneously detect *multiple* velocities. For example:

- Xu *et al*<sup>131</sup> have developed an ultrasonic technique for detection of the gas and liquid velocities in bubble flow. The liquid velocity was determined by a pulse-echo technique, while the gas velocity was detected due to the scattering of the sound by the passing bubbles.

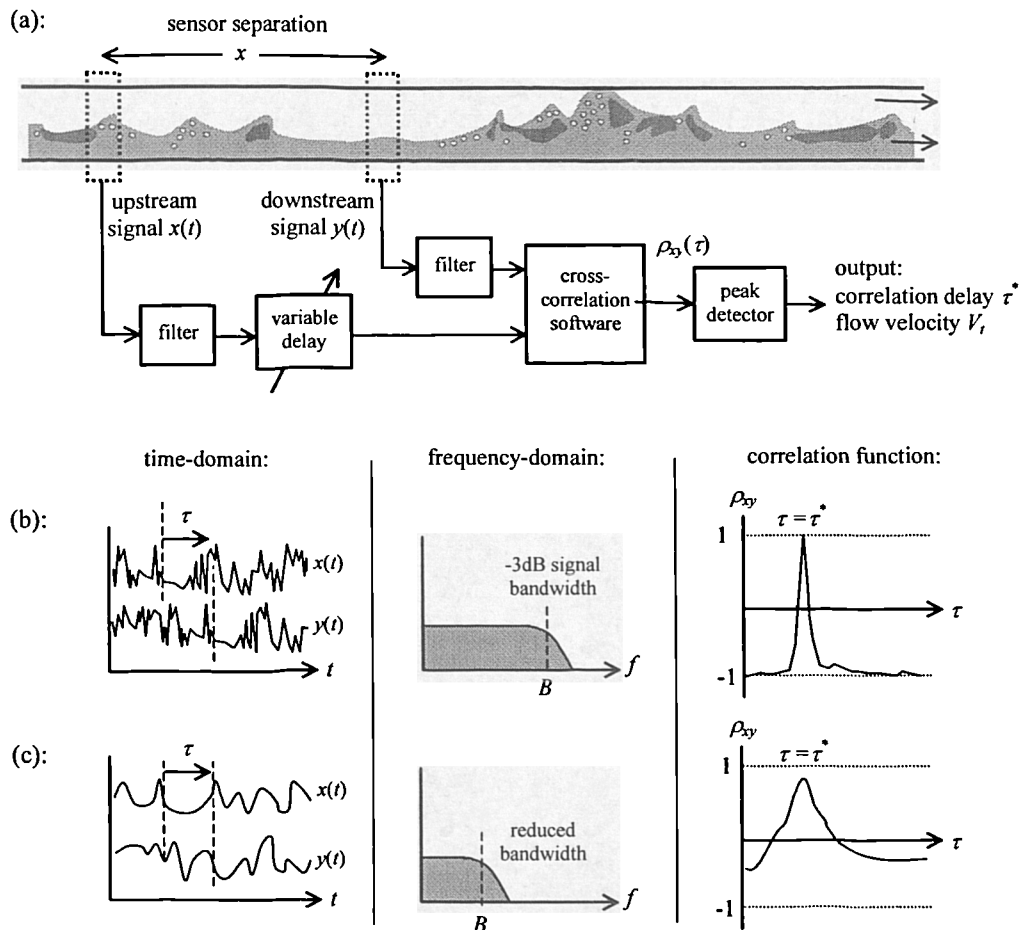


**Figure 2.5:** Cross-correlation velocity measurement. (a) system components; (b) the ideal sensor output and the normalised function  $\rho_{xy}$ ; (c) the actual sensor output and function  $\rho_{xy}$ , due to spatial filtering and flow evolution effects.

- Lucas & Albusaidi<sup>69</sup> developed an array of many conductivity sensors, for measuring the velocities in slug flow. By carefully choosing which pairs of signals to correlate, it was possible to simulate ‘movement’ through the flow, and measure the gas velocity relative to this movement.
- Olsvik *et al*<sup>92</sup> described a system of concentric capacitance electrodes, for separate measurement of phase velocities in homogenised mixtures. The outer electrode measured the velocities of passing slugs and waves, while the inner electrode was used to measure the velocities of the bubbles in the pipe core.

In general, it is not possible to measure all the phase velocities three-phase (oil-water-gas) flow, without the use of intrusive sensors. This measurement problem is particularly acute, for the *slug flow* regime.

### 2.1.3 Positive displacement method

In the positive displacement method, the inertia of the liquid phase is directly measured by inserting a contact plate into the flow. One of many possible designs is illustrated in figure 2.6. In this particular design (‘turbine-type’), the contact plates drive a rotating shaft. The momentum imparted to each plate is a function of the liquid phase velocity and the contact area. Therefore to a first approximation, the rotation frequency ( $\omega$ ) is proportional to the *volumetric flowrate*. Commercial multiphase systems that use this technique are discussed by Tuss *et al*<sup>120</sup>, and by Priddy<sup>98</sup>.

The major advantage of the displacement method is that it eliminates the need to measure the liquid phase fraction. However, the method must intrude into the flow to yield results, and it is incapable of measuring the gas phase flowrate. Furthermore, the system may not be able to respond quickly to large fluctuations in the liquid phase flowrate. Therefore, it may be necessary to homogenise or separate the phases beforehand, to obtain reliable results in slug flow.

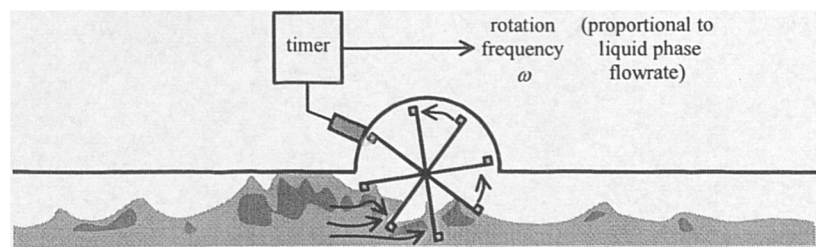
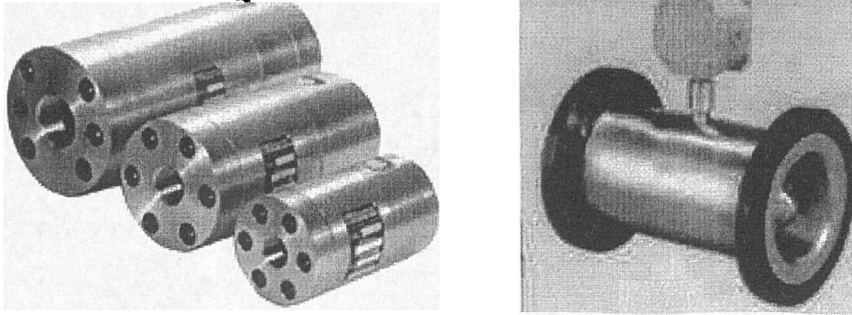


Figure 2.6: ‘Turbine’- type positive displacement flowmeter.



**Figure 2.7:** SRZ Series Geared positive-displacement meters (AW Company) and FTM turbine flowmeter.

#### **2.1.4 Nuclear magnetic resonance**

In nuclear magnetic resonance (NMR), strong magnetic fields are applied to the passing flow using the system illustrated in figure 2.8 below. These magnetic fields cause a realignment of the magnetic spins within each atom. Two magnetic field pulses are then applied, which introduce an axial sensitivity in the measurement. A radio-frequency coil is used, to measure the decay of the magnetic flux between these pulses. A distribution of the flow velocities within the pipe section is then obtained.

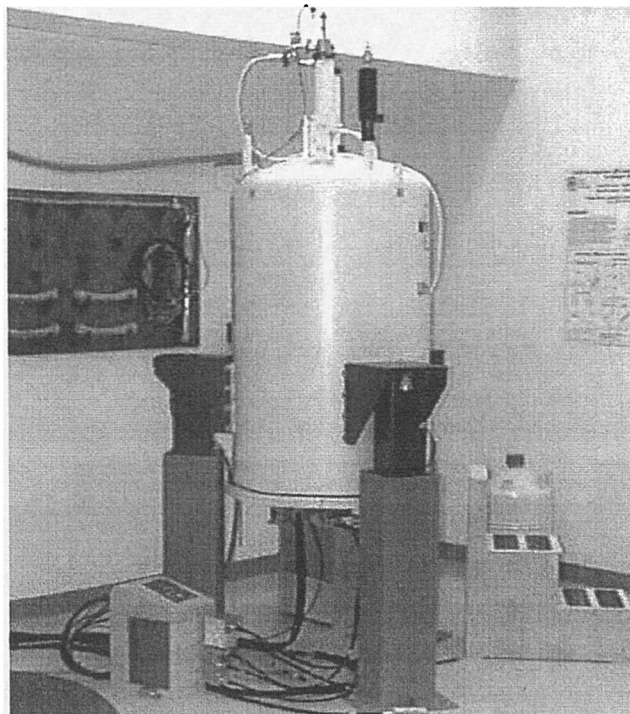


**Figure 2.8:** Two-phase NMR system (Sandia National Laboratory)

The NMR technique is non-intrusive, and has two significant advantages compared to the other techniques described in this section. These are:

- The magnetic fields can be used to target specific nuclei, so that independent measurements of phase velocities can be made.
- The strength of the decay pattern increases with the content of each phase present in the sensing volume. As a result, the phase holdups and the volumetric flowrates can also be measured.

Kruger *et al*<sup>62</sup> demonstrate how successful the NMR technique is at measuring two-phase (gas-water) flows. They report a high degree of accuracy in the velocity measurement over a wide range of conditions, and results that are independent of the flow regime encountered. In principle, NMR would be an ideal tool for metering multiphase flows, except that its potential is limited by the cost.

## **2.2 Phase fraction measurement**

A greater variety of techniques can be used to obtain the *phase fraction* measurement, ranging from gamma-ray attenuation, capacitance- or conductance- based impedance metering, to tomographic imaging. These techniques are described in detail sub-sections 2.2.1 to 2.2.3 below, for completeness. Alternatives such as pulsed neutron activation ('PNA') and microwave attenuation are not discussed in this thesis; for more details consult Hewitt *et al*<sup>52</sup> or Ashton<sup>13</sup> respectively.

### **2.2.1 Gamma-ray attenuation**

The phase fractions along a linear path may be determined, by using a dual-energy gamma-ray source and a photon detector. Several such measurements through the pipe cross-section are illustrated in figure 2.9a. For each energy level that is emitted by the source ( $E$ ), the count rate that is detected is defined by the equations:

$$\begin{aligned} I_1 &= I_{e1} e^{-(\mu_w \alpha_w + \mu_o \alpha_o + \mu_g \alpha_g) E_1 d} \\ I_2 &= I_{e2} e^{-(\mu_w \alpha_w + \mu_o \alpha_o + \mu_g \alpha_g) E_2 d} \end{aligned} \quad [2.5]$$

where  $I_e$  is the empty-pipe count rate,  $\mu_w$ ,  $\mu_o$  and  $\mu_g$  are linear radiation attenuation coefficients for each energy level, and  $\alpha_w$ ,  $\alpha_o$  and  $\alpha_g$  are the linear phase fractions along

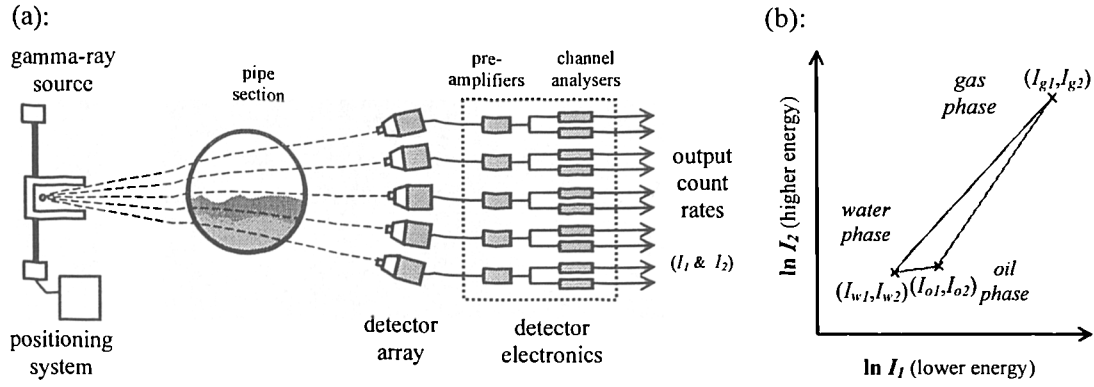


Figure 2.9: Principle of the multi-beam gamma-ray densitometer system. (a) system components; (b) calibration points for three-phase flow.

each path. The pipe section is calibrated with the oil, water and gas phases beforehand, so that the phase fractions in a general case can be determined by the solution of the equation:

$$\begin{bmatrix} \ln I_{w1} & \ln I_{o1} & \ln I_{g1} \\ \ln I_{w2} & \ln I_{o2} & \ln I_{g2} \\ 1 & 1 & 1 \end{bmatrix} \begin{bmatrix} \alpha_w \\ \alpha_o \\ \alpha_g \end{bmatrix} = \begin{bmatrix} \ln I_1 \\ \ln I_2 \\ 1 \end{bmatrix} \quad [2.6]$$

where  $I_w$ ,  $I_o$  and  $I_g$  are the *calibration count rates* for each energy level. These calibration count rates form a triangle, illustrated in figure 2.9b, within which all the possible permutations of phase fractions are contained.

In principle, the gamma-ray attenuation method offers a high level accuracy in the phase fraction measurement. For example, Pan<sup>96</sup> reported an *absolute* accuracy of 1% in the gas and liquid fractions, by using a  $\text{Ba}^{133}$  radiation source. However, the method suffers the following limitations:

- The measured count rates at each detector must be large enough to eliminate statistical uncertainty, which compromises the instrument dynamic response (typically 0.1-1s). A more intense source can be used to overcome this problem, at the expense of an increased radiation hazard.
- Poor discrimination between oil and water phases, due to very similar oil and water count rates. Similar count rates mean that equation [2.5] suffers from ill-conditioning, or in other words, the oil and water calibration points in figure 2.6b lie very close together. A careful choice of the radiation source is required to minimise this problem.

- There is a long-variation in the water phase attenuation coefficient ( $\mu_w$ ), due to the changing amount of salt contained salt in the reservoir. This problem may be calibrated out by using additional energy levels, and is discussed in greater detail by Scheers & Letton<sup>105</sup>.

There is one further problem with the gamma-ray system. The conversion of the linear phase fractions into area fractions ( $a_w$ ,  $a_o$  and  $a_g$ ) requires the homogenisation of phases beforehand, or assumptions to be made about the flow geometry. It may be possible to remove these difficulties by developing a *gamma-ray tomography* system, which is discussed in Section 2.2.3 below.

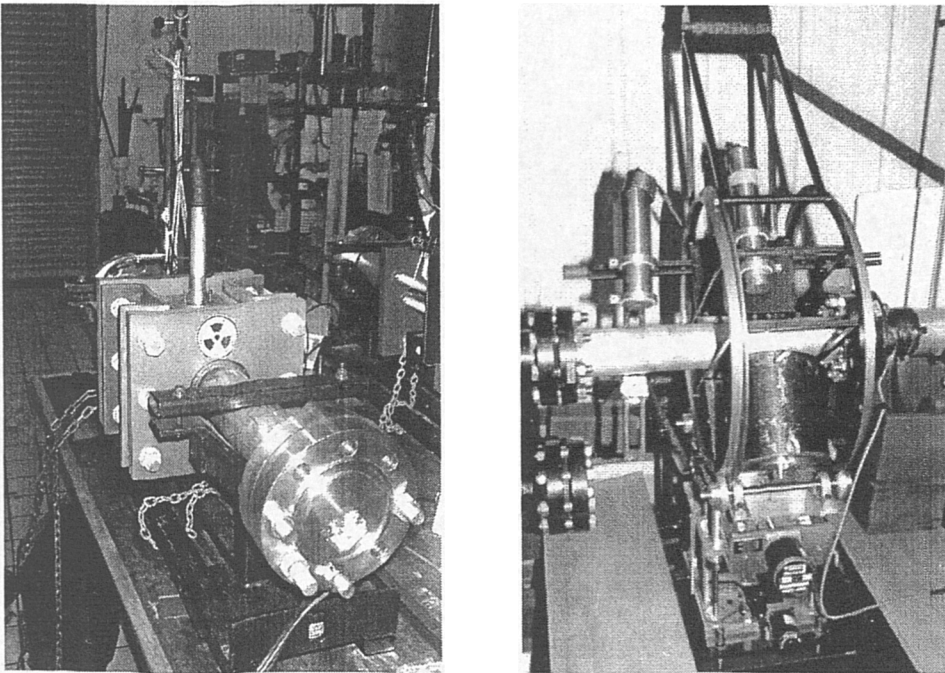


**Figure 2.10:** Single-beam and traversing-beam type gamma-ray densitometers (Imperial College).

### 2.2.2 Impedance electrodes

A measurement of the local phase fractions can be obtained by applying a voltage across a set of impedance electrodes. The electric field between these electrodes is governed by the equations:

$$\nabla \cdot \underline{\epsilon E} = 0 \quad \underline{J} = \sigma \underline{E} \quad \underline{E} = -\nabla V \quad [2.7]$$

where  $V$  is the local potential,  $\underline{J}$  is the current density,  $\epsilon$  is the permittivity distribution and  $\sigma$  is the conductivity distribution. At the electrode surfaces, the cell resistance ( $R_{cell}$ ) and the cell capacitance ( $C_{cell}$ ) are defined by:

$$\begin{aligned} R_{cell} &= V/I & I &= \oint_S \sigma \underline{E} \cdot d\underline{S} \\ C_{cell} &= Q/V & Q &= \oint_S \epsilon \underline{E} \cdot d\underline{S} \end{aligned} \quad [2.8]$$

where  $I$  and  $Q$  are the current and total charge contributions. Depending upon the shape and size of the electrodes and the flow geometry, the measured values for  $R_{cell}$  and  $C_{cell}$  can be used to infer the *phase holdup*.

Figure 2.11 illustrates the instrumentation that is used to obtain the resistance and the capacitance measurements. The cell is driven using an a.c. source, and the *total impedance* is calculated by measuring the ratio of the cell voltage to the cell current. The capacitive component of this impedance is then determined, by measuring the *phase angle* between the current and the voltage. This phase angle measurement requires that the frequency of the a.c. source be of the order:

$$\omega \sim \sigma_c / \epsilon_c \quad [2.9]$$

where  $\sigma_c$  and  $\epsilon_c$  are the electrical properties of the continuous fluid. As shown in table 2.1, the air and the oil are insulators, while the water phase is a weak conductor. This means that the phase measurement of air and oil-continuous flows is only possible at microwave frequencies. A phase measurement is also difficult to obtain below 10kHz, due to polarisation of the water molecules (Coney<sup>27</sup>). This polarisation results in an unwanted *double-layer capacitance* being formed at the cell electrodes.

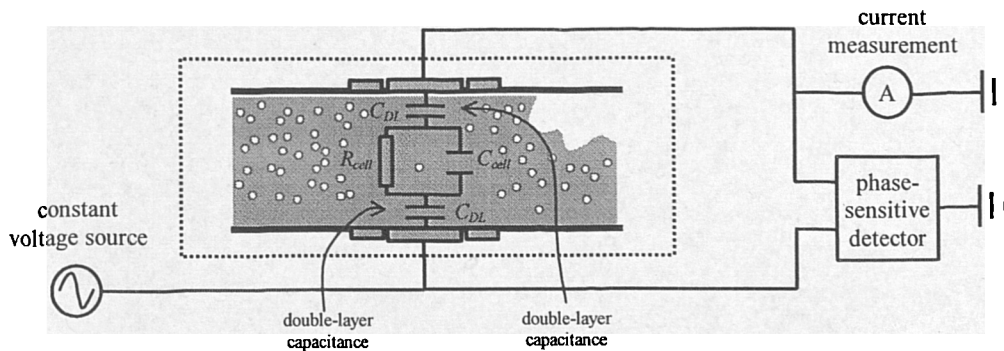


Figure 2.11: Simplified model for the impedance of a fluid mixture, between impedance sensor electrodes.

	<i>oil</i>	<i>water</i>	<i>gas</i>
$\sigma (\Omega^{-1} \text{ m}^{-1})$ :	$<10^{-10}$	$10^{-5} \rightarrow 10^1$	$<10^{-10}$
$\varepsilon (\text{F m}^{-1})$ :	$2.5\varepsilon_0$	$80\varepsilon_0$	$1\varepsilon_0$

**Table 2.1:** Electrical properties of the oil, water and gas phases (approximate values)

The electrical impedance technique is a relatively fast and inexpensive method for making the phase fraction measurement. However, for a distinction to be made between all three components in a multiphase flow, the *phase angle* in figure 2.11 must be measured with great accuracy. Furthermore, the relationship between the measured impedances and the phase fractions is dependent upon the flow geometry. This dependency can be eliminated to some extent, by homogenising the flow before it is metered. The electrical properties of the homogenised mixture can then be approximated by a ‘mixture model’ such as that by Maxwell<sup>79</sup>:

$$A_{mix}/A = \frac{2 - 2a - X}{1 + a - X} \quad X = \frac{\varepsilon_g + 2\varepsilon_l}{\varepsilon_g - \varepsilon_l} \quad [2.10]$$

In equation [2.10],  $a$  is the liquid holdup (i.e. the cross-section liquid content),  $\varepsilon_l$  and  $\varepsilon_g$  are either the conductivity or the permittivity of the liquid and gas phases, and  $A_{mix}/A$  is the relative change in the admittance (for a liquid-continuous flow). Similar models have been developed by Brügemann<sup>24</sup>, Ramo & Rau<sup>100</sup>, Hammer<sup>46</sup> (for two-phase mixtures), and by Dykesteen *et al*<sup>31</sup> (who implemented equation [2.10] twice in order to model three-phase flow). The predictions of these models agree well with experimental measurements, when the dispersion is *weak* and uniformly distributed.

Alternatively, the dependency on the flow geometry can be addressed by careful design of the sensor electrodes. The sensors can either be local or global, and intrusive or non-intrusive, depending on the system requirements. However, most multiphase meters will make a non-intrusive global measurement. This can be achieved by using one of the four designs illustrated in figure 2.12:

- *Arc electrodes* (figure 2.12a) allow a cross-section measurement of the liquid phase fraction. Guard electrodes must be installed at either side of these electrodes, in order to contain the ‘sensing volume’ within a narrow plane.

- *Ring electrodes* (figure 2.12b) allow a trade-off of the localised cross-section measurement, in the favour of a more uniform electric field within the sensing volume.
- *Helical electrodes* (figure 2.12c) are twisted round the pipe perimeter several times, in an attempt to overcome flow geometry dependence.
- *Rotating field electrodes* (figure 2.12d) achieve a similar averaging effect to helical electrodes, though through time rather than space. The electrode pairs are driven at  $120^\circ$  phase intervals, in order to produce a field vector that rotates within the core of the pipe.

For each of these four designs, the minimum *absolute* error (i.e. the fraction of the full-pipe measurement) is limited to approximately 1%. This minimum occurs, because it is difficult to maintain a uniform field within the ‘sensing volume’ (particularly within the pipe core). The measurement accuracy can be improved by using local sensors, which are discussed in more detail by Ceccio & George<sup>25</sup>. However, local sensors are not normally used in a commercial meter, because of their susceptibility to wax deposits.

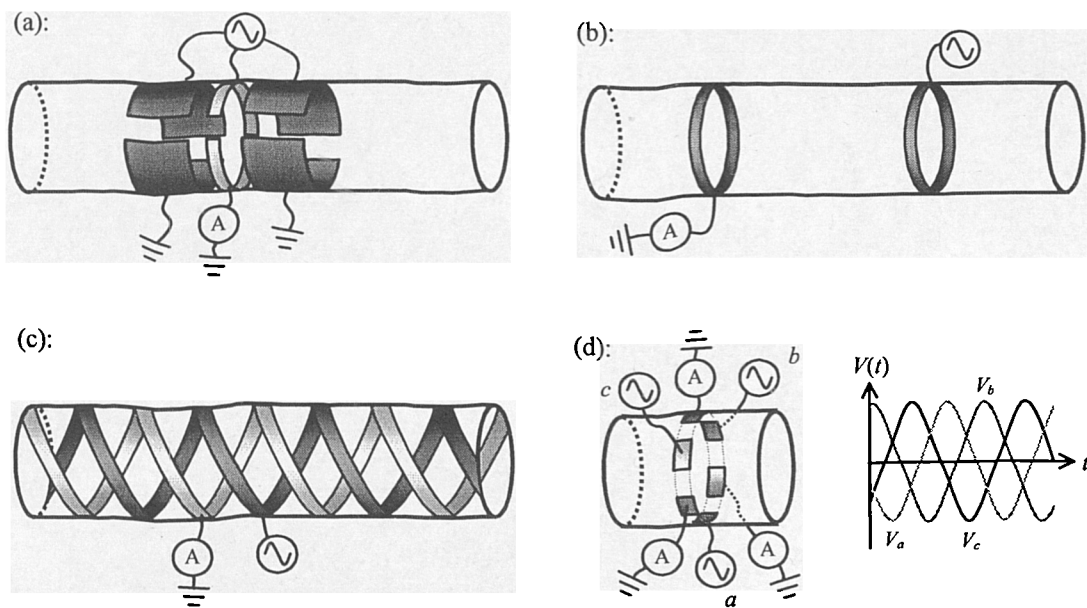


**Figure 2.12:** Non-intrusive sensors, for making a global phase fraction measurement: (a) arc electrodes (Xie et al<sup>130</sup>, Lemmonier et al<sup>65</sup>); (b) ring electrodes (Andreussi et al<sup>8</sup>); (c) helical electrodes (Abouelwafa & Kendall<sup>1</sup>, Geraets & Borst<sup>37</sup>); (d) rotating field electrodes (Merilo et al<sup>81</sup>, Snell et al<sup>109</sup> and Tournaire<sup>118</sup>).

### 2.2.3 Tomographic measurement

The gamma-ray and the electrical impedance techniques, described in sections 2.2.1 and 2.2.2 above, form the basis for a *tomographic measurement*. In this measurement, ‘projection data’ are gathered from the flow using a large array of sensors, and are then ‘back-projected’ in order to reconstruct the phase distributions in the pipe interior. For a general review of process tomography, consult Plaskowski *et al*<sup>97</sup>, while the reconstruction problem is described in detail by Kak & Slaney<sup>59</sup>.

In gamma-ray tomography, at least two gamma ray sources and two arrays of detectors are positioned around the pipe perimeter. One possible arrangement is shown in figure 2.13 below. At each detector, the photons are collected and measured using a dual-energy technique (described in section 2.2.1 above), so that three ‘projection vectors’  $\underline{\alpha}_w$ ,  $\underline{\alpha}_o$  and  $\underline{\alpha}_g$  are obtained. Since the rays passing through the pipe define a set of pixels (denoted by the vector  $\underline{X}$ ) it can then be written that:

$$\underline{\phi}_{N \times P} \times \underline{X}_N = \underline{\alpha}_P \quad [2.11]$$

where  $N$  is the total number of pixels,  $P$  is the total number of beams, and  $\underline{\phi}$  is a matrix representing the relative importance (i.e. the physical size) of each pixel. Given the matrix  $\underline{\phi}$  and the vector  $\underline{\alpha}$  for each phase, the ‘back projection’ problem is thus to obtain  $\underline{X}$ .

Equation [2.11] is normally solved, by computing the *inverse matrix*  $\underline{\phi}^{-1}$ . This inversion procedure varies, depending on whether the number of pixels  $N$  exceeds the number of beams  $P$ . If  $N$  is less than  $P$ , a unique solution can always be found, and iteration can then be used to improve the accuracy. On the other hand if  $N$  exceeds  $P$ , some form of minimum-error technique must be used to find the optimum solution (e.g. see Zwiens<sup>136</sup>), with assumptions made about the flow geometry. For the most accurate reconstruction, there should be *many beams* and *many pixels*.

Given enough projection data, gamma-ray tomography offers a very accurate reconstruction of the phase distributions within the pipe cross-section. However, the technique suffers from the following limitations:

- Long exposure times are required, to minimise the statistical uncertainty in the count rates and give good discrimination between the oil and the water phases. The count rates may be increased by using an X-ray source, but at the expense of *beam-hardening* errors.

- Since gamma-rays are photons, any intersecting beams are vulnerable to crosstalk errors. Each source must be shielded in turn, in order to prevent this crosstalk. As a result, an *instantaneous* measurement of the cross-section cannot be obtained.

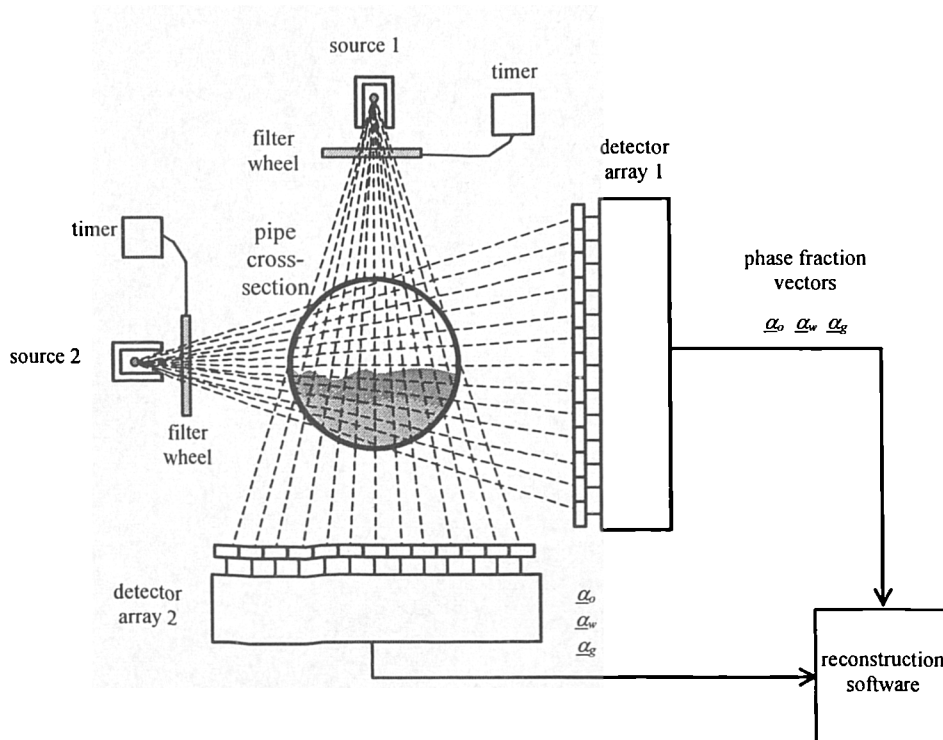


Figure 2.13: Example of a gamma-ray tomography system.

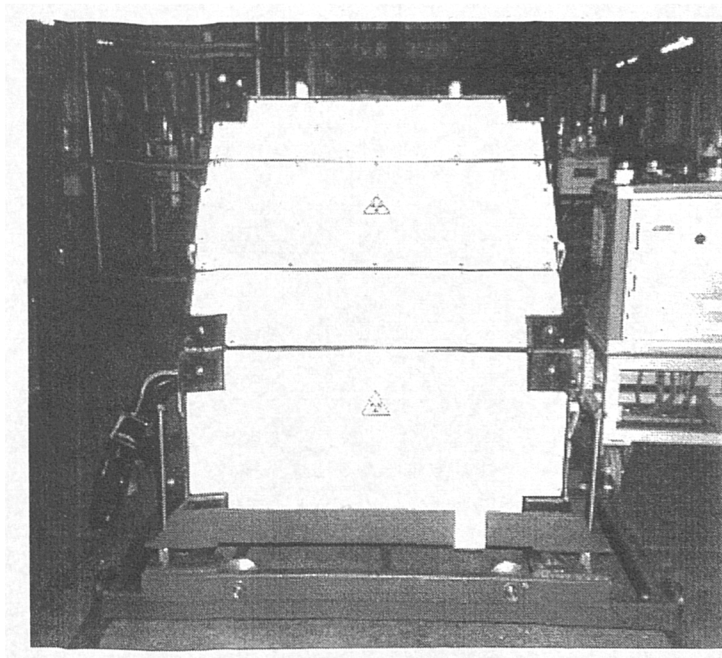


Figure 2.14: Three-phase X-ray tomography system (Imperial College)

An alternative form of tomographic measurement is called *electrical impedance tomography* (EIT). In EIT, the projection measurements are acquired using a series of  $n$  electrodes positioned around the pipe perimeter. A typical arrangement is illustrated in figure 2.15 below. A controlled current is injected between pairs of electrodes in quick succession, in order to produce a potential field within the pipe. This field is then measured at the  $n-1$  locations surrounding the injection point, so that  $\frac{1}{2}n(n-1)$  projection measurements are obtained. These measurements are used to solve the equation for the impedance distribution inside the pipe, which is as follows:

$$\underline{Y}_{N \times N} \times \underline{V}_{N \times P} = \underline{C}_{N \times P} \quad [2.12]$$

In equation [2.12],  $\underline{Y}$  is the network of  $n(n-1)$  impedance elements,  $N$  is the number of network nodes,  $P$  is the number of projection measurements, and  $\underline{V}$  and  $\underline{C}$  define voltage and current at each node. Given an estimate of the impedances in  $\underline{Y}$ , the voltages at the pipe perimeter are determined via equation [2.12], compared with actual measurement, and then  $\underline{Y}$  can be adjusted accordingly. This is a linear problem, though it is usually difficult because the matrix equations are strongly coupled. Some back-projection algorithms for EIT that help improve the result are described by Johansen *et al*<sup>58</sup>, Yorkey *et al*<sup>134</sup> and Barber & Brown<sup>14</sup>.

While electrical tomography is much less expensive to implement than gamma-ray tomography, it has the following disadvantages:

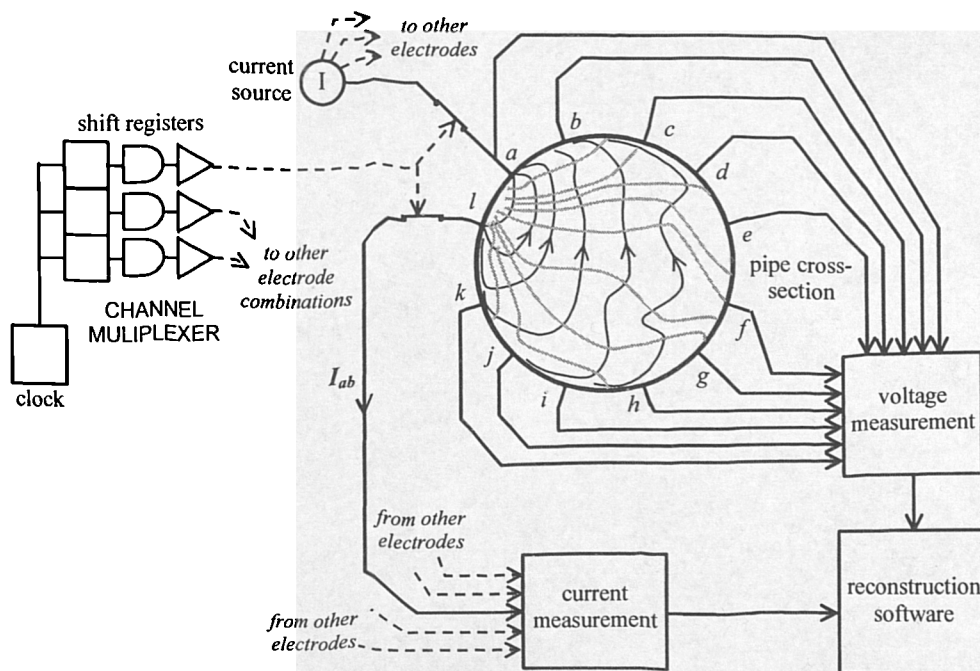
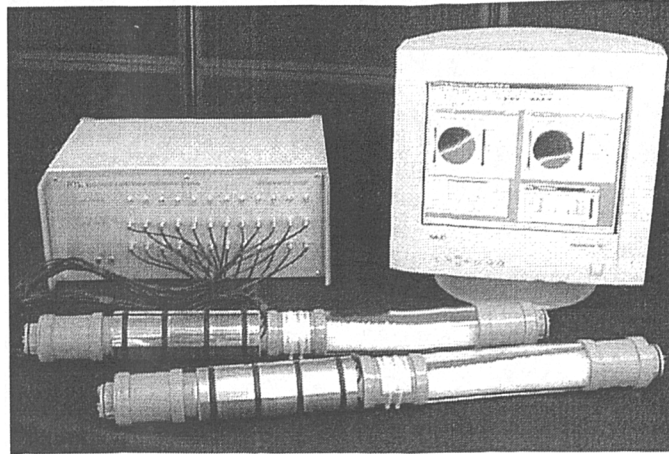


Figure 2.15: Electrical impedance tomography ('EIT') system



**Figure 2.16:** Capacitance tomography system (Process Tomography Ltd.)

- Equation [2.12] approximates the contents of the pipe as two-dimensional, whereas in reality there is a three-dimensional field. The installation of *guard electrodes* around the sensor is sometimes used to correct this effect, though these electrodes only work to a limited extent.
- EIT uses a ‘soft’ field technique, as opposed to a ‘hard’ field technique. As a result, there is great sensitivity of the reconstructed image to any noise in the projection data.

At present, the EIT technique is limited to applications where there are gradual changes in the electrical properties of the mixture. For example, Lucas *et al*<sup>71</sup> describe a system for phase fraction determination in dispersed solid-liquid flows, while Williams *et al*<sup>123</sup> used EIT for measuring the particle concentrations in mixing vessels. For applications where there is a sharp discontinuity, the difficulty in the reconstruction greatly increases. A capacitance-based system for metering gas-solid flows has been proposed by Yang & Liu<sup>132</sup>. Improvements in the measurement accuracy and the reconstruction algorithm are still required in order to image three-phase flow.

### **2.3 Phase density measurement**

To convert the phase volumetric flowrates into mass flowrates, a measurement of the phase densities is required (see figure 2.1). Unlike the phase velocity and phase fraction measurement techniques, however, this technique has been standardised, and it is divided into the following two stages:

- Sampling of the liquid and gas phase densities at the pipe exit, and the characterisation of the phase equations of state by a laboratory analysis. This sampling is repeated on a regular basis, to track the changing hydrocarbon content in the oil phase.
- Continuous acquisition of the local pressure and temperature at the point of metering. These measurements are combined with the equations of state, to resolve the discrepancy between phase densities at the point of metering and at the pipe exit.

The NEL test facility (which will be described in Chapter 8 of this thesis) is a closed-loop system. Therefore, the chemical components of the gas, water and oil phases do not show variations with time. Consequently, periodic sampling is not required to establish the phase densities.

## **2.4 Processing software**

As shown in figure 2.1, the multiphase flow meter requires a computer system to process the sensor data and deliver the phase flowrates. This system is not well described, within the existing literature. In this section, the software required to identify the flow pattern, extract the phase fractions and the phase velocities, and derive the flowrate via a predictive model, will briefly be summarised. These tasks are performed in *real time*, to ensure a continuous flowrate measurement.

### **2.4.1 Flow pattern identification**

To qualify whether the phase flowrates are ‘low’, ‘moderate’ or ‘high’, it is necessary to identify the *flow pattern*. This flow pattern information is also required to choose the predictive model.

Annuziato<sup>11</sup> developed a ‘look-up table’ for determining the flow regime. To create this table, two-phase flow data were gathered using *pressure* and *conductance* sensors, over a wide range of flowrates. The flow pattern, the mean signal values, the cross-correlation velocity, and the dominant frequency were gathered and recorded in a table. It was then possible to recognise the flow regime from the sensor signals, with a high degree of accuracy. However, this method was specific to two-phase (gas-water) flow, and could not be generalised to different pipe sizes or orientations.

In recent years, there has been a lot of interest in the use of *neural networks* to identify the flow pattern. Systems which automatically organise the sensor data and deliver the flow regime are discussed by Wu *et al*<sup>129</sup> and Mi *et al*<sup>82</sup>. The neural network must be ‘trained’ before it can be used. However, the major advantage of this approach is that no subsequent input is needed.

### 2.4.2 Parameter extraction

The sensor data must next be processed, in order to obtain the input parameters to the predictive model. Some typical tasks that are performed during this ‘parameter extraction’ process are to:

- Normalise the conductance sensor data and the count-rate data, using ‘full-pipe’ measurements.
- Calculate the mean phase densities, from the local pressure and temperature measurements.
- Identify the dominant features of the flow; for example, the ‘slug zone’ in slug flow, or ‘large waves’ in a stratified flow.

The processing software must also evaluate the *cross-correlation velocity* and the *mean phase fraction* from the sensor signals, in ‘real time’. These data should be passed to the predictive model, at regular intervals.

### 2.4.3 The predictive model

The ‘flow parameters’ are input to a predictive model, for the calculation of the phase flowrates. The simplest type of predictive model is for *homogeneous flow*. The mass flowrates are then the product of the mean velocities, the mean phase fractions and the phase densities. That is:

$$m_o = \overline{V_o a_o} \rho_o \quad m_w = \overline{V_w a_w} \rho_w \quad m_g = \overline{V_g a_g} \rho_g \quad [2.13]$$

Unfortunately, the flow is not usually ‘well-homogenised’, so that there will be *slip* between the different components. A more advanced model is required, which accounts for *local variations* in the phase velocity and the phase fraction measurements. This model is dependent upon the flow regime. For example in slug flow, the contribution to the flowrates

from the ‘slug zone’ and the ‘film zone’ must be separately considered.

It is not always possible to obtain reliable measurements for the phase fractions and the flow velocities. Therefore, the predictive model may need to make use of one (or more) *closure relationships*. These closure relationships can be separated into two categories, as follows:

- ‘Theoretical’ closure relationships. These relationships use ‘sub-models’ for the flow geometry and the flow profile, in order to establish the local phase fractions or the local velocities (e.g. Dukler & Hubbard<sup>30</sup> and Maron *et al*<sup>78</sup>). The assumptions made in these models must be realistic, to obtain reliable results.
- ‘Empirical’ closure relationships. These relationships are developed from direct experimental measurements, usually within a small-scale ‘test rig’ and using specialised instruments. For example, Lahey *et al*<sup>63</sup> measured the drift-flux parameter in horizontal slug flow using a *quick-closing valve* technique. On the other hand, Jepson<sup>57</sup> measured the velocity profile of slugs, by using a *stationary slug* apparatus and a local velocity probe.

Two situations are identified where the prediction of the flowrates becomes particularly difficult. First of all, near to the transition boundary between two flow regimes. Here, it may be difficult to select the most appropriate flow model. Secondly, accurate results may not be obtained during slug flow, because the phase fractions and the local velocities show large fluctuations. The modelling of slug flow, and the closure relationships required within the model, will be discussed in Chapter 3.

## **2.5 Performance**

Figures 2.17 and 2.18 illustrate two different types of commercially available multiphase flow meter. Ideally, these meters should monitor the oil, water and gas flowrates at regular intervals, and should have perfect accuracy. This performance should be achieved regardless of the flow pattern, the pipe size and orientation, and also the contents of the production field. In this section, the typical range of test conditions, the typical performance and some of the main limitations in this performance that can be expected will be summarised.

### **2.5.1 Test Conditions**

A commercial multiphase meter must be optimised, to work in all parts of the production

pipeline. The meter may be need to be installed near to the well head (high pressure and high temperature) to monitor incoming flowrates, or near to the separation equipment (low pressure and low temperature), for fiscal metering purposes. Accordingly, a rough guide to the range of operating conditions is as follows:

- A total superficial velocity ( $j$ ) between  $1 \text{ m s}^{-1}$  and  $20 \text{ m s}^{-1}$  (a ‘turndown ratio’ of 20:1), within which the total liquid superficial velocity ( $j_l$ ) lies between  $0.1 \text{ m s}^{-1}$  and  $10 \text{ m s}^{-1}$ .

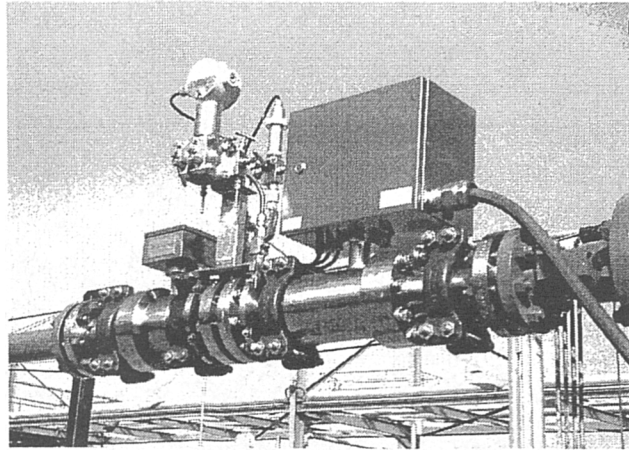


**Figure 2.17:** ESMER Multiphase flowmeter (Petroleum Software Ltd)

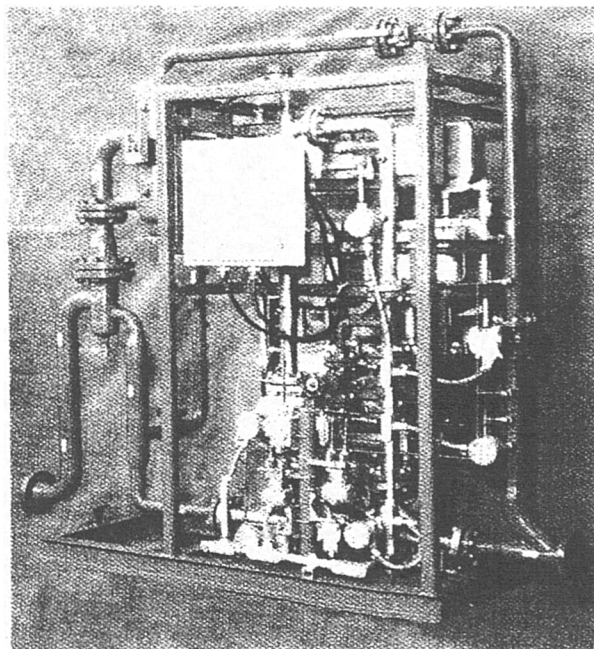


**Figure 2.18:** MPFM-400 multiphase flowmeter (Agar Inc.), for high gas volume fraction (GVF) flow measurement

- A ‘water cut’ (i.e. water flowrate as a percentage of total liquid flowrate) of between 0% and 95%.
- A pipe diameter of between 3 and 12 inches, in either a horizontal or a vertical orientation.
- Local pressures and temperatures lying between that experienced at the well head (typically 100 bar and 120°C) and the separator (typically around 1 bar and 20°C).

Figure 2.19 illustrates the test conditions superimposed against the two-phase flow pattern maps by Mandhane *et al*<sup>74</sup> and Taitel *et al*<sup>114</sup>. Although these flow pattern maps are for gas-water flow and a pipe diameter of approximately 3 inches, it is clear that a major part of the test range lies within the *slug flow* regime.

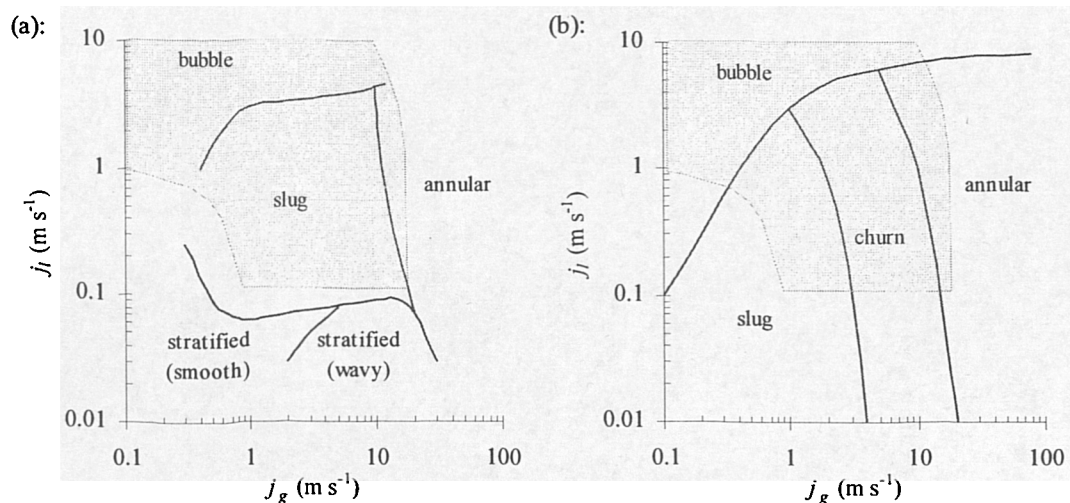


**Figure 2.19:** Typical range of test conditions, compared against flow pattern maps for horizontal flow (Mandhane *et al*<sup>74</sup>) and vertical flow (Taitel *et al*<sup>114</sup>).

### 2.5.2 Performance

The performance of the multiphase flow meter will depend upon the pipeline geometry, the flow conditions, the processing software, and most critically of all, the *sensing instrumentation*. Table 2.2, which is adapted from Thorn *et al*<sup>117</sup>, summarises some of the most common permutations of sensing instrumentation that are used in a commercial meter. A Venturi- or cross-correlation meter is normally used to measure the phase velocities, while a gamma-ray or an impedance-based system is used to estimate the phase fractions.

Several meters also employ phase homogenisation and separation techniques, in order to obtain improved results.

Though it is not possible to disclose the performance of individual flow meters in this thesis (this is commercially sensitive information), some general trends in the performance are as follows:

- A strong *flow regime dependency*. This dependency was observed by Whitaker<sup>125</sup>, and by Wolff<sup>126</sup>, after testing a large set of flow meters over the same range of phase flowrates.
- Deterioration in the *water cut measurement*, at low liquid flowrates. This deterioration occurs for both water-continuous and oil-continuous flows, when the gas volume fraction exceeds 50% (Whitaker<sup>125</sup>; Kjølberg & Berentsen<sup>60</sup>).
- Performance is independent of the *velocity measurement technique*, provided that the phases are homogenised beforehand the measurement (Hewitt *et al*<sup>52</sup>; Kjølberg & Berentsen<sup>60</sup>).

<u>Manufacturer(s)</u>	<i>phase fraction technique</i>			<i>phase velocity technique</i>			Reference	
	gamma-ray	impedance	other	Venturi	cross-correlation	Other		phase separation homogenisation
CSIRO	x				x			Roach & Watt <sup>102</sup>
Daniel Industries / Shell	x			x			x	Scheers & Letton <sup>105</sup>
Fluenta	x	x		x	x			Olsvik <i>et al</i> <sup>92</sup>
Tecnomore/AGIP	x	x		x			x x	Andreussi <i>et al</i> <sup>7</sup>
Kongsberg AS/ Shell		x			x			Hatlo & Sten-Halvosen <sup>49</sup>
Agar Inc.			x			x	x	Tuss <i>et al</i> <sup>120</sup>
Framo AS	x				x			Hanssen & Torkildsen <sup>47</sup>
SGS Redwood/ Imperial college	x				x	x	x	Hewitt <i>et al</i> <sup>52</sup>

**Table 2.2:** List of commercial multiphase flow meter manufacturers, the technology incorporated and the reference for further information (adapted from Thorn *et al*<sup>117</sup>)

In recent years, the relative error in the measurement of the total liquid flowrate and the gas flowrate has reduced from about 20% to 10% (see, for example, Dykesteen & Middtveit<sup>32</sup>), with *high repeatability* (though not necessarily *high accuracy*) in the results.

### 2.5.3 Limitations

In order to identify the limitations of the multiphase meter, it is first of all necessary to define a set of *performance criteria* for multiphase metering. As a guide, Slijkerman *et al*<sup>108</sup> recently survey a number of large oil companies, and found that they required a 5% relative accuracy in the gas and the total liquid flowrates, and a 2% *absolute* accuracy in the water-cut measurement. Wolff<sup>126</sup> expressed these criteria in the form:

$$\left| \frac{\Delta m_l}{m_l} \right| \leq C \quad \left| \frac{\Delta m_g}{m_g} \right| \leq C \quad 2.5 \left| \frac{\Delta m_w}{m_l} \right| \leq C \quad [2.14]$$

In equation [2.14],  $m_l$ ,  $m_g$  and  $m_w$  are the total liquid, gas, and water phase mass flowrates, and the ‘stringency parameter’  $C$  has a value of 5%. For fiscal metering purposes, Wolff proposed that the stringency parameter should be replaced with the smaller value  $C = 2\%$ .

As yet, most commercial multiphase meters do *not* meet the above criteria over the full range of conditions identified in Section 2.5.1. The shortcomings in the performance are due to a number of difficulties in the measurement and the modelling process, which can be summarised as follows:

- Poor accuracy in the velocity measurement, when the phases are travelling at different velocities or are fluctuating with time (slug flow).
- Dependency of the gamma-ray technique and the electrical impedance technique for measuring the phase fractions upon the *flow geometry*.
- A need to use empirical closure relationships within the flow model, when the flow variable measurements are *unreliable* or *unobtainable*.

In order to improve the measurement accuracy, three steps are required: more sensors must be used which obtain more detailed measurements of the flow; there must be a better understanding of three-phase flow regimes; and finally, much more extensive testing (both in the laboratory and in a subsea environment) is necessary.

## 2.6 Summary

This chapter described the *multiphase flow meter*. The first four sections discussed the internal components of a commercial meter - the sensing instrumentation and the processing software, and then the final section discussed the performance that is currently achieved by this system.

Section 2.1 described different techniques for measuring the phase velocities. The relative merits of the Venturi method, the cross-correlation method, the displacement method and the NMR methods were discussed. The first three of these techniques were relatively 'inexpensive', though the gas and the liquid velocities often needed to be equal for an accurate measurement. In contrast, the NMR method could make independent measurement of the velocities (regardless of the flow pattern), at the expense of its cost.

Section 2.2 described different techniques for measuring the phase fractions. The gamma-ray attenuation method offered good discrimination between all three phases, though it generally had a poor dynamic response. On the other hand, the impedance technique offered instantaneous response, though was dependent upon the geometry of the flow. The use of each technique to provide a tomographic image of the flow was then discussed. However, a major limitation of process tomography is the sensitivity to *noise* in the experimental data.

Section 2.3 described the technique for measuring the phase densities. The phases were sampled at the pipe outlet, and then the measured density was corrected using local measurements of the pressure and temperature.

Section 2.4 described the software used to process the sensor data and deliver the phase flowrates. The software combined routines for identifying the flow pattern, and extracting the model parameters, with an appropriate predictive model. This model needed to use closure relationships, where experimental data was unavailable.

Section 2.5 described the typical operating conditions, the instrumentation, and the performance of a commercial flow meter. The requirements of the oil industry were for a 5% relative accuracy in the total liquid flowrate and the gas flowrates, and a 2% absolute accuracy in the water cut. However, most meters only managed to meet these requirements over a limited part of the operating range. The shortcomings in the performance were due to difficulties making the *velocity measurement*, the dependency of sensing techniques upon the *flow geometry*, and the reliance upon empirical *closure relationships* within the predictive model. Each of these three problems must clearly be overcome, in order to obtain an accurate measurement of slug flow.

### 3. Modelling of slug flow

During offshore production, the gas and liquid phases are normally transported in a *slug flow* pattern. This slug flow is particularly difficult to meter, due to the large fluctuations in the local phase velocities. In this chapter a variety of *predictive models* will be presented, in order to understand the flow.

Section 3.1 describes the slug flow process. Particular attention will be paid towards the slug initiation and development, the structure of the ‘slug zone’, and the structure of the ‘film zone’, for a horizontal pipe. The effect of changing the pipe inclination upon each of these aspects will then be considered.

Section 3.2 presents a model for predicting the gas and liquid flowrates, in *developed* slug flow. The parameters that are used in this model are the translation velocity, the local phase velocities, the local phase fractions, and the lengths of the ‘slug’ and the ‘film’ zones. It is possible to simplify this model considerably, by assuming *stable* slug flow.

In the absence of suitable measurements for each parameter, it is necessary to use ‘sub-models’ to derive the phase flowrates. Sections 3.3 to 3.6 describe several different types of sub-model that may be used for slug flows:

- Section 3.3 describes models that relate the local slug zone velocities ( $V_{ls}$  and  $V_{gs}$ ) to the translation velocity ( $V_t$ ).
- Section 3.4 describes models for the *pressure drop* within the slug zone and the film zone. These models can be used to infer the local flow velocities, and predict the film zone profile.
- Section 3.5 discusses the models for the ‘pickup’ and the ‘shedding’ processes within the slug body.
- Section 3.6 describes empirical correlations for the slug frequency ( $\nu$ ), the slug zone holdup ( $\alpha_s$ ) and the slug length ( $l_s$ ).

This thesis is principally concerned with the study of gas-water slug flow within the NEL facility. However, in order to apply the material in this chapter to multiphase flow, it is necessary to develop a multiphase model. Therefore, Section 3.7 will briefly describe the development of a three-phase (oil-water-gas) model for slug flow.

### 3.1 Qualitative description of slug flow

Considerable insight into the slug flow process can be gained, though visual observations in the laboratory. In this section, the way in which the slugs initiate and develop along a section of horizontal pipe will be described. The detailed structure of the 'slug zone' and the 'film zones' in developed slug flow, and the effect of the pipe inclination upon what is seen, will then be discussed.

#### 3.1.1 Slug flow initiation

The simplest process by which a liquid slug can be initiated is the Kelvin-Helmholtz mechanism, shown in figure 3.1. This mechanism assumes that the inlet phases move at constant velocities, and are arranged in perfectly stratified, smooth, layers. A localised disturbance at the interface between the phases will then result in the following effects:

- an acceleration of the gas phase due to the restricted area, causing a local pressure drop (figure 3.1a).
- an upwards force on the liquid phase, which causes a wave to develop if it is comparable with the liquid layer weight (figure 3.1b).
- further acceleration of the gas phase and further pressure drop (figure 3.1c). Eventually, a complete blockage of the pipe will occur.

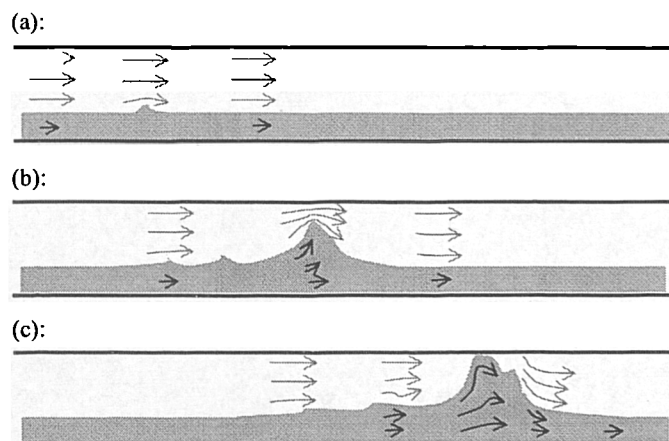


**Figure 3.1:** The formation of a liquid slug by the Kelvin-Helmholtz instability mechanism. (a) A localised disturbance on the stratified film; (b) Pressure drop and wave growth; (c) Bridging of the pipe, acceleration of the blockage, and pickup of fluid

In practice, the boundary between the incoming liquid and gas phases is rarely smooth. The effect of interfacial waves upon the initiation process may be considered, by using a *linear stability theory*. Many workers (for example Kordyban & Ranov<sup>61</sup>; Mishima & Ishii<sup>83</sup>, Lin & Hanratty<sup>66</sup>) have analysed this problem. The presence of the waves makes it more likely that a disturbance will grow, particularly if the liquid flowrate is low. The initiation process is further enhanced, if the incoming flowrates are not constant.

Not every blockage of the pipe will result in the formation of a liquid slug. For a ‘blockage’ to evolve into a ‘slug’, the following processes are required:

- There must be a build-up of pressure, at the rear of the blockage. This pressure causes acceleration and pushes the preceding liquid film into the core, creating a *mixing vortex*. The liquid film behind the blockage is then stabilised. As the film must rebuild to a certain height before initiation can repeat, there is a characteristic time delay between successive slugs.
- There must be rapid pickup of the preceding liquid film, and *slug growth*. The growth process is quickest, when the liquid film is very thick (Woods & Hanratty<sup>127</sup>). Therefore, any large waves in front of an advancing slug front will be assimilated.
- There must be pickup of sufficient liquid to form the *slug body* behind the mixing vortex. In a short slug, the process of boundary layer development does not complete (Maron *et al*<sup>78</sup>), causing the shedding of fluid from the tail and *slug decay*. The liquid within short slugs will thus eventually be lost to longer slugs following behind.

At a sufficient distance downstream from the inlet, the sequence of ‘slug’ and ‘film’ past a fixed point will stabilise. At this point, the flow can be referred to as ‘*quasi-stable*’. The frequency and the velocity of passing flow will be approximately constant, and the length of each slug will be at least 15 pipe diameters (Nydal *et al*<sup>88</sup>). The length of pipe that is required to reach such ‘quasi-stable’ flow conditions (the ‘development distance’) is typically between 300 and 600 pipe diameters.

In long pipelines that operate at high pressure, there is a long-term development of the flow caused by the expansion of the gas phase. This expansion causes a slow decrease in the slug frequency (Scott *et al*<sup>107</sup>). The expansion effects are most notable near the pipe exit, and their influence is seen to propagate upstream.

### 3.1.2 The slug zone structure

The structure of the slug zone is strongly dependent upon the gas phase flowrate. Figure 3.2 illustrates the effect of increasing the gas flowrate upon the *front*, *body* and *tail* regions, for a horizontal flow. The motion of the liquid phase relative to the front is also shown. Initially there is 'plug flow', followed by two distinct cases of 'slug flow', and then 'slug-annular' flow. These regimes have the following features:

- 'Plug flow' is characterised by a distinctive *Benjamin bubble* at the liquid front (figure 3.2a). The nose of this bubble is at the top of the pipe, and makes contact with the wall at an angle of  $60^\circ$ . At the contact point, the liquid is stagnant. The incoming liquid fills the pipe, decelerates, and moves along well-defined streamlines. There is no pickup of this incoming fluid, and no significant pressure drop. As the liquid moves out of the plug body, it contracts and accelerates, so that a second Benjamin bubble is formed at the tail.
- 'Slug flow' is characterised by a *mixing vortex* (figure 3.2b). The incoming fluid is accelerated to the slug velocity. This causes mixing and a large, irreversible, pressure drop. Gas bubbles may also be entrained periodically, depending on this incoming velocity. Behind the vortex, the liquid decelerates and turbulent boundary layers develop inwards from the pipe walls. The slug body quite closely resembles homogeneous flow. The gas rises up through the slug body, and emerges at the top of the slug tail. There is a further (irreversible) pressure drop as the fluid is ejected into the succeeding liquid film.
- As the gas flowrate rises, the incoming fluid enters the slug more quickly and the mixing vortex intensifies (figure 3.2c). As a result, there is an irregular film of *frothy liquid* immediately prior to the front (Gopal & Jepson<sup>39</sup>; Fan *et al*<sup>34</sup>). Much more gas passes into the slug body, and will tend to concentrate in the pipe core. These bubbles may be carried some distance into the succeeding film before they are released. The nose of the gas bubble behind the slug moves towards the centre of the pipe (resembling a 'Taylor bubble'). There is an increased pressure drop across the whole slug.
- At the highest gas velocities, *slug-annular* flow conditions are approached (figure 3.2d). There is now so much air within the slug body that a periodic breach of the pipe can occur. This causes the release of gas, which passes from the rear to the front of the slug (*'blow-through'*). The local holdup and pressure fluctuations throughout the slug body become large and unpredictable, and the assumption that there is *constant holdup* throughout the slug body becomes questionable.

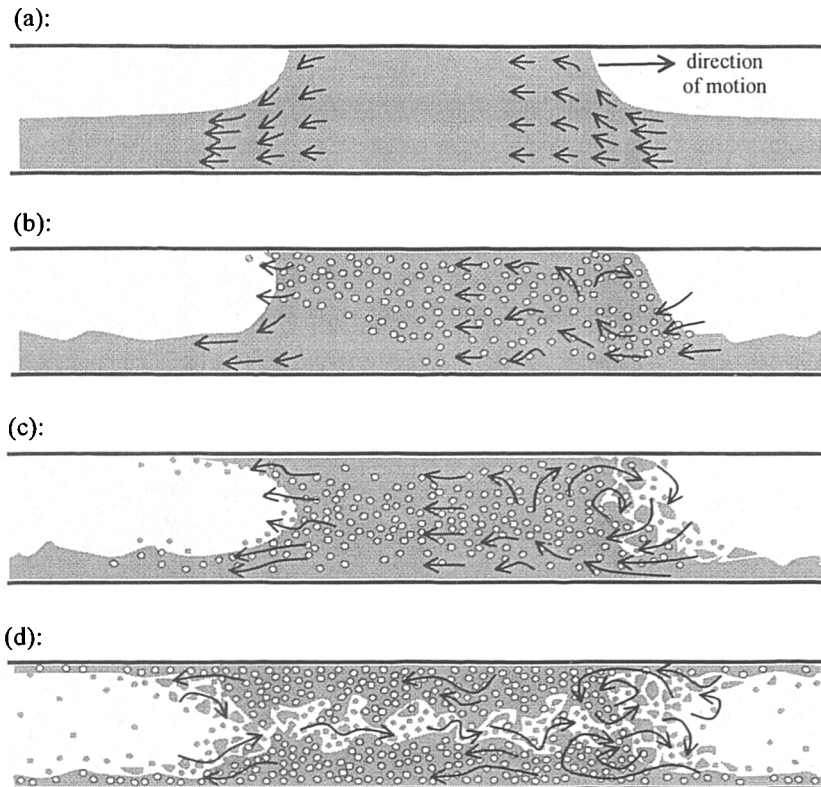


**Figure 3.2:** The relative motion of the liquid phase within the slug body, in a frame of reference translating with the slug front. (a) plug flow (low  $j_g$ ); (b) slug flow ( $j_g \sim 3 \text{ms}^{-1}$ ); (c) slug flow ( $3 < j_g < 7 \text{ms}^{-1}$ ); (d) slug-annular flow ( $j_g > 7 \text{ms}^{-1}$ ).

The liquid phase viscosity has a significant effect upon the structure of the slug zone. Increasing this viscosity will cause the rates of pickup and shedding to greatly increase, the pressure drop in the mixing zone to increase, and changes in the local void content within the slug body (Nadler & Mewes<sup>86</sup>).

### 3.1.3 The film zone structure

Relatively speaking, the ‘film zone’ between the slugs is rather uninteresting. Nevertheless, there are a number of features in the film that have a significant influence upon the phase flowrates, because the length of the ‘film’ is usually much longer than that of the ‘slug’. These features are as follows:

- At low gas and low liquid flowrates, the film is typically very stratified and smooth, but contains significant *large disturbances*. These disturbances can be ‘large amplitude’ waves that are initiated at the pipe inlet, remnants of decayed

slugs, as well as the ‘*precursor waves*’ observed by Tronconi<sup>119</sup>.

- As the gas flowrate is increased, a lateral curvature around the film interface will develop, and gas bubbles may be carried into the film from the previous slug. The film will eventually spread out and occupy the entire pipe perimeter (with considerable spray in the gas space) as annular flow conditions are approached.
- As the liquid flowrate is increased, the film zone will reduce dramatically in length, and will develop a curved profile near the slug tail. This profile is illustrated in figure 3.3 below. The number of disturbances along the film length is dramatically reduced. Near the transition boundary with bubble flow, the film zone and the slug zone are approximately equal in length.

Increasing the liquid phase *viscosity* will cause the length of the film zone, the amount of gas carried through from the preceding slug, and the frequency of any large disturbances to decrease.

### 3.1.4 Inclination effects

The slug flow initiation process, the development, and the slug structure are all affected by the pipe inclination. Sections 3.1.1 to 3.1.3 discussed the specific case of horizontal flow. However in general, the pipe emerging from a production well may be inclined and may pass through a series of bends. The most distinctive changes occur for *vertical flow*, and may be summarised as follows:

- The initiation of a slug requires the *coalescence* of gas bubbles, rather than the development of large waves. Enough gas material must collect together to form a ‘film zone’ behind a pipe blockage. This coalescence process is enhanced, if there are *void waves* (waves of high bubble concentration) emerging from the well head.
- The film region forms a *liquid annulus*. The fluid at the back of each slug drains down the pipe walls, and is picked up by the next slug. The nose of the film bubble is always in the centre of the pipe (i.e. *Taylor bubble* geometry). Dispersed gas bubbles will concentrate in the core of the slug body (van Hout<sup>56</sup>) and will rise up and emerge at the bottom of each film.
- The body of each slug may collapse and fall through the film, before being scooped up by the next liquid slug. This effect is particularly common at high liquid flowrates. There is insufficient buoyancy to balance the weight of the slug,

resulting in *churn flow*.

The presence of several peaks and dips in the pipeline will result in ‘severe’ slugging at downhill-uphill junctions. These severe slugs are initiated wherever is sufficient liquid to block the ‘dip’ section. The build-up of the liquid head, as more liquid flows downhill, balances the pressure of the gas that is trapped behind. The liquid head can only decrease when the top of the uphill section is released. The gas phase is suddenly released, leading to the formation of a very long, persistent, slug. Further descriptions of the severe slugging phenomenon are presented by Schmidt *et al*<sup>106</sup>, and Taitel<sup>111</sup>.

### **3.2 The phase flowrates**

In this section, a one-dimensional model for the phase flowrates within each passing slug unit will be described. This model will assume the slug flow is ‘well-developed’ and ‘quasi-stable’. The equations that are presented below, together with the closure relations discussed in sections 3.3 to 3.6 that follow, form the basis of the metering system to be described later in this thesis.

#### **3.2.1 Model parameters**

Slug flow may be divided into a series of ‘slug units’, which have the structure shown in figure 3.3. Each unit is split into two sections: a ‘slug zone’ of length  $l_s$ , followed by a ‘film zone’ of length  $l_f$ . The phase velocities and the local liquid fraction are constant within the ‘slug’, but are variable along the ‘film’. The parameter  $x$  is used, to denote the axial distance in an upstream direction. Where the film begins,  $x=0$ ; at the end of the film and the start of the succeeding slug,  $x = l_f$ ; and at the end of the slug and the start of the next unit,  $x = l_f + l_s = l_u$ .

Each slug unit moves at a constant *translation velocity*  $V_t$ . In general, this velocity is larger than the velocities within the slug and the film, due to the processes of *pickup* and *shedding* in the slug body. The following *local* velocities are defined within the model:

- The slug liquid velocity,  $V_{ls}$ , and the slug gas velocity  $V_{gs}$ . If the flow in the slug body is homogeneous, then  $V_{ls}$  is equal to  $V_{gs}$ .
- The film liquid velocity  $V_{lf}(x)$  and the gas liquid velocity,  $V_{gf}(x)$ . At the start of the film, where the slug zone ends,  $V_{lf}=V_{ls}$  and  $V_{gf}=V_{gs}$ . At the end of the film, and the



In practice, the gas phase will expand as the flow moves downstream. Therefore, the equations [3.2] and [3.3] are only locally true. The gas superficial velocity at the pipe outlet will be *larger* than the gas superficial velocity at the point of metering. It is necessary to correct for this expansion by taking measurements of the pressure and the temperature, as was previously described in Section 2.3.

Because of the local velocities within the slug unit are different, a considerable exchange of matter may take place between the slug body and the surrounding film. This exchange is defined by the *pickup* and *shedding* rates at the slug front and the slug tail. For the liquid and the gas phases respectively:

$$\begin{aligned} q_{lf} &= (V_i - V_{fe}) a_{fe} & q_{lt} &= (V_i - V_{ls}) a_s \\ q_{gf} &= (V_i - V_{fe}) (1 - a_{fe}) & q_{gt} &= (V_i - V_{gs}) (1 - a_s) \end{aligned} \quad [3.4]$$

where  $q_{lf}$  and  $q_{gf}$  refer to the slug front, and  $q_{lt}$  and  $q_{gt}$  refer to the tail. Empirical expressions for the liquid pickup rate, the gas pickup rate and the liquid shedding rate shall be presented, in section 3.5 below.

### 3.2.3 Stable slug flow

A considerable simplification to the flowrate equations is possible, by assuming that every slug unit is identical. This assumption results in the *stable slug flow* model. In stable slug flow, the pickup rates and the shedding rates for each slug are equal ( $q_{lf}=q_{lt}$  and  $q_{gf}=q_{gt}$ ). In other words:

$$\begin{aligned} (V_i - V_{le}) a_{fe} &= (V_i - V_{ls}) a_s \\ (V_i - V_{le}) (1 - a_{fe}) &= (V_i - V_{gs}) (1 - a_s) \end{aligned} \quad [3.5]$$

By substituting equation [3.5] into equation [3.1] and with some rearrangement, the superficial velocities are then defined by:

$$j_l = V_{ls} a_s + V_i (\bar{a}_f - a_s) \frac{l_f}{l_u} \quad j_g = V_{gs} (1 - a_s) - V_i (\bar{a}_f - a_s) \frac{l_f}{l_u} \quad [3.6]$$

where  $\bar{a}_f$  is the mean liquid holdup

$$\bar{a}_f = \int_{x=0}^{x=l_f} a_f dx \quad [3.7]$$

In equation [3.6], the local liquid velocity  $V_{lj}(x)$  and the local gas velocity  $V_{gj}(x)$  have been eliminated.

Andreussi *et al*<sup>6</sup> modified the stable slug flow model, to include the effect of dispersed gas bubbles within the liquid film. The notation  $a_f$  was used to represent the pipe fraction occupied by a bubbly liquid film, and  $r_f$  represented the local holdup within this bubbly film. The overall liquid holdup was thus given by the product  $a_f r_f$ . At the start of the liquid film,  $a_s=1$  and  $r_f=r_s$ . Equation [3.5] then became:

$$j_l = V_{ls} a_s + V_l (\overline{a_f r_f} - a_s) \frac{l_f}{l_u} \quad j_g = V_{gs} (1 - a_s) - V_l (\overline{a_f r_f} - a_s) \frac{l_f}{l_u} \quad [3.8]$$

in which  $\overline{a_f r_f}$  was the mean liquid film holdup:

$$\overline{a_f r_f} = \int_{x=0}^{x=l_f} a_f r_f dx \quad [3.9]$$

In most of the analysis that follows, the equations developed by Dukler & Hubbard<sup>30</sup> will be used. This is because of their simplicity.

### **3.3 The slug body velocities**

The most important, and the most studied, closure relationship in slug flow is that which relates the local slug velocities  $V_{ls}$  and  $V_{gs}$  to the translation velocity  $V_t$ . Some of the theoretical models that have been developed and the experimental data that have been obtained are now discussed.

#### **3.3.1 Dukler & Hubbard model**

One of the first models to define the liquid velocity  $V_{ls}$  was developed by Dukler & Hubbard<sup>30</sup>. In this model, the slug body was assumed to be a homogeneous mixture ( $V_{ls}=V_{gs}$ ), with a (fully-developed) turbulent velocity profile. The mean velocity of this mixture was denoted as  $V_{ls}$ . Therefore, the liquid close to the pipe wall was travelling more slowly than the mean, and a 'ring' of fluid was shed to the succeeding film zone. The shedding rate was defined by the expression:

$$q_{ll} = V_{ls} a_s - a_s \int_{r=0}^{r=r'} 2\pi r \cdot u(r) dr / A \quad [3.10]$$

where  $u(r)$  was the velocity profile for turbulent single-phase flow, and  $u(r')=V_{ls}$  represented the boundary of the shedding 'ring'. As the shedding rate  $q_{ll}$  is also defined by equation [3.4], equation [3.10] can be expressed as:

$$V_t = V_{ls} + \frac{q_{ll}}{a_s} = V_{ls} (1 + C) \quad C = \frac{q_{ll}}{a_s V_{ls}} \quad [3.11]$$

The integration of the turbulent flow profile, and substitution in equation [3.10], allowed a relationship between  $V_{ls}$  and  $V_t$  to be developed. For the exact relationship, the reader is referred to the original report. For practical applications, Dukler & Hubbard suggested the simpler approximation:

$$C = 0.021 \ln(\text{Re}_s) + 0.022 \quad \text{Re}_s = \frac{\rho_l a_s + \rho_g (1 - a_s)}{\mu_l a_s + \mu_g (1 - a_s)} V_{ls} D \quad [3.12]$$

in which the parameter  $C$  varied between the values 0.25 and 0.28. The liquid in the slug body therefore moves *more slowly* than the slug front.

Dukler & Hubbard compared their model against air-water data taken from a 1.5-inch horizontal pipe. These data covered a range of liquid superficial velocities  $j_l=0.4 \text{ m s}^{-1}$  to  $1.3 \text{ m s}^{-1}$ , and gas superficial velocities  $j_g=1 \text{ m s}^{-1}$  to  $10 \text{ m s}^{-1}$ . At the end of the test section, the liquid slugs were allowed to free-fall on to a tray. By examining the trajectory of the slugs at the pipe exits, the velocity  $V_{ls}$  could then be measured to about 5% relative accuracy. For the limited range of flowrates that was investigated, there was excellent agreement between the experiment and the model.

### 3.3.2 Maron *et al* model

Maron *et al*<sup>78</sup> proposed a similar type of model, for slug flow within in a two-dimensional channel. In this model, the liquid velocity  $V_{ls}$  depended on the development of turbulent *boundary layers* within the slug body, shown in figure 3.4. At the end of the 'mixing zone', it was assumed that a boundary layer could recover from the bottom wall of the channel. A similar boundary layer could also recover from the top wall of the channel, for the special case of un-aerated flow. The growth of each boundary layer was then defined by the single-phase equations:

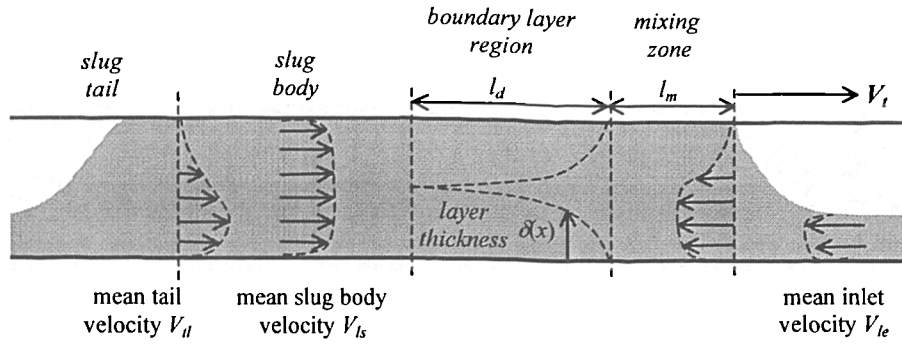


**Figure 3.4:** Idealised velocity profiles throughout the slug zone, assuming a homogeneous mixture of fluids.

$$\delta = 1.01x(V_t x \rho_l / \mu_l) \quad V_x / V_t = 1 - (y/\delta)^{1/7} \quad [3.13]$$

in which  $\delta$  was the layer thickness,  $V_x$  was the local fluid velocity, and  $y$  was the distance into the channel normal to the flow.

Maron *et al* assumed that the ‘slug zone’ ended, when the development of the boundary layers was complete. For an unaerated slug, this completion occurred when the both boundary layers met at the centre of the channel. For an aerated slug, however, the completion occurred when the single layer had reached the height  $\delta/y = h_s$  (where  $h_s$  is the slug holdup). The velocity profiles were integrated, and then used to match the liquid pickup and liquid shedding rates in the slug body. In both cases this resulted in the expression:

$$V_t = \frac{8}{7} V_{ts} \quad [3.14]$$

Despite taking a completely different approach to Dukler & Hubbard<sup>30</sup>, the local liquid velocities ( $V_{ts}$ ) that is predicted by equation [3.14] and that predicted by equation [3.10] are remarkably similar.

### 3.3.3 Bendiksen model

Bendiksen<sup>18</sup> studied the motion of long air bubbles in a 19.2mm diameter section, for a range of different liquid flowrates and pipe inclinations. The translation velocity of each bubble front ( $V_t$ ) was measured using emitter and detector diodes. There was no aeration in the liquid space between each bubble, so the local velocity  $V_{ts}$  was equal to the liquid superficial velocity  $j_l$ . The experimental data were analysed, and were fitted by the correlation:

$$V_t = CV_{ls} + V_o \quad [3.15]$$

in which the parameters  $C$  and  $V_o$  were dependent on the liquid phase Froude number  $Fr_l$  ( $j_l(gD)^{-1/2}$ ) and the pipe inclination  $\beta$ :

$$\begin{cases} C = 1.05 + 0.15 \sin^2 \beta & V_o = \sqrt{gD}(0.35 \sin \beta + 0.54 \cos \beta), & Fr_l < 3.5 \\ C = 1.20 & V_o = \sqrt{gD}(0.35 \sin \beta), & Fr_l > 3.5 \end{cases} \quad [3.16]$$

The changing values for the parameters  $C$  and  $V_o$  in this equation reflected a variety of physical phenomena:

- For low values of the Froude number (i.e. a low liquid flowrate) the coefficient  $C$  tends to unity. This marks the onset of the *plug flow* regime. The pickup of fluid at the slug front and the ejection of fluid at the slug tail cease to occur. Therefore, the liquid velocity  $V_{ls}$  tends towards the translation velocity  $V_t$ .
- As the pipe inclination changes from horizontal to vertical, the gas bubbles develop a *drift velocity* due to buoyancy forces. Benjamin<sup>19</sup> provided an analytic solution to this phenomenon, for vertical flow. The predicted result  $V_o = 0.35(gD)^{1/2}$  was in excellent agreement with equation [3.16] above.
- If the liquid Froude number is small, there is a drift velocity component in horizontal flow. This velocity is due to difference in the hydrostatic head between each 'slug body' and the preceding film. Benjamin<sup>19</sup> solved this problem for stagnant liquid, and observed that  $V_o = 0.54(gD)^{1/2}$ .

The drift velocity appears to disappear in horizontal flows, as the liquid flowrate is increased. This is because the nose of gas bubble drops down, from the top of the pipe to the pipe core (see figure 3.2). As a result, the difference in the hydrostatic head between the front and the film tends to zero.

### 3.3.4 Drift-flux models

Zuber & Findlay<sup>135</sup> developed the *drift-flux model*, for the description of vertical slug flows. In this model, the 'drift-flux' parameter  $j_{gl}$  was defined as the volumetric flux of the gas phase through the surface moving with the total superficial velocity  $j$ . The drift-flux parameter was correlated by the equation:

$$\langle j_g \rangle / \langle \alpha_g \rangle = C_0 \langle j \rangle + V_{gj} \quad [3.17]$$

in which the brackets ( $\langle \rangle$ ) denoted measurements that were averaged over the pipe cross-section. The expression  $\langle j \rangle$  represented the total superficial velocity, while the expression  $\langle \alpha_g \rangle$  represented the average gas fraction. In practice,  $\langle \alpha_g \rangle$  is measured by using a *quick-closing valve* technique. The ‘distribution parameter’  $C_0$  and the ‘drift velocity’  $V_{gj}$  were defined as:

$$C_0 = \langle \alpha_g j \rangle / \langle \alpha_g \rangle \langle j \rangle \quad V_{gj} = \langle \alpha_g (V_g - j) \rangle / \langle \alpha_g \rangle = \langle j_{gt} \rangle / \langle \alpha_g \rangle \quad [3.18]$$

Franca & Lahey<sup>35</sup> applied the drift-flux model to horizontal air-water slug flow, in a 19mm diameter pipe. For each set of flowrates, the difference between the quantities  $\langle j_g \rangle$  and  $\langle \alpha_g \rangle \langle j \rangle$  was calculated. This difference allowed the experimental data to be classified as either ‘plug flow’ or ‘slug flow’. The drift flux correlation for each flow regime was given by:

$$\langle j_g \rangle / \langle \alpha_g \rangle = 0.98 \langle j \rangle + 0.16 \quad \langle j_g \rangle / \langle \alpha_g \rangle = 1.2 \langle j \rangle - 0.20 \quad [3.19]$$

By comparing equations [3.19] and [3.15], it is seen that the expression  $\langle j_g \rangle / \langle \alpha_g \rangle$  is analogous to the translation velocity  $V_t$ , and that the parameter  $V_{jg}$  is analogous to the velocity  $V_o$ .

In a further study, Lahey *et al*<sup>63</sup> used the drift-flux model to correlate multiphase (air-oil-water) slug flows. In this work, the two liquid phases were initially treated as a homogeneous mixture. The slug flow data were classified as either ‘water-based’ or ‘oil-based’, depending on the continuous liquid phase. For these two types of flow, the drift flux correlations were respectively:

$$\langle j_g \rangle / \langle \alpha_g \rangle = 1.29 \langle j \rangle - 0.10 \quad \langle j_g \rangle / \langle \alpha_g \rangle = 2.33 \langle j \rangle - 0.27 \quad [3.20]$$

There is a notable increase in the distribution parameter  $C_0$ , for the oil-continuous slug flow. This increase is due to the large viscosity of the oil phase. The increased viscosity causes the velocity profile in the slug body to change from *turbulent* to *laminar*, and greatly increases the rates of liquid pickup and shedding. This behaviour is discussed in greater detail in section 3.7 below.

### 3.3.5 Woods & Hanratty model

Woods & Hanratty<sup>127</sup> conducted a similar study to Bendiksen<sup>18</sup>, for a range of superficial velocities  $j_t=0.5 \text{ m s}^{-1}$  to  $2 \text{ m s}^{-1}$  and  $j_g=0.2 \text{ m s}^{-1}$  to  $10 \text{ m s}^{-1}$ , in a horizontal 95.3mm pipe. In

these experiments, the aeration present within each liquid slug was measured using a conductance probe. The translation velocity  $V_t$  was correlated against the total superficial velocity  $j$ , according to:

$$V_t = C_o j + V_o, \quad \begin{cases} C_o = 1.10 & V_o = 0.54, & Fr < 3 \\ C_o = 1.20 & V_o = 0, & Fr > 3 \end{cases} \quad [3.21]$$

where the Froude number  $Fr$  was defined as:

$$Fr = j / \sqrt{gD} \quad [3.22]$$

The experimental data, and the correlation defined by equation [3.21], are illustrated in figure 3.5a. For a 95.3mm diameter pipe, the value  $(gD)^{1/2}$  is very close to unity. Therefore, the values for the parameters  $C_o$  and  $V_o$  are in close agreement with the values obtained by Bendiksen.

Woods & Hanratty also used their experimental data to investigate the *slip ratio* between liquid and gas velocities in the slug body. Equation [3.5] was substituted into equation [3.21] and rearranged, to derive the expression:

$$q_{ll} = V_t a_s - \frac{j a_s}{1 + (1-s)(1-a_s)} \quad [3.23]$$

in which the ‘slip parameter’ was the ratio of the gas velocity to the liquid velocity in the slug body,  $V_g/V_{ls}$ .

Woods & Hanratty<sup>127</sup> used an approximate method to estimate the shedding rate  $q_{ll}$  (described in section 3.5 below) and measurements of  $a_s$  and  $V_t$ , in order to derive ‘ $s$ ’. The results of this process are illustrated in figure 3.5b, as a function of the total superficial velocity  $j$ . Despite some considerable scatter, the slip ratio clearly increases from unity to a value of around 1.5, for large superficial velocities ( $j > 7 \text{ m s}^{-1}$ ). This observation is consistent with the ‘blow-through’ process, described in Section 3.1.2 above.

The data shown in figure 3.5b may be fitted by a *piecewise linear correlation*. An approximate fit, which will be made much use of in the later chapters of this thesis, is given by the equations:

$$s = \begin{cases} 1, & j < 3 \text{ ms}^{-1} \\ 1 + 0.125(j-3), & 3 < j < 7 \text{ ms}^{-1} \\ 1.5, & j > 7 \text{ ms}^{-1} \end{cases} \quad [3.24]$$

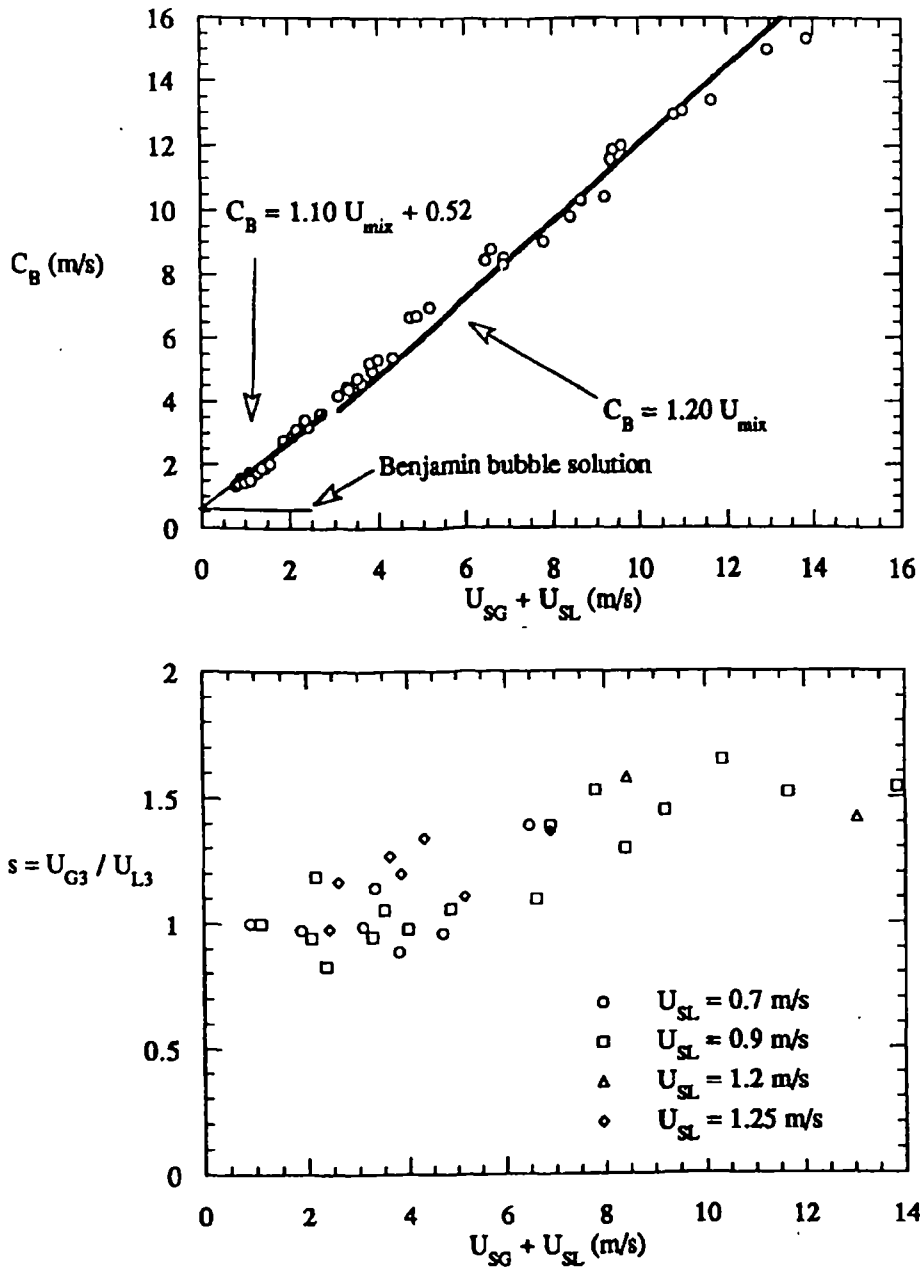


Figure 3.5: The correlation data of Woods & Hanratty<sup>127</sup>. (a) The translation velocity  $V_i$  ( $C_B$ ), as a function of the total superficial velocity  $j$  ( $U_{SG} + U_{SL}$ ); (b) Calculated values of the slip ratio  $s$ , as a function of the total superficial velocity  $j$  ( $U_{SG} + U_{SL}$ ).

### 3.3.6 Gas bubbles within the slug body

In flow with a vertical component, the gas bubbles in the slug body will rise due to *buoyancy forces* (see section 3.1.4). Therefore, there will be an increase in the slip parameter  $s$ , defined by the equation:

$$s = \frac{V_{gs} + V_d}{V_{ls}} \quad [3.25]$$

where  $V_d$  is the bubble rise velocity. Taitel & Barnea<sup>112</sup> approximated the rise velocity to the *terminal velocity* for a single bubble rising in a liquid column. This terminal velocity was given by the expression:

$$V_d = 1.54 \left( \frac{\sigma g (\rho_l - \rho_g)}{\rho_l^2} \right)^{0.25} \sin \beta \quad [3.26]$$

where  $\sigma$  is the liquid surface tension and  $\beta$  is the pipe orientation. In using equation [3.26], it is assumed that there is *no interaction* between the neighbouring bubbles in the slug body.

### **3.4 Pressure drop models**

A variety of closure relationships can be formed, by writing expressions for the *pressure drop* across the slug unit. In this section, models for the pressure drop across the slug zone and the film zone will be described. From these models it will be possible to determine the local velocities within the slug and the film, and to determine the film zone profile ( $a_f(x)$ ). The empirical information that is required to complete each model will then be summarised.

In what follows, much use is made of the *momentum equations* for two-phase flow. Two important assumptions are made when using these equations. First, the phases are arranged in a simple geometry, and second, the phases have a uniform velocity profile. These assumptions will allow frictional and inertial forces to be defined. For a detailed discussion of these momentum equations, consult Wallis<sup>122</sup> or Whalley<sup>124</sup>.

#### **3.4.1 The slug zone pressure drop**

The pressure drop across the slug zone may be divided into three components, which are illustrated in figure 3.6. There is a sharp drop due the mixing zone at the slug front,  $\Delta P_m$ ; a more gradual drop along the slug body due to friction,  $\Delta P_f$ , and a sudden drop due to contraction at the tail,  $\Delta P_r$ . The overall pressure drop is therefore:

$$\Delta P_{slug} = \Delta P_m + \Delta P_f + \Delta P_r \quad [3.27]$$

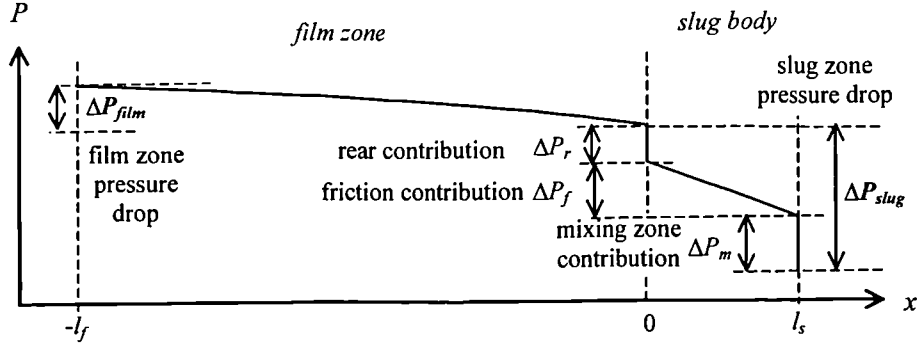


Figure 3.6: Idealised pressure drop profile along the slug zone and the film zone, for the slug unit illustrated in figure 3.3.

For gas-liquid two phase flow, the gas phase density is generally much lower than that of the liquid phase, i.e.  $\rho_g \ll \rho_l$ . Therefore, the effect of the *gas phase inertia* can be neglected in the analysis.

The mixing zone pressure drop  $\Delta P_m$  is caused by the acceleration of the liquid film (velocity  $V_{fe}$ ) as it enters into the slug body (velocity  $V_{ls}$ ). Applying a momentum conservation equation across the slug front results in:

$$\Delta P_m = \rho_l (a_s - a_{fe}) (V_t - V_{ls})^2 \frac{a_s}{a_{fe}} \quad [3.28]$$

The substitution of equation [3.5], and rearrangement for the liquid velocity  $V_{ls}$  then results in the expression:

$$V_{ls} = V_t - \left\{ \frac{\Delta P_m}{\rho_l a_s (a_s/a_{fe} - 1)} \right\}^{1/2} \quad [3.29]$$

Fan *et al*<sup>34</sup> identified an additional, though much smaller, contribution due to the hydrostatic head difference across the front. This contribution was given by the term:

$$\Delta P_m = \Delta P_m + \rho_l g D \{ a_{fe} \xi_{fe} - a_s \xi_s \} \quad [3.30]$$

The dimensionless hydrostatic pressures  $\xi_{fe}$  and  $\xi_s$  (the 'centroids') are defined in section 3.4.4 that follows.

The frictional pressure drop  $\Delta P_f$  is caused by shear forces in the slug body acting against the pipe walls. At sufficiently low gas flowrates, the slug body is a relatively homogeneous mixture. Therefore, the velocity profile resembles fully-developed turbulent flow. The shear

stress and the pressure drop are defined by:

$$\tau_l = \frac{1}{2} f \rho_m V_{ls}^2 \quad \Delta P_f = \frac{\tau_l S l_s}{A} \quad [3.31]$$

where  $f$  is an empirical friction factor,  $\rho_m$  is the mixture density, and  $S$  is the pipe perimeter. The rearrangement of equation [3.31] to obtain the liquid velocity  $V_{ls}$  results in the expression:

$$V_{ls} = \left\{ \frac{\Delta P_f \pi D}{2 f \rho_m l_s} \right\}^{1/2} \quad [3.32]$$

At large gas flowrates there is a further contribution to pressure drop, due to slip in the slug body. Packets of gas pass through from the rear of the slug to the front, introducing *drag forces*. To compensate for this effect, Andreussi *et al*<sup>7</sup> suggested that  $\Delta P_f$  should be multiplied by the empirical factor:

$$\phi_d = \frac{1}{a_s} \left\{ 1.0 + 15.3 \frac{1 - a_s}{a_s^{1.2}} \frac{V_d}{j} \right\} \quad [3.33]$$

The rear pressure drop,  $\Delta P_r$ , is caused by the change in liquid inertia between the slug body and the slug tail. The mean liquid velocity at the end of the slug body may be denoted as  $V_{lt}$  (figure 3.4). Neglecting the presence of any gas within the slug body,  $\Delta P_r$  can then be expressed as (Fan *et al*<sup>33</sup>):

$$\Delta P_r \sim \frac{1}{2} \rho_l (V_l - V_{ls})^2 - \frac{1}{2} \rho_l (V_l - V_{lt})^2 \quad [3.34]$$

An approximate method for estimating the tail velocity  $V_{lt}$  will be described in section 3.5 below. At low gas flowrates, the liquid slug changes to a liquid plug, and the tail becomes a *Benjamin bubble*. For these conditions,  $V_{ls}$  equals  $V_l$  and  $V_{lt}$  equals  $V_l$ , so that the pressure drop at the tail tends to zero.

The models that are described above are an *approximation* to the real slug flow. The theoretical pressure drop has been compared with experimental measurements by Dukler & Hubbard<sup>30</sup>, and by Fan *et al*<sup>34</sup>. Fan *et al*<sup>34</sup> measured the components  $\Delta P_m$ ,  $\Delta P_f$  and  $\Delta P_r$  for slugs in a 90.5mm horizontal pipe, by using an absolute pressure transducer. In these experiments, the limited set of superficial velocities  $j_f=0.5 \rightarrow 1 \text{ m s}^{-1}$  and  $j_g=1 \rightarrow 10 \text{ m s}^{-1}$  were examined. The pressure profiles for some typical slugs are illustrated in figure 3.7. From these profiles, it can be seen that:

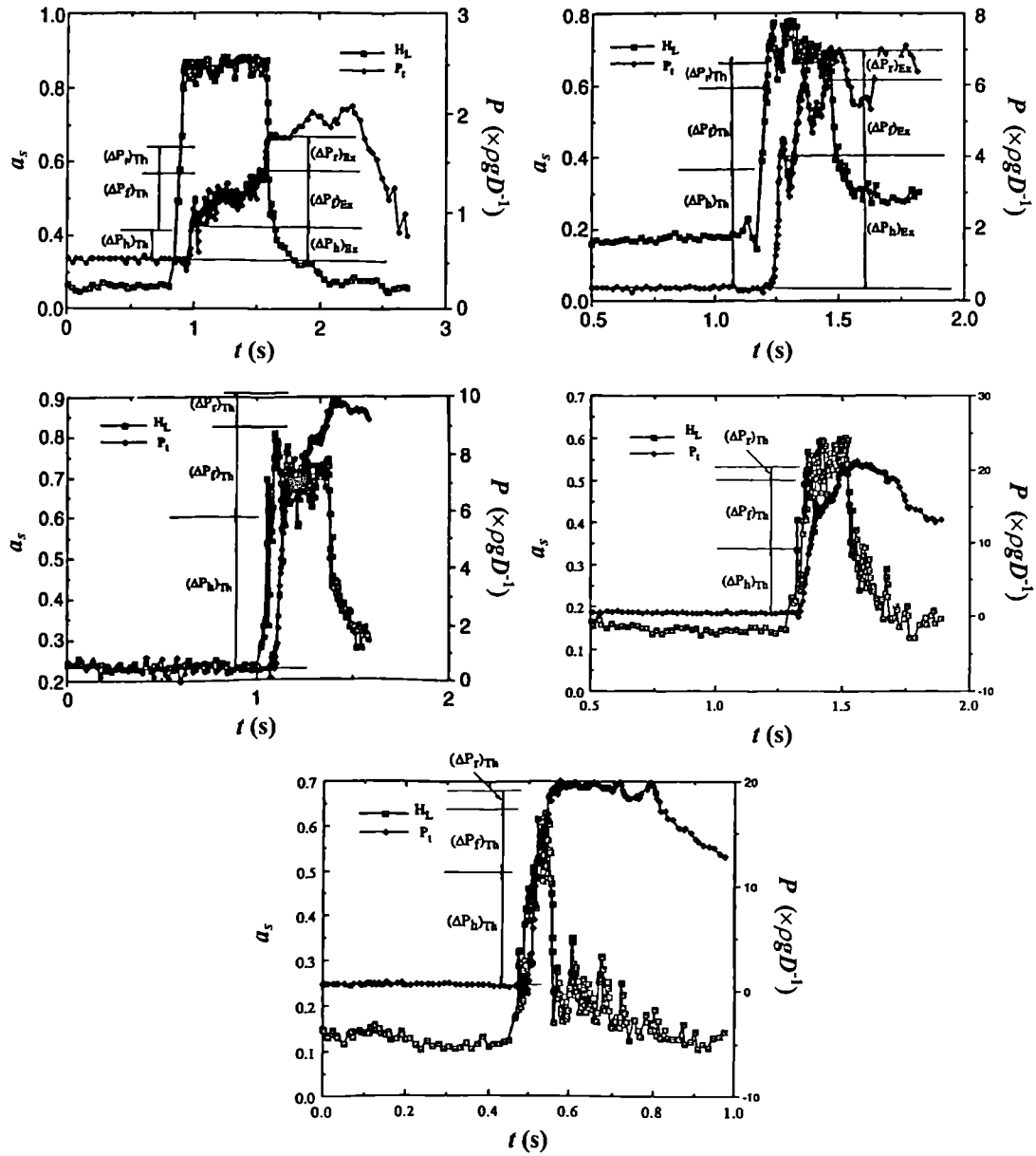


**Figure 3.7:** Slug holdup and pressure profiles, in air-water slug flow (from Fan *et al*<sup>34</sup>).  
 (a)  $j_f=0.6 \text{ m s}^{-1}$ ,  $j_g=1.1 \text{ m s}^{-1}$ ; (b)  $j_f=0.9 \text{ m s}^{-1}$ ,  $j_g=2.96 \text{ m s}^{-1}$ ; (c)  $j_f=0.5 \text{ m s}^{-1}$ ,  $j_g=4.06 \text{ m s}^{-1}$ ;  
 (d)  $j_f=0.9 \text{ m s}^{-1}$ ,  $j_g=7.03 \text{ m s}^{-1}$ ; (e)  $j_f=0.6 \text{ m s}^{-1}$ ,  $j_g=9.09 \text{ m s}^{-1}$ . The components  $\Delta P_m$ ,  $\Delta P_f$   
 and  $\Delta P_r$  are calculated using equations [3.28], [3.31] and [3.34].

- The overall pressure drop,  $\Delta P_{slug}$ , increases dramatically as the gas flowrate is increased. The dominant components of  $\Delta P_{slug}$  are the mixing zone pressure drop  $\Delta P_m$ , and the frictional pressure drop  $\Delta P_f$ .
- The calculated values for the components  $\Delta P_m$ ,  $\Delta P_f$  and  $\Delta P_r$  agree with the experimental values, to about 20% accuracy.

- There is considerably difficulty in distinguishing the individual components  $\Delta P_m$ ,  $\Delta P_f$  and  $\Delta P_r$ , as the gas flowrate is increased.

At large gas flowrates, there appear to be large irregular fluctuations in the pressure drop profile (see, for example, figure 3.7e). These fluctuations are, at present, not properly understood.

### 3.4.2 The film zone pressure drop

The pressure drop along the film zone can be broken into four components, which vary depending on the liquid film holdup. There is an inertial contribution due to the liquid velocity,  $\Delta P_i$ ; a gravitational contribution,  $\Delta P_g$ ; a frictional contribution due to shear stress,  $\Delta P_f$ , and a hydrostatic contribution due to the change in the height of the film,  $\Delta P_h$ . Therefore:

$$\Delta P_{film} = \Delta P_i + \Delta P_g + \Delta P_f + \Delta P_h \quad [3.35]$$

Each component is a function of the distance from the film front,  $x$ . To derive the overall pressure drop  $\Delta P_{film}$ , the four components must be written in differential form and integrated over the film zone length. That is:

$$\Delta P_{film} = \int_0^{x-l_f} \frac{dP}{dx} dx \quad [3.36]$$

Dukler & Hubbard<sup>30</sup> considered the forces acting upon the element of liquid film illustrated in figure 3.8a. The frictional contribution made by the gas phase was neglected in this analysis. The differential contributions made by  $dP_i$ ,  $dP_g$ ,  $dP_f$  and  $dP_h$  were then defined by the equation:

$$\frac{dP}{dx} = \left\{ \frac{d}{dt} (\rho_l a_f V_{lf}) + \frac{d}{dx} (\rho_l a_f V_{lf}^2) \right\} + \left\{ \rho_l g a_f \sin \beta \right\} + \left\{ \frac{\tau_l S_l}{A} \right\} + \left\{ gD \frac{d}{dx} (\rho_l a_f \xi) \cos \beta \right\} \quad [3.37]$$

As the pressure drop along the film is very small compared to the slug body, Dukler & Hubbard<sup>30</sup> assumed that the left-hand term  $dP/dx$  was zero. As a result, the overall pressure drop  $\Delta P_{film}$  in their model was also zero.

Andreussi *et al*<sup>6</sup> generalised equation [3.37], by including the forces acting upon the film interface, the presence of gas bubbles within the film, and by writing a separate momentum balance for the gas phase. These changes resulted in the equations:

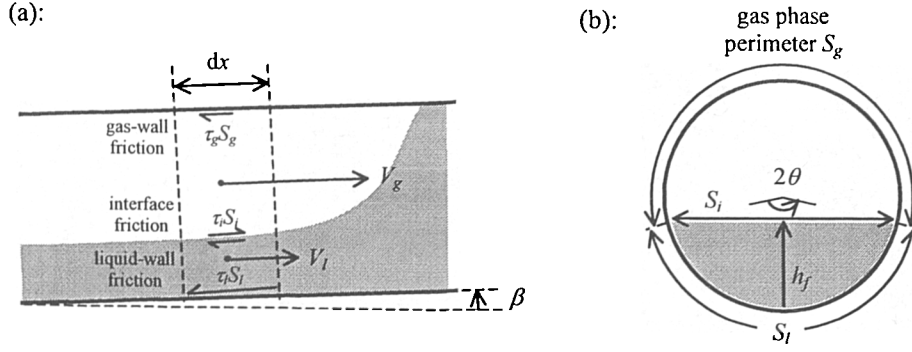


**Figure 3.8:** Modelling of the film zone: (a) the forces acting on a differential film zone element  $dx$ ; (b) the film zone stratified flow geometry

$$a_f \frac{dP}{dx} = \left\{ \frac{d}{dx} (\rho_l a_f r_f (V_l - V_g)^2) \right\} + \{ \rho_m g a_f \sin \beta \} + \left\{ \frac{\tau_l S_l}{A} - \frac{\tau_i S_i}{A} \right\} + \left\{ \rho_l g D \frac{d}{dx} (a_f r_f \xi) \cos \beta \right\} \quad [3.38]$$

and:

$$(1 - a_f) \frac{dP}{dx} = \left\{ \frac{d}{dx} (\rho_g (1 - a_f) (V_l - V_g)^2) \right\} + \{ \rho_g g (1 - a_f) \sin \beta \} + \left\{ \frac{\tau_g S_g}{A} + \frac{\tau_i S_i}{A} \right\} + \left\{ \rho_g g D \left( \frac{1 - a_f}{a_f} \right) \frac{d}{dx} (a_f r_f \xi) \cos \beta \right\} \quad [3.39]$$

where  $r_f$  was the local holdup within the liquid film (section 3.2) and the mixture density  $\rho_m$  was given by:

$$\rho_m = r_f \rho_l + (1 - r_f) \rho_g \quad [3.40]$$

An additional relationship was required to model the behaviour of the local holdup  $r_f$  with the distance  $x$ . It was assumed that the release of the gas bubbles into the film could be described by the transfer equation:

$$A \frac{d}{dx} \{ (V_l - V_g) a_f (1 - r_f) \} = k V_d S_l (1 - r_f) \quad [3.41]$$

where  $V_d$  is the bubble rise velocity defined by equation [3.26], and the release constant  $k$  was (very approximately) estimated to be around 0.25.

At low liquid flowrates, the film zone will become very long, and the holdup will rapidly tend towards its equilibrium value  $a_{fe}$  (see section 3.1.4). In this case, it is possible to considerably simplify the model. By making the approximation that  $a_f(x) \approx a_{fe}$  along the entire film, the inertial and hydrostatic terms will drop out of the momentum balance. As a result, equations [3.38] and [3.39] becomes the ‘constant film’ model:

$$a_f \frac{dP}{dx} = \frac{\tau_l S_l}{A} - \frac{\tau_l S_l}{A}$$

and:

$$(1 - a_f) \frac{dP}{dx} = \frac{\tau_g S_g}{A} + \frac{\tau_l S_l}{A} \quad [3.42]$$

These equations are identical to the pressure drop equations for stratified flow, developed by Taitel & Dukler<sup>112</sup>.

Two simplifications occur as result of the ‘constant film’ model. The total pressure drop along the film zone is given by:

$$\Delta P_{film} = l_f \frac{dP}{dx} \quad [3.43]$$

and at low liquid flowrates, where the film zone is much longer than the slug zone, the local film velocities can be approximated by:

$$V_{le} \sim \frac{j_l}{a_{fe}} \quad V_{ge} \sim \frac{j_g}{1 - a_{fe}} \quad [3.44]$$

The film velocities  $V_{le}$  and  $V_{ge}$  can also be predicted by using equation [3.42], and measurements of the holdup  $a_{fe}$  and the pressure drop  $\Delta P_{film}$ . The prediction requires an iterative process that is illustrated in figure 3.9. The film velocities are functions of the local shear stresses, and *empirical friction factors* which are defined in section 3.4.4 below.

The models described in this section are only *approximate* methods for estimating the pressure drop  $\Delta P_{film}$ . To prove their validity, it is necessary to compare with experimental measurements. The pressure drop  $\Delta P_{film}$  has been experimentally measured in stratified flow (see section 3.4.4 below), but has (at present) not been measured in slug flow. Therefore, a direct verification for the slug flow regime is unavailable. However, it is possible to obtain *indirect* verification, by computing the holdup profile along the film. This process is now described.

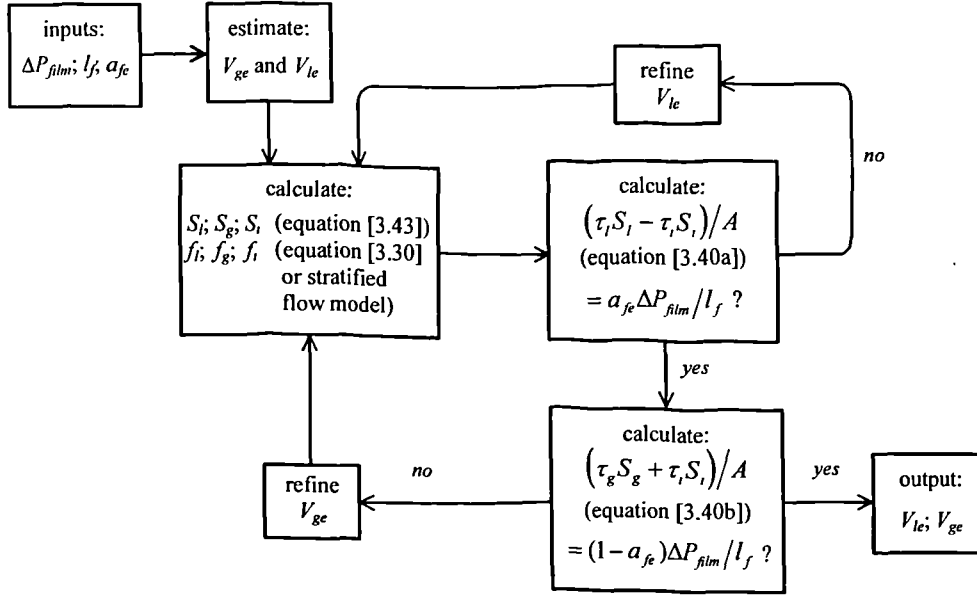


Figure 3.9: Iterative solution procedure for the local film velocities  $V_{lc}$  and  $V_{ge}$ , using the 'constant film' equations.

### 3.4.3 Prediction of the film profile

The holdup profile  $a(x)$  can be predicted, by rearranging the momentum equations for the two phases. The basis of this approach is to substitute the liquid phase equation into the gas phase equation, to eliminate the pressure gradient  $dP/dx$ . A considerable amount of rearrangement then results in:

$$\frac{da_f}{dx} = \left\{ \left[ \rho_l \frac{(V_l - V_b)^2 r_s^2}{a_f^2 r_f^2} + 2P \frac{\rho_g (V_l - V_b) a_s}{r_f^2 (1 - a_f)^2} + (\rho_l - \rho_g) \xi g D \cos \beta \right] \frac{dr_f}{dx} - \frac{\tau_l S_l}{a_f A} + \frac{\tau_l S_l}{a_f (1 - a_f) A} + \frac{\tau_g S_g}{(1 - a_f) A} - r_f (\rho_l - \rho_g) g \sin \beta \right\} \left\{ \frac{\rho_g P^2}{(1 - a_f)^3} + \rho_l \frac{(V_l - V_b)^2 r_s^2}{a_f^3 r_f} - (\rho_l - \rho_g) r_f \left( \frac{d\xi}{d\theta} \frac{d\theta}{da_f} + \frac{\xi}{a_f} \right) g D \cos \beta \right\}^{-1} \quad [3.45]$$

in which:

$$\frac{dr_f}{dx} = \frac{kV_d S_l r_f^2 (1 - r_f)}{A a_s (V_l - V_b)} \quad P = V_l (1 - a_s / r_f) - V_b a_s (1 - 1 / r_f) - V_g (1 - a_s) \quad [3.46]$$

Since the length of the film zone is defined by the limits:

$$l_f = \int_{a_f}^{a_f - a_s} \frac{da}{dx} dx = \int_{x=l_f}^{x=0} \frac{dx}{da} da \quad [3.47]$$

it is possible to obtain the profile  $a_f(x)$  by numerical solution, given the length  $l_f$  and the boundary condition for the holdup:  $a_f(0)=a_s$ . For successful results, the distance  $x$  must be a unique function of  $a_f$ . If there are dispersed bubbles present in the liquid layer, the simultaneous solution of equations [3.45] and [3.46a] is necessary, with two boundary conditions:  $a_f(0)=1$  and  $r_f(0)=a_s$  (Andreussi *et al*<sup>6</sup>).

Cook & Behina<sup>28</sup> calculated the holdup profile for air-water slug flow in a horizontal pipe, using a simple version of equation [3.45]. The gas superficial velocities covered a range  $j_g=1 \text{ m s}^{-1}$  to  $4 \text{ m s}^{-1}$ , while the liquid superficial velocity was fixed at  $1 \text{ m s}^{-1}$ . For this limited set of conditions, the predicted holdup profile and the measured profile were in very good agreement. However, it was necessary to make a correction to the initial value for the gradient  $da_f/dx$  at the start of the film (at  $x=0$ ). This gradient was positive, implying an *increase* in the holdup with the distance  $x$ . Two possible explanations for this error can be offered:

- The empirical friction factors which define the shear stresses  $\tau_l$ ,  $\tau_g$  and  $\tau_i$  are not applicable at the rear of the slug zone.
- The effect of the velocity profile upon the liquid phase inertia has not been considered. The typical velocity profile at the rear of the slug body is shown in figure 3.4.

To correct the error, Cook & Behina<sup>28</sup> decreased the initial holdup ( $a_f(x=0)$ ) in small amounts, until the gradient  $da/dx$  eventually became negative. At this point, the holdup *decreased* along the length of the film zone, in agreement with the experimental data. However, there was no theoretical basis for this correction. The forces near the start of the film zone are clearly not well described by the model.

### 3.4.4 Closure relationships

Empirical expressions for the shear stresses, the contact perimeters and the hydrostatic pressures are required, in order to close the models described in this section. These closure relationships are now summarised.

The shear stresses define the frictional forces acting on each phase, due to the *pipe walls* and the *liquid-gas interface*. In the slug body, the wall shear stress is approximately defined by:

$$\tau_l = \frac{1}{2} f \rho_m V_s^2 \quad [3.48]$$

while for the film zone, the shear stresses  $\tau_l$ ,  $\tau_g$ , and  $\tau_i$  are defined by:

$$\tau_l = \frac{1}{2} f_l \rho_l V_{lf}^2 \quad \tau_g = \frac{1}{2} f_g \rho_g V_{gf}^2 \quad \tau_i = \frac{1}{2} f_i \rho_g (V_{gf} - V_{lf})^2 \quad [3.49]$$

where  $V_{lf}$  and  $V_{gf}$  are the local film velocities, and  $f_l$ ,  $f_g$  and  $f_i$  are the friction factors for the liquid-wall, gas-wall and gas-liquid interfaces.

The *friction factors* account for the roughness of each interface. For the liquid-wall boundary, and the gas-wall boundary in the film zone, the single-phase Blasius equation is commonly used. This has the form:

$$f = C Re^{-n} \quad Re = \frac{\rho V D}{\mu} \quad [3.50]$$

where the parameters  $C$  and  $n$  have the values 16 and 1 for a laminar flow, and 0.046 and 0.2 for turbulent flow.

The Reynolds number  $Re$  must be modified in the slug body, to account for the density and viscosity of the liquid-gas mixture. Assuming a homogeneous mixture, the Reynolds number is approximately given by:

$$Re_s = \frac{\rho_l a_s + \rho_g (1 - a_s)}{\mu_l a_s + \mu_g (1 - a_s)} V_s D \quad [3.51]$$

The Reynolds number must also be modified for the film zone, to take account of the flow geometry. The pipe diameter  $D$  should be replaced by the *hydraulic diameters* defined by Agrawal *et al*<sup>3</sup>:

$$D_l = \frac{4 a_f A}{S_l} \quad D_g = \frac{4 (1 - a_f) A}{S_g + S_l} \quad [3.52]$$

As an alternative to the Blasius equation, the friction in the film zone may be modelled using friction factors developed for *stratified flow*. Such friction factors have been obtained by Taitel & Dukler<sup>115</sup>, Andritsos & Hanratty<sup>10</sup>, Hart *et al*<sup>48</sup>, and Vlachos *et al*<sup>121</sup> amongst others.

The principle is to measure the pressure drop in stratified flow, and use the ‘constant film’ model (equation [3.41]) to derive empirical expressions for  $f_i$  and  $f_g$ . However, it is assumed that the film zone closely resembles a stratified flow.

The interfacial friction factor  $f_i$  is much harder to define, because it is not possible to directly measure the interfacial stress. Cook & Behina<sup>28</sup> and Taitel & Barnea<sup>112</sup> assumed that  $f_i$  had the constant value:

$$f_i = 0.014 \quad [3.53]$$

while Dukler & Hubbard<sup>30</sup> assumed there was no interfacial friction, as implied in section 3.4.2 above. However, there is no theoretical basis behind either of these approaches.

The frictional force acting on each phase is the product of the shear stress and the *constant perimeter*  $S$ . In the body of the slug, the stress is assumed to act round the entire perimeter, so that:

$$S = \pi D \quad [3.54]$$

while in the film zone, the contact perimeters  $S_l$ ,  $S_g$  and  $S_i$  are defined assuming a perfectly stratified flow geometry. This geometry is illustrated in figure 3.8b. Each perimeter is a function of the dimensionless film height  $h_f$ :

$$S_l = \pi - \cos^{-1}(2h_f - 1)D \quad S_g = \cos^{-1}(2h_f - 1)D \quad S_i = \sqrt{1 - (2h_f - 1)^2}D \quad [3.55]$$

where  $h_f$  is related to the film holdup  $a_f$  and the subtended angle  $\theta$  by:

$$a_f = 1 - \frac{1}{\pi} \cos^{-1}(2h_f - 1) + \frac{1}{\pi} (2h_f - 1) \left\{ 1 - (2h_f - 1)^2 \right\}^{1/2} \quad [3.56]$$

$$h_f = \frac{1}{2} \cos(\pi - \theta) + \frac{1}{2}$$

Finally, the hydrostatic centres of pressure (the ‘centroids’) must be defined at the front of slug and in the film zone. Dukler & Hubbard<sup>30</sup> integrated the pressure over the stratified geometry shown in figure 3.8b, to derive the dimensionless centroid  $\xi$ . This integration resulted in:

$$\xi = -\frac{1}{2} \cos(\theta/2) + \frac{1}{3\pi a_f} \sin^3(\theta/2) \quad [3.57]$$

For the case where the pipe is full of liquid (e.g. in the slug body), the centroid  $\xi$  will have the value 0.5.

The empirical expressions that have been presented in this section are most appropriate for 'well behaved' slug flow, at low gas and low liquid flowrates. However, a number of shortcomings are identified. These shortcomings are summarised as follows:

- As the gas flowrate increases, the film zone will change gradually from a stratified to an annular geometry. In this case, the shear stresses, the contact perimeters and the hydrostatic pressures must be modified for annular flow.
- It has been assumed that the shear stress distribution is uniform around the pipe perimeter. This is unlikely to be the case, in particular for the *mixing zone* at the front of the slug.
- The friction factor expressions are only applicable to *steady flow*. Therefore, they are not applicable to large waves or rapid changes in height within the film zone, or if there are large pulses of gas passing through the slug body.

In order to correctly model the pressure drop, additional measurements for the shear stress and the interface profile are clearly required.

### **3.5 Pickup and shedding processes**

The pickup and shedding processes within the slug are important, because they relate the incoming and outgoing phase velocities to the translation velocity  $V_t$ . In this section, models that define the minimum pickup rate and the minimum shedding rate for the liquid phase will be presented. Some experimental measurements of the gas pickup rate ( $q_{gf}$ ) and some simple models for developing slug flow will then be discussed.

#### **3.5.1 Liquid pickup and shedding**

The liquid pickup rate  $q_{lf}$  and the liquid shedding rate  $q_{lt}$  in slug flow are subject to *minimum limits*. These limits can be determined, by assuming that the flow in the slug body is irreversible. Two-dimensional slug flow in a channel (which is a simpler case to analyse) will first be considered, and then the basic principles will be extended to three-dimensional slug flow in a pipe.

Ruder *et al*<sup>103</sup> developed a model for unaerated slug flow in a 2D channel, illustrated in figure 3.4. A momentum conservation equation was applied across the slug front, in order to determine the *irreversible* pressure drop due to the liquid phase. A Bernoulli equation was then applied along a liquid streamline, to determine the *reversible* pressure drop across the slug front. Since the pressure drop across the slug front had to be real positive (i.e. real), the former pressure drop had to exceed the latter. This resulted in the condition:

$$q_{lf} \geq h_{fe} \sqrt{gH} \quad [3.58]$$

where  $h_{fe}$  was the holdup of the film zone immediately prior to the slug front, and  $H$  was the height of the flow channel.

Ruder *et al*<sup>103</sup> conducted a similar analysis upon the slug *tail*. In this analysis, it was assumed that the slug tail behaved as a Benjamin bubble. This extra condition meant that the shedding rate at the back of the slug was defined by:

$$q_{lt} = 0.5 \sqrt{gH} \quad [3.59]$$

and therefore, stable slug flow within the channel was defined by:

$$h_{fe} \geq 0.5 \quad [3.60]$$

In the limiting case of plug flow, there was zero pressure drop across the channel front, so that the film holdup  $h_{fe}$  had a minimum value of 0.5.

The above expressions can be modified for a pipe geometry, by introducing a dimensionless ‘wall curvature’ function denoted as  $\phi_{fe}(\alpha_f)$ . The exact values for the function  $\phi_{fe}$  can be derived by consulting the original report. As a result of this change, equations [3.58] to [3.60] became:

$$q_{lf} \geq a_{fe} \phi_{fe} \sqrt{gD} \quad [3.61]$$

$$q_{lt} = 0.542 \sqrt{gD} \quad [3.62]$$

$$a_{fe} \geq 0.542 / \phi_{fe} \quad [3.63]$$

Ruder *et al*<sup>103</sup> obtained experimental measurements of the pickup rate and the shedding rate from a 93mm pipe, over the range of superficial velocities  $j_f=0.2 \rightarrow 1 \text{ m s}^{-1}$  and  $j_g=1 \rightarrow 5 \text{ m s}^{-1}$ . By comparing these measurements against the above expressions, the following observations

were made:

- The measured pickup rate ( $q_{lf}$ ) was always greater than the minimum limit defined by equation [3.61].
- As the pickup rate ( $q_{lf}$ ) increased, the shedding rate ( $q_{ll}$ ) increased by the same amount, so that the slugs remained *stable*.

It was concluded that equation [3.62] above defined the minimum limit, for the liquid shedding rate  $q_{ll}$ .

In a different experiment, Fan *et al*<sup>33</sup> measured the pickup and shedding rates for slugs in 25 mm and 50 mm pipes. This was done using the stationary slug apparatus of Jepson<sup>57</sup>, which allowed the ‘incoming’ velocity of the liquid at the slug front ( $V_f - V_{fe}$ ) to be accurately controlled. Two important changes to the flow were observed, as the gas flowrate was increased:

- There was aeration present, within the slug body (see figures 3.2b to 3.2d).
- The profile of the film behind the slug tail was notably different from the Benjamin bubble profile (Benjamin<sup>19</sup>).

To account for these changes, Fan *et al* proposed that the liquid at the back of the slug should move *more slowly* than the liquid in the slug body. This ‘back velocity’, which is illustrated in figure 3.4, is denoted by the symbol  $V_{ll}$ . As a result, the shedding rate for slugs in the channel is given by:

$$q_{ll} = (V_f - V_{ls})h_s = \left\{ 0.51 + \frac{(V_f - V_{ll})^2}{gH} \right\} \sqrt{gH} \quad [3.64]$$

The shedding rate for slugs in a *pipe* geometry requires the iterative solution of several equations. For these equations, the reader is referred to the original report.

According to equation [3.64], a decrease in the back velocity  $V_{ll}$  causes an increase in the shedding rate  $q_{ll}$ . Fan *et al*<sup>33</sup> observed this increase experimentally, by increasing the velocity of the film layer entering the slug body. As the ‘slug’ structure remained stable, there was a corresponding increase in the shedding rate. Further evidence that the back velocity had reduced was obtained from by measuring the *pressure drop profile*. Upon increasing the incoming film velocity, there was a corresponding rise in the rear pressure drop  $\Delta P_r$ , in agreement with equation [3.34] above.

### 3.5.2 Gas Entrainment

The gas entrainment into the slug body rises, upon making the transition from the plug flow to the slug flow regime (see section 3.1.2). A theoretical model and experimental measurements for the entrainment process are now presented.

Andreussi & Bendiksen<sup>5</sup> proposed a model in which the gas entrainment was split into 'production rate' ( $q_{g1}$ ) and 'return rate' ( $q_{g2}$ ) components. The net entrainment rate  $q_{gf}$  was thus defined by:

$$q_{gf} = q_{g1} - q_{g2} \quad [3.65]$$

The production rate ( $q_{g1}$ ) was modelled according to the incoming velocity of the liquid film layer,  $V_i - V_{le}$ . When the incoming velocity was smaller than a limiting value  $V_{mf}$ , no bubble production was observed. This corresponded to a slug holdup of unity. However, when the incoming velocity exceeded  $V_{mf}$ , bubble production increased *linearly* with the incoming velocity. This observation resulted in the expression:

$$q_{g1} = C_1 \{ a_s (V_i - V_{le}) - V_{mf} \} \quad [3.66]$$

The return rate ( $q_{g2}$ ) was modelled according to the 'rise velocity' of the gas bubbles  $V_d$  (defined in section 3.3.6) and the slug holdup  $a_s$ . Bubble return was largest, in air-free slugs according to:

$$q_{g2} = C_2 (1 - a_s) V_d \quad [3.67]$$

Andreussi & Bendiksen developed a rather complex expression for the velocity  $V_{mf}$  using measurements of the slug holdup  $a_s$ . Crucially, however, they did not define the proportionality constants  $C_1$  and  $C_2$  in their report.

Nydal & Andreussi<sup>89</sup> examined the entrainment of gas into a liquid *front* in a 50mm pipe, for the range of liquid superficial velocities  $j_l = 1.2 \rightarrow 6.0 \text{ m s}^{-1}$ . This front differed from a conventional 'slug' in that it had no tail region. Consequently, it was possible to measure the entrainment rate  $q_{gf}$  by using a series of conductance sensors. These measurements were correlated by the equation:

$$q_{gf} = c_1 \left\{ (V_i - V_{le}) - c_2 \right\} \quad [3.68]$$

in which:

$$c_1 = 0.076S_i/D \quad c_2 = 1.97D/S_i \quad [3.69]$$

and where the interface perimeter  $S_i$  was related to the holdup  $a_{fe}$  by assuming a stratified flow geometry (see figure 3.8b). By comparing equations [3.66]-[3.67] and equations [3.68]-[3.69], the following expressions are derived:

$$C_1 = \frac{c_1}{a_{fe}} = \frac{0.076S_i}{a_{fe}D} \quad [3.70]$$

$$V_{mf} = c_2 a_{fe} = \frac{1.97a_{fe}D}{S_i} \quad [3.71]$$

A similar experiment to measure the gas entrainment rate was conducted by Manolis<sup>76</sup>. The resulting correlation was used to develop a model for tracking the motion of individual slugs, which is described by Manfield<sup>75</sup>.

### 3.5.3 Developing slug flow

Developing slugs occurs immediately downstream of the pipe inlet, and after any series of pipe bends. As the *development distance* in gas-liquid flow is quite considerable (typically several hundreds of pipe diameters), such slugs have a significant effect upon what emerges at the pipe outlet. In a developing slug, the rates of liquid pickup and liquid shedding do not match, so that the overall holdup in the slug body and the overall slug length ( $l_s$ ) change with time. This change can be modelled by the expressions:

$$q_u = q_{lf} - \frac{dV}{dt} \quad [3.72]$$

or:

$$q_u = q_{lf} - (V_t - V_u)a_s \quad [3.73]$$

in which  $dV/dt$  is the rate of change of liquid content within the slug body (Woods & Hanratty<sup>127</sup>), and where  $V_u$  is the translation velocity for the slug tail (Fan *et al*<sup>34</sup>). As a result, the continuity equation for the liquid phase (equation [3.5a]) is modified, and takes the form:

$$(V_t - V_{ls})a_s = (V_t - V_{fe})a_{fe} - \frac{dV}{dt} \quad [3.74]$$

Some theoretical models and experimental measurements for the rate of change  $dV/dt$  (i.e. the tail velocity  $V_u$ ) are now described.

The liquid shedding rate  $q_{ll}$  normally increases as the slug length reduces, because there is no opportunity for *boundary layers* to develop within the slug body. As a result, short slugs are prone to decay and assimilation into longer slugs that follows (see section 3.1.1 above). Maron *et al*<sup>78</sup> proposed that a slug would decay, when the length of the ‘boundary layer region’ ( $l_d$ ) was below the limit:

$$l_d \leq (Ha_s/1.01)^{1.25} (V_f \rho_l / \mu_l)^{0.25} \quad [3.75]$$

in which  $l_d$  is related to the overall slug length ( $l_s$ ) by:

$$l_d + l_m = l_s \quad [3.76]$$

Moissiths & Griffiths<sup>84</sup> measured the translation velocity ( $V_f$ ), the tail translation velocity ( $V_u$ ), and the length ( $l_s$ ) of liquid plugs near the entrance of a 19mm vertical pipe. The difference between the tail and the front velocities, which defined the decay rate of the slug, were then fitted by the correlation:

$$V_u - V_f = 5.5V_f \exp(-\beta l_s / l_{stab}) \quad [3.77]$$

in which the ‘stable slug length’ parameter  $l_{stab}$  was of the order of  $10D$ , and where the empirical coefficient  $\beta$  was of the order of 0.6. This correlation was therefore in good agreement with the model proposed by Maron *et al*<sup>78</sup>.

Barnea & Taitel<sup>15</sup> used the correlation of Moissiths & Griffiths<sup>84</sup>, to develop a model for tracking the slugs passing along a horizontal pipe. This model involved the input of a random series of ‘slug units’ and ‘film units’ at the entrance section. Some typical output, for the superficial velocities  $j_f=0.1 \text{ m s}^{-1}$  and  $j_g=0.25 \text{ m s}^{-1}$ , is illustrated in figure 3.10 below. At a distance of approximately 100 pipe diameters downstream, the slug length distribution was measured. Regardless of the input sequence or the phase flowrates, the *mean slug length* was always of the order:

$$l_s \sim 15D \quad [3.78]$$

This value is in excellent agreement with the measured slug length, which is presented in section 3.6.3 that follows. Therefore, it is implied that equation [3.77] is correct, for a wide range of phase flowrates and pipe inclinations.

Woods & Hanratty<sup>127</sup> measured the rate of change of liquid ( $dV/dt$ ) parameter, for slugs in a horizontal pipe at a distance of 200 diameters downstream of the inlet. This measurement was performed using two pairs of conductance sensors, which could track changes in the slug body holdup ( $a_s$ ) and duration ( $t_s$ ). The *average value* and the *statistical variation* in  $dV/dt$  were recorded, for the wide range of flowrates  $j_l=0.5 \rightarrow 2 \text{ m s}^{-1}$  and  $j_g=1 \rightarrow 10 \text{ m s}^{-1}$ . These results indicated that:

- At low total flowrates ( $j < 3 \text{ m s}^{-1}$ ) the mean value of  $dV/dt$  and the standard deviation in  $dV/dt$  were both zero. Therefore, the flow had reached ‘quasi-stable’ conditions.
- At larger total flowrates ( $j > 3 \text{ m s}^{-1}$ ) the mean value of  $dV/dt$  remained close to zero, though the standard distribution in  $dV/dt$  increased notably (to about  $5 \text{ l s}^{-1}$ ). Therefore, there were still a significant number of growing and decaying slugs in the pipe.

The results indicate that the slug development process is a strong function of the total superficial velocity ( $j$ ), and is notably different in *plug flow* than *slug flow*. The mechanism by which the slugs are being initiated (which was discussed in section 3.1) is likely to be different for these two cases. The growth of large-amplitude waves at the pipe inlet, and their subsequent growth into slugs, is discussed in further by Hale<sup>43</sup>.

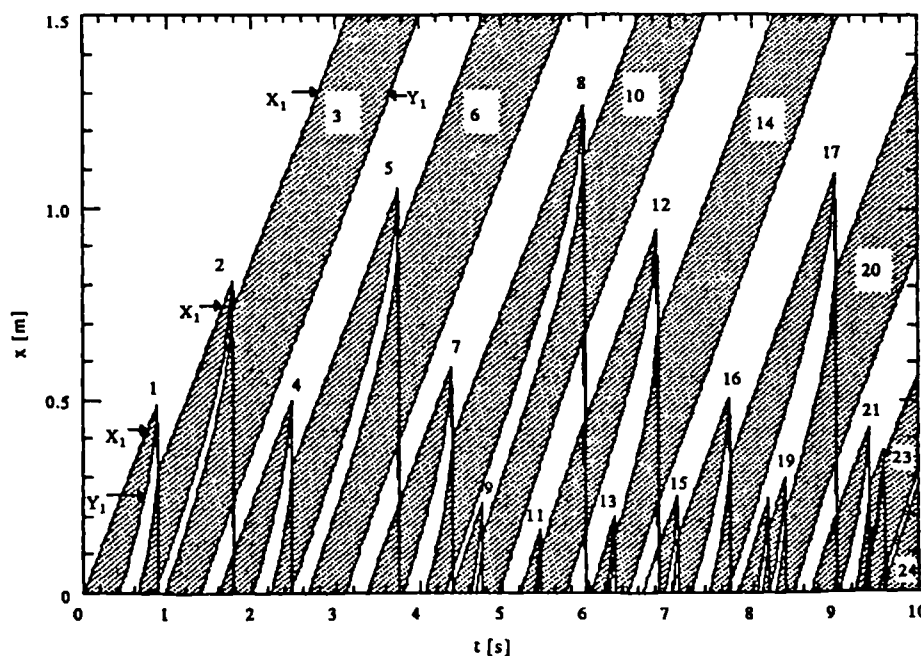


Figure 3.10: The slug tracking model of Barnea & Taitel<sup>15</sup>. The evolution of a random pattern of slugs at the pipe inlet, for the flowrates  $j_l=0.1 \text{ m s}^{-1}$ ,  $j_g=0.25 \text{ m s}^{-1}$ . (In this example, slug numbers 3, 6, 10, 14 and 20 develop into *stable slugs*).

### 3.6 Other correlations

Aside from the correlations for the translation velocity ( $V_t$ ), the local slug velocities ( $V_{ls}$  and  $V_{gs}$ ) and the pickup and shedding rates, many other correlations have been developed for stable slug flow. In this section, some important correlations for the *slug frequency*, the *slug holdup* and the *slug length* will be presented. Considerable use of this material will be made, in the following chapter of this thesis.

#### 3.6.1 Slug frequency correlations

The slug frequency ( $\nu$ ) is a particularly important correlation, because it is used to determine the mean pressure drop across the slug unit. The slug frequency increases strongly with the liquid flowrate but is only minimally dependent upon the gas flowrate. Amongst others, correlations have been developed by Hubbard<sup>30</sup>; Gregory and Scott<sup>41</sup>; Greskovich & Shrier<sup>42</sup>, Heywood & Richardson<sup>53</sup>, and Manolis<sup>76</sup>.

Gregory & Scott<sup>41</sup> developed the following correlation for carbon dioxide-water flow in a 19mm horizontal pipe:

$$\nu = 0.0226 \left( \frac{j_l}{gD} \cdot \frac{19.75 + j^2}{j} \right)^{12} \quad [3.76]$$

where  $j$  is the total superficial flow velocity. However, equation [3.76] is restricted to use in low-pressure flow.

Manolis *et al*<sup>77</sup> noted that the position of the stratified-slug flow pattern boundary, and the slug frequency, were strongly affected by the *operating pressure*. They obtained frequency data for air-water flow and fitted it with the correlation:

$$\nu = 0.0037 \left( \frac{j_l}{gD} \cdot \frac{25 + j^2}{j} \right)^{18} \quad [3.77]$$

Increases in frequency close to the transition boundary with stratified flow, and as the pipe diameter  $D$  is reduced, were noted.

Tronconi<sup>119</sup> modelled the slug frequency as a function of unstable ‘precursor waves’ observed in the film zone. It was assumed that only every second ‘precursor wave’ was capable of developing into a slug. Linear stability theory (Lin & Hanratty<sup>66</sup>) was then used to postulate that:

$$v \sim 0.61 \frac{V_{ge} \rho_g}{h \rho_l} \quad [3.78]$$

where  $V_{ge}$  and  $h$  were the local gas velocity, and the local height of the stratified film layer, prior to the next passing slug. The parameters  $V_{ge}$  and  $h$  were estimated from experimental pressure drop data and the correlation of Chisholm<sup>26</sup>.

The above correlations neglect the influence of the liquid phase *viscosity*. Increasing this viscosity causes the slug frequency to increase due to the changing flow profile in the slug body. For example, Odozi<sup>91</sup> observed a doubling of the slug frequency in oil-water flow as compared to gas-water flow. Tronconi<sup>119</sup>, and Manolis<sup>76</sup>, have also made similar observations.

### 3.6.2 Slug holdup correlations

The slug holdup ( $a_s$ ) reduces with the gas phase flowrate, due to the increasingly vigorous process of *gas entrainment* at the slug front. This continues, until the slug holdup approaches a minimum value of around 0.4. Below this limit, At this point, it is physically impossible to maintain a blockage of the pipe (Gopal & Jepson<sup>39</sup>) and the phases will flow in an *annular* geometry.

Gregory *et al*<sup>40</sup> correlated the slug holdup  $a_s$  for air-oil flow in 25.8mm and 51.2mm diameter horizontal pipes. By using capacitance sensors to measure the holdup, they predicted that:

$$a_s = \left(1 + (j/8.66)^{1.39}\right)^{-1} \quad [3.79]$$

Equation [3.79] is only minimally affected by the liquid phase flowrate. However at large *total* flowrates, the predicted value for the slug holdup is well below the minimum defined above.

Andreussi & Bendiksen<sup>5</sup> studied the effect of pipe inclination upon the slug holdup, for air-water flow in 50mm and 90mm horizontal pipes. They proposed (as discussed in section 3.5.2) that the holdup  $a_s$  was strongly dependent on the ‘incoming’ film velocity,  $V_f - V_{le}$ . This fact was used to develop a correlation of the form:

$$a_s = \frac{V_{ls} - V_{mf}}{\beta V_{ls} + V_{m0}} \quad [3.80]$$

in which the parameters  $\beta$ ,  $V_{mf}$  and  $V_{m0}$  are defined in the original report. The resulting correlation is rather complex. A simpler fit to the experimental data, which are illustrated in figure 3.11, is given by the correlation:

$$a_s = \begin{cases} 1 & j < 2.5 \text{ms}^{-1} \\ 1.242 - 0.263 \ln j & j \geq 2.5 \text{ms}^{-1} \end{cases} \quad [3.81]$$

The slug holdup is also affected by the *difference in density* between the liquid and gas phases, and the liquid phase *surface tension*. As discussed by Nydal & Andreussi<sup>89</sup>, the entrainment of gas bubbles into the slug body increases as each of these parameters is reduced.

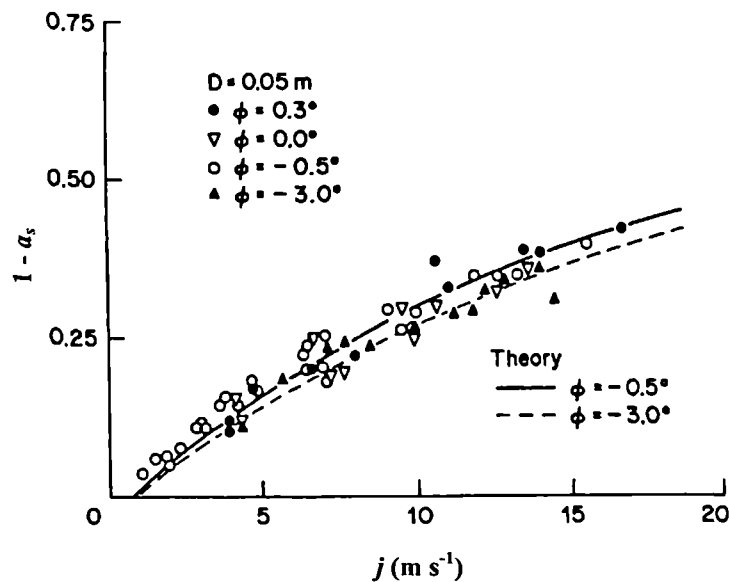


Figure 3.11. Slug holdup data of Andreussi & Bendiksen<sup>5</sup>.  $\phi$  represents the pipe inclination.

### 3.6.3 Slug length

The slug length,  $l_s$ , has been experimentally measured by many workers (for example by Brill *et al*<sup>21</sup>; Sæther *et al*<sup>104</sup>, and Nydal *et al*<sup>88</sup>) and has also been predicted theoretical models, (for example Dukler & Hubbard<sup>30</sup> and Barnea & Taitel<sup>15</sup>). Unlike the slug frequency and the slug holdup, the slug length is relatively independent of *both* the liquid and the gas phase flowrates.

Dukler & Hubbard<sup>30</sup> developed a model for the slug length, based on the assumption that the

local film holdup  $\alpha_f$  rapidly approaches the equilibrium value  $\alpha_{fe}$ . This assumption resulted in the equation:

$$l_s = \frac{V_{ls}}{v(a_s - \alpha_{fe})} \left\{ \frac{j_l}{V_{ls}} - \alpha_{fe} + C(a_s - \alpha_{fe}) \right\} \quad [3.82]$$

Measurements of the slug length were obtained in horizontal flow, and were compared against the values predicted by equation [3.82]. (This comparison used the correlations for the parameters  $C$  and  $V_{ls}$  given in section 3.1.2). In general, the measured and the predicted values were in good agreement.

Nydal *et al*<sup>88</sup> measured the slug length in 53 mm and 90 mm horizontal pipes, over the range of superficial velocities  $j_f=0.6$  to  $3.5 \text{ m s}^{-1}$  and  $j_g=0.5$  to  $20 \text{ m s}^{-1}$ . Their data were divided into 'developing' and 'developed' slugs. After neglecting the developing slugs, the mean slug length was then:

$$l_s \sim 15D \quad [3.83]$$

regardless of the phase superficial velocities. This length represented the mean value of a log-normal distribution, and was in good agreement with the theoretical model of Barnea & Taitel<sup>15</sup>.

Strictly speaking, the 'slug body' does not include the highly aerated *mixing zone* at the slug front. The length of the mixing zone is useful, in order to calculate of the mixing zone pressure drop (section 3.4) and the slug 'development length' (section 3.5.3). By analysing photographs of air-water slugs, Dukler & Hubbard<sup>30</sup> estimated that the mixing zone length ( $l_m$ ) to be of the order:

$$l_m \sim 0.15(V_{ls} - V_{le})^2 \quad [3.84]$$

On the other hand, Andreussi *et al*<sup>6</sup> correlated the mixing zone length by using conductance probe measurements. This approach resulted in the expression:

$$l_m \sim 30(1 - \alpha_s)D \quad [3.85]$$

As seen from equations [3.84] and [3.85], the length of the mixing zone increases from zero, with the total flow velocity. At the slug-annular transition boundary, the mixing zone occupies up to half the total slug length.

### **3.7 Multiphase slug flow model**

Sections 3.2 to 3.6 specifically discussed the modelling of two-phase (gas-water) slug flow. However, slug flows containing both oil and water components will always be encountered during offshore production. Therefore, it is necessary to develop a model for *multiphase* (oil-water-gas) slug flow. Though the material presented in this section will not be used again within the thesis, it is essential for completeness.

#### **3.7.1 Flowrate equations**

Many experimental studies of three-phase flow have now been published, with those by Stapelberg & Mewes<sup>110</sup> and Acikgoz<sup>3</sup> being of particular note. These studies indicate that the distributions of liquid and gas in each three-phase slug unit are very similar to those in two-phase flow. Therefore, it is possible to visualise a multiphase ‘slug unit’ shown in figure 3.11, in which the superficial velocities are defined by:

$$j_o = V_{os} a_{os} \frac{l_f}{l_u} + \frac{1}{l_u} \int_0^{l_f} a_o V_o dx \quad [3.85]$$

$$j_w = V_{ws} a_{ws} \frac{l_f}{l_u} + \frac{1}{l_u} \int_0^{l_f} a_w V_w dx \quad [3.86]$$

$$j_g = V_{gs} (1 - a_{os} - a_{ws}) \frac{l_f}{l_u} + \frac{1}{l_u} \int_0^{l_f} (1 - a_{os} - a_{ws}) V_g dx \quad [3.87]$$

where  $V_t$  is the translation velocity as before,  $V_o(x)$ ,  $V_w(x)$ ,  $V_{os}$  and  $V_{ws}$  are the local velocities of the liquid components, and  $a_{os}$ ,  $a_{ws}$ ,  $a_{of}$  and  $a_{wf}$  are the phase fractions within the slug and the film zones.

Depending on the degree of mixing between the two liquids, two sets of *closure relationships* can be developed to complement equations [3.85] to [3.87]. These closure relationships are now described.

#### **3.7.2 ‘Homogeneous flow’ model**

Usually, the mixing zone in the slug will cause the homogenisation of the oil and water components throughout the slug unit (Acikgoz<sup>3</sup>). This homogenisation results in two considerable simplifications: the local slug velocities ( $V_{os}$  and  $V_{ws}$ ) and the local film

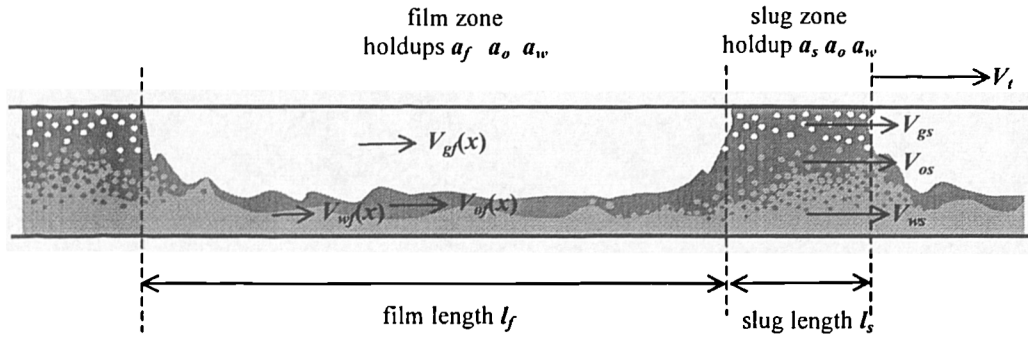


Figure 3.12: Simplified 'slug unit' for three-phase (gas-oil-water) flow.

velocities ( $V_{of}$  and  $V_{wf}$ ) will become equal. The liquid phase flowrates are then given by the equations:

$$j_o = (1 - \lambda)j_i \quad j_w = \lambda j_i \quad [3.86]$$

in which  $\lambda$  is the in-situ water fraction:

$$\lambda = \frac{a_w}{a_o + a_w} \quad [3.87]$$

Assuming that the water fraction remains constant throughout the length of the slug unit, the oil and the water flowrates can be derived from a measurement of the total liquid velocity ( $j_i$ ) and the *water-cut* ( $\lambda$ ).

The relationship between the translation velocity  $V_i$  and the local velocity  $V_{is}$  is strongly influenced by the *mixture viscosity*. Amongst many others, Brinkman<sup>22</sup>, Hatscheck<sup>50</sup> and Richardson<sup>101</sup> and have observed that this viscosity rises exponentially, around the point where the mixture inverts from water-continuous to oil-continuous. This phenomenon can be approximately modelled by the expression:

$$\mu_{mix} \sim \frac{\mu_c}{(1 - \lambda)^k} \quad [3.88]$$

where  $\mu_c$  is the viscosity of the continuous liquid phase,  $\lambda$  is the water fraction, and  $k$  is a 'tightness parameter' with a value of the order of 2.5. The switch in continuity normally occurs within the range  $0.4 < \lambda < 0.6$ , and causes the behaviour shown in figure 3.12. However, the inversion process is further complicated, by its dependency upon the *phase flowrates* (Donnelly<sup>29</sup>).

Should the mixture viscosity become sufficiently large, the local Reynolds number will drop and there will be a transition from turbulent flow to *laminar flow* within the slug body. This change causes a large increase in the ‘distribution parameter’  $C_o$ , that was discussed in section 3.3 above. Lahey *et al*<sup>63</sup> and Odozi<sup>91</sup> have both observed that  $C_o$  rises from about 1.2 to 1.8 as phase inversion occurs, and then rises to 2.0 for oil-continuous flow. The increase in the mixture velocity also causes a significant increase in the overall pressure drop, the slug frequency  $\nu$ , and the slug length  $l_s$  (Odozi<sup>91</sup>).

### 3.7.3 ‘Separated flow’ model

At low slug frequencies (low liquid flowrates) the mixing zone is not sufficiently strong to keep the liquid components homogeneously mixed. There will therefore be a gradual separation of the liquids along the film zone, with these components eventually adopting different velocities. Direct measurements, or empirical relationships, for the film velocities  $V_{of}$  and  $V_{wf}$  are thus required.

If the liquid layers are sufficiently distinct, the velocities  $V_{of}$  and  $V_{wf}$  can be estimated by using a *stratified flow model*, illustrated in figure 3.13. By balancing the forces acting on each stratified layer, Taitel *et al*<sup>113</sup> derived the expressions:

$$\begin{aligned} \tau_g \frac{S_g}{a_g A} - \tau_o \frac{S_o}{a_o A} - \tau_{i1} \frac{S_{i1}}{a_w A} + \tau_{i2} \left( \frac{S_{i2}}{a_g A} + \frac{S_{i2}}{a_o A} \right) &= 0 \\ \tau_l \frac{S_o}{a_o A} - \tau_w \frac{S_w}{a_w A} - \tau_{i2} \frac{S_{i2}}{a_o A} + \tau_{i1} \left( \frac{S_{i1}}{a_o A} + \frac{S_{i1}}{a_w A} \right) &= 0 \end{aligned} \quad [3.89]$$

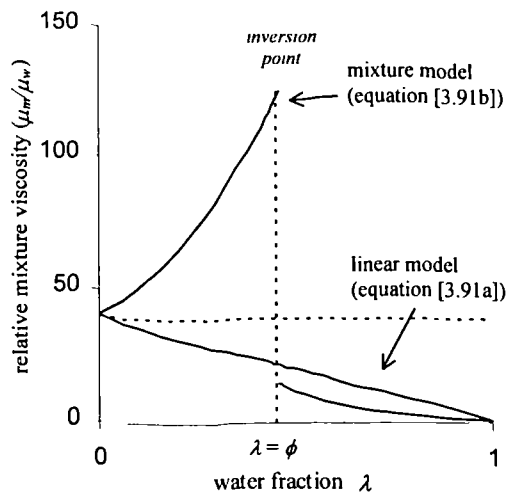


Figure 3.13: The effect of varying the in-situ water fraction  $\lambda$  upon the *mixture viscosity* (oil-water flow).

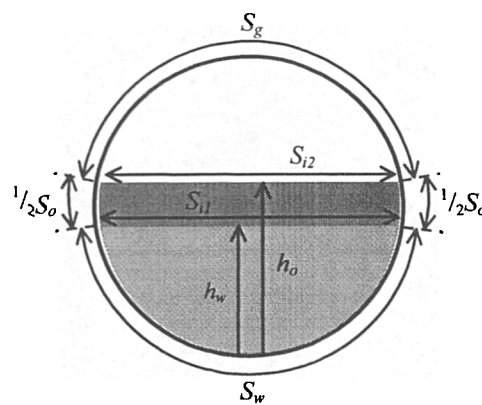


Figure 3.14: Three-phase (oil-water-gas) stratified flow geometry.

in which the shear stresses  $\tau_{i1}$  and  $\tau_{i2}$  act upon the oil-water and the gas-water interfaces respectively. Equation [3.89] can be iteratively solved for  $V_{of}$  and  $V_{wf}$ , given measurements of the pressure drop  $\Delta P_{film}$  and suitable closure relationships for the shear stresses. (This solution process is analogous to that shown in figure 3.9). The results of Neogi, Lee & Jepson<sup>87</sup> indicate that this prediction may give reasonable results at low gas flowrates, though the empirical uncertainty (which was discussed in section 3.4.4) will clearly be worse for the three-phase flow case.

The gradual separation of the liquid phases in the film zone also has an effect upon the liquid mixture viscosity  $\mu_m$ . This is a complex three-dimensional effect, and cannot be modelled without knowing the *droplet size distribution* throughout the pipe section. However, as a simple approximation, Pan<sup>96</sup> proposed that mixture viscosity for a case intermediate between ‘stratified’ and ‘well-mixed’ flow could be interpolated using the formula:

$$\mu_m = C_m \mu_{lin} + (1 - C_m) \mu_{nonlin} \quad [3.90]$$

where  $\mu_{lin}$  and  $\mu_{nonlin}$  are linear and non-linear mixture viscosity components, respectively defined as:

$$\mu_{lin} = \lambda \mu_w + (1 - \lambda) \mu_o \quad \mu_{nonlin} = \mu_c (1 - \lambda^{1/3}) \quad [3.91]$$

The parameter  $C_m$  in equation [3.90] will gradually reduce from unity to zero, as the components in the film zone separated. However, Pan was unable to specify exactly *how* this reduction should take place. In order to implement this model, an equation for the characteristic *separation length* (such as that proposed by Hall<sup>44</sup>) or experimental measurements of the separation phenomenon is required.

### **3.8 Summary**

In this chapter, the modelling of two-phase, and three-phase slug flow in pipelines was examined in detail.

Section 3.1 described the processes of slug initiation and slug development, initially in a horizontal pipe section. The structure of the ‘slug body’ and the ‘film zone’ regions of a developed ‘slug unit’ were then described, with particular attention being paid towards the influence of the gas phase flowrate. Lastly, the effect of the pipe orientation upon the initiation and development processes was discussed.

Section 3.2 presented a predictive model for two-phase developed slug flow, as a function of the characteristic velocities  $V_t$ ,  $V_{ls}$ ,  $V_{gs}$ ,  $V_{lf}$  and  $V_{gf}$ , the phase fractions  $\alpha_s$  and  $\alpha_f$ , and the lengths  $l_f$  and  $l_s$  within each ‘slug unit’. Expressions for the phase superficial velocities and the mass flowrates were derived from these variables. The simplification that could be made to this model by assuming *stable slug flow* was demonstrated.

Sections 3.3 to 3.6 presented a variety of empirical relations that can be used to close the predictive model, in the absence of reliable experimental measurements. These empirical relations were categorised into:

- Correlations for the slug liquid velocity  $V_{ls}$  and the slug gas velocity  $V_{gs}$ , as a function of the unit translation velocity  $V_t$  (section 3.3).
- Models for the pressure drop in the slug and the film zones, from which the local velocities  $V_{ls}$ ,  $V_{lf}$  and  $V_{gf}$  can be inferred. (section 3.4). The film zone model also allows prediction of the film holdup profile,  $a(x)$ .
- Models for the pickup and shedding of liquid and gas phases from the slug body, for both stable and unstable slug flow conditions (section 3.5).
- Correlations for the mean slug frequency  $\nu$ , the mean slug body holdup  $\alpha_s$ , and the mean slug length  $l_s$  (section 3.6).

Table 3.1 summarises some of the most important closure relationships, presented in sections 3.3 to 3.6 of this chapter. Considerable use of these equations will be made, in the following chapters of the thesis.

Finally, section 3.7 described the multiphase (oil-water-gas) slug flow model. This model was split into two distinct cases: homogeneous liquid components (section 3.7.1), and separated liquid components (section 3.7.2). The effect of the overall liquid mixture viscosity for a homogeneous liquid flow was described. The additional closure relations required for a separated liquid flow were then presented.

Having discussed the *sensing instrumentation* and the *predictive model*, the following four chapters of this thesis (Chapters 4 to 7) will describe the development of a prototype system for metering gas-water slug flow. The performance of this system will then be assessed using the NEL multiphase facility, and the results will be analysed in Chapter 8.

Correlation variable	inputs required	equation number	Reference:	Comments:
$V_{ls}$	$V_l$	[3.12]	Duker & Hubbard <sup>30</sup>	assumes homogeneous flow (i.e. $V_{gs}=V_{ls}$ )
$V_{ls}$	$V_l$	[3.14]	Maron <i>et al</i> <sup>78</sup>	
$V_{ls}$	$V_l$	[3.15]	Bendiksen <sup>18</sup>	unacrated plug flow conditions only ( $V_l=j_l$ )
$j$	$V_l$	[3.21]	Woods & Hanratty <sup>127</sup>	
$s$	$j$	[3.24]	Woods & Hanratty <sup>127</sup>	additional component required for vertical flows (equation [3.26])
$V_{ls}$	$V_l; V_{fe}; a_{fe}; \Delta P_m$	[3.27]	Fan <i>et al</i> <sup>34</sup>	
$V_{ls}$	$a_s; \Delta P_f$	[3.30]	Fan <i>et al</i> <sup>34</sup>	requires empirical friction factor input
$V_{lc} \& V_{ge}$	$a_{fe}; l_s; \Delta P_{film}$	see figure 3.9	Taitel & Dukler <sup>115</sup>	uses <i>constant film</i> model (valid only for low slug frequency)
$V_{ge}$	$j_g; a_{fe}$	[3.44]	Fan <i>et al</i> <sup>34</sup>	limited applicability ( $j_g$ is required as input)
$v$	$j_l$	[3.77]	Manolis <i>et al</i> <sup>77</sup>	extension of the Gregory & Scott correlation, for high pressure flows
$a_s$	$j$	[3.79]	Gregory <i>et al</i> <sup>40</sup>	inaccurate holdup prediction for high gas velocities
$a_s$	$j$	[3.81]	Andreussi & Bendiksen <sup>5</sup>	simplified version of original correlation (equation [3.80])
$l_s$	-	[3.83]	Nydal <i>et al</i> <sup>88</sup>	<i>constant slug length</i> ( $l_s=15D$ for all conditions)

**Table 3.1:** Summary of the most important closure relationships defined between Sections 3.3 and Section 3.6.

## 4. Metering approach

In this chapter, the approach that shall be used to meter two-phase (gas-water) slug flow will be defined. This approach will combine a ‘stable slug flow’ model, instrumentation for measuring each of the model parameters, and a computer system for processing the sensor data. Therefore, much use will be made of the material presented in Chapters 2 and 3 of this thesis. In order to be of practical use, the overall system should be *non-intrusive* to the flow, and of *minimal cost*.

The description is divided into three sections discussing the *equations*, the *sensitivity analysis* and the *instrumentation*, as follows:

- Section 4.1 summarises the equations for the flowrates that were presented in chapter 3, and the parameters that must be measured in order to implement the stable slug flow model.
- Section 4.2 will describe a sensitivity analysis. In this analysis, the sensitivity of the flowrates to each measurement parameter will be determined, using the existing correlations in the literature. The most critical measurement parameters will then be highlighted.
- Section 4.3 will describe suitable instrumentation for measuring each of the parameters in gas-water slug flow. This instrumentation will be non-intrusive and inexpensive. The requirements of the computer system, which processes the sensor data and delivers the flowrates, will also be defined.

Figure 4.1 is a ‘top-level’ diagram of the system, and illustrates the components that will be developed in the coming chapters. Conductance electrodes will be designed to measure the local phase fractions and the translation velocity (Chapter 5). Novel instrumentation will be developed to measure the conductance between these electrodes (Chapter 6). A computer system, which acquires the sensor data and delivers the phase flowrates, will then be described (Chapter 7). These components will then be assembled, and used to meter the slug flow within the NEL facility.

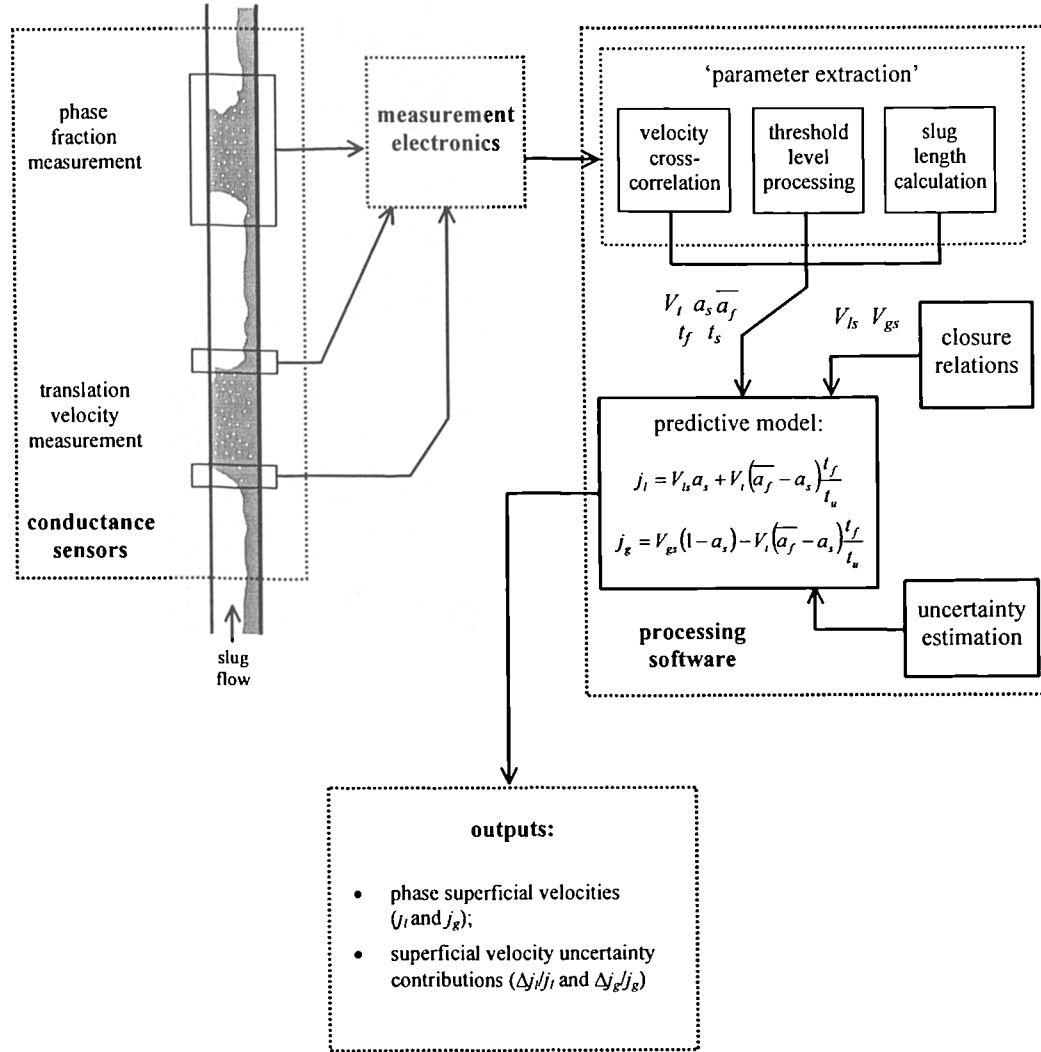


Figure 4.1: Components of the proposed metering system

#### 4.1 Parameter specification

Equations for the phase flowrates within each passing ‘slug unit’ were described in Chapter 3. These flowrates are the product of the phase densities, the pipe cross-section area and the superficial velocities:

$$m_l = \rho_l j_l A \qquad m_g = \rho_g j_g A \qquad [4.1]$$

The superficial velocities ( $j_l$  and  $j_g$ ) were obtained using a mass balance for the passing ‘slug’ and ‘film’ zones. This resulted in the equations:

$$j_l = V_{ls} a_s \frac{l_s}{l_u} + \frac{1}{l_u} \int_0^{l_f} a_f V_{lf} dx \quad j_g = V_{gs} (1 - a_s) \frac{l_s}{l_u} + \frac{1}{l_u} \int_0^{l_f} (1 - a_f) V_{gf} dx \quad [4.2]$$

where  $a_s$  and  $a_f(x)$  were the slug and the film zone phase fractions,  $V_{ls}$  and  $V_{gs}$  were the local slug velocities,  $V_{lf}(x)$  and  $V_{gf}(x)$  were the local film velocities, and  $l_f$  and  $l_s$  were the slug and film lengths.

There are nine parameters in equation [4.2] that must be known, in order to meter the flowrates. This number can be reduced, by assuming that the slug flow is *developed* and *stable*. This assumption is reasonable, provided that there is a ‘development distance’ of about 300 pipe diameters before the metering takes place (see section 3.1). In stable slug flow, the rates of pickup and shedding are equal in each slug unit, so that:

$$\begin{aligned} (V_t - V_{lf}) a_f &= (V_t - V_{ls}) a_s \\ (V_t - V_{gf}) (1 - a_f) &= (V_t - V_{gs}) (1 - a_s) \end{aligned} \quad [4.3]$$

Equation [4.3] can be used to eliminate either the local slug velocities  $V_{ls}$  and  $V_{gs}$  or the local film velocities  $V_{lf}$  and  $V_{gf}$  from equation [4.1]. However, the film velocities are variable along the length of the film zone, and are difficult to measure directly (see section 4.3 below). Therefore, equation [4.1] has been written in the form:

$$j_l = V_{ls} a_s + V_t (\bar{a}_f - a_s) \frac{l_f}{l_u} \quad j_g = V_{gs} (1 - a_s) - V_t (\bar{a}_f - a_s) \frac{l_f}{l_u} \quad [4.4]$$

where  $\bar{a}_f$  is the mean holdup along the film zone. By analysing equations [4.1] to [4.4], the following parameters must be measured to establish the flowrates:

- The phase densities at the point of metering ( $\rho_l$  and  $\rho_g$ ).
- The mean film zone and the slug zone phase fractions ( $a_s$  and  $\bar{a}_f$ ).
- The translation velocity ( $V_t$ ).
- The duration of the film zone and the slug zone film ( $t_f$  and  $t_s$ ). (From which  $l_f = V_t t_f$  and  $l_s = V_t t_s$ ).
- *Any two* local velocities from within the slug zone ( $V_{ls}$  and  $V_{gs}$ ) and the film zone ( $V_{lf}$  and  $V_{gf}$ ).

Two important points are worth noting. First of all, the NEL multiphase test facility can

automatically monitor the phase densities at the meter location. Therefore, in this specific application, the system only needs to be able to measure the phase superficial velocities  $j_l$  and  $j_g$ .

Secondly, the stable slug flow model assumes that each slug unit has exactly identical characteristics. In practice, slug flow is 'quasi-stable', i.e. there is some variation in the length, the velocity, and the holdup within each passing unit. There is a need to resolve the discrepancy between the experimental data and the model, by *averaging* the parameter measurements in some way before they are used. This averaging technique shall be discussed in Chapter 7 that follows.

## 4.2 Sensitivity analysis

To establish the relationship between the accuracy in the measurement of the parameters  $V_t$ ,  $\overline{a_f}$ ,  $a_s$ ,  $V_{ls}$ ,  $V_{gs}$ ,  $t_f$  and  $t_s$  and the accuracy in the phase flowrates, a *sensitivity analysis* will now be conducted. This analysis is split a background section, where the method and the relevant correlations are presented. The results will then be presented and analysed, in several different ways. It is assumed that the 'stable slug flow' model is an accurate representation of the real flow.

### 4.2.1 Background

If the phase densities are known, the flowrate uncertainties are equivalent to the superficial velocity uncertainties,  $\Delta j_l/j_l$  and  $\Delta j_g/j_g$ . The overall uncertainty in each superficial velocity is the sum of six terms, according to:

$$\begin{aligned} \left| \frac{\Delta j_l}{j_l} \right| &= \sum_X \left| S_{j_l}(X) \frac{\Delta X}{X} \right| & X \in \{V_t, V_{ls}, \overline{a_f}, a_s, t_f, t_s\} \\ \left| \frac{\Delta j_g}{j_g} \right| &= \sum_Y \left| S_{j_g}(Y) \frac{\Delta Y}{Y} \right| & Y \in \{V_t, V_{gs}, \overline{a_f}, a_s, t_f, t_s\} \end{aligned} \quad [4.5]$$

The sensitivity parameters  $S_y(x)$  are defined by:

$$S_y(x) = \frac{\partial y}{\partial x} \cdot \frac{x}{y} \quad [4.6]$$

To obtain the sensitivity coefficients  $S_{j_l}$  and  $S_{j_g}$ , the partial differentiation of equation [4.4] is

required. In this differentiation, it will be assumed that the total duration of the slug unit  $t_u$  ( $t_f+t_s$ ) is a constant, so that the terms in table 4.1 are derived.

To investigate the effect of the liquid and the gas flowrates upon the uncertainty, the sensitivity coefficients need to be expressed in terms of the phase superficial velocities. To do this, it is necessary to use the existing relationships. In this work, the correlations by Woods & Hanratty<sup>127</sup> (for the translation velocity  $V_t$ ), Manolis *et al*<sup>77</sup> (for the slug frequency  $\nu$ ), Nydal *et al*<sup>88</sup> (for the slug length  $l_s$ ), equation [3.81] (for the slug holdup  $a_s$ ), and equation [3.24] (for the slip ratio  $V_{gs}/V_{ls}$ ) have been used. These correlations are as follows:

$$V_t = C_o j - V_o, \begin{cases} C_o = 1.10, & V_o = 0.54, & j(gD)^{-1/2} < 3 \\ C_o = 1.20, & V_o = 0, & j(gD)^{-1/2} > 3 \end{cases}$$

$$\nu = 0.0037 \left( \frac{j_l}{gD} \cdot \frac{25 + j^2}{j} \right)^{1.8} \quad l_s = 15D$$

$$a_s = \begin{cases} 1, & j < 2.5 \text{ms}^{-1} \\ 1.242 - 0.263 \ln j, & j > 2.5 \text{ms}^{-1} \end{cases} \quad s = \begin{cases} 1, & j < 3 \text{ms}^{-1} \\ 1 + 0.125(j - 3), & 3 < j < 7 \text{ms}^{-1} \\ 1.5, & j > 7 \text{ms}^{-1} \end{cases} \quad [4.7]$$

	$S\{j_l\}$	$S\{j_g\}$
$V_t$	$(\overline{a_f} - a_s) \frac{t_f}{t_u} \frac{V_t}{j_l}$	$(a_s - \overline{a_f}) \frac{t_f}{t_u} \frac{V_t}{j_g}$
$V_{ls}$	$a_s \frac{V_{ls}}{j_l}$	-
$V_{gs}$	-	$(1 - a_s) \frac{V_{gs}}{j_g}$
$a_f$	$V_t \frac{t_f}{t_u} \frac{\overline{a_f}}{j_l}$	$-V_t \frac{t_f}{t_u} \frac{\overline{a_f}}{j_g}$
$a_s$	$\left( V_{ls} - \frac{V_t t_f}{t_u} \right) \frac{a_s}{j_l}$	$\left( \frac{V_t t_f}{t_u} - V_{gs} \right) \frac{a_s}{j_g}$
$t_f$	$V_t (\overline{a_f} - a_s) \frac{t_f}{t_u j_l}$	$V_t (a_s - \overline{a_f}) \frac{t_s}{t_u j_g}$
$t_s$	$V_t (a_s - \overline{a_f}) \frac{t_f}{t_u j_l}$	$V_t (\overline{a_f} - a_s) \frac{t_s}{t_u j_g}$

Table 4.1: Table of sensitivity parameters, obtained by partial differentiation of equations [4.4a] and [4.4b].

By using the above correlations and equations [4.3] to [4.4], the following expressions for the local slug velocities  $V_{ls}$  and  $V_{gs}$ , the mean film holdup  $a_f$ , the film zone duration  $t_f$ , and the slug zone duration  $t_s$  are also derived:

$$V_{ls} = \frac{j}{a_s + s(1 - a_s)} \quad V_{gs} = \frac{sj}{a_s + s(1 - a_s)}$$

$$\overline{a_f} = (j_l - V_{ls}a_s) \frac{t_u}{V_l t_f} + a_s \quad t_f = \frac{1}{v} - \frac{l_s}{V_l} \quad t_s = \frac{l_s}{V_l} \quad [4.8]$$

Equations [4.7] and [4.8] contain all the information that is necessary to evaluate the uncertainties in equation [4.5], given the superficial velocities  $j_l$  and  $j_g$ . However, the correlations used in this analysis have been developed for different test fluids, different pipe diameters, different flowrates and a range of pipe inclinations. Therefore, it is uncertain whether these correlations are applicability to slug flow in the NEL multiphase facility.

#### 4.2.2 Results

The sensitivity coefficients  $S_{j_l}$  and  $S_{j_g}$  are illustrated in figure 4.2, for gas superficial velocities in the range  $1 \text{ m s}^{-1}$  to  $15 \text{ m s}^{-1}$ , and the four liquid superficial velocities  $j_l=0.1 \text{ m s}^{-1}$ ,  $j_l=0.3 \text{ m s}^{-1}$ ,  $j_l=1.0 \text{ m s}^{-1}$  and  $j_l=3.0 \text{ m s}^{-1}$ . This set of superficial velocities corresponds to ‘plug’ flow, ‘slug’ flow, and ‘slug-annular’ flow. There are six sensitivity coefficients for each phase, in accordance with equation [4.5]. The larger each coefficient, the greater the precision required in the measurement parameter. For example, if  $S = 10$ , a 0.5% error in any one parameter causes a 5% error in the flowrate.

From figure 4.2, it is apparent that:

- The liquid phase sensitivities are much larger than the gas phase sensitivities. Therefore, accurate metering of the *liquid phase* flowrate presents the greatest difficulty.
- The liquid and the gas phase sensitivities are largest for the lowest liquid superficial velocity,  $j_l=0.1 \text{ m s}^{-1}$ . Therefore, accurate metering is most difficult near the transition boundary with stratified flow.
- The sensitivities  $S(V_l)$ ,  $S(V_{ls})$  and  $S(V_{gs})$  are usually equal to, or larger than, the sensitivities  $S(a_f)$  and  $S(a_s)$ . Therefore, it is more important to obtain accurate velocity measurements, than accurate holdup measurements.

- The sensitivity  $S(a_f)$  is generally larger than the sensitivity  $S(a_s)$ . Therefore, it is more important to accurately measure the holdup in the film, than the holdup in the slug.

The results for two specific conditions  $\{j_f=0.1 \text{ m s}^{-1}, j_g=1.0 \text{ m s}^{-1}\}$  and  $\{j_f=1.0 \text{ m s}^{-1}, j_g=6.0 \text{ m s}^{-1}\}$  have been redisplayed in figure 4.3, in bar chart form. The dominant sensitivity coefficients (i.e. the *most critical* parameters in the slug flow model) can now be identified. From figure 4.3, it emerges that:

- Near the boundary with stratified flow, accurate measurements of the velocity  $V_f$  (and  $V_{fs}$  for the liquid phase), the phase fractions  $a_f$  and  $a_s$ , and the time  $t_f$ , are of equal importance.
- As the total flowrate is increased, accurate measurements of the local velocity  $V_{fs}$  (for the liquid phase) and  $t_s$  (for the gas phase) increase in importance. On the other hand, however, accurate measurements of the slug holdup  $a_s$ , the film holdup  $a_f$  and the translation velocity  $V_f$ , become less significant.

As discussed above, the sensitivity coefficients are much larger for the liquid phase than for the gas phase. The sensitivity coefficients will also tend to reduce, as the total flowrate is increased.

The results in figure 4.2 can also be used, to determine the *maximum permissible* uncertainty in the measurement of each model parameter. The rearrangement of equation [4.5] will result in:

$$\left| \frac{\Delta X}{X} \right| = \left| \frac{\Delta j_l}{j_l} \cdot \frac{1}{S_{j_l}(X)} \right| \quad \left| \frac{\Delta Y}{Y} \right| = \left| \frac{\Delta j_g}{j_g} \cdot \frac{1}{S_{j_g}(Y)} \right| \quad [4.9]$$

where  $X$  and  $Y$  are the sets of parameters defined in section 4.2.1. In a commercial multiphase meter, the liquid and the gas flowrates should ideally be measured to within 5% relative accuracy (Wolff<sup>126</sup>). Table 4.2 summarises the maximum permitted uncertainty, to achieve this 5% accuracy over the whole of the slug flow regime. The results in this table indicate that:

- For the gas flowrate, the velocities  $V_f$  and  $V_{gs}$  and the phase fractions  $a_f$  and  $a_s$  need to be measured with 5% accuracy.
- For the liquid flowrate, the velocity  $V_{fs}$  needs to be measured with 0.1% accuracy, while the translation velocity  $V_f$  and the phase fractions  $a_f$  and  $a_s$  with 0.2%

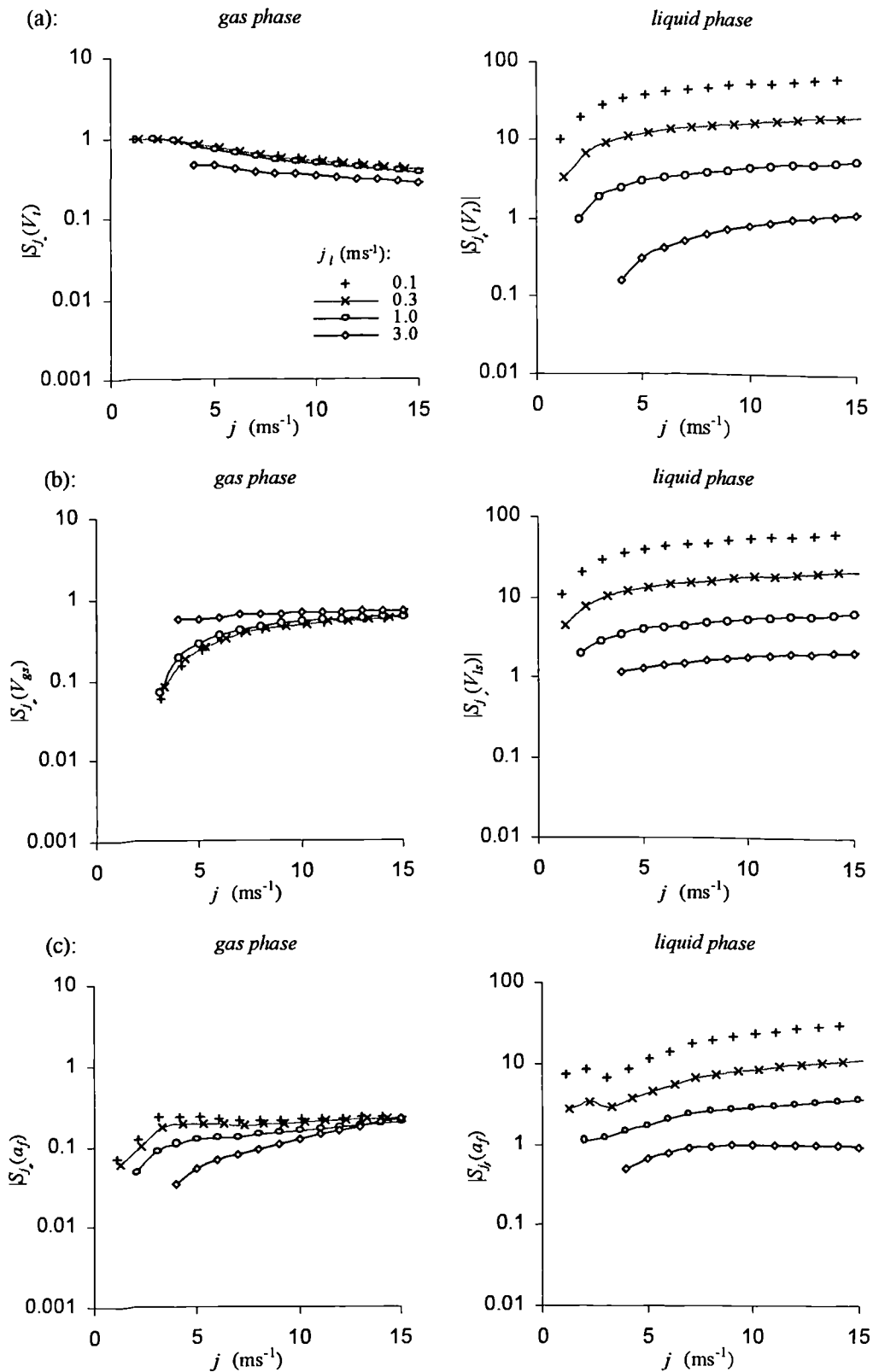


**Figure 4.2:** Sensitivity parameters  $S(V_l)$ ,  $S(V_{gs})$ ,  $S(V_{ls})$  and  $S(V_{gs})$ , for the gas and liquid phases. (Calculated using the correlations in section 4.2.1).

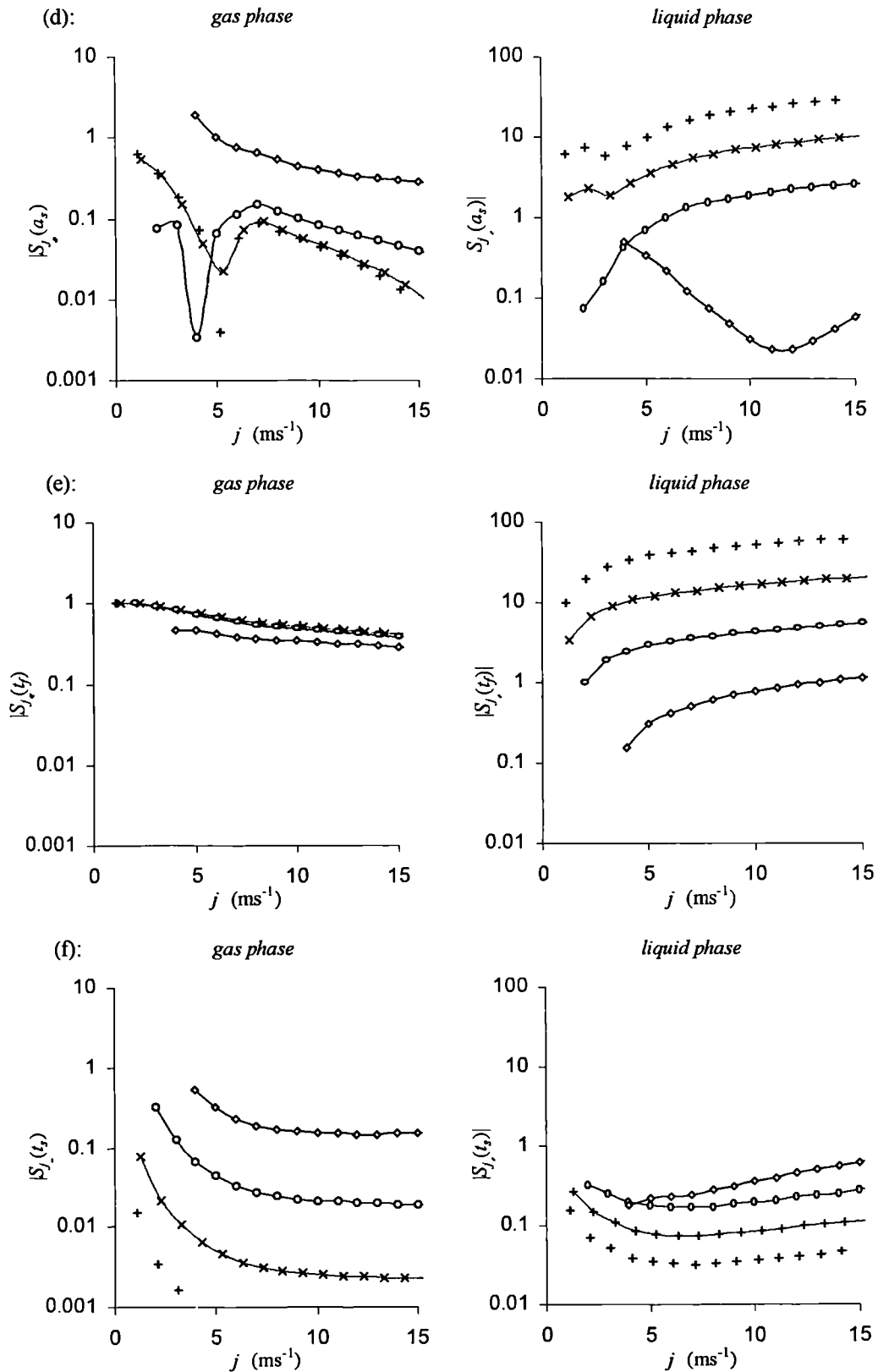
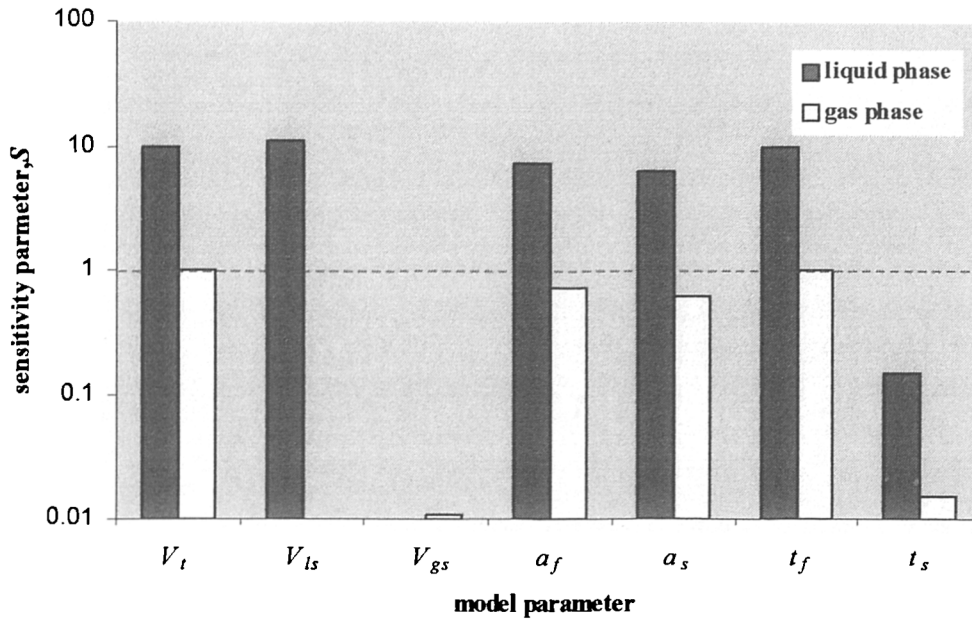


**Figure 4.2 (continued):** Sensitivity parameters  $S(a_s)$ ,  $S(t_f)$ , and  $S(t_s)$  and  $S(V_{gs})$ , for the gas and liquid phases. (Calculated using the correlations in section 4.2.1).

(a):  $j_f=0.1 \text{ m s}^{-1}$ ;  $j_g=1.0 \text{ m s}^{-1}$



(b):  $j_f=1.0 \text{ m s}^{-1}$ ;  $j_g=6.0 \text{ m s}^{-1}$

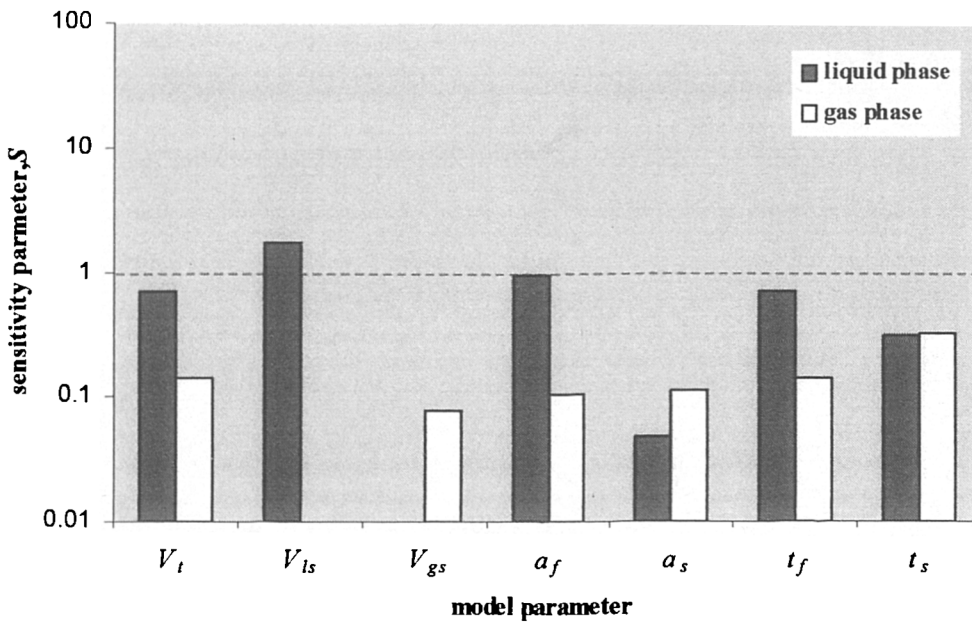


**Figure 4.3:** Comparison of the sensitivities for each model parameter, for the two conditions  $\{j_f=0.1 \text{ m s}^{-1}; j_g=1.0 \text{ m s}^{-1}\}$  and  $\{j_f=1.0 \text{ m s}^{-1}; j_g=6.0 \text{ m s}^{-1}\}$ .

	$V_t$	$V_{ls}$	$V_{gs}$	$a_f$	$a_s$	$t_f$	$t_s$
liquid phase: $\Delta j_l/j_l \leq 5\%$	0.2%	0.1%	-	0.2%	0.2%	0.1%	5%
gas phase: $\Delta j_g/j_g \leq 5\%$	5%	-	5%	5%	5%	5%	10%

**Table 4.2:** Maximum permissible error in each parameter, for 5% relative accuracy in the flowrates over the test range.

accuracy. These values occur near the transition boundary with stratified flow. Therefore, it is particularly difficult to obtain an accurate measurement of the liquid flowrate.

In this analysis, it has been assumed that the total error is caused entirely by the error in *any one* of the model parameters. The total error will of course exceed 5%, if more than one parameter approaches its limit.

### **4.3 Measurement techniques**

Chapter 2 described a variety of general methods for measuring the component phase fractions and phase velocities. However, there was no specific discussion about the measurement of the phase fractions  $a_f$  and  $a_s$ , the translation velocity  $V_t$ , or the local velocities  $V_{ls}$ ,  $V_{gs}$ ,  $V_{lf}$  and  $V_{gf}$  within *slug flow*. In this section, a suitable technique for measuring each parameter will be proposed. Each technique should be *non-intrusive* and of *minimal cost*.

#### **4.3.1 Phase fraction measurement**

In this thesis, the local phase fractions  $a_f$  and  $a_s$  will be measured by a conductive impedance technique. This is because *gas-water* two-phase flow is being metered, and because the alternative techniques described in Chapter 2 (NMR, gamma-ray attenuation, and tomography) are restricted by their cost.

Impedance sensors can be divided into two categories: ‘conductance-based’, and ‘capacitance-based’ (see sub-section 2.2.2). The differences between the measurement processes are as follows:

- In the conductance measurement, the ratio of the current to the voltage across two cell electrodes is required. This measurement can be made at a relatively low a.c. frequency, and with relatively high accuracy. However, conductance sensors only operate in water-continuous mixtures and the fluid conductivity must be regularly calibrated, in order to obtain good results.
- In the capacitance measurement, an additional measurement - the *phase angle* between the cell current and the cell voltage (see figure 2.11) - is required. This measurement must be made at a high frequency (complicating the instrumentation and reducing the measurement accuracy) and guard electrodes must surround the cell, in order to minimise stray capacitance. However, the advantage is that both oil-continuous and water-continuous mixtures can be measured.

The design of the sensor electrodes is a compromise between the need for good accuracy and a localised measurement. These issues will be discussed in detail in Chapter 5 of this thesis, with particular emphasis upon the calculation of the *measurement uncertainties*  $\Delta\alpha_f$  and  $\Delta\alpha_r$ . The instrumentation required to activate the cell electrodes and make the conductance measurement will then be discussed, in Chapter 6.

#### 4.3.2 Translation velocity measurement

The translation velocity will be measured in this thesis, by cross-correlating the signals from a pair of conductance sensors. This is because the alternatives described in section 2.1 (Venturi metering and positive displacement metering) are intrusive to the flow. Since the phase fraction measurement is also being made with conductance sensors, this is an economic choice.

Many different types of sensing technique could have been used for the cross-correlation measurement. These have the following advantages and disadvantages:

- Gamma-ray sensors offer separate measurement of the oil and the water liquid components (e.g. see Roach & Watt<sup>102</sup>). However, there is a *low measurement bandwidth*, because of the long count times that are required to obtain accurate data.
- Ultrasonic transducers (Ong & Beck<sup>94</sup>; Xu *et al*<sup>131</sup>) offer a very high measurement

bandwidth. However, a disadvantage is that there must always be a *continuous liquid phase* between the transmitter and the detector, for a successful measurement.

- Differential pressure sensors (Lin & Hanratty<sup>65</sup>) also offer a high measurement bandwidth, if the sensor tapings are close together. However, it is often very difficult to get coherent signals in slug flow, due to *liquid contamination* in the sensor arms.
- Capacitance sensors (Xie *et al*<sup>130</sup>) and conductance sensors (Nydal *et al*<sup>88</sup>) also offer a wide measurement bandwidth. However, the sensor signals are particularly vulnerable to *crosstalk*, unless the electric field between the sensor electrodes is suitably contained.

The optimum design of the cross-correlation sensors is a compromise between the need for a wide bandwidth, good coherence between the signals, and negligible crosstalk between the electrode pairs. These issues will be discussed, in Chapter 5 of the thesis, and again the measurement uncertainty will be estimated. The electronic instrumentation (identical to that required for the phase fraction sensor) will be discussed in Chapter 6.

#### 4.3.3 Local velocity measurement

At least two of the local velocities  $V_{ls}$ ,  $V_{gs}$ ,  $V_{lf}$  and  $V_{gf}$  must be measured, in order to determine the phase flowrates. These local velocities are considerably more difficult to measure than the translation velocity  $V_t$ , and suitable (non-intrusive) techniques are not described within the literature. In this section, some *direct* and *indirect* measurement techniques will be proposed, and the potential problems with each technique will be summarised.

The local film velocity  $V_{lf}$  and the slug gas velocity  $V_{gs}$  may be measurable with a system of *cross-correlation sensors*. These sensors must be responsive to local disturbances within the liquid film and the core of the slug, in order to yield useful results. However, this approach suffers the following disadvantages:

- It is difficult to obtain an accurate measurement of the film velocity if the disturbances upon the interface are very small, or are periodic in nature. The interface velocity is generally not equal to the mean film velocity that is required by the model.
- It is difficult to make the sensor field penetrate the core of the pipe, unless intrusive

sensors or a ‘hard field’ (i.e. gamma-ray) technique is used. As discussed above, the system should ideally be non-intrusive to the flow, and the sensors must have a wide bandwidth.

A further problem must also be overcome. The frequency content of the signals that corresponds to the translation velocity  $V_t$  must be filtered out *before* the correlation can take place. If this filtering is not possible, then a local velocity measurement cannot be obtained.

Alternatively, the local velocities may be indirectly determined by measuring the *pressure drop profile*. Table 3.1 summarises the relationships (described in chapter 3) that can be used to measure the velocities  $V_{ls}$ ,  $V_{lf}$  and  $V_{gf}$ . The slug velocity ( $V_{ls}$ ) can be estimated from either of the equations:

$$V_{ls} \sim V_t - \left\{ \frac{\Delta P_m}{\rho_l a_s (a_s / a_{fe} - 1)} \right\}^{1/2} \quad V_{ls} \sim \left\{ \frac{\Delta P_f \pi D}{2 f \rho_m l_s} \right\}^{1/2} \quad [4.10]$$

in which  $\Delta P_m$  is the ‘mixing zone’ pressure drop and  $\Delta P_f$  is the ‘friction’ pressure drop within the slug body. On the other hand, the film velocities ( $V_{lf}$  and  $V_{gf}$ ) can be estimated by simultaneous solution of the equations:

$$a_f \frac{dP}{dx} = \frac{\tau_l S_l}{A} - \frac{\tau_l S_i}{A} \quad (1 - a_f) \frac{dP}{dx} = \frac{\tau_g S_g}{A} + \frac{\tau_l S_i}{A} \quad [4.11]$$

given experimental measurements of pressure drop  $\Delta P_{film}$ , the film holdup  $a_{fe}$ , and the film length  $l_f$ . (The solution process, which requires iteration for  $V_{lf}$  and  $V_{gf}$ , is illustrated in figure 3.7). However, both of these measurement techniques suffer from the following disadvantages:

- Empirical friction factors are required, to close equations [4.10a] and [4.11] above. These friction factors are generally not reliable, as the gas phase flowrate is increased.
- The pressure drop components  $\Delta P_m$ ,  $\Delta P_f$  and  $\Delta P_{film}$  cannot always be obtained, from the pressure drop profile. This is because there are large pressure fluctuations within the slug body (see figure 3.5), and large-amplitude waves within the film zone.

Given the difficulties with the proposed direct and indirect measurements, the local velocities will be estimated in this thesis by using *empirical correlations*. As described in

Chapter 3 (and as can be seen from table 3.1), it is currently only possible to correlate the local slug velocities  $V_{ls}$  and  $V_{gs}$ . The correlation for the local liquid velocity ( $V_{ls}$ ) depends upon the translation velocity  $V_t$  and takes the form:

$$j = \frac{V_t - V_a}{C_0} \quad V_{ls} = \frac{j}{a_s + s(1 - a_s)} \quad [4.12]$$

while the correlation for the gas velocity ( $V_{gs}$ ) takes the form:

$$V_{gs} = \frac{sj}{a_s + s(1 - a_s)} \quad [4.13]$$

where  $j$  is the total superficial velocity, and  $s$  is the slip ratio between the phases in the slug body. As a result, the local film velocities ( $V_{lf}$  and  $V_{gf}$ ) must be derived from measurements for  $V_t$ ,  $a_f$ ,  $a_g$ , and the estimates for  $V_{ls}$  and  $V_{gs}$ , according to equation [4.3].

Table 3.1 summarises only some of correlations that can be used to infer the total superficial velocity  $j$  and the slip parameter  $s$ . The most suitable correlations (for gas-water horizontal slug flow) will be discussed in Chapter 7 of this thesis. However, it is important to realise that these relationships will introduce *systematic errors* and *uncertainty* into the local velocity measurement. While it is assumed that the relationship between the correlated and measured variables is unique, in practice there is likely to be an element of scatter in the experimental data.

#### 4.3.4 Software specifications

In addition to the sensing instrumentation, the slug flow meter requires a *computer system* to process the raw sensor data and deliver the phase flowrates. This computer system should contain the following components:

- A data acquisition card and suitable acquisition software, to log the data obtained by the phase fraction and the cross-correlation sensors.
- Routines to cross-correlate the velocity sensor data, and to identify the ‘slug’ and ‘film’ regions from the holdup sensor data. These routines will establish the values for the model parameters  $V_t$ ,  $t_f$  and  $t_s$ ,  $a_f$  and  $a_s$ .
- A set of empirical closure relationships, to obtain the local slug velocities  $V_{ls}$  and  $V_{gs}$ .

- Routines for calculating the gas and liquid phase flowrates, and for estimating the *uncertainty* due to the imperfections in the sensor design, the use of empirical relationships, and the process of extracting the measurement parameters from the sensor data.

These four components will be discussed in greater detail, in chapter 7 of this thesis. To avoid the need for any dedicated hardware, the computer system will first acquire the slug flow data for each test run, and will perform the data analysis *off-line*.

#### **4.4 Summary**

In this chapter, the use of the ‘stable slug flow model’ to predict the phase flowrates in two-phase slug flow, was assessed. This assessment consisted of presenting the model and identifying the *measurement parameters*, conducting a *sensitivity analysis* upon each parameter, and then identifying a set of measurement techniques, which were inexpensive and non-intrusive to the flow.

In section 4.1, the equations for the phase flowrates and the ‘stable slug flow’ model were restated. The parameters that needed to be measured were then identified. These parameters were the translation velocity  $V_t$ , the local holdups  $a_f$  and  $a_s$ , the timing measurements  $t_s$  and  $t_f$ , and the local velocities  $V_{ls}$  and  $V_{gs}$ .

Section 4.2 described a sensitivity analysis, which related the accuracy in each parameter to the accuracy in the phase flowrates. This sensitivity analysis used a set of empirical correlations, which were originally presented in chapter 3. The results of the analysis indicated that: (i) it was more important to obtain accurate measurements of the phase velocities than the phase holdup; and (ii) that it was difficult to measure the liquid phase accurately, at low liquid flowrates. It was particularly difficult to obtain enough accuracy in the model parameters, to ensure a 5% relative accuracy in the liquid phase flowrate.

Section 4.3 described the instrumentation for measuring each parameter, given that the system is to be *non-intrusive* and *low-cost*. For the measurement of the phase fractions  $a_f$  and  $a_s$ , and for the cross-correlation of the translation velocity  $V_t$ , conductance sensors were suggested. The direct measurement of the local velocities, however, posed a considerable difficulty. As a result, empirical correlations for the slug velocities  $V_{ls}$  and  $V_{gs}$  were proposed. Also in this section, the tasks to be performed by the processing software were summarised.

The following three chapters of this thesis will describe the development of the sensor

electrodes, the sensor electronics and the processing software, for metering gas-water slug flows in the NEL multiphase facility. The overall system will then be assessed, in Chapter 8.

## 5. Conductance sensor design

This chapter will describe the design of conductance sensors for measuring the *phase fractions* and the *translation velocity* in gas-water slug flow. These sensors should be non-intrusive, inexpensive, and should provide an accurate measurement of the model parameters  $V_t$ ,  $a_f$  and  $a_s$ . The sensitivity analysis that was presented in Chapter 4 indicated that accurate measurements for the holdup and the translation velocity were particularly important, at low liquid flowrates.

Sections 5.1 and 5.2 will describe the development of ring shaped sensors, for measuring each parameter:

- Section 5.1 will describe the design of the ring electrodes for making the holdup measurements. The models that define the conductance between the electrodes will be presented, and then the measurement uncertainties  $\Delta a_f$  and  $\Delta a_s$  will then be estimated by analysing simple geometries. The accurate measurement of the film holdup and the slug holdup are seen to be in conflict.
- Section 5.2 describes the design of a pair of sensors, for the cross-correlation of the translation velocity  $V_t$ . The theory of the cross-correlation process is discussed, then the need to maximise the signal bandwidth  $B$ , optimise the sensor separation  $x$ , and maximise the record duration  $T$  for good measurement accuracy are described. The need to obtain real flow data will prevent the measurement uncertainty  $\Delta V_t/V_t$  from being estimated at this stage.

Section 5.3 will describe the implementation of the two types of design, for use in the NEL multiphase facility. The manufacture of the ‘sensor units’, the assembly process, and the need to prevent crosstalk between the neighbouring sensor electrodes will each be discussed. Finally, the performance of the sensor units will then be verified, by a set of simple experiments.

## 5.1 Phase fraction sensor design

The phase fraction sensor should be designed to minimise the dependency of the conductance upon the flow geometry. That is, the measured conductance should be independent of the liquid distribution between the electrodes. In this section, the use of *ring electrode* type sensors will be justified. Simple theoretical models will then be used, to estimate the measurement uncertainties  $\Delta a_f$  and  $\Delta a_s$ . The chosen design must find a compromise between the need for *good accuracy*, and a *localised measurement*.

### 5.1.1 Design Selection

Various types of conductance sensors for measuring the global holdup were described in Chapter 2. Figure 2.12 illustrated several types of non-intrusive sensor, which minimised the dependency upon the flow geometry (by Xie *et al*<sup>126</sup>; Geraets & Borst<sup>37</sup>; Snell *et al*<sup>106</sup>; and Andreussi *et al*<sup>8</sup>). The ring electrode design (Andreussi *et al*<sup>8</sup>) is chosen, because it offers the following advantages:

- The design consists of only two parameters: the dimensionless electrode separation  $D_e/D$ , and the dimensionless electrode width  $s/D$ . This design is very simple to optimise, and is simple to manufacture.
- The measurement accuracy appears to be very similar to the *arc electrodes*, the *helical electrodes* and the *rotating field* designs that are shown in figure 2.12. This has been demonstrated by numerical simulation and direct experimental measurement.

Two disadvantages with the ring electrode design are its poor ability to spatially filter the flow, and the likelihood that it will be a source of crosstalk current. These problems will be described in greater detail, in section 5.1.5 and section 5.4 below.

### 5.1.2 Theory

The conductance between a pair of ring electrodes has been theoretically modelled by Andreussi *et al*<sup>8</sup>. This theory is based upon the analytical solution of Coney<sup>27</sup>, for flat electrodes (figure 5.1). The conductance  $G$  between the flat electrodes, for a covering liquid film of height  $h$  is given by:

$$G = G^+ \sigma l \quad [5.1]$$

in which:

$$G^+ = \frac{K(m_1)}{K(1-m_1)} \quad m_1 = \frac{\sinh^2(\pi s/2h)}{\sinh^2(\pi(s+D_e)/2h)} \quad [5.2]$$

and where  $\sigma$  is the fluid conductivity,  $l$  is the contact distance of the electrode in the third dimension, and  $K(m)$  is the complete elliptic integral of the first kind:

$$K(m) = \int_0^{\pi/2} (1 - m \sin^2 \theta)^{-1/2} d\theta \quad [5.3]$$

To modify this theory to the ring electrode geometry, Andreussi *et al*<sup>8</sup> proposed an equivalent ‘film thickness’  $h$  and ‘contact distance’  $l$  for an arbitrary cross-section, defined by:

$$h = \frac{a_f A}{\theta r} \quad l = \theta r \quad [5.4]$$

where  $r$  is the pipe radius,  $A$  is the pipe cross-sectional area,  $a_f$  is the film zone holdup, and  $\theta$  is the wetted perimeter. The parameters  $h$  and  $l$  are dependent upon the flow geometry. For

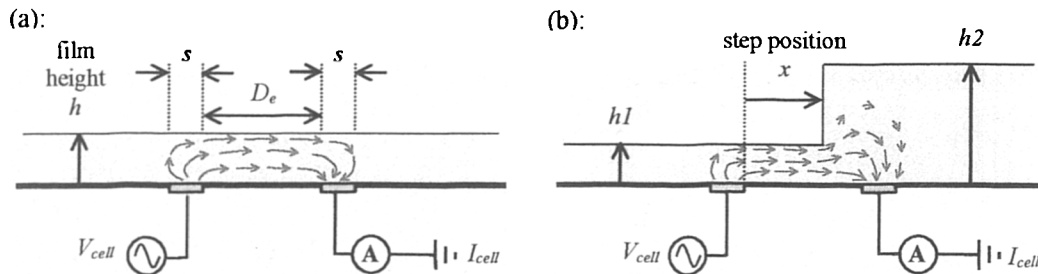


**Figure 5.1:** The analytic solution geometry of Coney<sup>27</sup> for a 2D liquid film above flat electrodes: (a) flat-liquid layer; (b) stepped layer.

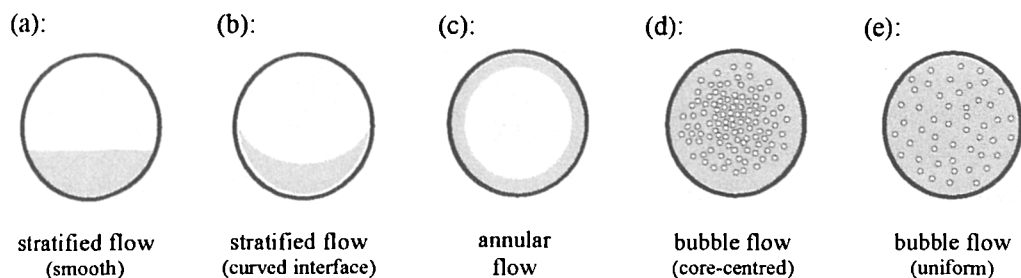


**Figure 5.2:** Simplified models for the fluid within each ‘slug unit’.

example, for a stratified geometry (figure 5.2a):

$$\begin{aligned} a_f &= 1 - \frac{1}{\pi} \cos^{-1}(2h-1) + \frac{1}{\pi} (2h-1) \left\{ 1 - (2h-1)^2 \right\}^{1/2} \\ l &= \left\{ \pi - \cos^{-1}\left(\frac{1}{2}h-1\right) \right\} r \end{aligned} \quad [5.5]$$

whereas for an annular geometry (figure 5.2c):

$$h = \frac{1}{2} a_f r \quad l = 2\pi r \quad [5.6]$$

Though this theory is approximate, equations [5.5] and [5.6] agree well with experimental measurements (particularly as the electrode separation  $D_e$  becomes large relative to the pipe diameter). Eventually, the local field effect around the electrodes became negligible compared to the field in the bulk, in which case *flat plates* can effectively replace the ring electrodes.

Within the ‘slug zone’, the glow geometry is different, so the model described above is not appropriate. To a first approximation, the slug body can be modelled as *homogeneous mixture* (see figure 5.2e). In this mixture, the individual bubbles cause a very weak perturbation in the electric field. Therefore, the relative conductance  $G/G^*$  can be defined by the ‘mixture model’ of Maxwell<sup>79</sup>:

$$G/G^* = 2a_s / (3 - a_s) \quad [5.7]$$

Equation [5.7] is independent of the separation between the sensor electrodes, and the sensor geometry. Similar formulae have been developed by Bruggeman<sup>24</sup>, and by Dykesteen *et al*<sup>31</sup> for three-phase mixtures.

### 5.1.3 The film holdup measurement

The sensitivity analysis presented in section 4.2 indicated that it was more important to measure the film holdup ( $a_f$ ) than the slug holdup ( $a_s$ ). The effect of the ring electrode separation and the flow geometry upon the measurement uncertainty ( $\Delta a_f$ ) will now be investigated.

At low gas flowrates, the film region will adopt a *stratified flow* geometry. Figure 5.3 illustrates the ability of ring electrodes to measure this stratified flow, for the fixed width ratio  $s/D=0.05$ , as the dimensionless electrode separation  $D_e/D$  is varied. The conductance ratio  $G/G^*$  is calculated using equations [5.1] and [5.5]. The effect of the electrode width  $s$  upon these results is negligible, as long as  $s$  is much smaller than  $D_e$ . The following

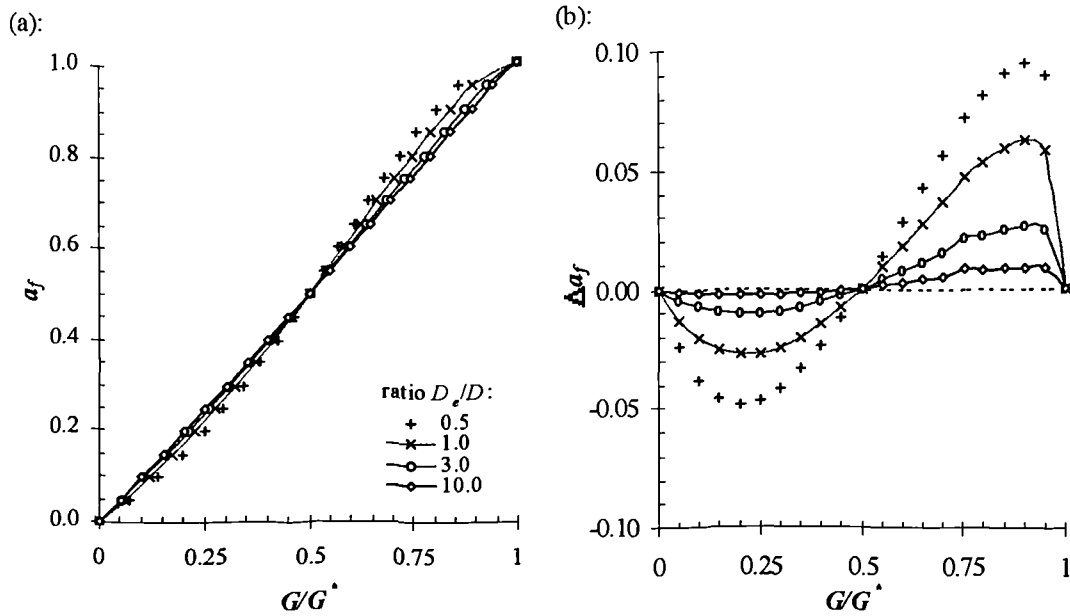


Figure 5.3: The effect of the electrode separation ratio  $D_e/D$  on the conductance predictions for stratified flow: (a)  $a_f$  versus  $G/G^*$ ; (b)  $\Delta a_f$  versus  $G/G^*$  (separation ratio  $s/D=0.05$ )

conclusions are drawn:

- The measurement uncertainty  $\Delta a_f$  will improve, as the relative separation  $D_e/D$  increases.
- The measurement uncertainty  $\Delta a_f$  will worsen, if the holdup has a value around 0.25 or around 0.75.

The sensor electrodes should be spaced far apart, to make a good measurement of the film holdup. However, to ensure a good measurement of the holdup in the slug body, a maximum separation must be defined. It is proposed that:

$$D_e/D = 3.0 \quad [5.8]$$

Since the film holdup almost always has a value below 0.5 (see section 3.1.3), the maximum uncertainty  $\Delta a_f$  is therefore about 1% of full-scale.

As the gas flowrate is increased, the film zone will change its shape to a *curved* and then an *annular* geometry (figure 5.2). The effect of this change upon the measurement uncertainty can be calculated using equation [5.4]. The uncertainty  $\Delta a_f$ , which is illustrated in figure 5.4, increases as the holdup ( $a_f$ ) and the wetted perimeter ( $\theta/2\pi$ ) increase. The measurement

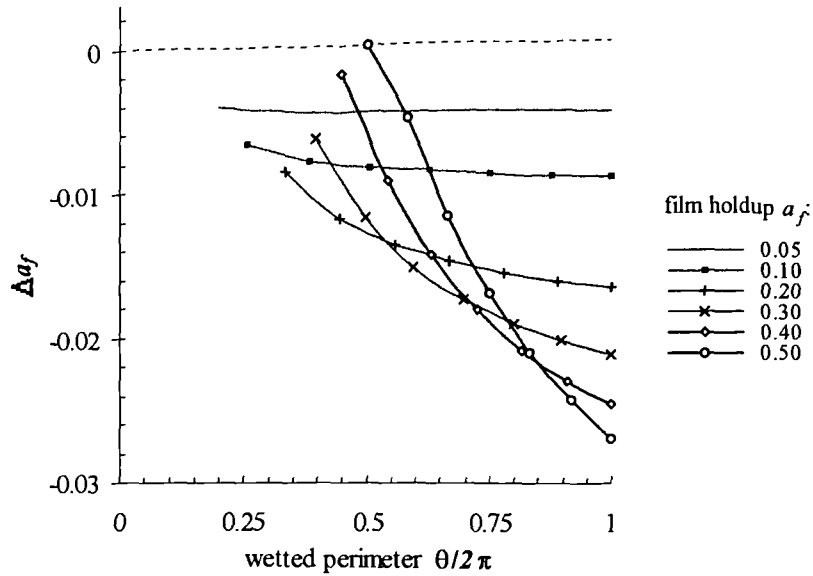


Figure 5.4: The effect of moving from a stratified to an annular geometry upon the measurement uncertainty  $\Delta a_f$  ( $D_e/D=3.0$ ;  $s/D=0.05$ )

accuracy will therefore deteriorate, for the same amount of liquid content. However, increasing the gas phase flowrate generally *reduces* the amount of liquid in the film zone (see section 3.1.3). Assuming that the holdup reduces to a value of 0.2 at the highest flowrates, the maximum uncertainty is:

$$|\Delta a_f| \cong 0.02 \quad [5.9]$$

As the gas flowrate rises, there will be aeration within the liquid film, and liquid spray present in the gas phase above the film. These effects will cause a further increase in the measurement uncertainty  $\Delta a_f$ . However, it is not possible to quantify these increases, without having detailed measurements of the holdup profile within the film zone.

It is useful to compare the theoretical model of Andreussi *et al*<sup>8</sup> against a numerical simulation. An annular flow geometry, with the electrode simulation ratio  $D_e/D=3.0$ , has been simulated using ANSYS software (see appendix A for the source code). The rotational symmetry means that this problem relatively simple to analyse. The predictions for the conductance ratio  $G/G^*$  are compared against the theory in figure 5.5, and are in excellent agreement.

### 5.1.3 Slug holdup measurement

An accurate measurement of the 'slug holdup'  $a_s$  is less critical to the model than an accurate

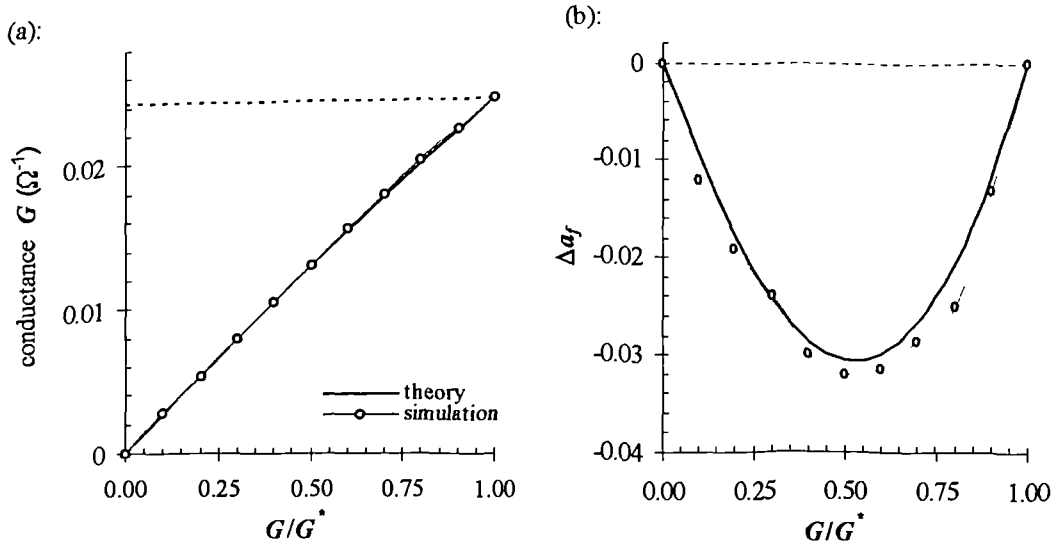


**Figure 5.5:** Comparison of the Coney-Andreussi predictions for annular flow geometry, with the ANSYS simulations described in appendix A. (a)  $G$  versus  $G/G^*$ ; (b)  $\Delta a_f$  versus  $G/G^*$  ( $D_e/D=3.0$ ;  $s/D=0.05$ ).

measurement of  $a_f$ . However for a measurement of  $a_s$  to be made at all, the electrode separation must be shorter than the shortest slug. The effect of the electrode separation and the flow geometry upon the uncertainty  $\Delta a_s$  will now be described.

Several experimental correlations for the slug length ( $l_s$ ) were described, in section 3.6.3 of this thesis. The slug length is normally independent of the gas and the liquid phase flowrates. Nydal *et al*<sup>85</sup> established that the mean slug length, for developed flow, was of the order:

$$l_s \sim 15D \quad [5.10]$$

For the purposes of the model, the ‘slug holdup’ measurement corresponds the region of constant holdup in the back of each slug. Andreussi *et al*<sup>6</sup> observed that as the gas flowrate increases, there is a highly aerated ‘mixing zone’ at the front of the slug. This mixing zone must therefore not be measured. At the highest flowrates the mixing zone will occupy about half of the slug length (equation [3.84]), so the electrode separation:

$$D_e/D = 3.0 \quad [5.11]$$

is proposed. This separation allows for the statistical variation that occurs in the slug length (see Nydal *et al*<sup>88</sup>), and also allows the measurement of local holdup fluctuations within longer slugs.

At low gas flowrates, the slug body can be approximated to the uniform ‘bubble flow’ geometry (see figure 5.2e). This approximation allows the ‘mixture model’ to be used for the conductance ratio  $G/G^*$ . The validity of the mixture model has been investigated by Andreussi *et al*<sup>8</sup> and Fossa<sup>36</sup>. Their experiments on vertical bubble flow between ring electrodes indicate that:

- For a holdup content greater than 0.75, the predicted value for the ratio  $G/G^*$  and the actual value are in good agreement.
- For very large holdup values (above 0.95), the measured ratio  $G/G^*$  is also independent of the void fraction *distribution*.

As the gas flowrate increases, the void fraction in the slug will increase, and the bubbles will concentrate in its core. The geometry is then intermediate between the ‘bubble flow’ and ‘annular flow’ cases (see figure 5.2d). Figure 5.6 illustrates the effect on the ratio  $G/G^*$  and the measurement uncertainty  $\Delta a_s$ . At large holdup values the ‘bubble’ curve is closely followed, but as the void fraction increases the ‘annular’ curve is approached. The exact path of this curve is not known, since the *distribution* of bubbles within the slug body cannot be measured. However, the actual value of  $G/G^*$  will be closer to the bubble flow curve, since there is always a complete blockage of the pipe in slug flow.

By comparing the different curves in figure 5.6, the measurement uncertainty  $\Delta a_s$  is expected to be of the order:

$$|\Delta a_s| \sim 0.2(1 - a_s) \quad [5.12]$$

The uncertainty  $\Delta a_s$  becomes much larger than  $\Delta a_f$  as the gas flowrate is increased ( $\Delta a_s \sim 0.1$  when  $a_s = 0.5$ ). However, since the predictive model is less sensitive to the measurement of  $a_s$  (section 4.2), the effect upon the phase flowrates should be relatively small.

### 5.1.5 Spatial filtering between the electrodes

The inability of the ring electrode sensor to *spatially filter* the flow results in additional measurement errors. Coney<sup>27</sup> originally demonstrated the spatial filtering problem, for a step change in the film layer above flat electrodes (figure 5.1b). The effect worsens as the separation between the electrodes is increased, and as the rate of change in the liquid content is increased. Therefore in slug flow, the spatial filtering effect is poorest as the *slug front* and the *slug tail* pass through the sensing volume.

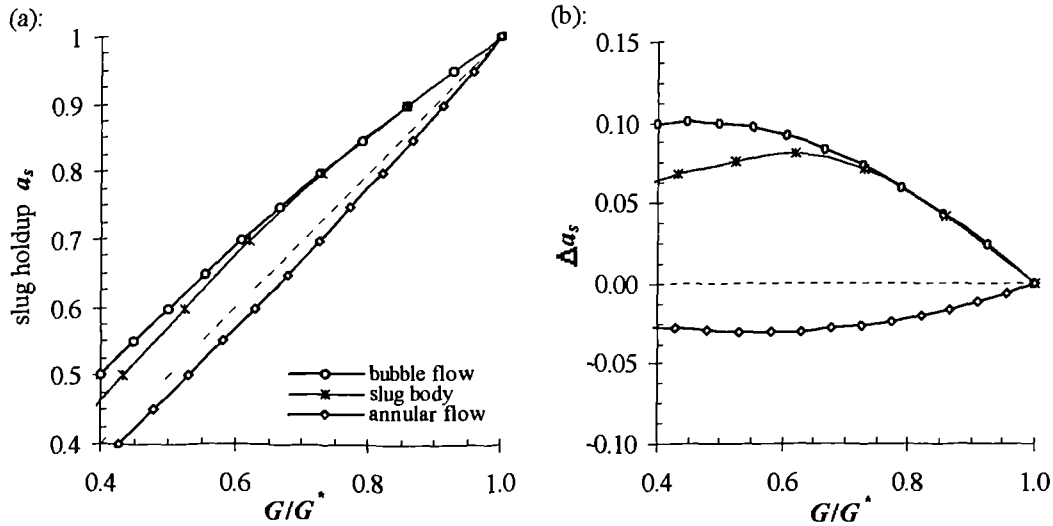


**Figure 5.6:** The effect of the flow geometry upon the conductance predictions for the slug body: (a)  $a_s$  versus  $G/G^*$ ; (b)  $\Delta a_s$  versus  $G/G^*$  ( $D_d/D=3.0$ ;  $s/D=0.05$ )

To quantify the error effect, a simplified model of the slug front has been constructed and simulated using ANSYS. This simulation geometry is illustrated in figure 5.7a. A step change from a liquid annulus, holdup  $a_{fe}$ , to pipe-full conditions occurs at a distance  $x$  between the ring electrodes. The input parameters required for each simulation are described in appendix A. Three annular film conditions:  $a_{fe}=0.5$ ;  $a_{fe}=0.2$ ; and  $a_{fe}=0.1$ , have been investigated.

Figure 5.7b compares the predicted holdup, and actual (volume-averaged) holdup as the step traverses between the sensor electrodes. Two measurement errors are identified, which worsen as the magnitude of this step is increased:

- Underestimation of the mean film holdup  $a_f$ , which worsens as the film zone length is reduced and the magnitude of the step increases. For the step change  $a_{fe}=0.1$  to  $a_s=1$  (the worst case), the uncertainty is of the order:

$$\overline{\Delta a_f} \sim \frac{1.5D}{l_f} \quad [5.13]$$

(which must be doubled to account for the slug front and slug tail). A similar, or larger, error is expected if the film zone has a stratified geometry.

- Changes to the film zone duration  $t_f$  and the slug zone duration  $t_s$ , due to the shift in the position of the step. However, the contribution to the errors  $\Delta t_f$  and  $\Delta t_s$  is expected to be minimal. The threshold technique that is used to identify the 'slug

region' (described in section 7.2.1) is triggered at the *top* of the rising edge between the slug zone and the film zone.

The above model ignores the *fine structure* within the slug body, which will introduce further errors in the holdup measurement. For example, at large gas flowrates, there is a complex 'froth' region that precedes the mixing zone (section 3.1.2). Since the flow structure is much smaller than the separation  $D_e$ , this region cannot be properly measured. In similar fashion, there is a very weak mixing zone in front of the slug body, at low gas flowrates. If there are pockets of air within this mixing zone that are not properly homogenised, there will be similar measurement errors.

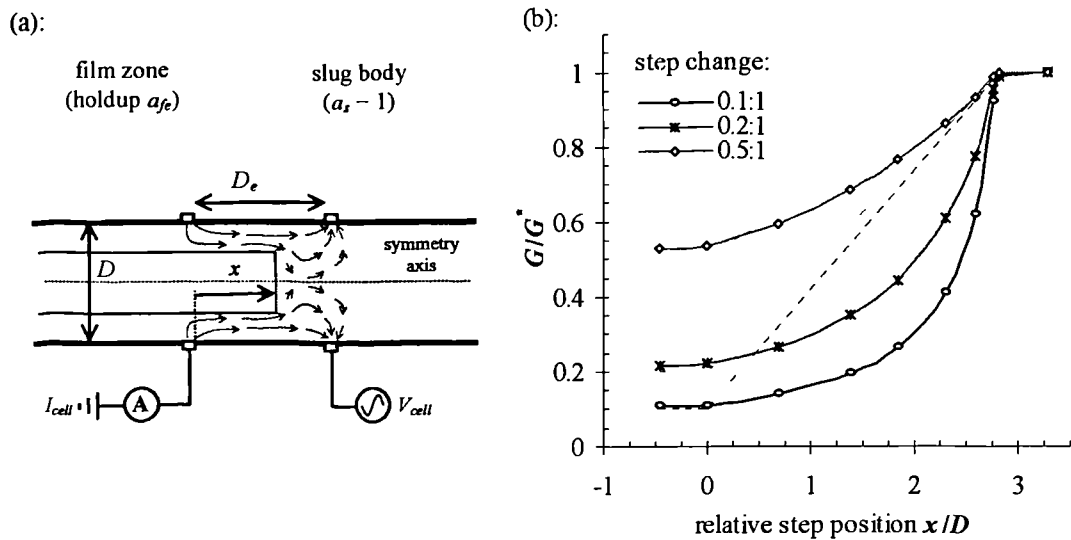


**Figure 5.7:** Simulated response to a step change in holdup passing between the sensor electrodes. (a) Simulation geometry ( $D_e/D=3.0$ ;  $s/D=0.05$ ); (b) Calculated conductance ratio  $G/G^*$ , for  $a_s=1$  and  $a_f=0.1, 0.2, 0.5$  respectively.

### 5.1.6 Conductivity calibration

In order to correctly measure the phase fractions  $a_f$  and  $a_s$ , the water phase conductivity ( $\sigma$ ) must be accurately measured. The full-pipe conductance ( $G^*$ ) is the product of the cell constant  $C_h$  and this conductivity  $\sigma$ , according to:

$$G^* = \sigma C_h \quad [5.14]$$

The conductivity of the water phase is strongly dependent upon the *salt content*, and will vary between formation water salinity and seawater salinity in an offshore pipeline. This salinity corresponds approximately to the range:

$$\sigma = 0.1 \Omega^{-1}m^{-1} \rightarrow 10 \Omega^{-1}m^{-1} \quad [5.15]$$

As a result of the salt content, the conductance that is measured between the sensor electrodes can change by a factor of up to 100 during the well lifetime. The electronic instrumentation, which is discussed in chapter 6 of this thesis, must therefore be designed in order to comply with this range.

The conductivity is also sensitive to changes in the *operating temperature* (typically about 3% per K). Therefore, in order to cope with long-term drift, it is necessary to perform a periodic calibration. The procedure for doing this within the NEL facility will be discussed, in Chapter 8 of this thesis.

## **5.2 Cross-correlation sensor design**

The cross-correlation sensors should be designed, in order to minimise the uncertainty in the measurement of the translation velocity  $V_t$ . This is achieved by having a wide sensor bandwidth, and good coherence between the sensor signals. In this section, a ring electrode design will be proposed, and a theoretical model for the measurement uncertainty ( $\Delta V_t$ ) will be presented. The effect of the sensor width ( $a$ ), the sensor separation ( $x$ ) and the cross correlation record duration ( $T$ ) upon the measurement uncertainty will then be examined.

### **5.2.1 Design Selection**

A *non-intrusive* method for cross-correlating the translation velocity  $V_t$  is required (see Chapter 4). The non-intrusiveness is required in order not to interfere with the flow, while the cross-correlation is required in order to obtain a true measurement of  $V_t$  (which is a *wave* velocity). Many workers have used ‘parallel wire’ probes (such as Manfield<sup>75</sup> and Manolis<sup>76</sup>), and others have used a non-intrusive ‘threshold level’ technique (Dukler & Hubbard<sup>30</sup>, Nydal *et al*<sup>88</sup>) for this measurement. However, a system that satisfies *both* requirements has not been developed.

In this thesis, two pairs of ring electrode sensors will be used to make the velocity measurement. In contrast to the holdup design, the separation distance between the electrodes ( $D_e$ ) should be very small. This design offers the following advantages:

- Rapid response to changes in the flow. In other words, a wide measurement

bandwidth.

- A *simple* and *inexpensive* manufacture process, compared to the alternative designs that are illustrated in figure 2.12.

Two disadvantages are apparent. The ring electrodes are likely to be insensitive to fine structure in the flow. Therefore, the simultaneous measurement of any local flow velocities in the slug unit (such as  $V_b$  and  $V_{gs}$ ) will not be possible. In addition, the closely spaced electrodes will result in a much larger conductance than the phase fraction sensor. Special electronic instrumentation, which is described in Chapter 6, is thus necessary to make the conductance measurement.

### 5.2.2 Theory

The theory behind the cross-correlation of flow velocity has been comprehensively described by Beck & Plaskowski<sup>17</sup>. The cross-correlation function between the two sensor signals  $x(t)$  and  $y(t)$  is defined as:

$$R_{xy}(\tau) = \frac{1}{T} \int_0^T x(t)y(t-\tau)dt \quad [5.16]$$

in which the record duration  $T$  should approach infinity, for a unique result. From the cross-correlation function  $R_{xy}$ , the translation velocity  $V_t$  is inferred by:

$$V_t = x/\tau^* \quad [5.17]$$

In equation [5.17],  $x$  is the sensor separation, and  $\tau^*$  is the position of the peak. The measurement uncertainty  $\Delta V_t/V_t$  is therefore the sum of the uncertainty in the timing measurement  $\Delta \tau^*/\tau^*$ , and the separation measurement  $\Delta x/x$ , according to:

$$\left| \frac{\Delta V_t}{V_t} \right| = \left| \frac{\Delta \tau^*}{\tau^*} \right| + \left| \frac{\Delta x}{x} \right| \quad [5.18]$$

The uncertainties  $\Delta \tau^*/\tau^*$  and  $\Delta x/x$  must both be minimised, to ensure good measurement accuracy.

The timing uncertainty  $\Delta \tau^*/\tau^*$  is defined by the model of Beck & Plaskowski<sup>17</sup>. This model assumes that the evolution of flow between sensors  $n(t)$  (where  $n(t) = y(t+\tau^*)-x(t)$ ) is a bandwidth-limited white noise signal. The statistical uncertainty in the position of the peak

( $\sigma_r$ ) is then defined by:

$$\sigma_r = \frac{0.038^{1/2}}{T^{1/2} B^{3/2} (R_{xx}(0)/R_{nn}(0))^{1/2}} \quad [5.19]$$

where  $T$  is the correlation record duration,  $B$  is the measurement signal bandwidth and  $R_{xx}(0)/R_{nn}(0)$  is the mean square signal-to-noise ratio. The signal-to-noise ratio  $R_{xx}(0)/R_{nn}(0)$  can be estimated from experimental data, using the normalised cross-correlation function peak  $\rho_{xy}(\tau^*)$ :

$$R_{xx}(0)/R_{nn}(0) = \frac{\rho_{xy}^2(\tau^*)}{1 - \rho_{xy}^2(\tau^*)} \quad [5.20]$$

The ratio  $R_{xx}/R_{nn}$  becomes infinite as  $\rho_{xy}(\tau^*)$  tends towards its maximum value of 1. That is, a perfect correlation between the signals results in zero uncertainty.

The separation uncertainty  $\Delta x/x$  depends upon the separation distance and the physical size of the cross-correlation sensors. There are two components to this uncertainty. The first component is due to error in the distance measurement ( $\Delta x$ ), and can be made negligible by making an accurate measurement of  $x$ . The second component is due to the inability to define an exact centre to the ‘sensing volume’, and cannot be easily eliminated. The position of the sensor field will vary, as the slug flow passes between the electrodes. The resultant uncertainty is of the order:

$$\Delta x/x \propto a/x \quad [5.21]$$

where  $a$  is the ‘characteristic width’ of the sensor (see section 5.2.3 below). In order to minimise this uncertainty, therefore, the sensors should be *widely spaced* and *physically small*.

### 5.2.3 Signal bandwidth

To obtain good measurement accuracy, it is particularly important to obtain signals that have a wide bandwidth (see equation [5.17]). The signal bandwidth  $B$  is dependent upon both the sensor bandwidth ( $B_s$ ) and the characteristics of the slug flow passing between the sensor electrodes.

The *sensor* bandwidth depends upon the size of the sensing volume between each ring electrode pair. This bandwidth may be estimated, by considering a flow impulse (a step

change in local holdup from ‘gas only’ to ‘liquid only’) passing between the electrodes. Assuming that perfect spatial filtering takes place between these electrodes, the impulse results in the step signal shown in figure 5.8a. The frequency spectrum of this signal is therefore:

$$S(\omega) \sim n_1 \frac{\sin(\omega a/2V)}{\omega a/2V} \quad [5.22]$$

where  $n_1$  is a normalisation constant,  $a$  is the width of the sensing volume, and  $V$  is the flow velocity. The bandwidth is thus approximately given by:

$$B_s \sim V/a \quad [5.23]$$

The separation between the ring electrodes ( $D_e$ ) should be minimised, in order to maximise this bandwidth. However, if the separation becomes very small, the conductance becomes difficult to measure (see Chapter 6) and the electrodes become susceptible to *wax* and *salt deposition*. (Whitaker<sup>125</sup>). A reasonable compromise is achieved by:

$$D_e/D \sim 0.05 \quad [5.24]$$

The width of the ‘sensing region’ is assumed to be approximately equal to the sensor separation (that is,  $a \sim D_e$ ). Therefore, for a 4-inch pipe diameter and a translation velocity  $V_t$  between  $1 \text{ m s}^{-1}$  and  $10 \text{ m s}^{-1}$ , the sensor bandwidth lies between 200Hz and 2 kHz.

The *signal* bandwidth depends upon the contents of the flow mixture that passes between the sensor electrodes. As a limiting case, the passage of liquid slugs can be approximated a periodic ‘step’ signal of duration  $l_s/V_t$  (see figure 5.8b). The frequency content of this step function is described by:

$$S(\omega) \sim n_2 \frac{\sin(\omega l_s/2V_t)}{\omega l_s/2V_t} \quad [5.25]$$

from which the bandwidth is given by:

$$B \sim V_t / l_s \quad [5.26]$$

Assuming that the slug length  $l_s \sim 15D$  (Nydal *et al*<sup>88</sup>), the ratio of the signal to the sensor bandwidth ( $B/B_s$ ) is given by:

$$B / B_s \sim 1/300 \quad [5.27]$$

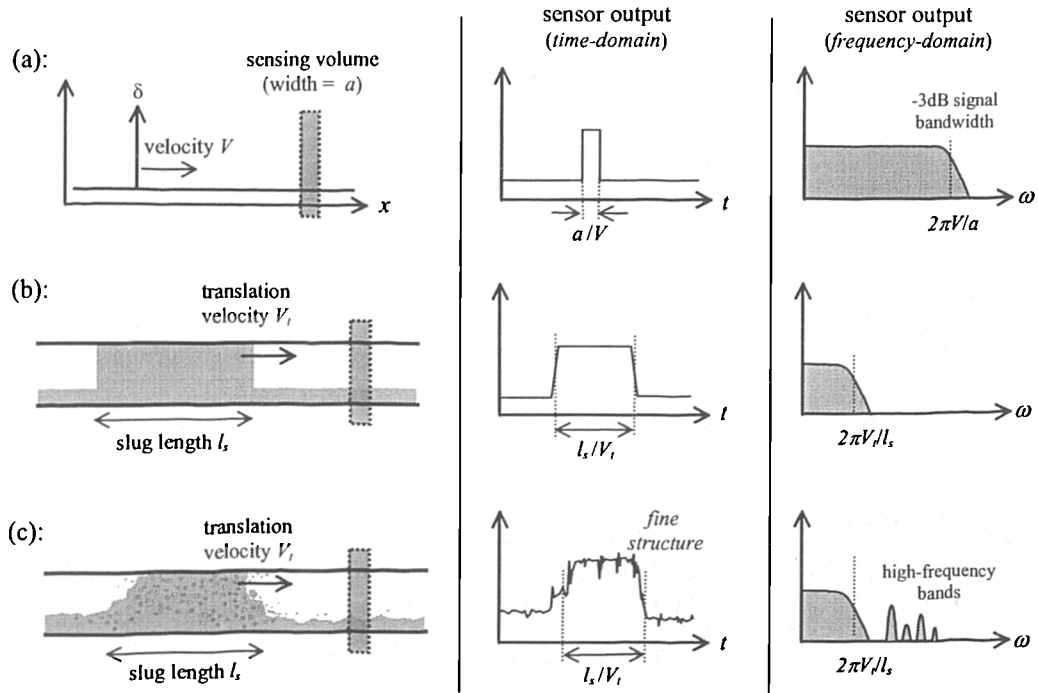


**Figure 5.8:** The effect of the input to the sensing volume sensing volume upon the signal bandwidth  $B$ . (a) Flow impulse; (b) 'simplified' slug flow; (c) 'real' slug flow.

That is, the signal bandwidth is much smaller than the sensor bandwidth in slug flow. As a consequence, there must be a high degree of coherence between the signals for good accuracy in the measurement.

The 'step change' model is only an approximation to the real flow. The real signals may have a considerable amount of fine structure, which will cause increase the signal bandwidth. This increase depends upon the ability of the sensors to detect *local disturbances*, such as void fraction surges within the slug body or waves on the film interface (see figure 5.8c). Figure 5.9 illustrates the conductance  $G/G^*$  between the sensor electrodes, for the 'stratified', 'bubble' and 'annular' flow geometries. There is considerable sensitivity to the fluid around the pipe perimeter, but less sensitivity to the fluid in the core. Therefore, any fine structure in the flow will probably not be detected.

For a successful measurement, it is very important that the *instrumentation bandwidth* (i.e. the bandwidth of the electronics driving the electrodes) exceeds the sensor bandwidth  $B_s$ . The design of high-bandwidth electronic instrumentation will be discussed, in Chapter 6 of this thesis.

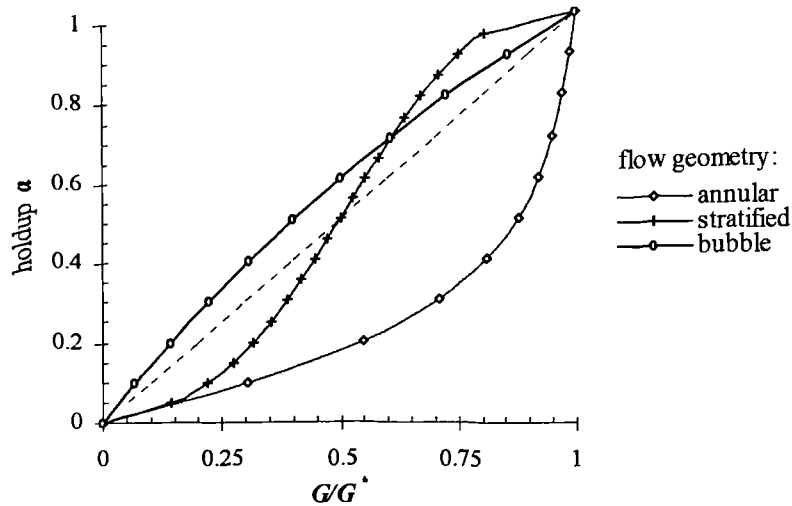


**Figure 5.9:** Conductance predictions, for different geometries between the cross-correlation sensor electrodes ( $D_e/D=0.05$ ;  $s/D=0.05$ ).

### 5.2.4 Sensor separation

The sensor separation  $x$  should be *small* to minimise the possibility of flow evolution between signals, though should also be *large* to ensure that the time delay  $\tau^*$  can be accurately measured. This section will describe the choice of the optimum distance, for the slug flow process.

The uncertainty in the cross-correlation peak ( $\Delta\tau^*/\tau^*$ ) is smallest for the separation where the quantity  $x(R_{xx}(0)/R_{nn}(0))^{1/2}$  is maximised (equation [5.18]). In a single-phase flow, this maximisation occurs when the sensor separation  $x$  is of the order of the pipe diameter  $D$  (for example, Beck & Plaskowski<sup>17</sup>; Ong<sup>93</sup>; Lucas *et al*<sup>70</sup>). This is because the sensor signals  $x(t)$  and  $y(t)$  represent a *turbulent* process. In slug flow, however, the signals have a strong periodic component that is related to the *slug frequency*. This invalidates the single-phase analysis. To determine the optimum separation for slug flow, the following factors should be considered:

- The separation error  $\Delta x/x$  is minimised, for large values of  $x$ . The inability to locate the exact sensor of the ‘sensing volume’ then becomes insignificant.
- Crosstalk between the sensors reduces significantly, as the separation between the sensors is increased.
- Developed slugs do not change significantly, as they translate through a straight section of pipe (Woods & Hanratty<sup>127</sup>). Therefore, the additive noise signal  $n(t)$  should be relatively small.

Therefore, it is proposed that the sensor separation  $x$  should be large compared to the pipe diameter  $D$ . In this work, the two cross-correlation sensors will be positioned on *opposite sides* of the phase fraction sensor. This arrangement results in a separation distance of approximately:

$$x \sim 17D \quad [5.28]$$

The effect upon the velocity uncertainty  $\Delta V_t$  cannot be determined until Chapter 8 of this thesis, since an experimental measurement of  $\rho_{xy}$  is required to evaluate equation [5.18]. However, the effect of separation upon the uncertainty should certainly be investigated, in future experiments.

### 5.2.5 Record duration

The record duration  $T$  should be as large as possible, to minimise the measurement uncertainty. However, the correlation of a large amount of data is an intensive process. The computer effort ( $T_c$ ) required to cross-correlate two data samples containing  $n$  points is of the order:

$$T_c \propto n \log_2 n \quad [5.29]$$

using the fast Fourier transform (FFT) technique. To obtain a real-time measurement with a fairly typical  $n \sim 10^4$  (10 seconds of data at a 1kHz sampling frequency), dedicated computer hardware is required.

At least one ‘slug unit’, i.e. one slug zone and one film zone, must be correlated in order to obtain a reliable measurement of the translation velocity  $V_t$ . By adding extra ‘slug units’ to the correlation data, the measurement uncertainty  $\Delta V_t$  will be reduced since the record duration  $T$  is increased. The most accurate result is obtained when *all* the available data is correlated. However, if each slug unit happens to be travelling at a different velocity (as is the case in developing slug flow), then the localised nature of the measurement will be lost.

In this thesis, the sensor data will first be acquired and stored, and will then be cross-correlated *off-line*. This off-line process has two significant advantages. First of all, the need to evaluate the function  $\rho_{xy}$  at regular intervals (which requires specialised hardware) is eliminated. Secondly, the effect of the record duration  $T$  upon the velocity measurement can be freely investigated.

### **5.3 Implementation**

This section will describe implementation of the chosen design, within the NEL multiphase facility. The manufacture of the sensor components, the arrangement of the ‘sensor units’ and a method for preventing the crosstalk currents between adjacent electrodes will be discussed. Then, a number of parameters that are required in order to design the electronic instrumentation (see Chapter 6 that follows) will be determined, by numerical simulation.

#### **5.3.1 Manufacture**

Three ‘sensor units’ – two cross-correlation units and one phase fraction unit – need to be developed. These units need to be sized accordingly, to fit the NEL test section ( $D=0.1016\text{m}$ ; 4 inches). Each sensor unit is constructed from a set of ‘spacing blocks’, which contain ring electrodes, and is held together by an ‘assembly frame’. These components are manufactured as follows:

- The ‘spacing blocks’ (figure 5.10a) are machined from a 165mm square section of clear acrylic, cut into 100mm thick blocks. Into each block, a 4-inch hole, a protruding edge and a recess (allowing an easy assembly), and an O-ring groove are machined. One face of each block is highly polished, to allow the flow to be visualised.
- The electrodes are made from 6mm stainless steel rings, which are embedded into four of the spacing blocks (figure 5.10b). At each electrode, a current and a voltage connection is made, through a shaft rod that protrudes at the surface and is attached to two 4mm plugs. A recess is machined in two of the blocks to allow the installation of a *second* electrode. This second electrode is isolated from the first electrode by a 6mm plastic ring (figure 5.10c).
- The ‘assembly frame’ is made from two stainless steel flange plates, which mount at the end of each unit (figure 5.10d). Each flange plate contains the boltholes necessary for pipeline installation. In addition, four extra holes allow the sensor sections to be held together by (precisely measured) lengths of screw rod. A cavity is machined to house the nuts at the end of each screw bar. This cavity also ensures a flush installation.

Two sets of ‘single electrodes’, two ‘double electrodes’, six flange plates, and a limited number of spacing blocks (13 in total) were manufactured. These components must be suitably assembled to form the ‘sensor units’. However, the assembly process is complicated

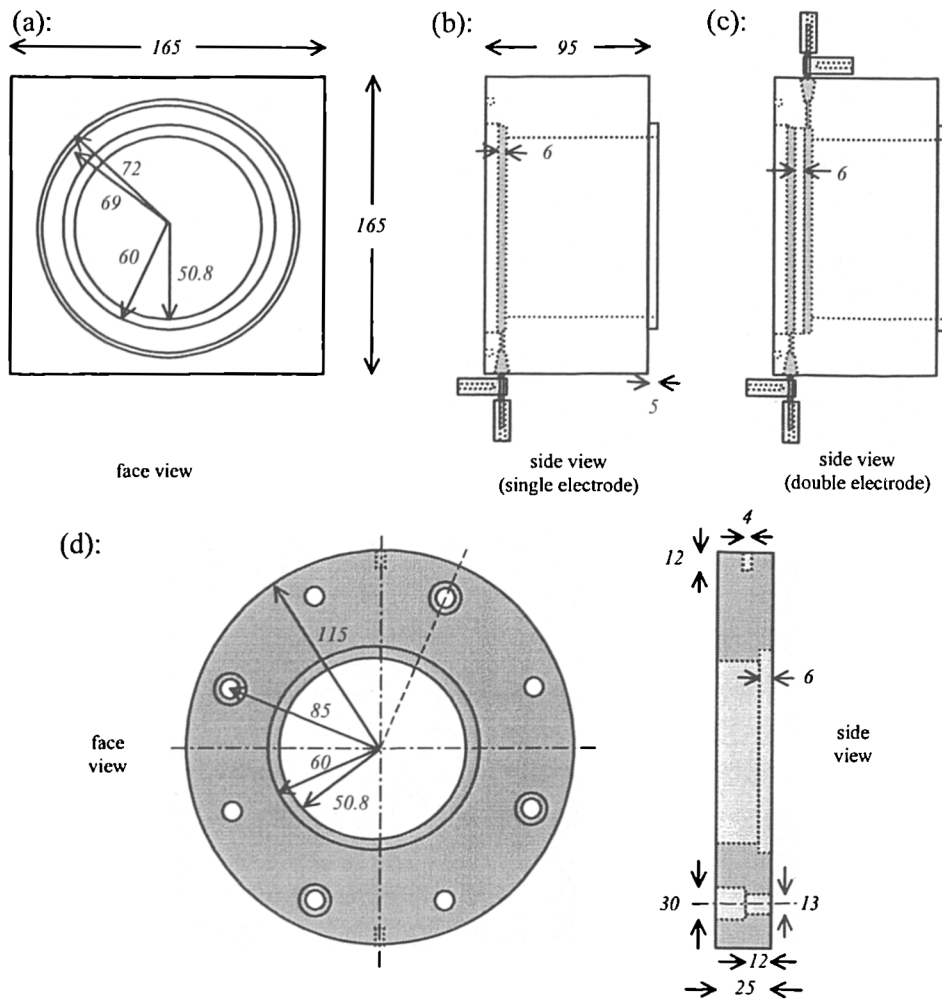


**Figure 5.10:** Manufacture diagrams: (a) the block section face view; (b) a single embedded electrode (holdup sensor); (c) a double embedded electrode (correlation sensor); (d) the flange plates used for pipeline installation.

by the presence of *grounded pipework* around the sensor electrodes.

### 5.3.2 Assembly

Any pipework that is at ground potential, and near to the sensor electrodes, will have two undesirable effects upon the conductance measurement. These effects are summarised by figure 5.11 below. The sensor field will expand outside of the ‘sensing volume’, and a ‘leakage current’ will be drawn from the live electrode to the ground. In order to minimise the measurement error, the electrodes must be suitably isolated from the pipework. That is, the separation distances  $z_1$  and  $z_2$  in figure 5.11 must be large relative to the electrode spacing  $D_e$ .

It is not possible to fully isolate the sensors, due to constraints on their *size* and the *overall cost* of the system. At least five of the ‘spacing blocks’ must be used to isolate the holdup sensor, since its electrode separation  $D_e$  is large compared to the pipe diameter  $D$ . As shown by figure 5.12a, this will result in the separation ratios:

$$z_1/D_e \sim 1 \quad z_2/D_e \sim 1 \quad [5.30]$$

Two spacing blocks remain, which are placed on the ‘near face’ of the blocks containing the cross-correlation sensor electrodes. As shown by figure 5.12b, this results in the ratios:

$$z_1/D_e \sim 10 \quad z_2/D_e \sim 10 \quad [5.31]$$

As the separation ratio  $z:D_e$  is reduced, and the measurement of the cell conductance is altered, the potential for measurement error increases. This error effect is therefore most likely to affect the holdup sensor. The effect of the grounded pipework upon the measurement uncertainties  $\Delta a_f$  and  $\Delta a_s$  will be assessed in section 5.4 below.

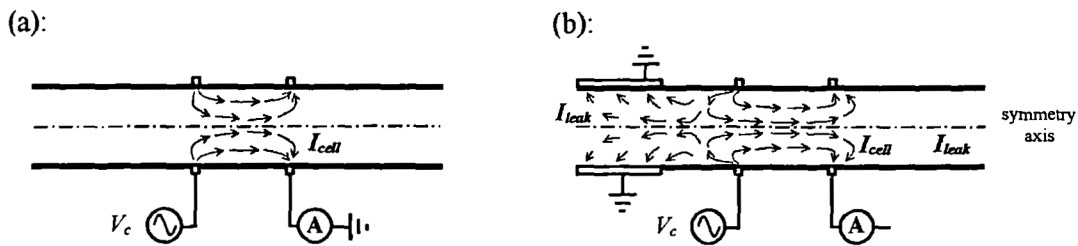


Figure 5.11: Changes to the *sensor field* and the *leakage current* due to the presence of grounded pipework.

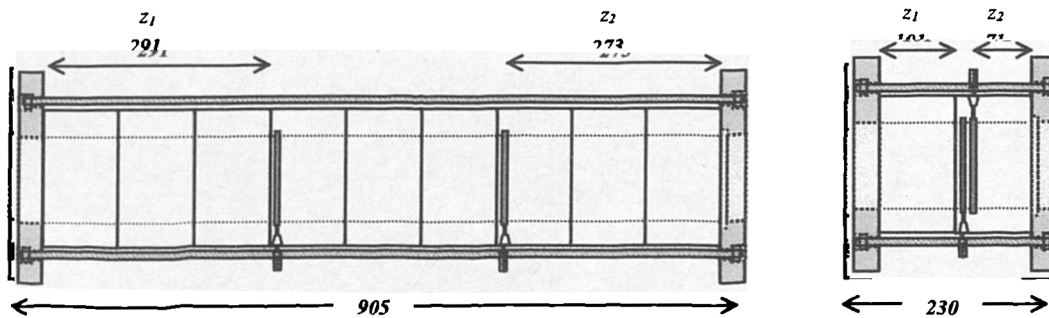


Figure 5.12: Assembly diagrams: (a) the holdup sensor unit, (b) the cross-correlation sensor unit (dimensions in millimetres).

### 5.3.3 Crosstalk prevention

A further problem in the implementation process is to prevent the *crosstalk currents* that flow between adjacent sensors. These currents are illustrated, in figure 5.13. A constant voltage  $V_{cell}$  is applied to each of the ‘drive electrodes’ and a current  $I_{cell}$  is measured at each of the ‘sink electrodes’, as described in chapter 6 of this thesis. Ideally, if there is no crosstalk current flowing between neighbouring sensors (figure 5.13a), the conductance is defined by:

$$G_{cell} = I_{cell} / V_{cell} \quad [5.32]$$

However, when a crosstalk current flows between the two sensors (figure 5.13b), the measurement error  $\Delta G_{cell} / G_{cell}$  is of the order:

$$\frac{\Delta G_{cell}}{G_{cell}} = \frac{I_X}{I_{cell}} \sim \frac{D_e}{X} \quad [5.33]$$

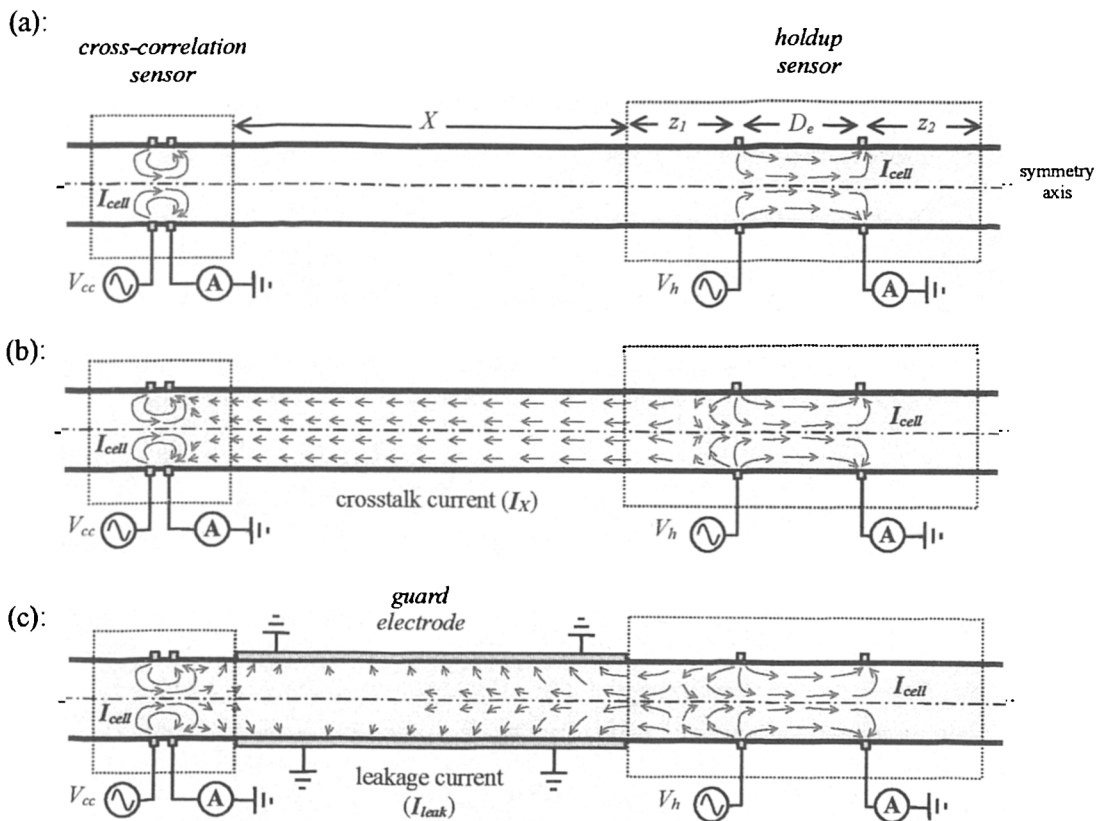


Figure 5.13: Crosstalk current between the cross-correlation and holdup sensors, for a full-pipe of liquid. (a) the ideal situation; (b) the crosstalk current, without a guard electrode; (c) the crosstalk current, with a guard electrode.

where  $I_X$  is the crosstalk current,  $D_e$  is the distance between the ‘measurement’ electrodes, and  $X$  is the distance to the neighbouring sensor. In fact, figure 5.13b illustrates the ‘worst-case’ scenario that can occur, in which the pipe is full of liquid and the crosstalk current flows from the holdup sensor to the cross-correlation sensor.

The crosstalk error worsens dramatically, as the electrode spacing  $D_e$  increases and the separation distance  $X$  is reduced. In order to reduce this error, a variety of techniques can be used; for example:

- The currents flowing within each sensor can be isolated, by driving the electrodes through transformers (Coney<sup>27</sup>). The current in one transformer loop cannot flow into the neighbouring circuits.
- The sensors can be ‘multiplexed’ (Brown *et al*<sup>23</sup>), so that only one electric field exists at any given time. During the multiplexing cycle, each pair of electrodes is activated in rapid sequence.
- Each sensor can be driven at a different a.c. frequency, and the crosstalk current from the neighbouring sensors can then be rejected with a ‘narrow-band’ filter.
- Sections of grounded pipework can be installed between the sensors, to act as guard electrodes. Though these electrodes modify the electric field within each sensor (see section 5.3.2 above), they will also attenuate the crosstalk current between adjacent sensors.

The first three techniques will not be implemented in this thesis. The solution using transformers makes the instrumentation very bulky, while the multiplexing and filtering solutions degrade the measurement bandwidth and the system stability (see Chapter 6 for more details). A system of *grounded pipework* between sensors will therefore be used to reject the crosstalk. The amount of pipework required for adequate rejection will now be determined.

### 5.3.4 Guard electrode simulation

The arrangement shown in figure 5.13c is used, to simulate the use of the pipework as guard electrodes. In this arrangement, current flows from the holdup sensor to the cross-correlation sensor (this is the worst possible case), and the voltage applied across the holdup electrodes ( $V_h$ ) is ten times the voltage across correlation electrodes ( $V_c$ ) in order to maintain equal

operating currents (see section 5.3.5 below). Further details of the simulation geometry are summarised, in appendix A). Figure 5.14 summarises the resulting error in the conductance measurement  $\Delta G_{cell}/G_{cell}$ , as a function of the relative length of the guard electrode  $X/D$ .

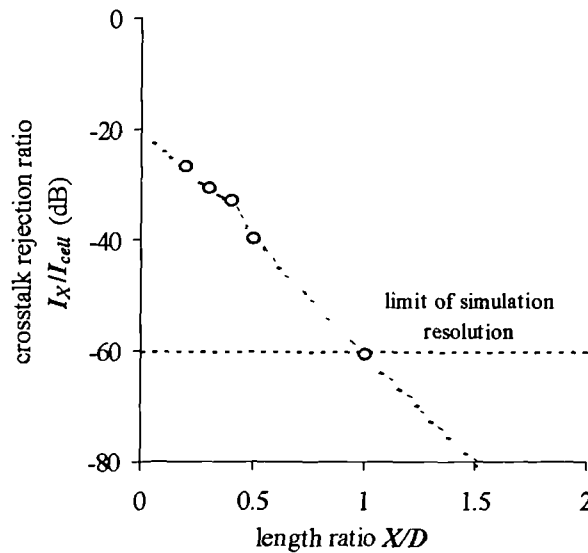


**Figure 5.14:** The effect of the guard electrode length  $X$  upon the crosstalk current rejection. (Cell voltage ratio  $V_h/V_{ce}=10$ ).

As the measurement error reduces by a factor of 20dB for each  $0.5D$  increase in length, it seems relatively easy to prevent crosstalk using this technique. For a measurement error that is less than 0.1% (i.e. -80dB), the separation ratio should be at least:

$$X/D \geq 2.0 \quad [5.34]$$

In the NEL test facility (4-inch pipe diameter) this ratio corresponds to a fairly modest distance of 20 centimetres.

Figure 5.15 illustrates the final assembly of the sensor units, including the intervening guard electrodes. Moving in the downstream direction, the first cross-correlation sensor is followed by a section of grounded pipework (40 cm long), the holdup sensor, a second section of pipework (also 40 cm long), and the second cross-correlation sensor. The total length of the test section is about 2 metres, while the separation between the cross-correlation sensors ( $x$ ) is 1.701 metres. As shown by the diagram, the amount of crosstalk is expected to be minimal.

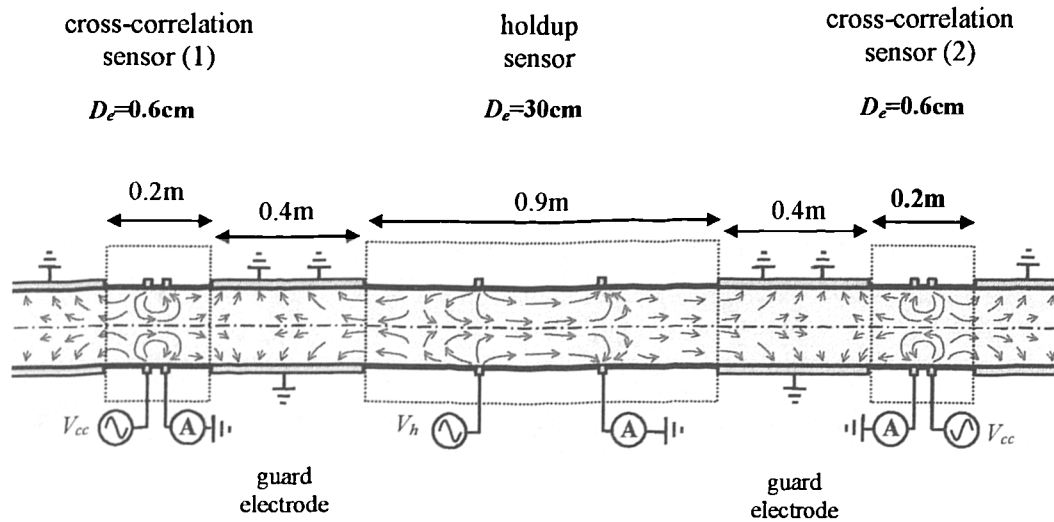


Figure 5.15: Assembly diagram

### 5.3.5 Design parameters

The design of the instrumentation used to activate the sensor electrodes (described in Chapter 6) depends upon the *geometry* of the each sensor unit. In this section, the ‘cell constant’, the ‘leakage current’ and the ‘leakage resistance’ parameters will be defined for each sensor by using numerical simulations. Considerable use of these results will be made, in Chapter 6 that follows.

The ‘cell constant’ is required, in order to specify the *measurement range* of the instrumentation (see section 6.1). This constant is derived by calculating the ratio of the cell current to the cell voltage in the simulation illustrated by figure 5.13c. The result for the holdup sensor is:

$$C_h = 0.0230 \text{ m} \quad [5.35]$$

and:

$$C_{cc} = 0.210 \text{ m} \quad [5.36]$$

for the cross-correlation sensors. As discussed in appendix A, these results are expected to be accurate to at least 1%.

The leakage current, which passes between the live electrode and the surrounding ground

pipework, is required in order to determine the *operating current* (see section 6.3.2). The ratio of the leakage current to the cell current,  $I_{leak}/I_{cell}$ , is approximately:

$$\left(\frac{I_{leak}}{I_{cell}}\right)_h \sim 1 \quad \left(\frac{I_{leak}}{I_{cell}}\right)_{cc} \sim 0.2 \quad [5.37]$$

for the sensor holdup and the cross-correlation sensors respectively. The leakage ratio is smallest for cross-correlation sensors, since the separation distances  $z_1$  and  $z_2$  are large compared to the electrode spacing  $D_e$ .

The minimum ‘leakage resistance’  $R_{leak}$  is required, in order to analyse the *cell impedance network* (section 6.3.3). This resistance depends upon the ratio of the leakage resistance to the cell resistance and the minimum cell resistance (denoted by  $R_{cell}^*$ ).  $R_{cell}^*$  depends upon the cell constant and the maximum fluid conductivity ( $10 \Omega^{-1} \text{m}^{-1}$ , from section 5.1.5) and is respectively:

$$\left(R_{cell}^*\right)_h = 4.3 \Omega \quad \left(R_{cell}^*\right)_{cc} = 0.48 \Omega \quad [5.38]$$

Since the ratio  $R_{leak}/R_{cell}^*$  is equal to current ratio  $I_{leak}/I_{cell}$ , the minimum leakage resistance is therefore:

$$\left(R_{leak}\right)_h \sim 5 \Omega \quad \left(R_{leak}\right)_{cc} \sim 2.5 \Omega \quad [5.39]$$

The values  $R_{cell}=0.5\Omega$  and  $R_{leak}=2.5\Omega$  will be used in the numerical simulation of the electronic system, which is described in sub-section 6.3.6.

## **5.4 Performance assessment**

Figure 5.16 illustrates the complete set of ‘sensor units’, installed within the NEL multiphase facility. The ability of these sensor units to accurately measure the film zone, the slug zone and the intervening ‘transition region’ (between the slug and the film) will now be assessed, through a set of simple experiments. In particular, the effect of the *guard electrodes* upon the measurement uncertainty will be quantified.

### **5.4.1 Film zone measurement**

The accuracy with which the film zone can be measured is assessed, by three sets of tests

upon a stratified geometry. These tests are as follows:

- An experimental measurement, where the sensor units are filled with known volumes of liquid, and the electronic instrumentation (discussed in chapter 6) is used to measure the conductance.
- A numerical simulation, using the two-dimensional geometry illustrated in figure A2 (see appendix A for details). The conductance values are converted to a stratified geometry, by using equations [5.4] and [5.5].
- The analytic solution of equation [5.1] for a stratified geometry. This solution indicates the equivalent performance that is achieved, *without* the presence of guard electrodes.

The results of these experiments are compared in figure 5.17. There is good agreement between each of the three cases, despite some geometric discrepancy. However, the measurement obtained by the *holdup sensor* is clearly affected by the guard electrodes. This is because the separation distances  $z_1$  and  $z_2$  are relatively large compared to the electrode separation  $D_e$ . As a result of this change, the measurement uncertainty  $\Delta a_f$  may increase by a modest amount.

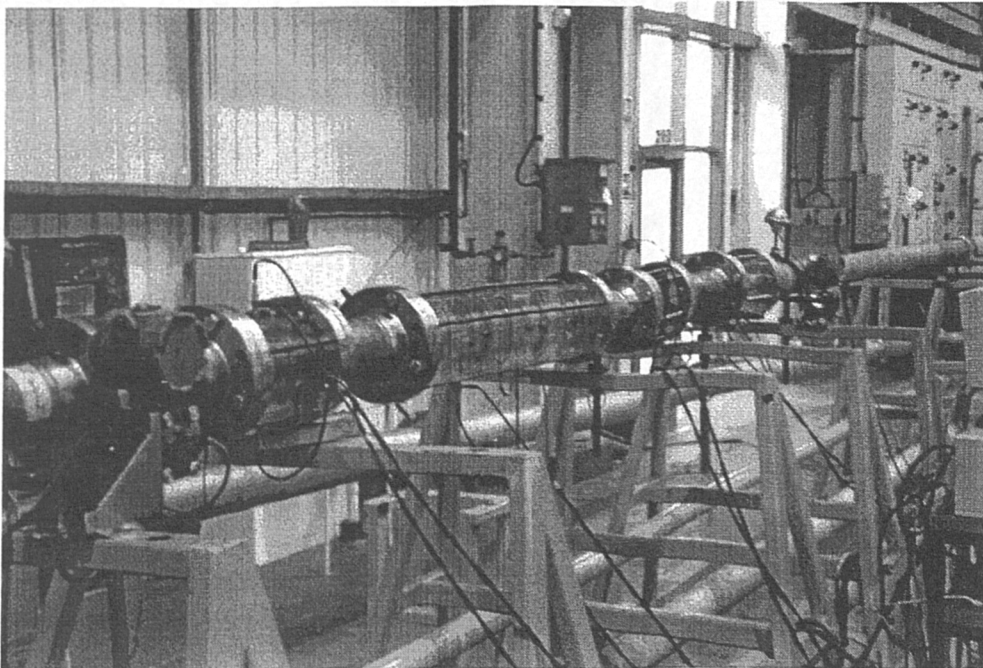


**Figure 5.16:** The system of sensor units, within the NEL facility.

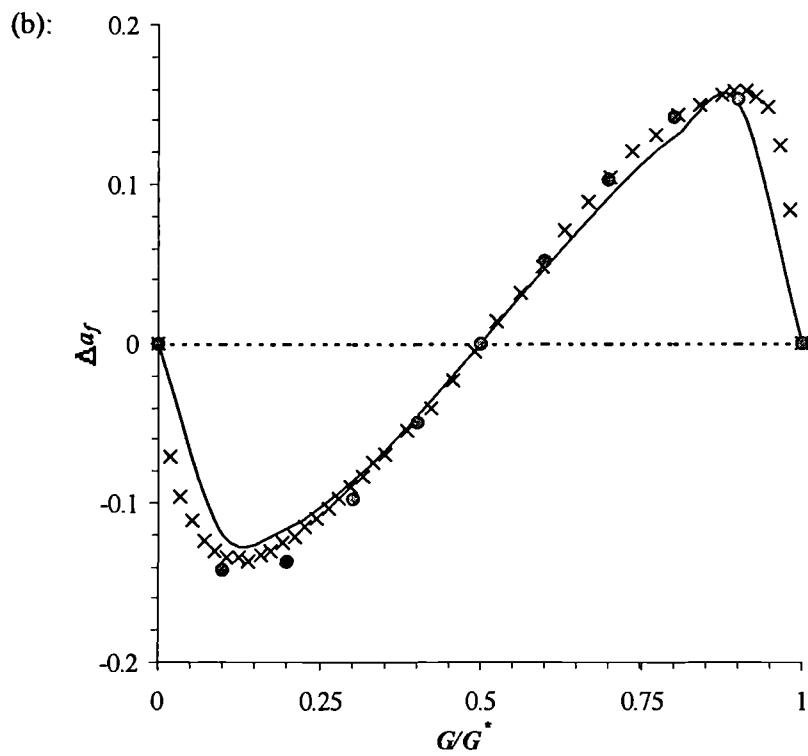
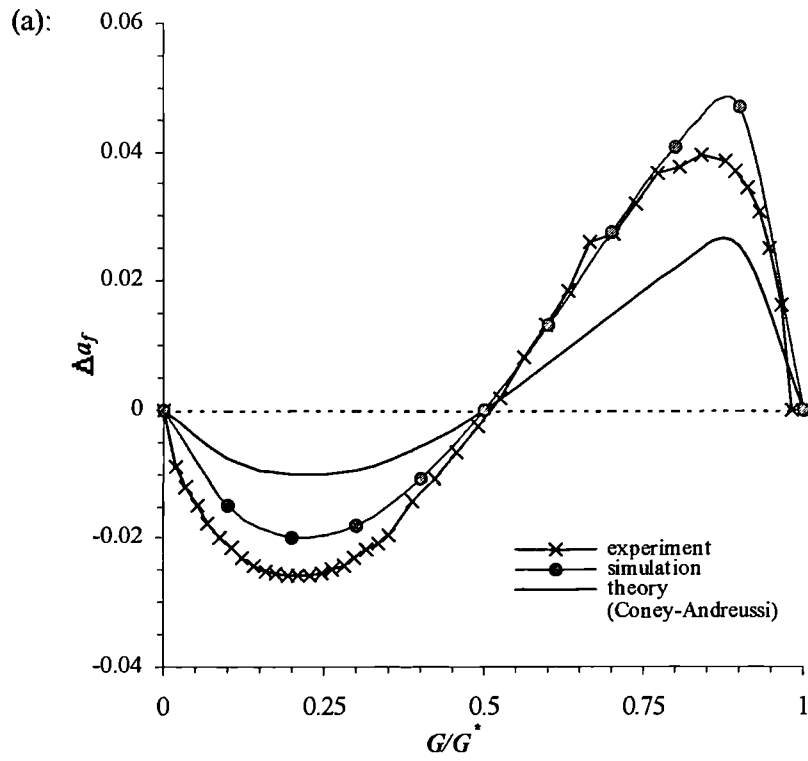


**Figure 5.17:** Performance assessment. Comparison of the experimental measurements, the prediction obtained using ANSYS simulation (appendix A) and the Coney-Andreussi theoretical model, for a stratified flow geometry: (a) the phase fraction sensor ; (b) the cross-correlation sensors.

### 5.4.2 Transition zone measurement

The transition region between the film zone and the slug body has a complex structure, which means it is difficult to simulate accurately (see Fan *et al*<sup>33</sup>). Therefore, it is only possible to simulate this region by using a 'step change' model. The numerical experiments described in section 5.1.4 were repeated, with two guard electrodes added at a distance of 30cm from the holdup sensor (i.e.  $z_1 = z_2 = D_e$ ). These results were identical to the results illustrated in figure 5.7. Therefore, the presence of the guard electrodes has a negligible effect upon the measurement of the transition zone.

### 5.4.3 Slug holdup measurement

The slug zone is also difficult to simulate accurately, particularly as the void fraction *decreases*. The gas bubbles cannot be controlled in an experimental measurement (see Andreussi *et al*<sup>8</sup> and Fossa<sup>36</sup>) and they are too time-consuming to include in a numerical simulation. Therefore, experiments were not attempted in this thesis. However, to a first approximation, the measurement will be dependent upon the accuracy of the *mixture model* and not the electrode geometry.

To determine what affect the guard electrodes have on the slug holdup, the cell constants  $C_h$  and  $C_{cc}$  were calculated, *without* these guards present. This simulation resulted in the values:

$$C_h = 0.0240 \text{ m} \quad C_{cc} = 0.223 \text{ m} \quad [5.40]$$

for the holdup and the cross-correlation sensors respectively. Since the values  $C_h=0.0230$  m and  $C_{cc}=0.210$  m are computed with the guard electrodes (section 5.3.5) the measurement of inside the sensing volume is independent of the contents between the sensing volume and the guard electrodes, to at least a 95% level.

## 5.5 Summary

This chapter described the design and manufacture of a set of ring electrode sensors, for the measurement of the phase fractions  $a_s$  and  $a_f$ , and cross-correlation of the translation velocity  $V_t$  in slug flow. In accordance with the specifications presented in Chapter 4, these sensors are *non-intrusive* and *inexpensive*.

Section 5.1 discussed the design of the ‘holdup sensor’, which is used to measure the phase fractions  $a_f$  and  $a_s$ . A wide electrode separation ( $D_e$ ) was required to measure the film holdup  $a_f$ , but this was conflicted with the shorter separation required to measure the slug holdup  $a_s$ , and the ‘transition zone’ between the slug and the film. It was therefore necessary to make a compromise with the separation ratio  $D_e/D=3.0$ . This resulted in measurement uncertainties:

$$|\Delta a_f| \sim 0.02 + \frac{1.5D}{l_f} \quad |\Delta a_s| \sim 0.2(1 - a_s) \quad [5.41]$$

Further increases in the  $\Delta a_f$  and  $\Delta a_s$  were expected, as the gas phase flowrate was increased towards annular flow conditions. This was due to the spray above the liquid film, and the bubbly core in the slug body.

Section 5.2 discussed the design of a pair of ‘cross-correlation’ sensors, used for measuring the translation velocity  $V_t$ . These sensor electrodes were closely spaced ( $D_e=0.05D$ ) in order to maximise the sensor bandwidth  $B_s$ . However, the sensors themselves were widely spaced ( $x \sim 17D$ ) to take advantage of the *good coherence* that was assumed to exist between the slug flow signals. The uncertainty in the velocity measurement ( $\Delta V_t$ ) was then estimated using the model of Beck & Plaskowski<sup>17</sup> to be:

$$\Delta V_t \sim \frac{V_t^2}{x} \frac{0.038^{1/2}}{T^{1/2} B^{3/2}} \left\{ \frac{1 - \rho_{xy}^2(\tau^*)}{\rho_{xy}^2(\tau^*)} \right\}^{1/2} \quad [5.42]$$

in which  $B$  was the signal bandwidth,  $T$  was the record duration, and  $\rho_{xy}(\tau^*)$  was the position of the correlation peak. While the parameters  $B$  and  $T$  could be estimated, it was not possible to predict  $\rho_{xy}$  without having experimental data. This meant that the uncertainty  $\Delta V_t$  could not be quantified.

Section 5.3 described the implementation of the chosen designs. The components used to build each ‘sensor unit’ were described, and then an assembly arrangement was developed so the surrounding pipework did not introduce *crosstalk errors* into the measurement. Various ‘spacing blocks’ had to be inserted around the electrodes, to ensure the separation distances  $z_1$  and  $z_2$  were large compared to the electrode separation  $D_e$ . Grounded pipework were then positioned between the sensor units, so that the crosstalk could be reduced to an acceptably small level (a 0.1% error). The resulting system, which was illustrated in figure 5.15, had an overall length of approximately 2 metres.

Section 5.4 described the tests that were used to verify the sensor performance. Measurement of the *film zone* region was investigated by a set of physical experiments and numerical

simulations, with these results being in good agreement with each other. However, measurement of the *transition zone* and the *slug body* was not attempted, because their structure was too complex to simulate accurately. In these cases, however, the guard electrodes were shown to have a minimal effect upon the measurement.

## 6. Instrumentation design

This chapter will describe the development of electronic instrumentation, for measuring the conductance between the sensor electrodes. This instrumentation will be designed to operate over a wide range of conductance, so that a range of different fluids can be tested, and will offer a wide measurement bandwidth and good measurement accuracy. This solution shall be developed, at minimal cost.

Section 6.1 will explain the specifications for the *functionality* and the *performance*. The ‘functionality specifications’ concern the measurements required, the user interface, and the output. The ‘performance specifications’ define the necessary operating range, measurement accuracy, and the measurement bandwidth.

The core of this chapter will then describe the development of a suitable *design solution* and its *implementation*. This process is divided into three sections:

- Section 6.2 will discuss the ‘classical’ design solution by Coney<sup>27</sup>, which is normally used for measuring the conductance between electrode pairs. Two serious limitations in this design (a limited range and low bandwidth) will be highlighted. As a result, a new solution that uses *voltage feedback* to keep the cell voltage stable will be presented.
- Section 6.3 will describe the *detail* of the new design. The operating frequency and the operating current, the impedance network surrounding the cell, the demodulation method, and the stability of the feedback loop will each be discussed. The design shall then be numerically simulated, and the effect of bandpass filters (which reject interference) upon the performance shall be assessed.
- Section 6.4 will describe the *implementation* of the design, using real electronic components. As these components have non-ideal performance, the real performance of the system will be worse than the ‘ideal’ performance. The effect of the operating range, signal distortion errors and ‘d.c.-type’ errors will be examined, and then the steps required to minimise the effects of external interference will be discussed.

Finally, section 6.5 will demonstrate the performance of the manufactured instrument, by a series of simple bench-tests. These tests indicate that the overall performance is excellent.

## **6.1 Instrument specifications**

The specification for the instrumentation is divided into two parts. The *functionality specification* defines the instrument capability and user interface, while the *performance specification* is a guarantee of measurement accuracy over a range of different conditions. Both these specifications, which must be met at *minimum cost*, are now outlined.

### **6.1.1 Functionality specifications**

The instrumentation must measure the conductance as the flow passes between the holdup and cross-correlation sensors (designed in Chapter 5) and provide this measurement at an output port. Three measurement channels are required; a fourth channel is also specified, in order to allow an extra sensor to be added to the system at a future date. Each of these four channels will provide the following functions:

- An a.c. measurement of the cell conductance, using shielded coaxial cables. This measurement will be made at a frequency of at least 1kHz, in order to avoid electrolysis of the flow.
- Multiple operating ranges, in order to cover all the possible combinations of fluid conductivity and cell geometry.
- A BNC output port, for transmitting the measured conductance to a data acquisition (DAQ) card. This output signal will be a d.c. voltage, between 0V and 10V.
- The capability to perform simple diagnostic checks, in the event of channel failure.

Figure 6.1 presents a schematic diagram of the user interface. Four identical *measurement channels* will provide connections to the cell, a BNC output port, and a rotary switch for selecting the conductance range. A separate *display module* will house a 'channel selection' switch, a digital display, and 'output' and 'sync' ports that can be connected to an external oscilloscope. The 'channel selection' switch and the 'break switch' can be used to route various signals to the output port, so that diagnostic tests can be performed. Each of the five modules will be rack-mounted, and will be compatible with the Eurocard and the Eurocase formats.

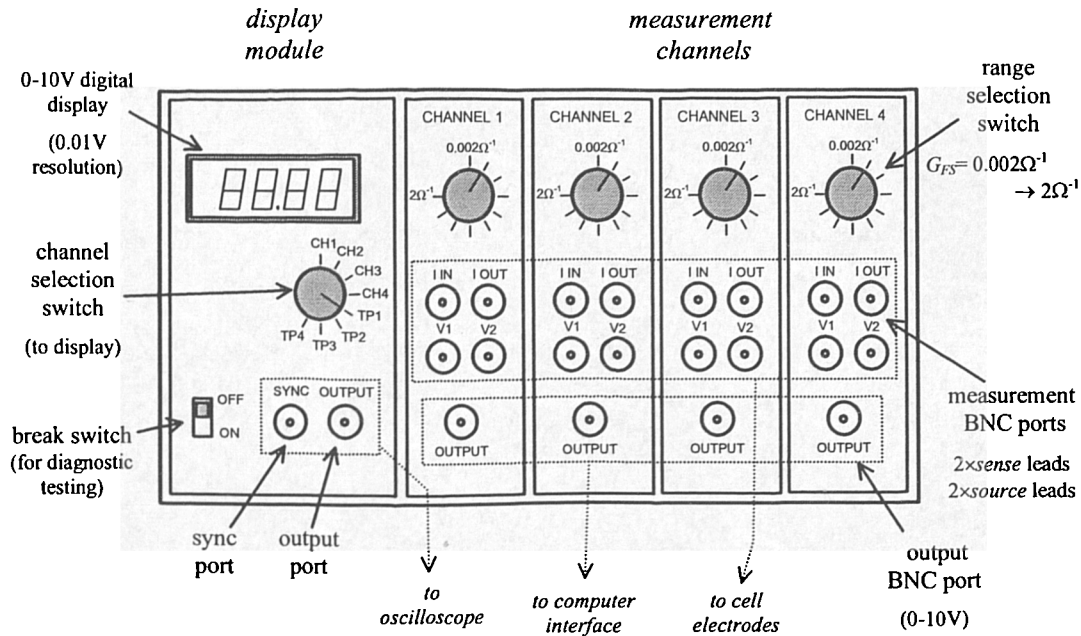


Figure 6.1: Schematic diagram of the user interface.

### 6.1.2 Performance specifications

The performance specifications reflect the need to make an accurate measurement of the phase fractions  $a_f$  and  $a_s$  and the translation velocity  $V_t$ , using the system of ring electrodes developed in chapter 5. These specifications can be summarised, as follows:

- A full-scale conductance between  $0.002\Omega^{-1}$  and  $2\Omega^{-1}$ , which will be divided into ten *operating ranges*. That is,  $G_{FS}=0.002\Omega^{-1} \rightarrow 2\Omega^{-1}$ .
- A full-scale measurement accuracy of 0.2%, for each operating range. That is,  $\Delta G/G_{FS} < 0.2\%$ .
- A measurement bandwidth in excess of 2kHz, for each operating range. That is,  $B_I > 1\text{kHz}$ .

These specifications must be satisfied by each of the four system channels, for the range of operating temperature between  $0^\circ\text{C}$  and  $40^\circ\text{C}$ . The origin of each specification is now explained.

The *measurement range* is determined by the minimum and maximum values for the full-pipe conductance  $G^*$ . This conductance is the product of the cell constant  $C$  and the fluid

conductivity  $\sigma$ , according to:

$$G^* = \sigma C \quad [6.1]$$

The cell constant ( $C$ ) is a function of the electrode geometry. The numerical simulations in chapter 5 of this thesis indicated that:

$$C_h \sim 0.02 \text{ m} \quad C_{cc} \sim 0.2 \text{ m} \quad [6.2]$$

for the holdup sensor and the cross-correlation sensor respectively. On the other hand, the water conductivity ( $\sigma$ ) is a function of salt content and temperature. The conductivity range:

$$\sigma \sim 0.1 \rightarrow 10 \Omega^{-1} \text{ m}^{-1} \quad [6.3]$$

was specified in section 5.1.6. Combining equations [6.2] and [6.3] results in the *full-scale* conductance range:

$$G_{FS} = 0.002 \Omega^{-1} \rightarrow 2 \Omega^{-1} \quad [6.4]$$

To ensure that the output signal is large enough to be accurately sampled, this range is subdivided into ten operating ranges. These operating ranges will have a full-scale conductance  $G_{FS} = 0.002 \Omega^{-1}; 0.004 \Omega^{-1}; 0.008 \Omega^{-1}; 0.02 \Omega^{-1}; 0.04 \Omega^{-1}; 0.08 \Omega^{-1}; 0.2 \Omega^{-1}; 0.4 \Omega^{-1}; 0.8 \Omega^{-1};$  and  $2 \Omega^{-1}$  respectively.

The *measurement accuracy* should be good enough, to prevent significant contribution to the uncertainties  $\Delta a_f$  and  $\Delta a_s$ . Since these are of the order of 1% to 10% for ring electrode sensors (see section 5.1), it is proposed that the measurement uncertainty should not be greater than 0.5%. That is:

$$\Delta G / G^* \leq 0.005 \quad [6.5]$$

To ensure that this criterion is satisfied, the operating range must be carefully chosen. The full-scale conductance ( $G_{FS}$ ) should exceed the full-pipe conductance ( $G^*$ ), but should not be excessively large or the output signal will be very small. With ten operating ranges, it is always possible to choose a value for  $G_{FS}$  such that  $2.5 G^* < G_{FS} < G^*$ . In this case, equation [6.5] becomes:

$$\Delta G / G_{FS} \leq 0.002 \quad [6.6]$$

This is, the full-scale measurement uncertainty should be 0.2% or less on each operating range.

The *instrument bandwidth* should be larger than the sensor bandwidth  $B_s$ , in order to ensure an accurate measurement of the translation velocity  $V_t$ . This sensor bandwidth was estimated, in section 5.2, by the approximate formula:

$$B_s \sim V/a \quad [6.7]$$

where  $V$  was the ‘characteristic velocity’ of the flow, and  $a$  was the ‘characteristic width’ of the sensor volume. For the cross-correlation sensors,  $a \sim 0.005\text{m}$  and  $V_t \sim 10 \text{ m s}^{-1}$  corresponded to a maximum bandwidth:

$$B_s \sim 2 \text{ kHz} \quad [6.8]$$

Therefore, the instrumentation bandwidth  $B_I$  should be 2kHz or greater, to ensure accurate measurement of the flow. This is roughly equivalent to specifying a *dynamic response* of no longer than 0.5 milliseconds.

## 6.2 Design solution

The cell conductance is defined as the inverse of the cell resistance, i.e. the ratio of the cell current to the cell voltage. In the notation that shall be adopted in this chapter of the thesis, that is:

$$G_{\text{cell}} = I_{\text{cell}} / V_{\text{cell}} \quad [6.9]$$

To obtain  $G_{\text{cell}}$  either  $V_{\text{cell}}$  and  $I_{\text{cell}}$  can both be measured,  $V_{\text{cell}}$  can be measured and  $I_{\text{cell}}$  controlled (the ‘constant-current’ method), or  $I_{\text{cell}}$  can be measured and  $V_{\text{cell}}$  controlled (the ‘constant-voltage’ method). However, the ‘constant-voltage’ method is preferred, because the current is directly proportional to the conductance. The ‘constant-voltage’ technique used by Coney<sup>27</sup>, Brown *et al*<sup>23</sup> and others is illustrated in figure 6.2.

In order to prevent the formation of double-layer capacitances at the cell electrodes (see section 2.2), the cell must be driven using an *a.c. source*, of frequency  $\omega_c$ , and amplitude  $V_d$  (Coney<sup>27</sup>). This source current passes through the cell, gets converted to a voltage by the transimpedance amplifier, and is gets demodulated to extract the envelope signal around the carrier. From the output signal  $V_o$ , the conductance is given by:

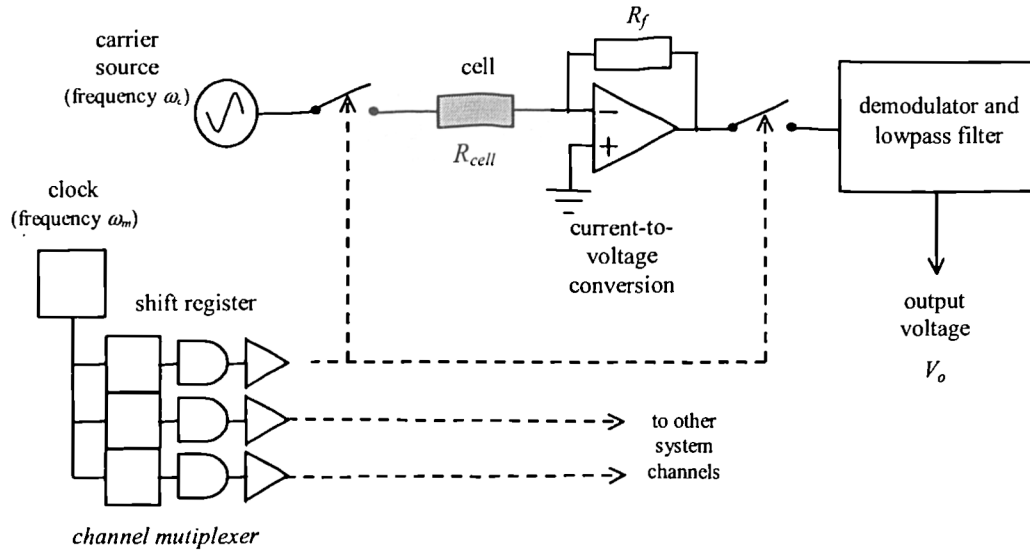


**Figure 6.2:** Constant-voltage system for conductance measurement, developed by Coney<sup>27</sup> and Brown *et al*<sup>23</sup>.

$$G_{cell} = -\frac{V_o}{V_d R_f} \quad [6.10]$$

where  $R_f$  is the feedback resistance of the transimpedance amplifier, shown in figure 6.2. Therefore, as long as the source amplitude  $V_d$  remains constant, the output signal is proportional to the conductance.

Usually, the measurement system will consist of two (or more) pairs of conductance electrodes. Therefore to prevent the possibility of crosstalk, each cell is activated in quick succession by using *shift registers*. This process is termed ‘multiplexing’. If there are  $n$  sensors in the system, an active measurement of each cell is only made for a  $1/n^{\text{th}}$  fraction of the multiplexing cycle. Therefore, the signal from each channel must be fed through a lowpass filter to produce meaningful output.

Figure 6.2 actually illustrates the measurement of the cell *admittance*. This cell admittance is only equal to the cell conductance, when there are no capacitive components between the electrodes. As a result, the operating frequency should be exceeded 10kHz (to prevent ‘double layer’ capacitances), but should be less than 1MHz (to ensure the cell capacitance and stray capacitance are negligible). Under these conditions, the cell voltage and the cell current are exactly in phase. The carrier signal component can be removed by using *amplitude demodulation*. The circuit used to perform this demodulation illustrated in figure 6.3 below.

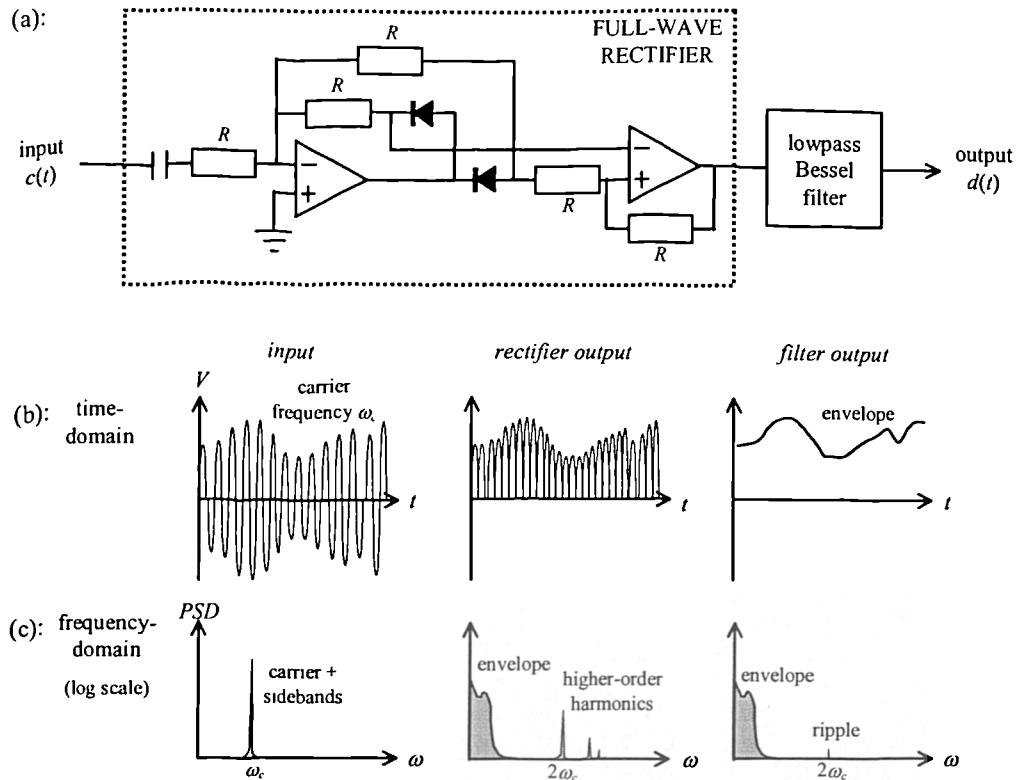


**Figure 6.3.** Circuit used to perform amplitude demodulation of the carrier, and its performance in the time- and frequency domains.

### 6.2.1 Limitations

Unfortunately, the solution described in the previous section has two limitations that will degrade the measurement accuracy and the measurement bandwidth. These limitations, which are illustrated in figures 6.4 and 6.5, are a *voltage divider* effect across the cell electrodes and a *rise-time* error within the channel multiplexer. The causes are as follows:

- The ‘voltage divider’ effect is due to the network of impedances around the cell electrodes. The transimpedance amplifier impedance ( $Z_T$ ), the connection impedance ( $Z_{con}$ ) and the net cable impedances ( $Z_{WL}$  and  $Z_{WC}$ ) develop a significant voltage drop, if the cell resistance decreases below  $10\Omega$ . As a result the driving voltage  $V_d$  will exceed the cell voltage  $V_{cell}$ . The measurement error worsens, as the *cell constant*, the *local holdup* and the *fluid conductivity* are increased.
- The transient error is due to the lowpass filter that follows the transimpedance amplifier. Once each pair of electrodes is activated, this filter will take a finite

amount of time to respond to the incoming signal. The 'rise-time' error increases, as the ratio of the multiplexing to the carrier frequency ( $\omega_m/\omega_c$ ) and the bandwidth of the lowpass filter are reduced. The error is worse still, if the multiplexing system is not synchronised with the carrier waveform.

In order to prevent these limitations, it is necessary to make two changes to the design. First of all, the cell voltage must be directly measured in order to compensate for the 'voltage divider' effect. Secondly, the system for multiplexing the electrodes must be modified, in order to prevent the measurement errors as each channel is being activated. Therefore, a new design is now proposed.

### 6.2.2 Modified design

The solution that shall be developed in this thesis is illustrated in figure 6.6. The cell voltage is measured by using sensing leads and an instrumentation amplifier. This measurement is input into a feedback loop, which controls the amplitude of the a.c. source ( $V_d$ ). *Guard electrodes* are also inserted between the sensors, to prevent crosstalk and therefore eliminate the need for multiplexing. The design of these guard electrodes was discussed in considerable detail, in Chapter 5.

The use of this design results in the following improvements:

- The feedback loop keeps the voltage across the cell terminals  $V_{cell}$  constant, regardless of the values of the impedances in figure 6.4. This arrangement therefore prevents a 'voltage divider' effect, and also eliminates the need that the amplitude of the voltage source ( $V_d$ ) be stable.
- The four measurement channels are able to make *simultaneous* measurements of the cell conductance. As a result, errors during the activation of the sensor electrodes are avoided.

The cell measurement and the multiplexing problems could also be addressed, by using *digital signal processing* (DSP) techniques. For example, the measurements of the cell voltage and the cell current could be digitally divided in real-time, in order to obtain the cell conductance. On the other hand, the demodulator signals could be processed by using a 'mathematical morphology' filter (Rafael & Woods<sup>96</sup>), in order to prevent any 'rise time' errors. However, the proposed solution is more elegant than these alternatives, and it is less costly to implement.

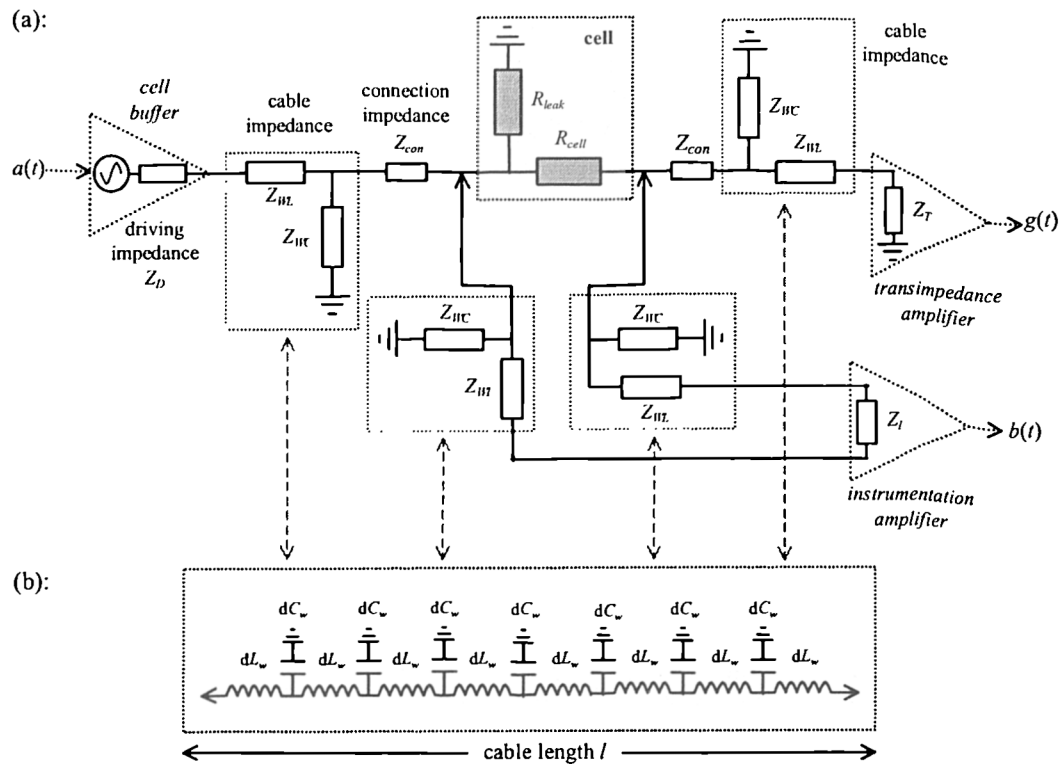


Figure 6.4: Model illustrating the network of impedances surrounding the cell. (a) 'Top level' diagram. (b) Coaxial cable impedance.

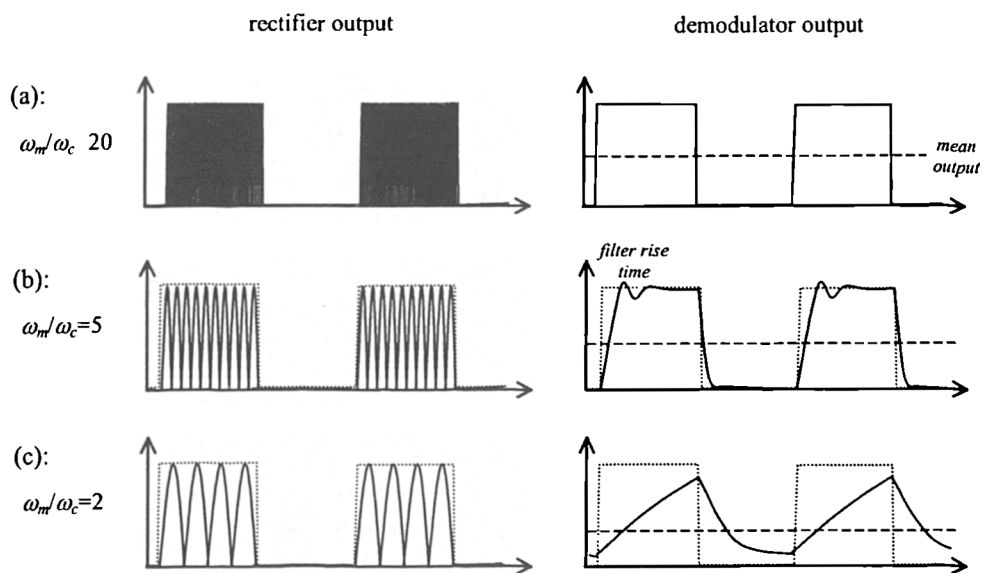


Figure 6.5: Deterioration of the demodulator output, with increasing carrier-to-multiplexing frequency ratio: (a)  $\omega_c/\omega_m=20$ ; (b)  $\omega_c/\omega_m=5$ ; (c)  $\omega_c/\omega_m=2$ .

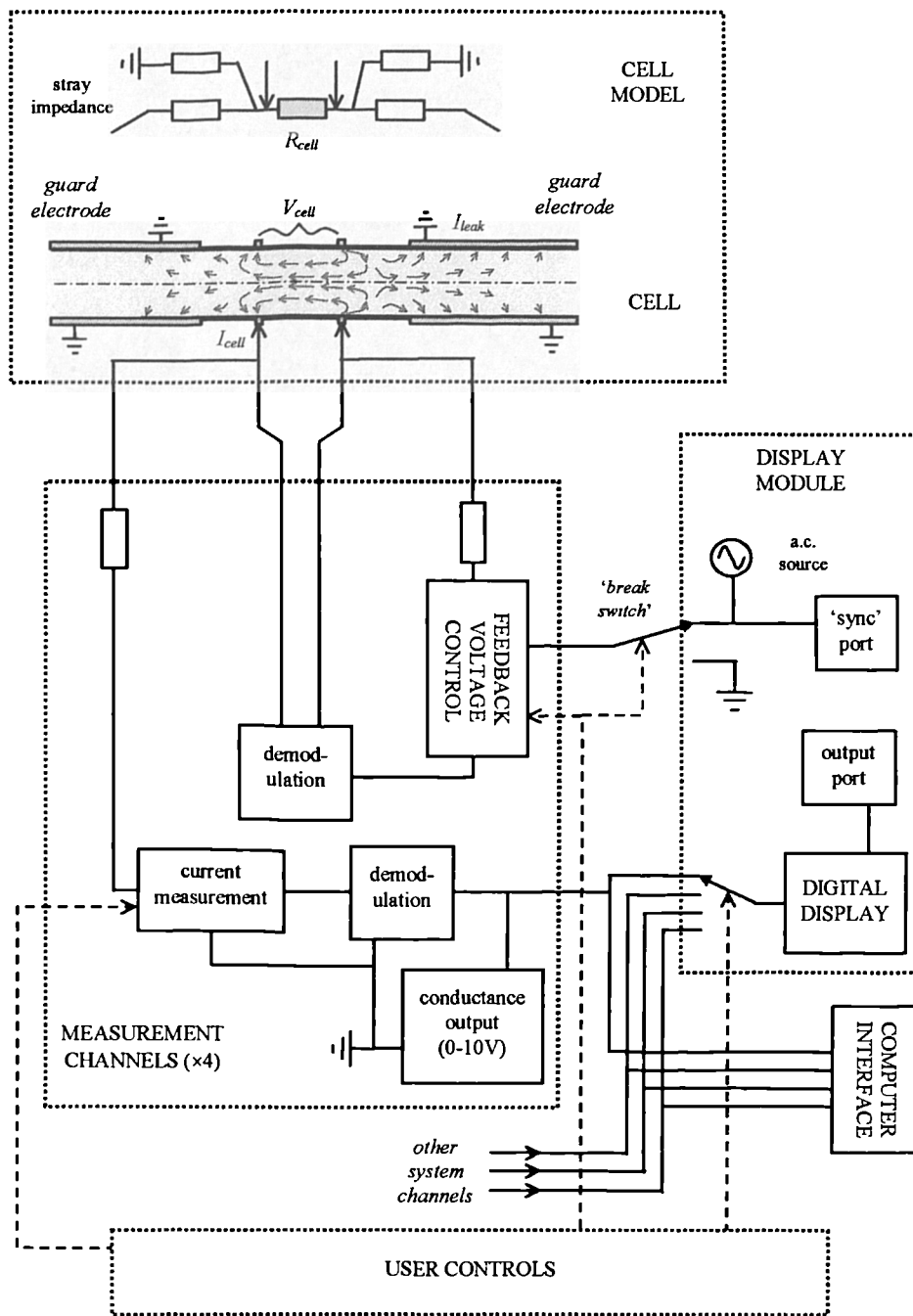


Figure 6.6: Schematic diagram of the proposed design solution

### 6.3 Detailed design

Each of the measurement channels can be separated into ‘forward gain’, ‘feedback gain’ and ‘current measurement’ stages. These three stages can then be broken down into the key components shown in figure 6.7. In this section, the *detailed design* of the system shall be discussed, starting from top-level design and working downwards. The performance of the

system will then be assessed, by using a numerical simulation.

### 6.3.1 Channel structure

Figure 6.5 illustrates the *feedback loop* and the *current measurement* processes within a single system channel. The feedback loop is split into a forward gain  $A$ , a feedback gain  $\beta$ , and a junction stage (which provides negative feedback) in the conventional manner. Within the loop, the signals  $a(t)$  to  $f(t)$  are defined as follows:

- A buffer amplifier drives the cell with the voltage waveform  $a(t)$ . The waveform  $a(t)$  is generated by modulating (i.e. multiplying) the d.c. envelope signal with an a.c. carrier source.
- An instrumentation amplifier senses the waveform across the cell terminals  $b(t)$ . The relationship between the signals  $a(t)$  and  $b(t)$  is defined by the *voltage transfer function*  $G(\omega)$  (see section 6.3.2). There follows a gain stage (dependent on the operating range) and bandpass filtering (to reject interference), resulting in the signal  $c(t)$ .
- A demodulator removes the carrier component from the signal  $c(t)$ , producing the envelope signal  $d(t)$ . The design of this demodulator is discussed in detail in section 6.3.3 below.
- The feedback junction compares the signal  $d(t)$  against the d.c. reference voltage  $V_{ref}$ , so the gain can be adjusted accordingly. The output  $e(t)$  is passed to a gain stage, and then to a PI controller (necessary for stability), producing the signal  $f(t)$ . The signal  $f(t)$  is the d.c. input to the modulator.

Assuming that perfect modulation and demodulation take place, the carrier signal can be neglected. The application of linear feedback theory to the envelope signal in figure 6.5 results in:

$$V_{cell} = V_{ref} \left( \frac{A}{1 + A\beta} \right) \quad [6.11]$$

where  $A$  and  $\beta$  are the ‘forward gain’ and the ‘feedback gain’ acting upon the envelope. Therefore, for 0.2% measurement accuracy, the product  $A\beta$  should at least 500 at d.c. frequency. A large value of  $A\beta$  should be maintained at higher frequencies, to ensure a good

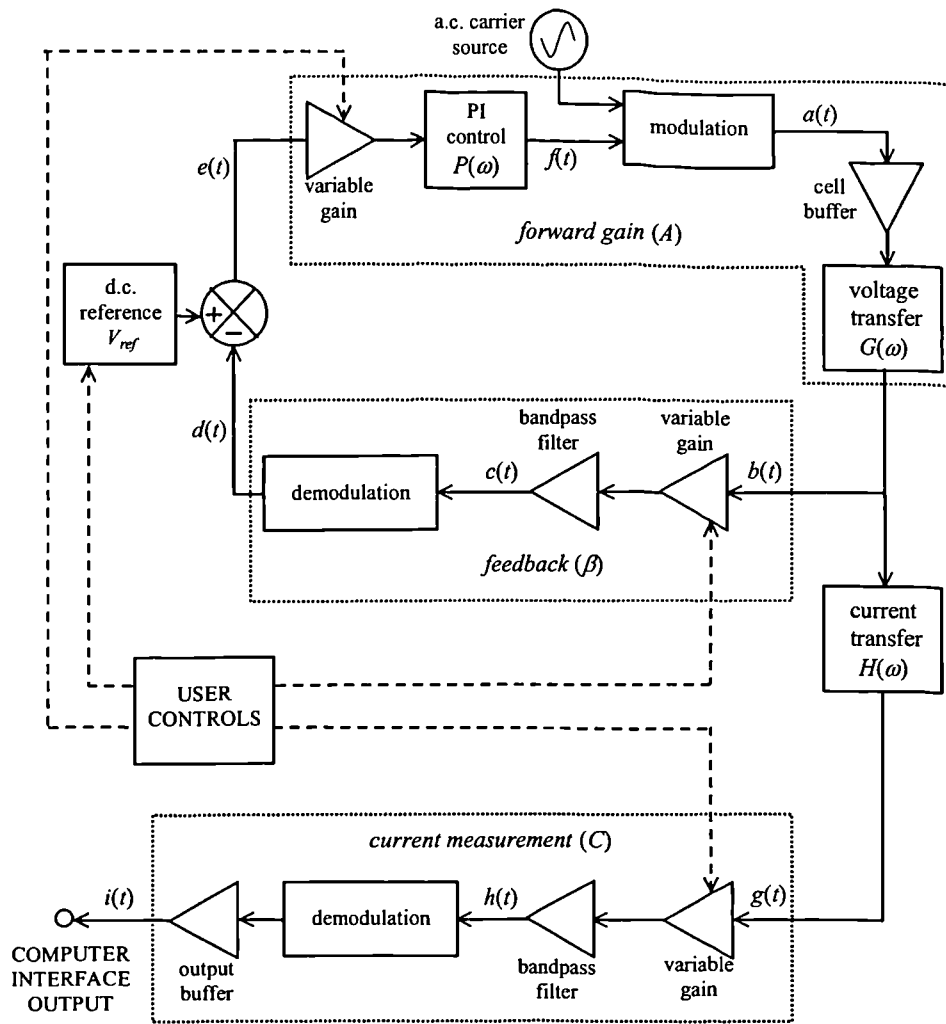


Figure 6.7: Structure of a single measurement channel.

dynamic response.

Between the forward gain  $A$  and the feedback gain  $\beta$ , the *current measurement* will take place. The current through the cell is collected and measured using a transimpedance amplifier. The output signal  $g(t)$  is related to the waveform across the cell  $b(t)$ , by the transfer function  $H(\omega)$ . There follows a gain stage and a set of interference filters, resulting in the signal  $h(t)$ . Finally,  $h(t)$  is demodulated, to produce the output signal  $i(t)$ . The signal  $i(t)$  ranges from between 0V to 10V. The overall ‘transimpedance gain’ is denoted by the symbol  $C$ .

Assuming that all the current passing through the cell is measured, the transfer function  $H(\omega)$  is equal to the resistance ratio  $R_f/R_{cell}$ . The output  $i(t)$  is then related to feedback signal  $d(t)$  by:

$$i(t) = \frac{10}{V_{ref}} \cdot \frac{G_{cell}}{G_{FS}} d(t) \quad [6.12]$$

The system illustrated in figure 6.5 contains at least three non-linear elements: the transfer function  $G(\omega)$ , and the amplitude demodulators within the feedback loop and the current measurement stages. Therefore, a numerical simulation must be used, to assess the system performance.

### 6.3.2 Operating frequency and operating current

In order to achieve good performance, the carrier frequency ( $\omega_c$ ) and the operating current ( $I_{cell}$ ) must be carefully chosen. Each of these choices is a compromise between conflicting factors.

The operating frequency ( $\omega_c$ ) should be greater than about 10kHz, to prevent ‘double-layer’ capacitances forming at the cell electrodes. However, the frequency should be less than 1MHz to ensure a negligible cell capacitance (section 6.2), and should also be less than 100kHz to prevent the system components being degraded by *gain roll-off* and *stray capacitance*. For best performance, the system should thus operate at the intermediate frequency:

$$\omega_c \sim 30kHz \quad [6.13]$$

As this frequency is relatively high for an analog system, it complicates the design as discussed in section 6.4 below.

The cell current  $I_{cell}$  should be as large as possible, to minimise the effect of external interference upon the measurement. However, it is both difficult and unsafe to supply an excessive current to the electrodes. A good compromise is reached by using a standard operation amplifier, which can supply a 20mA current. Since both the cell ( $R_{cell}$ ) and the leakage resistance  $R_{leak}$  must be driven, and since  $R_{leak}$  is comparable to  $R_{cell}$  (section 5.4) the cell current should therefore be of the order:

$$I_{cell} \sim 10mA \quad [6.14]$$

In order to maintain a full-scale current of 10mA on each operating range, it is necessary to vary the cell voltage. This is done by adjusting the reference voltage  $V_{ref}$  and gains  $A$  and  $\beta$ , as shown in table 6.1.

### 6.3.3 Transfer functions $G(\omega)$ and $H(\omega)$

The system performance is critically dependent upon the voltage transfer function,  $G(\omega)$ , and the 'current transfer function,  $H(\omega)$ , that are illustrated in figure 6.3. These transfer functions will now be defined by analysing the *impedance network* in greater detail. The minimum and the maximum states for  $G(\omega)$  will be used in order to simulate the system performance, in section 6.3.6 which follows.

A total of eight different types of impedance are illustrated in figure 6.4, including the cell impedance  $R_{cell}$ . Approximate estimates for each of these impedances are obtained as follows:

- The driving amplifier impedance ( $Z_D$ ) is a function of the internal amplifier impedance  $Z_D'$  and the amplifier open-loop gain  $A_v(\omega)$ , and is defined by the formula:

$$Z_D = \frac{Z_D'}{(1 + A_v(\omega))} \quad [6.15]$$

$Z_D'$  is of typically the order of  $10\Omega$  and  $A_v(\omega)$  is typically of the order of  $1000j$  at 30kHz (depending on the amplifier bandwidth). Therefore, the impedance  $Z_D$  is approximately  $0.01j\Omega$ .

- The cable impedance is a function of the differential elements  $dL_w$  and  $dC_w$  shown in figure 6.4b, and the overall cable length  $l$ . At sufficiently low frequencies (below about 1MHz) it is possible to group these differential elements together, to form the impedances  $Z_{wC}$  and  $Z_{wL}$  in figure 6.4a. The net effect is that:

$$Z_{wC} = -j/\omega l C_w \quad Z_{wL} = j\omega l L_w \quad [6.16]$$

where  $C_w$  is the cable capacitance per unit length, and  $L_w$  is the inductance per unit length. For  $75\Omega$  impedance cables,  $C_w$  is of the order  $100\text{pF m}^{-1}$ , and  $L_w$  is of the order  $0.25\mu\text{H m}^{-1}$ . As a result:

$$Z_{wC} \sim 0.05j \Omega m \quad Z_{wL} \sim 50k j\Omega m^{-1} \quad [6.17]$$

per metre of cable, at 30kHz. An overall cable length ( $l$ ) of between 1 and 10 metres will be assumed in the analysis below.

- The connection impedance  $Z_{con}$  depends on the quality of the contacts between measurement cables and the cell. These contacts were illustrated in figure 5.10. Here it is estimated that:

$$Z_{con} \leq 0.1\Omega \quad [6.18]$$

Note that the voltage drop across  $Z_{con}$  is not measured, as long as the leads that carry the current are connected *outside* the leads measuring the voltage.

- The cell resistance  $R_{cell}$  is a function of the cell constant, the fluid conductivity, and the local holdup between the cell electrodes. The maximum cell resistance approaches infinity, as the holdup tends to zero. The minimum resistance is the reciprocal of the maximum cell conductance.  $(G_{cell})_{max}=2\Omega^{-1}$  for the cross-correlations sensors (section 5.3.5), so that:

$$(R_{cell})_{min} = 0.5\Omega \quad [6.19]$$

- The leakage resistance  $R_{leak}$  also depends upon the cell constant, the conductivity and the holdup. The maximum leakage resistance is infinity, as the local holdup between the cell and the guard electrodes tends to zero. The numerical simulations described in section 5.3.5 determined the minimum resistance. For the holdup sensor and the cross-correlation sensors respectively:

$$(R_{leak})_{min}^h = 5\Omega \quad (R_{leak})_{min}^{cc} = 2.5\Omega \quad [6.20]$$

Note that the leakage resistance is smallest for the cross-correlation sensors, because they have the largest cell constant (section 5.3.4).

- The instrumentation amplifier impedance ( $Z_I$ ) is estimated to be at least  $10^7\Omega$  or greater at 30kHz. Therefore, the effect of this impedance and the connecting leads upon the cell voltage measurement is expected to be negligible.
- The transimpedance amplifier impedance  $Z_T$  is a function of the amplifier open loop gain  $A_v(\omega)$  and the feedback resistance  $R_f$ , according to:

$$Z_T = \frac{R_f}{A_v(\omega) - 1} \approx -\frac{R_f \omega}{B} j \quad [6.21]$$

where  $B$  is the amplifier bandwidth. The use of a 30MHz amplifier and a  $200\Omega$

feedback resistance therefore results in  $Z_T \sim -0.2j\Omega$  at 30kHz. Note that the phase angle of this impedance will cancel out some of the cable impedance  $Z_{WL}$ .

In this thesis, the impedance of the driving amplifier  $Z_D$ , the connection resistance  $R_{cell}$ , and the instrumentation amplifier impedance  $Z_I$  will be neglected. Analysis of the network in figure 6.4 then results in the expressions:

$$G(\omega) = \frac{Z_1}{Z_D + j\omega L_w + Z_1} \cdot \frac{R_{cell}}{R_{cell} + Z_2} \quad [6.22]$$

and:

$$H(\omega) = \frac{R_f}{R_{cell}} \cdot \frac{Z_2}{j\omega L_w + Z_T} \quad [6.23]$$

in which the impedances  $Z_1$  and  $Z_2$  are defined as:

$$Z_1 = (R_{cell} + Z_2) \parallel R_{leak} \parallel j/\omega C_w \quad Z_2 = (j\omega L_w + Z_T) \parallel j/\omega C_w \quad [6.24]$$

The voltage transfer  $G(\omega)$  will vary with time, depending on the fluid passing between the cell electrodes and the surrounding pipework. For proper control of the cell voltage, the system has to compensate for any change in  $G(\omega)$  within 0.5 milliseconds (section 6.1.2). This compensation is most difficult when  $G(\omega)$  switches between its *maximum* and *minimum* states. The maximum state occurs when  $R_{cell} \rightarrow \infty$ , so that all the driving voltage appears across the cell, and:

$$G(\omega) = 1 \quad [6.25]$$

The minimum state occurs when the resistances  $R_{cell}$  and  $R_{leak}$  are small, and when the impedances  $Z_{WL}$  and  $Z_T$  are large. This represents a liquid slug passing through the cross-correlation sensors, under high fluid conductivity conditions. By substituting the appropriate values into equation [6.22]:

$$G(\omega) = \frac{2.5}{12.5 \times 10^{-7} j\omega l + (0.5 - 0.2j + 2.5 \times 10^{-7} j\omega l)(5 + 2.5 \times 10^{-7} j\omega l)} \quad [6.26]$$

$G(\omega)$  in equation [6.26] is clearly dependent on the coaxial cable length  $l$ . For any cable length in the range 1 to 10 metres:

$$|G(\omega)| \geq 0.5 \quad [6.27]$$

at the operating frequency (30kHz). In other words, at least half of the driving amplifier voltage appears across the cell. The value  $|G(\omega)|=0.5$  is used in the simulation experiments described in section 6.3.5 below.

The current transfer function  $H(\omega)$  relates the voltage across the cell  $b(t)$  to the output of the transimpedance amplifier  $g(t)$ .  $H(\omega)$  will vary, depending upon the ratio of the series impedance  $Z_{WL}+Z_T$  to the leakage impedance  $Z_{WC}$ . By substitution of the appropriate values into equation [6.24], it emerges that:

$$|j\omega L_W + Z_T| < 10^{-4} j/\omega C_W \quad [6.28]$$

Therefore, to an accuracy level of better than  $10^{-4}$ :

$$H(\omega) = \frac{R_f}{R_{cell}} \quad [6.29]$$

at 30kHz. That is to say, all the current that passes through the cell is measured, to a -80dB level of accuracy. However, increasing the operating frequency  $\omega_c$  clearly causes the current leakage (hence the measurement error) to worsen as a second-order effect.

### 6.3.4 Demodulation method

The accuracy and speed with which the signals  $c(t)$  and  $h(t)$  can be demodulated is crucial to the system performance. The demodulator must have a measurement accuracy of 0.1% and a measurement bandwidth of at least 2kHz, in order to meet the specifications presented in section 6.2.1. This represents a considerable challenge, at an operating frequency of 30kHz.

In this thesis, the ‘rectifier and filter’ circuit shown in figure 6.3 is used to perform amplitude demodulation. The principle of this circuit is described by Beams<sup>16</sup> and Wright<sup>128</sup>. The full-wave rectifier exposes the envelope signal, but leaves a ‘carrier component’ centred on the frequency  $2\omega_c$ . A lowpass filter is then used, to reject this carrier component. A major advantage of this circuit is its relatively *low cost*.

The lowpass filter in figure 6.3 must be carefully selected, to ensure that three criteria are satisfied. These are as follows:

- The frequency band around the frequency  $2f_c$  must be strongly rejected, so that there is a minimal ripple component upon the output. An attenuation of at least

-60dB at twice the carrier frequency (60kHz) is required, for 0.1% measurement accuracy.

- The gain product  $A\beta$  should be as large as possible at high frequencies, in order to obtain a wide measurement bandwidth. For a 2 kHz measurement bandwidth, the -3dB cut-off frequency of the lowpass filter should be at least 1kHz.
- The gain product  $A\beta$  should roll-off to unity before -180 degrees, otherwise the feedback will become unstable (Bissel<sup>20</sup>). Therefore the lowpass filter, which affects the gain and phase of the envelope signal, should have a *minimal phase shift*.

In practice, it is not possible to satisfy all three of these criteria simultaneously. The best compromise is to use a second order Bessel filter (this has the best phase characteristics), with a -3dB cut-off frequency:

$$f_c = 1.1\text{kHz} \quad [6.30]$$

The effect upon the gain  $A\beta$  is shown in figure 6.8a below. The filter proves -60dB rejection at 60kHz, which brings the system gain down to unity at 60kHz. However, the phase shift approaches -180 degrees as a result. A higher-order Bessel filter (which improves the measurement bandwidth) is seen to worsen this phase margin yet further. A controller must be inserted into the feedback loop, to restore the system stability.

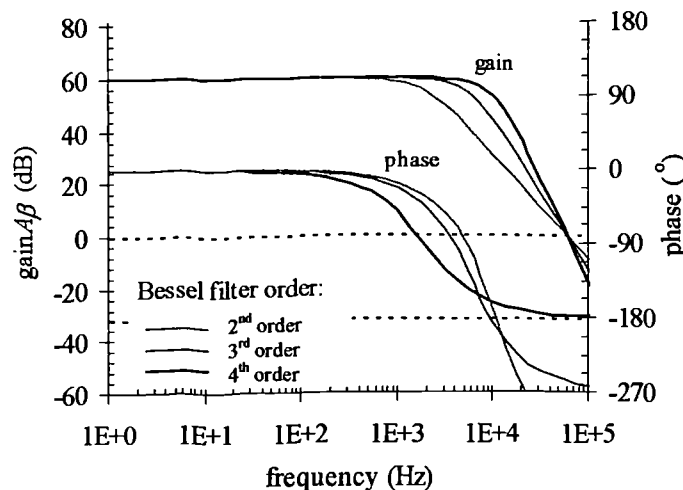


Figure 6.8: Bode plots of the system open-loop gain  $A\beta$ . The demodulator filter provides -60dB attenuation at 60kHz.

### 6.3.5 The 'PI' controller

Proportional-integral ('PI') control is introduced within the forward-gain part of the feedback loop, in order to restore the phase margin. The transfer function of this controller takes the form:

$$P(\omega) = a + \frac{p}{qj\omega + 1} \quad [6.31]$$

where  $a$  is the 'proportional' gain, and  $p$  and  $q$  are respectively the gain and the -3dB frequency of the 'integral' controller. The parameter values  $a=0.01$ ,  $p=10$  and  $q=0.2$  have been chosen to give the optimum performance. Figure 6.9 compares the open-loop gain  $A\beta$  with the controller, and without the controller. The 'phase margin' at unity gain improves from about  $+3^\circ$  to  $+30^\circ$ , indicating much improved stability. In addition, the open loop gain at d.c. frequency is increased from  $10^3$  to  $10^4$ . This means that d.c. errors defined by equation [6.8] are reduced to 0.01%.

The PI controller is implemented by using the circuit shown in figure 6.10. Since  $p \gg a$ , it is observed that:

$$P(\omega) \approx p \left( \frac{1 + (a/p)qj\omega}{1 + qj\omega} \right) = \frac{R_2}{R_1} \cdot \frac{1 + R_1 C_1 j\omega}{1 + R_2 C_2 j\omega} \quad [6.32]$$

The input impedance and the feedback impedance are thus formed, by resistors and capacitors in parallel.

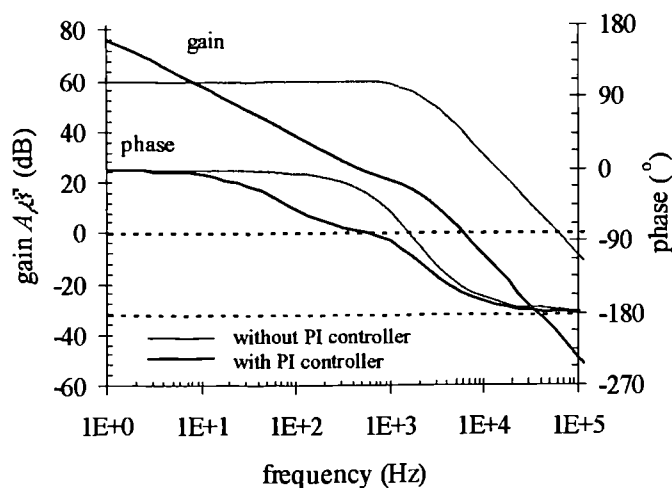


Figure 6.9: Effect of the PI controller upon the open-loop gain and phase.

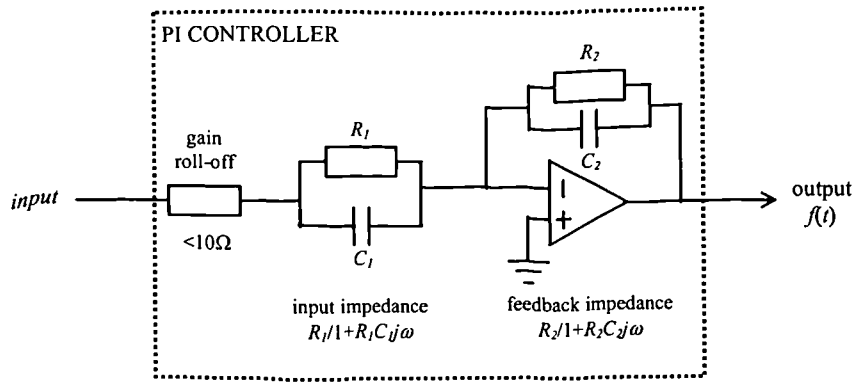


Figure 6.10: Circuit diagram of the PI controller

### 6.3.6. Performance simulation

Since the system contains a variety of non-linear components (e.g. the modulator and demodulator devices in figure 6.7), its performance must be assessed by *numerical simulation*. Therefore, a model of the system has been constructed using Simulink, and is illustrated in figure 6.11. In this simulation, the cell impedance is initially assumed to be  $2\Omega^{-1}$  and the parameters  $A$ ,  $\beta$  and  $C$  are chosen to correspond to the  $2\Omega^{-1}$  operating range.

In order to ensure that accurate results are obtained, the model in figure 6.11 includes the following features:

- The transfer function  $G(\omega)$  is switched between the states  $|G(\omega)|=1$  and  $|G(\omega)|=0.5$  every 50 carrier cycles, to simulate a sudden change in the voltage across the cell. This represents a sudden change in the liquid holdup, such as the passing of the slug front in slug flow.
- Each component is followed by a saturation function, which limits the signal within the range  $-15V < V < 15V$ . This function simulates the use of real operational amplifiers.
- A clamp function ( $V > 0V$ ) is introduced before the PI controller in the forward gain. This is found necessary, to prevent all the signals within the system entering into a saturated state. The clamp function is also necessary in the real design, which is discussed in section 6.4 below.

Figure 6.12 illustrates the simulation output, at several locations around the feedback loop and at the output port. To generate these results, the *simulation time step* is set to 0.33

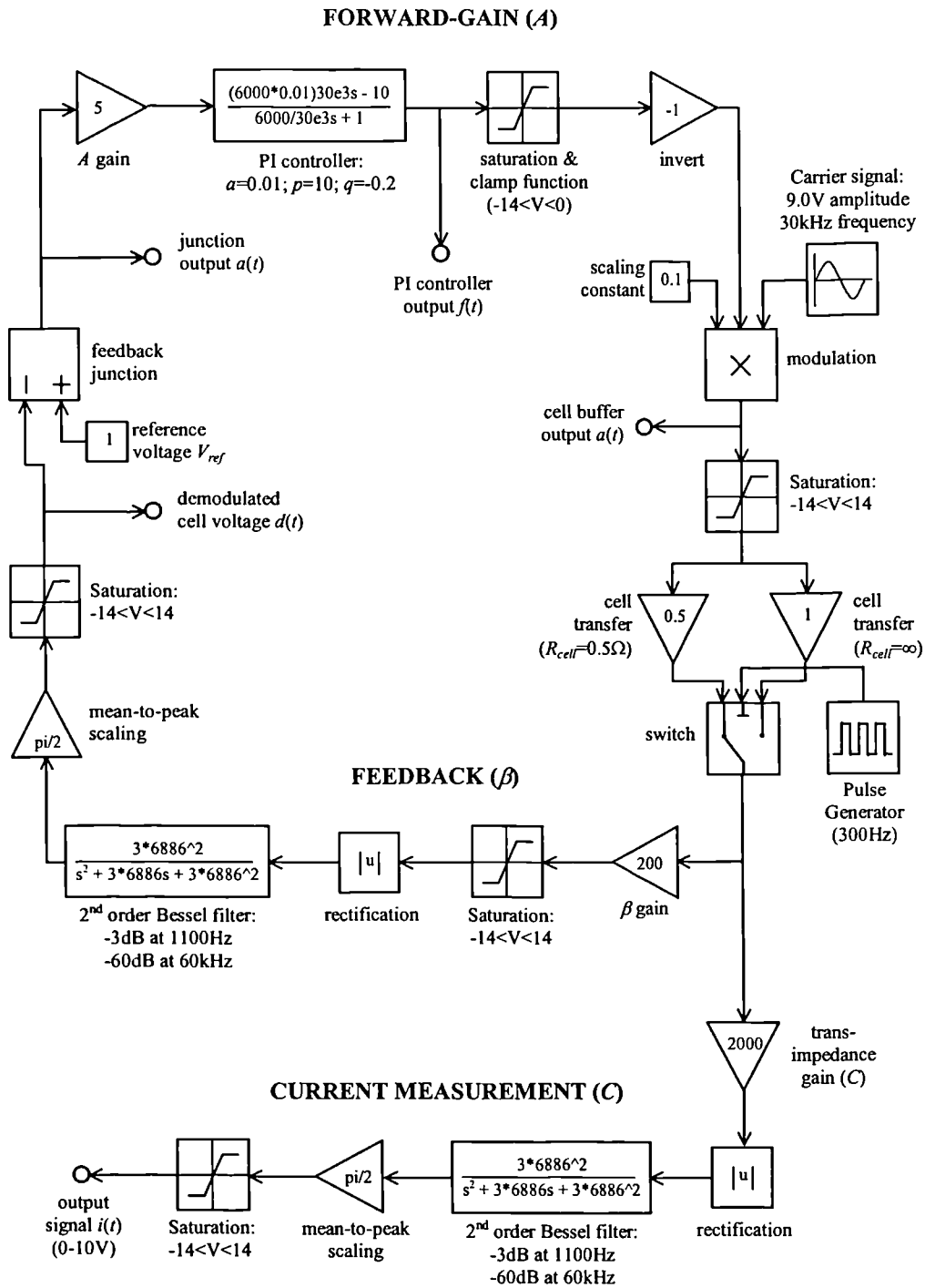


Figure 6.11: Block diagram of the Simulink model.

microseconds, i.e. a  $1/100$  fraction of the carrier waveform period. By inspecting the output signal  $i(t)$ , the following observations are made:

- After each change in  $G(\omega)$ , the output settles to a -20dB level within 0.25

milliseconds, and to a -60dB level in 0.8 milliseconds (figure 6.12f). Therefore, the measurement bandwidth is well in excess of 2kHz.

- Except for a -60dB ripple component at the carrier frequency, the output settles exactly to 10.00V. Therefore, the d.c. measurement accuracy is approximately 0.1%.

Figure 6.13 illustrates the system *stability*, by increasing the d.c. open-loop gain  $A\beta$  (i.e. reducing the gain margin) and repeating the above experiments. Figure 6.13 displays the effect upon the output signal  $i(t)$  as  $A\beta$  is increased by factors of +10dB. There is initially an improvement in the dynamic response, at the expense of vulnerability to capacitive phase shift. Increasing the gain  $A\beta$  by a +20dB factor clearly makes the output unstable.

### 6.3.7 Interference rejection

The feedback loop keeps the *demodulated* voltage  $d(t)$  constant, rather than keeping the cell voltage  $b(t)$  constant. This means that the system is vulnerable to *interference* upon the carrier signal. If the carrier signal  $b(t)$  and a distortion component  $b_d(t)$  enter the full-wave rectifier, the effect is highly non-linear; that is:

$$|b(t) + b_d(t)| \neq |b(t)| + |b_d(t)| \quad [6.33]$$

The inequality causes substantial *d.c.* and *ripple* errors in the output, which increase with the relative size of  $b_d(t)$  compared to  $b(t)$ . To prevent these errors, a bandpass filter must be introduced before demodulation. The filter bandwidth should be as narrow as possible, but should not affect the signals within the carrier band.

The design solution means that the performance is affected, even by small amounts of phase shift within the carrier band. This point is demonstrated by introducing a range of eighth-order Bessel bandpass filters (i.e., fourth-order highpass and lowpass stages) within the Simulink model. The transfer functions of these filters and the effect upon the output signal are illustrated in figure 6.14. The *dynamic response* and *stability* clearly degrade as the filter bandwidth is reduced. The bandwidth must be at least 300kHz or wider, to maintain a good performance.

Since the filter bandwidth is broad, it is very important to minimise the amount of *interference* and *noise* present upon the carrier signals. This is done by careful design of the circuit boards and selection of the electronic components and is discussed in section 6.4 below.

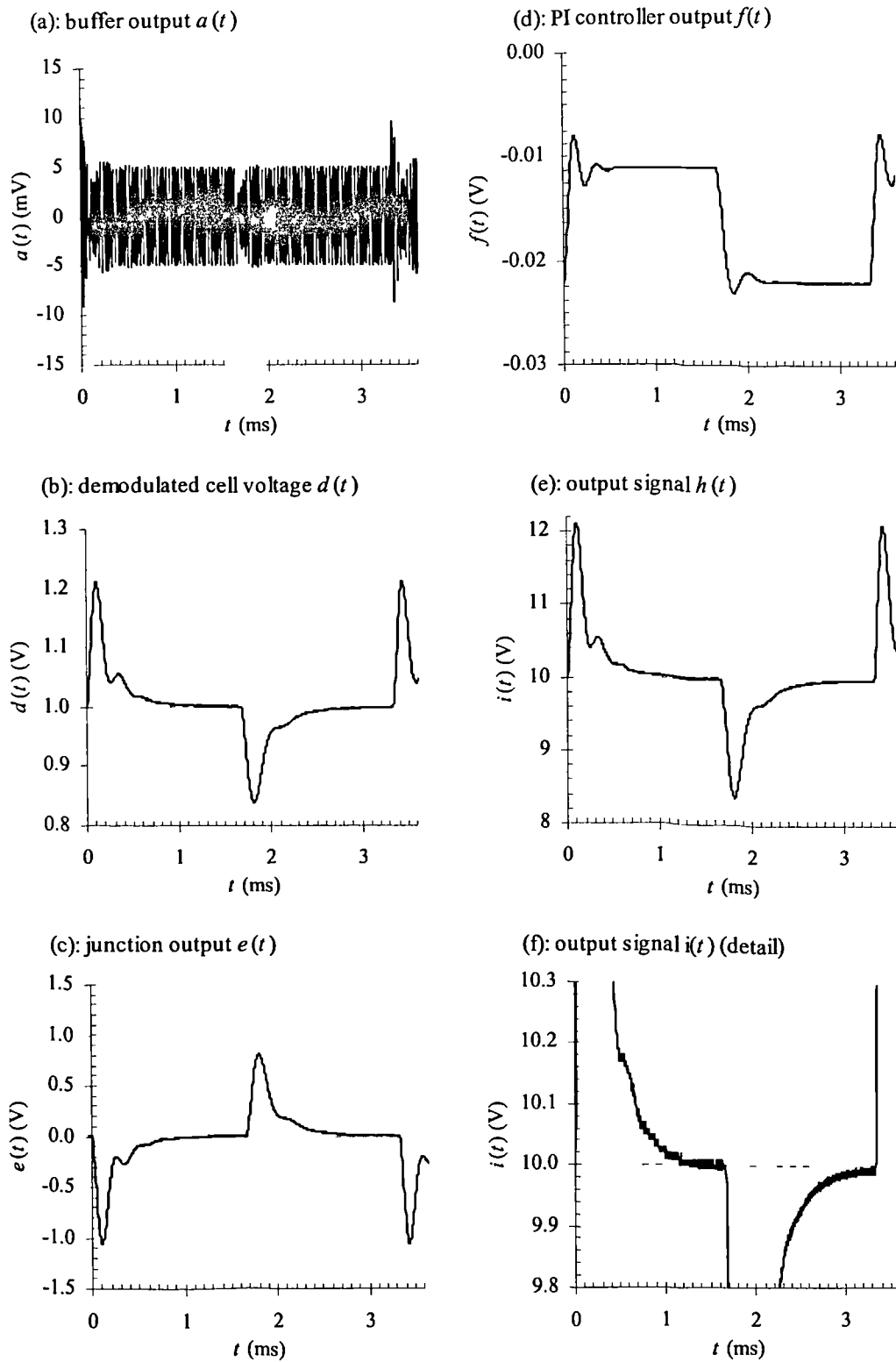


**Figure 6.12:** Simulation results. Response to a periodic step change in the transfer function  $G(\omega)$  ( $|G(\omega)|=1$  to  $|G(\omega)|=0.5$ ), at various locations within the system.

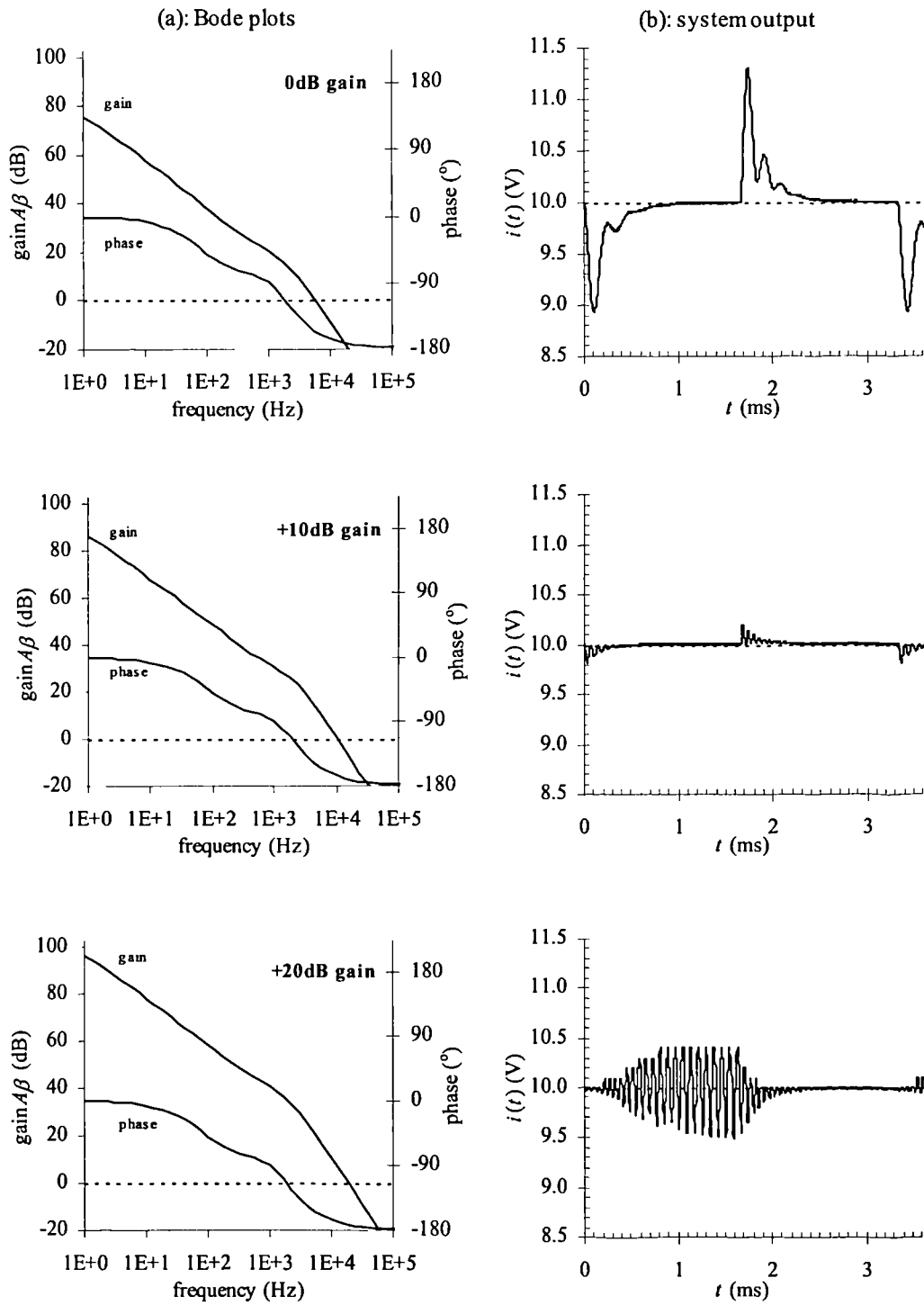


Figure 6.13: The effect of increasing the d.c. gain upon the system stability: (a) the open-loop gain  $A\beta$ ; (b) the system output  $i(t)$ .

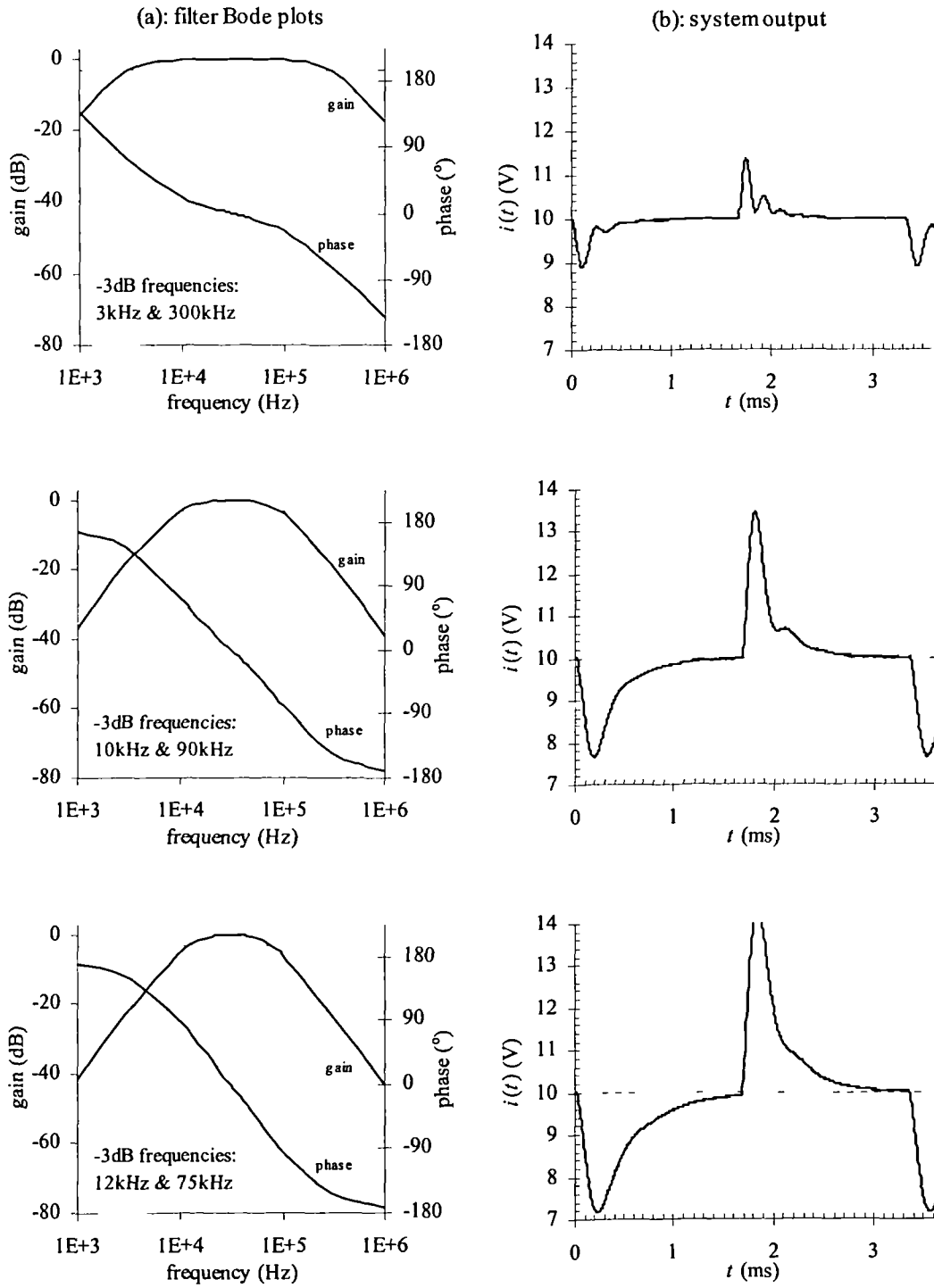


Figure 6.14: The effect of different 8<sup>th</sup> order Bessel bandpass filters upon the system performance. (a) Open-loop gain  $A\beta$ ; (b) System output  $i(t)$ .

## 6.4 Implementation

The measurement system, which is illustrated in figures 6.2, must be implemented using real electronic components. These components do not have ideal behaviour, and will therefore degrade the performance. In this section, three specific problems will be addressed: the choice of settings for each operating range, the distortion of the system signals, and the sources of ‘d.c. errors’. The steps required to minimise the effect of interference, and the manufacture process will then be described.

Schematic diagrams for each of the four *measurement channels* and the *display module* are illustrated in appendix B of the thesis. This appendix also illustrates the PCB layout diagrams, and lists all of the electronic components that are used.

### 6.4.1 Operational settings

Each of the ten operating ranges (from  $0.002\Omega^{-1}$  to  $2\Omega^{-1}$ ) is implemented, by choosing suitable values for the *gain parameters*  $A$ ,  $\beta$  and  $C$  and the *d.c. reference voltage*  $V_{ref}$ . This can be seen from the equations:

$$G_{FS} = I_{FS}/V_{cell} \quad [6.34]$$

in which:

$$I_{FS} = \frac{10.00}{C} \quad V_{cell} = \frac{A}{1 + A\beta} V_{ref} \quad [6.35]$$

Though a variety of values for  $A$ ,  $\beta$ ,  $C$  and  $V_{ref}$  can be used to satisfy equations [6.34] and [6.35], the following restrictions exist:

- The full-scale operating current should be 10mA on each range, to minimise vulnerability to external interference.
- The d.c. reference voltage  $V_{ref}$  should be at least 1V, to ensure that the carrier signals  $c(t)$  and  $h(t)$  can be accurately demodulated by the circuit shown in figure 6.3.
- The forward-loop gain signal  $f(t)$  should be at least 50mV, to ensure that the envelope signals can be accurately modulated by using the analogue multiplier described in section 6.4.2 below.

- The instrumentation amplifier must have a *gain* of at least  $\times 10$  greater, to maintain a high common-mode rejection ratio ('CMRR').

Table 6.1 lists the values that have been chosen, in order to satisfy the above criteria. Decade changes in the full-scale conductance  $G_{FS}$  are made by individually varying the parameters  $A$  and  $\beta$  by factors of 10, with the product  $A\beta$  kept constant at 10000. The reference voltage  $V_{ref}$  is reserved, for the *fine control* of  $G_{FS}$  within each decade. As a result, the cell voltage  $V_{cell}$  reduces as the full-scale conductance  $G_{FS}$  increases. The maximum current is 10mA, except on the four lowest operating ranges ( $0.02\Omega^{-1}$  to  $0.002\Omega^{-1}$ ) where it must be reduced to 1mA. This is because it is not possible to reduce  $\beta$  without degrading the performance of the instrumentation amplifier (see above). The susceptibility of the system to external interference is therefore increased on these ranges; this is discussed further in sub-section 6.4.4 below.

$G_{FS}$ ( $\Omega^{-1}$ )	$V_{ref}$ (V)	$A$ (d.c. value)	$\beta$ (d.c. value)	current gain $C$ ( $\Omega$ )	switch logic (figure 6.15)	control logic <i>ab cdef</i>	cell voltage (mV)
2.0	1	50	200	1k $\Omega$	1000000000	10 0001	5
0.8	2.5	50	200	1k $\Omega$	0100000000	10 0010	12.5
0.4	5	50	200	1k $\Omega$	0010000000	10 0100	25
0.2	1	500	20	1k $\Omega$	0001000000	00 0001	50
0.08	2.5	500	20	1k $\Omega$	0000100000	00 0010	125
0.04	5	500	20	1k $\Omega$	0000010000	00 0100	250
0.02	1	500	20	10k $\Omega$	0000001000	01 0001	50
0.008	2.5	500	20	10k $\Omega$	0000000100	01 0010	125
0.004	5	500	20	10k $\Omega$	0000000010	01 0100	250
0.002	10	500	20	10k $\Omega$	0000000001	01 1000	500

**Table 6.1:** Settings for the parameters  $V_{ref}$ ,  $A$ ,  $\beta$ , and  $C$ , the control logic and the cell voltage, for each operating range.

Figure 6.15 illustrates how each of the operating ranges can be selected, by using a single 10 position switch. The reference voltage  $V_{ref}$  is produced by a voltage divider network and four 1-way analog switches, while the gains  $\beta$  and  $C$  are selected by activating  $\times 10$  gain stages with a 2-way 'on-off' analog switch. The control logic required to implement these switches (indicated by 'a' to 'f' respectively in figure 6.15) is generated by six triple-input OR gates.

#### 6.4.2 Signal distortion

To ensure good performance, the carrier signals throughout the system should be free from

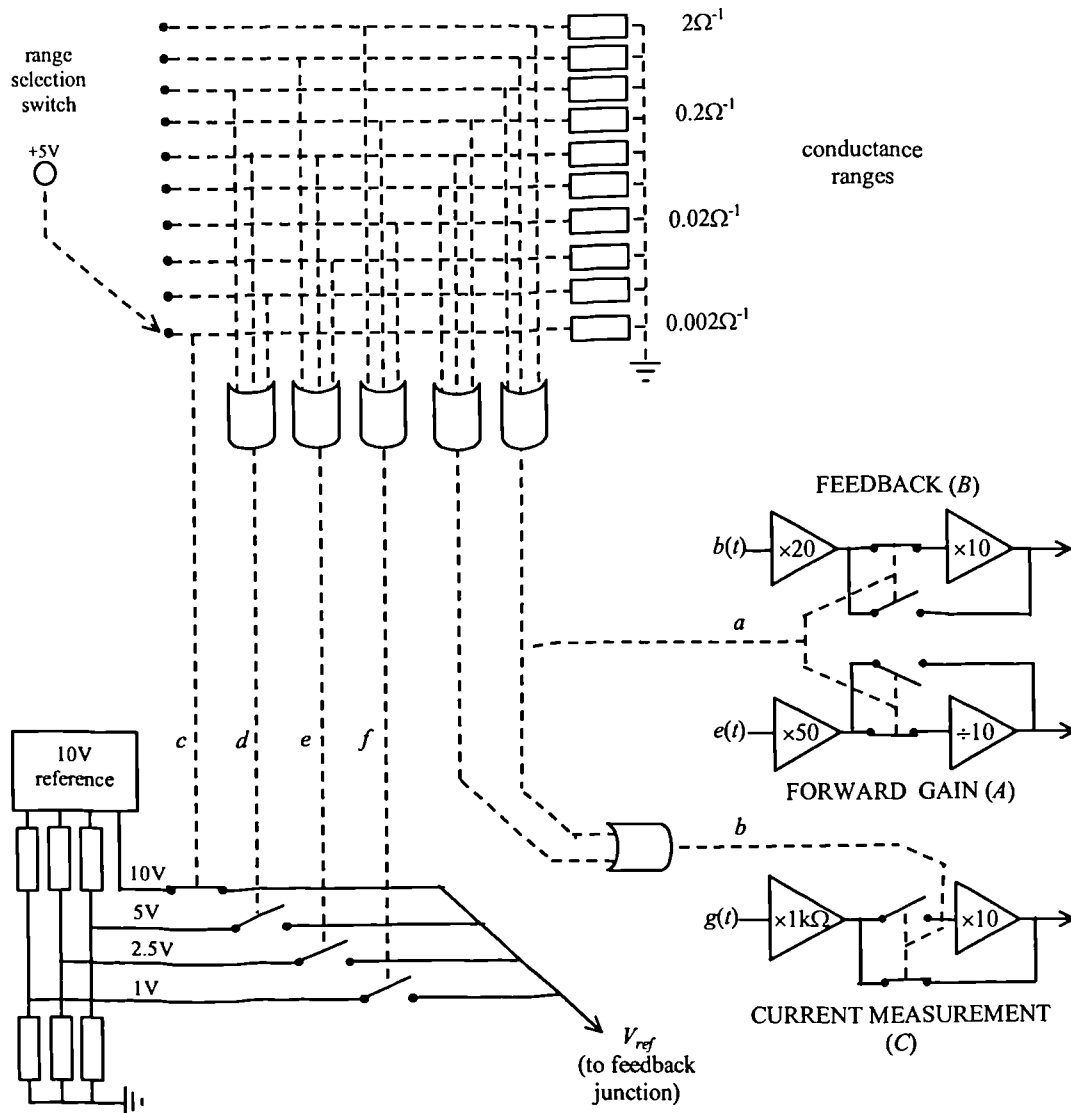
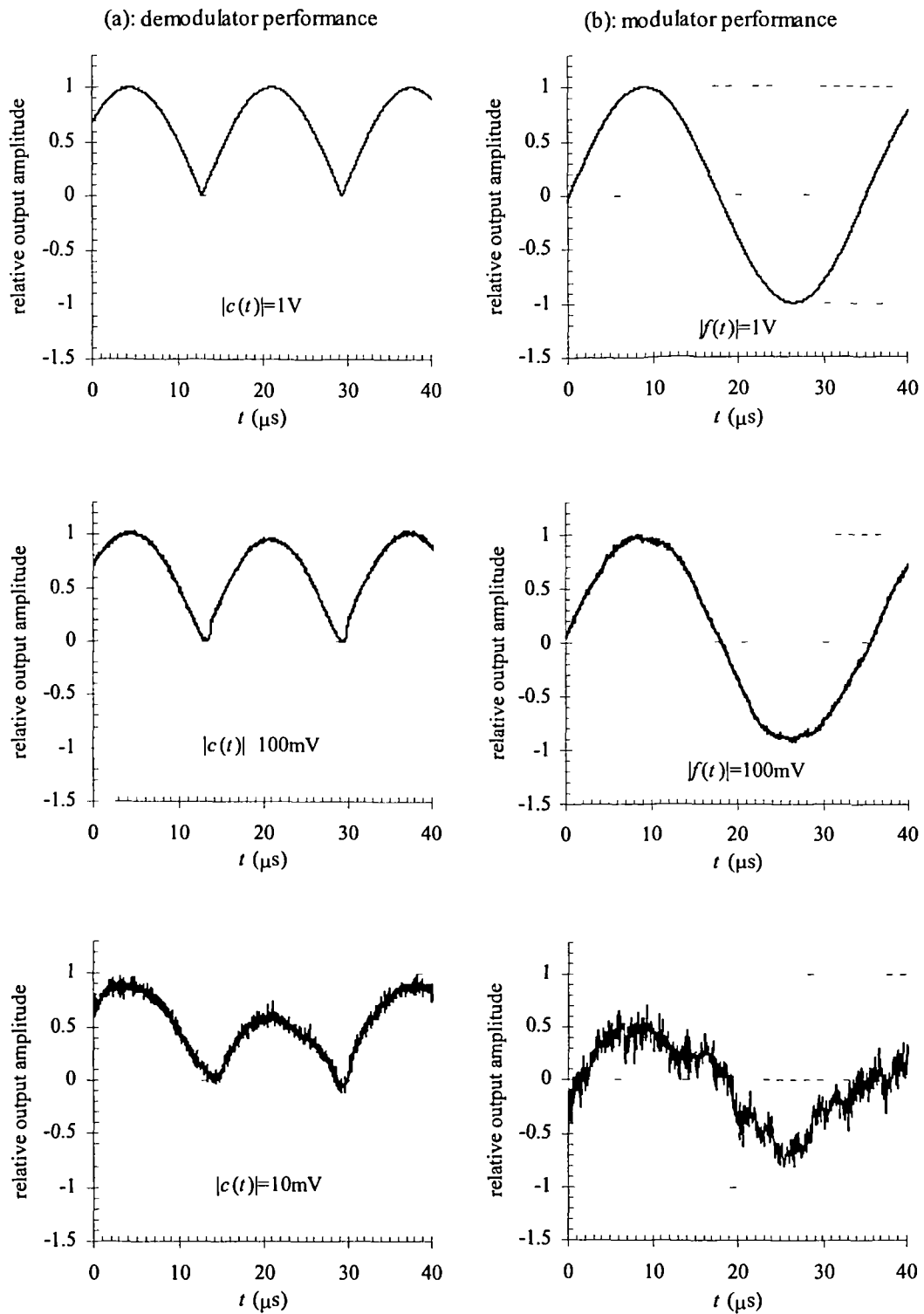


Figure 6.15: System of logic used to set the gains  $A$ ,  $\beta$ , the reference voltage  $V_{ref}$  and the transimpedance gain  $C$ , for each operating range.

distortion and noise. This is necessary, because the bandpass filter before the demodulator (described in section 6.3.6 above) needs a bandwidth of 300kHz to prevent *phase shift* from degrading the response. As a result, the following three components should be carefully chosen:

- The *analogue multiplier*, within the forward-loop gain  $A$ . This is the most non-linear component in the system, and the dominant source of noise. In this application, the AD633 multiplier (Analog Devices,  $0.9\mu\text{V}/\text{Hz}^{1/2}$ ) is used. The effect upon the output signal  $a(t)$  is shown in figure 6.16. The signal-to-noise ratio reduces and distortion clearly occurs, as the input  $f(t)$  becomes small.



**Figure 6.16:** Ideal and actual performance, for (a) the system demodulator; (b) the system modulator. The input signals are progressively reduced in amplitude.

- The *buffer amplifier* that drives the cell. This is a source of crossover distortion (each time the output crosses 0V), and can easily become overloaded if the input waveform  $a(t)$  is small and offset from 0V. To minimise these problems, the OPA604 (Burr-Brown) amplifier is used. This amplifier has fast JFET-type output transistors that prevent glitches during crossover, and a reasonably small offset voltage of 1mV.
- The amplifiers used to form the *full-wave rectifier* (see figure 6.3). This circuit is becomes ineffective if the input waveform becomes small, due to the 0.6V voltage drop across the rectifier diodes and the amplifier offsets. To minimise these errors, each amplifier should have a large gain-bandwidth product *and* a small offset voltage (usually in conflict). In this application, the dual LT1361 (Linear Technology) amplifier (60MHz GBW product; 0.5mV offset voltage) is used as a compromise. The effect upon the output signal  $d(t)$  is summarised, by figure 6.16b.

To avoid a serious loss of performance due to the above effects, three further steps should be taken. The signal  $f(t)$  should be kept greater than 50mV, by introducing a  $\times 0.1$  attenuation stage within the forward-gain (see figure 6.15). In addition, the cell voltage ( $V_{cell}$ ) should be kept large (this is not always possible) and the d.c. reference voltage ( $V_{ref}$ ) should be at least 1V.

#### 6.4.3 D.C. performance errors

At a number of places throughout the system, the circuit components will introduce 'd.c.'-type errors. These errors accumulate, and (depending on the particular operating range) cause fixed *relative* and *absolute* errors in the output signal  $i(t)$ . Though there are many sources, the most significant are as follows:

- *Demodulator nonlinearity*, which affects the signals  $d(t)$  and  $i(t)$  when  $c(t)$  and  $h(t)$  are small (see section 6.4.2). To quantify the error effect, the ratio of the d.c. output signal to the a.c. input into the demodulator has been measured, and the results are illustrated in figure 6.17. In this system, the absolute error in the output voltage is about 1mV regardless of the input amplitude. This causes a relative error of up to 0.1% in the feedback loop (when  $V_{ref}=1V$ ), and an absolute error of 0.01% within the transimpedance stage.
- *Voltage offsets* immediately prior to the feedback junction (figure B3). The reference voltage  $V_{ref}$  and the demodulated cell voltage waveform  $d(t)$  are subject

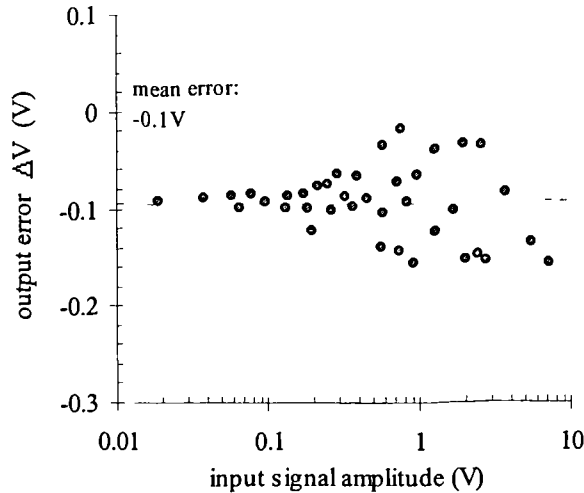


**Figure 6.17:** D.C. error in the demodulator output, as a function of the input signal amplitude.

to voltage offsets ( $V_-$  and  $V_+$  respectively), which cause fixed a relative error defined by:

$$\Delta G/G_{cell} = (V_+ - V_-)/V_{ref} \quad [6.36]$$

The negative offset  $V_-$  depends upon the resistor tolerances within the voltage divider circuit (shown in figure 6.15): 0.1% tolerance resistors cause a maximum 0.2% error, when  $V_{ref}=1V$ . The positive offset  $V_+$  depends upon the amplifiers in the full-wave rectifier: two LT1361's produce a maximum offset of  $\pm 1.5mV$ , or a 0.15% error when  $V_{ref}=1V$ . Note that offsets prior to the rectifier are removed, with the capacitor C20 illustrated in figure B2.

- The  $\times 10$  *gain circuit* that is illustrated in figure 6.18. The source and drain capacitances ( $C_s$  and  $C_d$ ), the cross-switch capacitance  $C_{ds}$  and the finite 'on' resistance  $R_{on}$  mean that the real circuit resembles figure 6.18b. To minimise the error effect, the resistance  $R$  is as small as possible ( $1k\Omega$ ), and the DG303 analogue switch is used ( $C_s=C_d\sim 15pF$ ,  $C_{ds}\sim 40pF$  and  $R_{on}=50\Omega$ ). The resulting gains at 30kHz are  $\times 1.000$  and  $\times 9.995$  respectively, causing a small (0.05%) error effect. However, a further error of up to 0.2% is also caused, if 0.1% tolerance resistors are used for  $9R$  and  $R$ .
- *Cumulative errors* due to the finite amplifier common-mode rejection ratio (CMRR) and the finite resistor tolerances within each gain stage (see figures B2 to B6). The net error effect is substantial, but as this error is identical for each range it

can be calibrated out. As these errors are identical for each operating range, they can be calibrated out. A *trimming resistor* is included in the final gain stage (component R56 in figure B4), which is chosen by the user to ensure that the full-scale output is 10.00V.

Table 6.2 summarises the error contribution that is made by each of the above effects, for each of the ten system operating ranges ( $G_{FS}=0.002\Omega^{-1}$  to  $2\Omega^{-1}$ ). As shown, the error components reduce as the conductance  $G_{FS}$  increases, and (by comparison with table 6.1) as the reference voltage  $V_{ref}$  reduces. The cumulative error effect is substantial (approaching 1%) if each error source is assumed to be absolute. However, it is more reasonable to assume that the error contributions are statistical in nature, in which case the error is usually less than 0.4%.

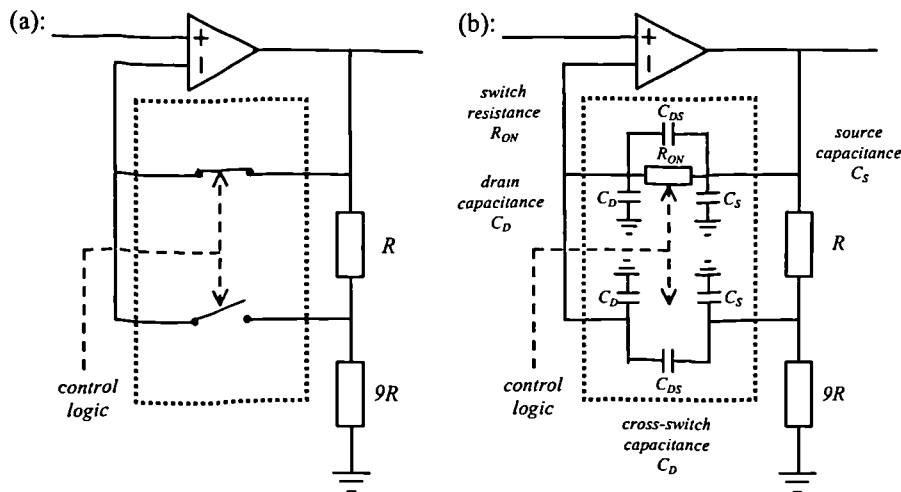


Figure 6.18: Effect of the analogue switch properties upon a  $\times 10$  gain stage: (a) ideal circuit; (b) actual circuit.

$G_{FS} (\Omega^{-1})$ :	2	0.8	0.4	0.2	0.08	0.04	0.02	0.008	0.004	0.002
error type: demodulator	0.10	0.04	0.02	0.10	0.04	0.02	0.10	0.04	0.02	0.01
$V_+$ junction	0.15	0.06	0.03	0.15	0.06	0.03	0.15	0.06	0.03	0.01
$V_-$ junction	0.20	0.08	0.04	0.20	0.08	0.04	0.20	0.08	0.04	0.02
$\times 10$ gain circuit ( $A$ )	0.25	0.25	0.25	0.00	0.00	0.00	0.00	0.00	0.00	0.00
$\times 10$ gain circuit ( $\beta$ )	0.25	0.25	0.25	0.25	0.25	0.00	0.00	0.00	0.00	0.00
Maximum total error (%)	0.95	0.68	0.59	0.70	0.43	0.34	0.45	0.18	0.09	0.04
Total statistical error (%)	0.44	0.37	0.36	0.37	0.27	0.05	0.27	0.11	0.05	0.02

Table 6.2: Cumulative effect of each d.c. error source upon the relative error  $\Delta G/G$ , for each operating range.

#### 6.4.4 Electromagnetic compatibility

In order to guarantee good performance, it is necessary to protect the system from the effects of external and internal interference. This is achieved by using shielding, or by careful selection of the circuit components and the circuit layout. A comprehensive review of prevention techniques is presented by Horowitz & Hill<sup>52</sup>. The three main sources of interference affecting this system, and suitable preventative action, are summarised as follows:

- *Capacitive coupling*, which causes unwanted feedback and current leakage paths around the circuit. To minimise the internal coupling, all resistors have low values (typically  $<10\text{k}\Omega$ ) wherever the carrier signal is being processed. To minimise the external coupling, a grounded screen surrounds the circuit boards and the measurement cables. The coupling to the cell itself (which increases with the physical cell size and the cell resistance) cannot be eliminated in this way, but is expected to be insignificant due to the 300kHz bandpass filters before the demodulators.
- Currents flowing in the *ground tracks*, which cause significant errors in the measurement of small signals at 30kHz frequency. The ground track between the output buffer and transimpedance amplifier (figure 6.19a) is most vulnerable to this effect. If  $R_G$  is the track resistance between these points, an unwanted current  $I_G$  results in a measurement error of the order:

$$\frac{\Delta G}{G_{FS}} \sim \frac{I_G R_G}{V_{cell}} \quad [6.37]$$

To minimise this effect, both  $R_G$  and  $I_G$  should be small. Short, thick copper pour tracks around the input circuitry reduce the track resistance  $R_G$  to  $\sim 1\text{m}\Omega$ . Large system currents are prevented from flowing through  $R_G$ , by laying out *local ground network* away from the general system ground. In addition, the coaxial shield of the measurement cables, and guard electrodes between the sensors, are connected to the caseframe at a single point.

*Electromagnetic induction*, which induces unwanted voltages depending upon the magnetic flux and the loop area. The loop containing the measurement cables and the cell is the largest loop in the system, and is most vulnerable to this effect (figure 6.19b). The flux linkage is minimised by having compact circuit boards, electromagnetic screening, and twisting the cable pairs that connect to the cell. However, the flux caused by the current within the cell itself cannot be eliminated

in this way. A voltage is thus induced between the cell electrodes which is of the order:

$$V_i = \int \frac{d\Phi}{dt} \cdot dS \sim \frac{\mu_0 D_e}{4\pi} \omega_c I_{cell} \quad [6.38]$$

where  $\Phi$  is magnetic flux,  $\mu_0$  is the permeability of the water phase, and  $D_e$  is the electrode separation. The error effect caused by the voltage  $V_i$  increases with the cell size and the operating current, and as the cell voltage  $V_{cell}$  reduces. For the holdup sensor,  $V_i$  is of the order  $50\mu\text{V}$ , while for the cross-correlation sensors,  $V_i$  is of the order  $5\mu\text{V}$ . In both these cases, the maximum error effect is of the order of 0.1%.

Depending upon the surrounding environment, the system is affected by a combination of all of the effects described above. To quantify the amount of interference that is present, the system includes a switch to route the signal  $b(t)$  to the local output port ('test point' in figure B2). This port can be connected to an oscilloscope, from which the interference component  $b_d(t)$  can be viewed upon the carrier. To improve the viewing of small signals, the system also includes a 'break switch' (figure B1b) which breaks the feedback loop and routes the cell buffer input  $a(t)$  to ground. In this way the component  $b_d(t)$  can thus be seen, even if it is very small compared to the carrier.

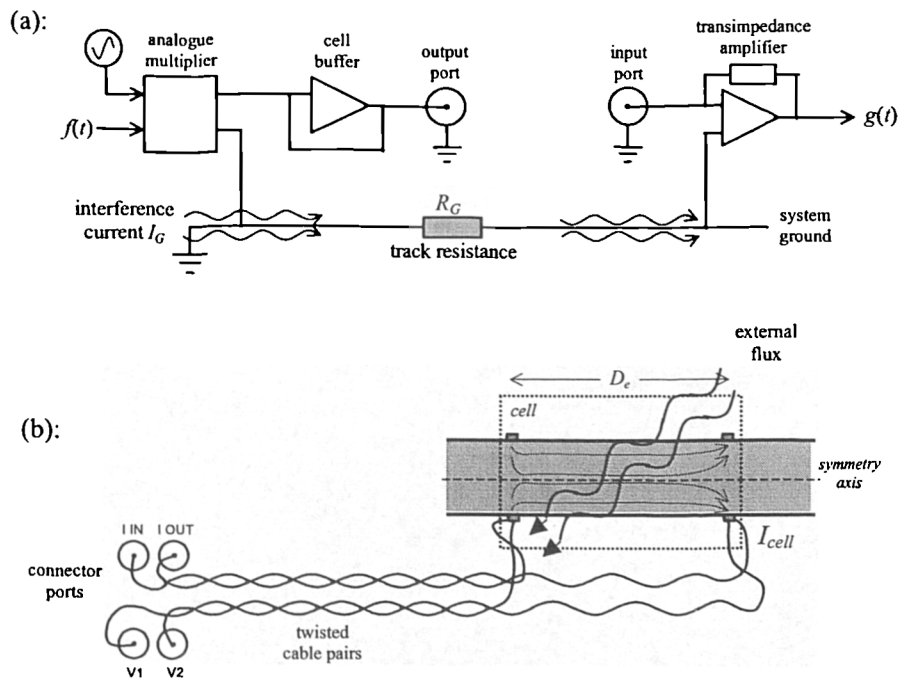


**Figure 6.19:** Sources of external interference: (a) ground currents between the output and input stages; (b) magnetic flux acting upon the cell.

### 6.4.5 Manufacture

The *manufacture* requires the specification of the instrument enclosure, the power supplies, the front panel ('user') interface, and the PCB layout. These aspects are now briefly described.

The instrument enclosure should be compact, ergonomic, and offer easy access to the measurement boards. A 'Diplomat'-type caseframe (VERO electronics) is used, with outer dimensions 320×160×320mm, and a panel area of 300×160mm. The case contains a KM 6-II rack system, which holds circuit boards that are based upon the Eurocard 3U format (approx 100mm×300mm board area). The circuit boards can connect to each other and to the power supply through a backplane, and can be easily accessed for testing and repair.

A special short-circuit-proof, power supply unit was built and installed at the rear of the caseframe. This supply delivers a total current of 0.5A (at ±15V) and 100mA (at +5V). The total power consumption for each measurement channel was measured to be 80mA (at ±15V) and 10mA (at +5V), and 50mA (±15V), 50mA (+5V) for the display module.

Figure 6.20 illustrates the caseframe and the user interface, which is divided into five panel areas. Four of these panels hold the measurement ports and the range selection switch for each channel, while the fifth (leftmost) panel houses the digital display and associated functions. This layout corresponds to the schematic diagram that was presented in section 6.1 above.

Figures 6.21a and 6.21b illustrate the electronic circuit boards. The track lengths are kept short (particularly around the measurement ports), resistor values are generally kept below 10kΩ, and the ground network has been carefully arranged, to prevent large currents affecting the measurement. The measurement boards contain a large number of components in a small area, so that the layout requires careful consideration. The PCB is divided into 'Control logic and  $V_{ref}$ ', 'current measurement', and 'feedback loop' zones, located towards the front, middle, and rear of the board respectively, and 'dual' and 'quad' operational amplifiers are used whenever possible, to optimise space.

Table B3 (appendix B) presents a list of all the materials required in the manufacture process, the manufactures of components, and the approximate costs (at the time of writing). The total manufacture cost was around £1500, split roughly equally between the PCB manufacture, the electronic components, and the materials used for the caseframe, the power supplies and the user interface.

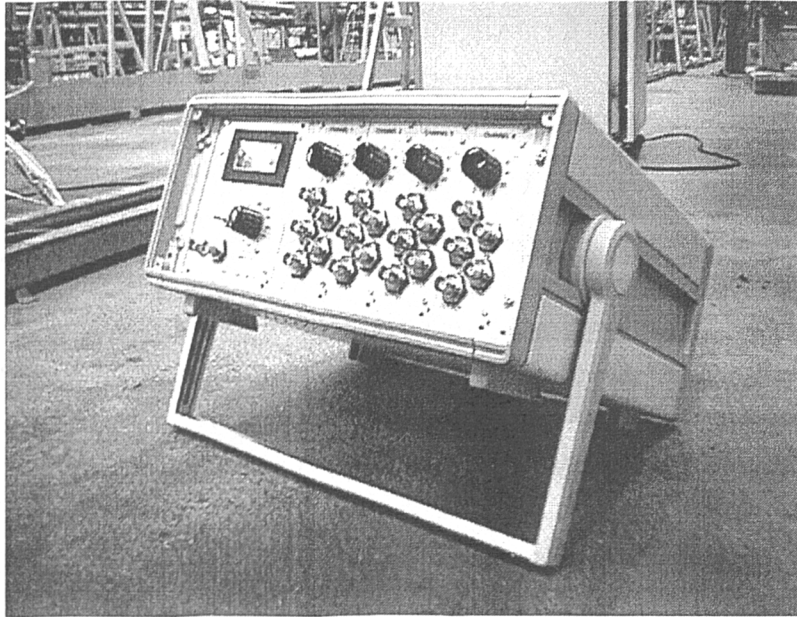


**Figure 6.20:** Photograph of the user interface.

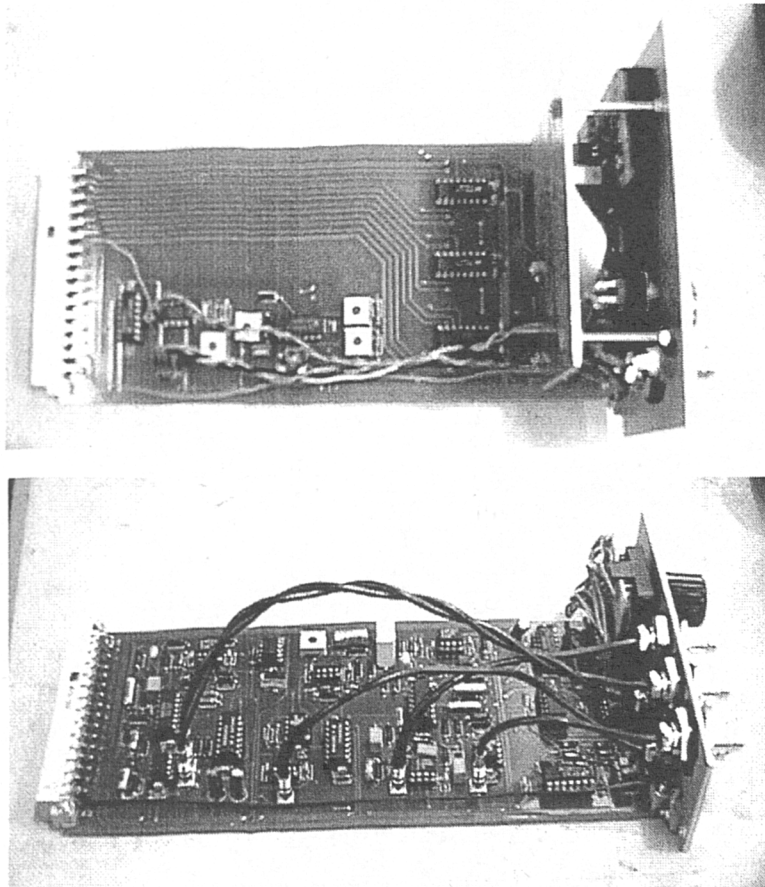


**Figure 6.21:** Photographs of the PCB boards: (a) the display module; (b) a single measurement channel.

## 6.5 Performance assessment

The finished instrument is subjected to a series of benchtests, in order to compare its performance against the specifications made in section 6.1. Four different types of tests were conducted, as follows:

- To test the *d.c. measurement accuracy*, a series of resistors in the range  $0.5\Omega$  to  $100\text{k}\Omega$  (measured to 0.01% accuracy with a Datron10701A voltmeter) were substituted for the cell, and the output conductance was measured. The full-scale error in the output ( $\Delta G/G_{FS}$ ) is illustrated in figure 6.22 for a typical measurement channel, as a function of the conductance ratio  $G/G_{FS}$ . The error  $\Delta G/G_{FS}$  is around 0.2% near full-scale, but reduces in proportion to the conductance ratio  $G/G_{FS}$ . A residual error of about 0.02% remains at very small values of  $G/G_{FS}$ , which is due due to demodulator non-linearity.
- To test the *measurement bandwidth*, the carrier waveform was modulated between full and half amplitude at regular intervals, using a network of voltage dividers and an analogue switch. This action is equivalent to switching the transfer function  $G(\omega)$  between the states  $|G(\omega)|=1$  and  $|G(\omega)|=0.5$ , within the Simulink model. The response is captured at several circuit locations using a digitising oscilloscope. As shown in figure 6.23, the agreement between this experiment and the numerical simulation (figure 6.12) is excellent.
- To test *channel crosstalk*, a range of resistor values (including an open circuit, i.e.  $R=0\Omega$ ) were connected to each system channel, while the output on other three channels was recorded. During these experiments, no change to the actual conductance could be observed.
- To test *temperature stability*, the air temperature inside the instrument case was heated to  $60^\circ\text{C}$ , and then the d.c. tests described above were repeated. As a result of the change, a temperature coefficient of approximately 0.05% per 10K was observed.

The measurement accuracy and bandwidth of the instrument comply with the specification made in section 6.1, and negligible errors are caused by channel crosstalk and temperature fluctuations. An accurate measurement of the cell conductance is therefore guaranteed, over all of the measurement range.

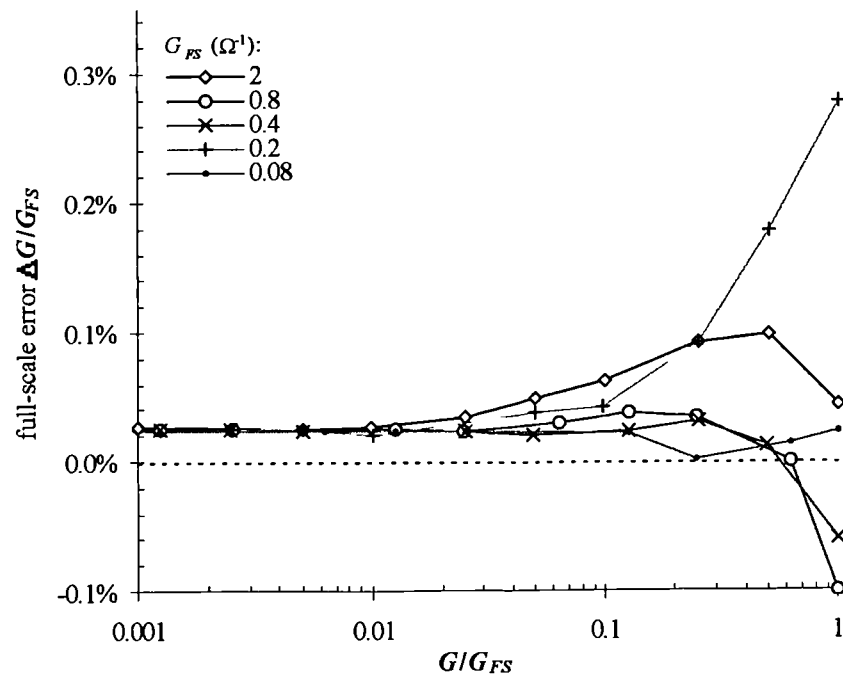
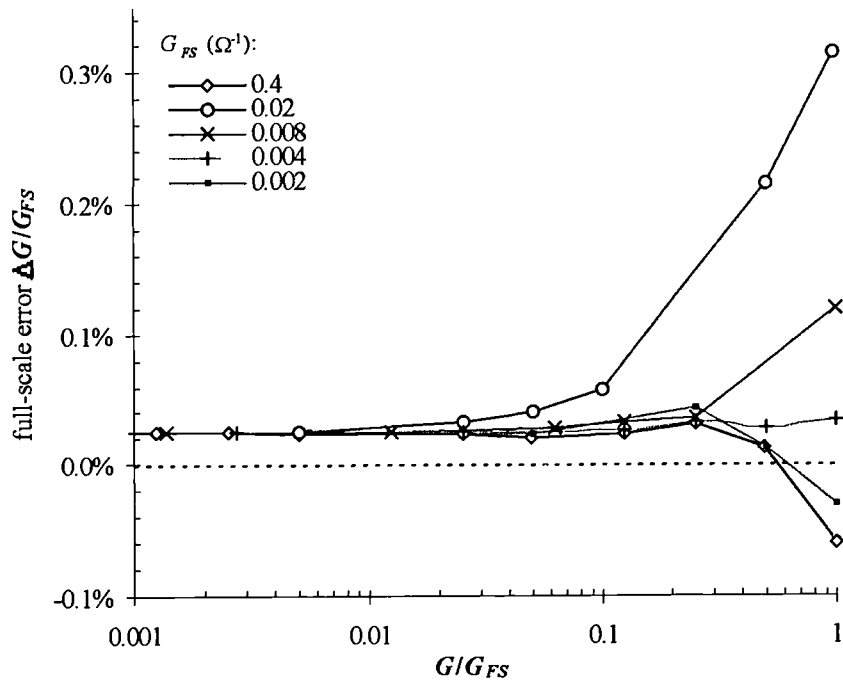
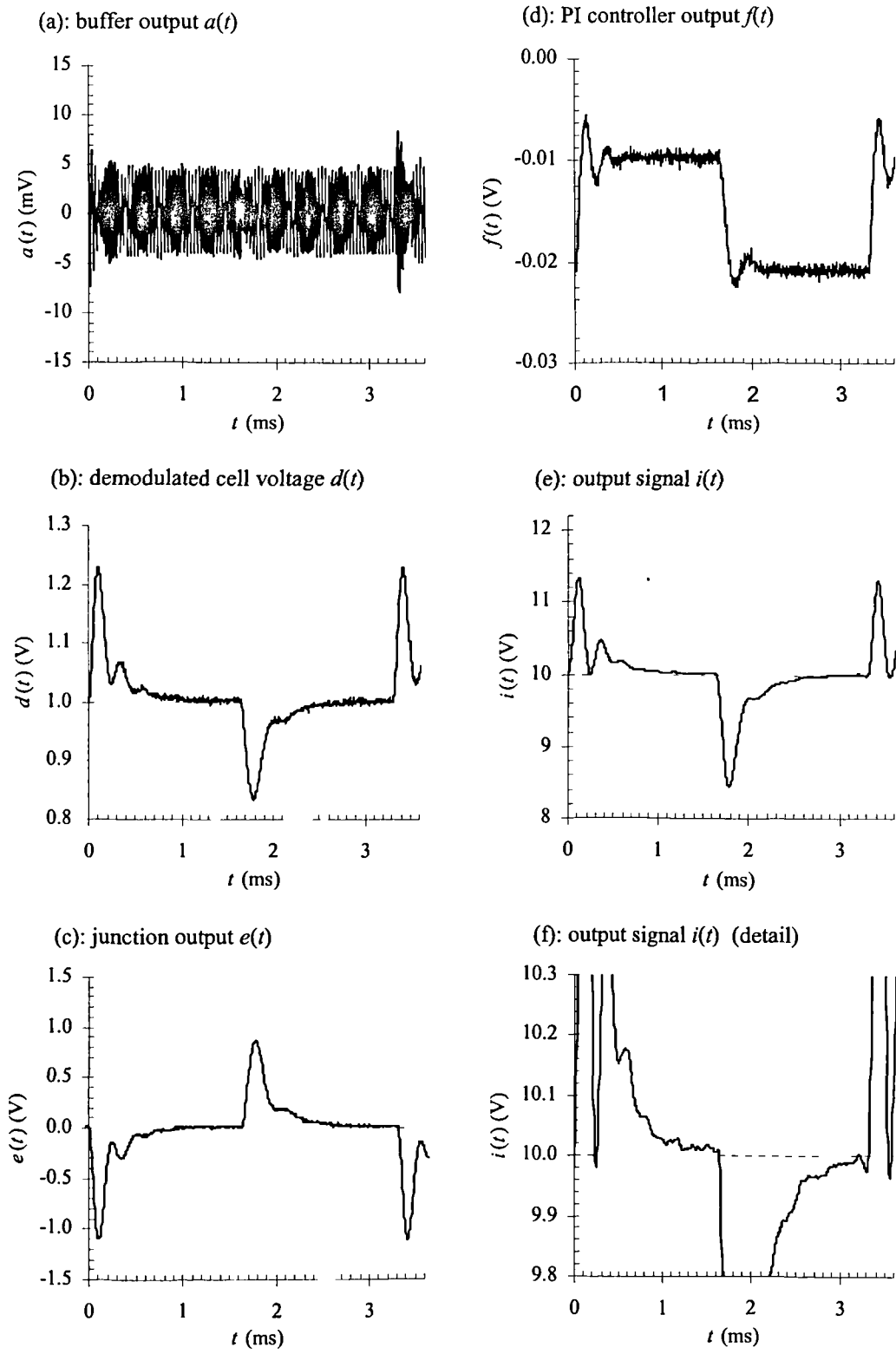


Figure 6.22: Typical performance of a system channel. (a)  $2\Omega^{-1}$  to  $0.08\Omega^{-1}$  operating ranges; (b)  $0.04\Omega^{-1}$  to  $0.002\Omega^{-1}$  ranges.



**Figure 6.23:** Experimental results. The response to a periodic step change in the transfer function  $G(\omega)$  ( $|G(\omega)|=1$  to  $|G(\omega)|=0.5$ ), at various locations within the system. Note the level of agreement with figure 6.12.

## 6.6 Summary

This chapter described the development of electronic instrumentation, for measuring the conductance between the electrode pairs described in Chapter 5. The design specification, design solution and the implementation processes were presented, in sections 6.1 to 6.4 respectively:

- Section 6.1 described the instrumentation specifications. A four-channel a.c. conductance measurement, with 0.2% full-scale accuracy and a 1kHz bandwidth, was required over the conductance range  $G_{FS}=0.002\Omega^{-1}$  to  $2\Omega^{-1}$ . The output from each channel was a 0 to 10V at a BNC port, for connection to the computer interface.
- Section 6.2 described the previous design solution by Coney<sup>27</sup> and its major limitations: a poor measurement accuracy for large conductances, and a poor measurement bandwidth. A novel solution, incorporating feedback voltage control, was proposed to overcome these limitations. The crosstalk between adjacent sensors was addressed, by using a system of *guard electrodes* already described in section 5.4.
- Section 6.3 expanded upon the design solution, in greater detail. The operating frequency (30kHz) and the operating current (10mA) were justified; the transfer functions  $G(\omega)$  and  $H(\omega)$  and the demodulation method were defined; and a PI controller was developed to ensure good feedback stability. This design was verified using simulation experiments, and then the effect of bandpass filters upon the performance was quantified.
- Section 6.4 described the implementation process. Because of imperfections in the electronic components, the system gains ( $A$  and  $\beta$ ) and the d.c. reference voltage ( $V_{ref}$ ) had to be carefully chosen for each operating range. In addition, the main sources of signal distortion and d.c. errors had to be identified and controlled, and a number of steps taken in order to minimise the disruption due to external interference.

Finally, section 6.5 described the assessment of the instrument performance, by a set of simple experiments. The performance was compliant with the specifications presented in section 6.1.

## 7. Analysis system

This chapter will describe the computer system used to analyse the sensor data and deliver the phase flowrates. This system consists of *acquisition hardware*, which continuously writes data to a hard disk, and *processing software*, which extracts ‘model parameters’ from these data and calculates the flowrates. A schematic diagram of these two components is shown in figure 7.1.

Section 7.1 will briefly comment upon the hardware, which consists of the measurement electronics (developed in Chapter 6), a sampling interface, a data acquisition (DAQ) card, and a standard desktop PC.

Sections 7.2 to 7.4 will then describe the key components of the processing software, which are as follows:

- Section 7.2 will describe the routines used to calculate the translation velocity ( $V_t$ ), the phase fractions ( $a_f$  and  $a_s$ ), the lengths ( $l_f$  and  $l_s$ ) and the slug frequency ( $\nu$ ) for each identified ‘slug unit’. The method for estimating the cross-correlation signal bandwidth ( $B$ ) will also be discussed.
- Section 7.3 will discuss the ‘stable slug flow’ model used to calculate the phase superficial velocities. The *closure relationships* necessary to define the local slug velocities  $V_{ls}$  and  $V_{gs}$  will be presented, and then methods for ‘averaging’ the model parameters (in order to be consistent with the stable slug flow model) will be discussed.
- Section 7.4 will describe the calculation of the *uncertainty* in the phase flowrates. Here the equations used to estimate an uncertainty in each of the model parameters will be presented, and the method by which these uncertainties are combined in order to compute an overall uncertainty will be discussed.

The software described in this thesis will perform an off-line analysis of the data, rather than delivering a continuous flowrate measurement. The computer code that performs each of the tasks described above is written in the Matlab programming language, and is listed in appendix C.

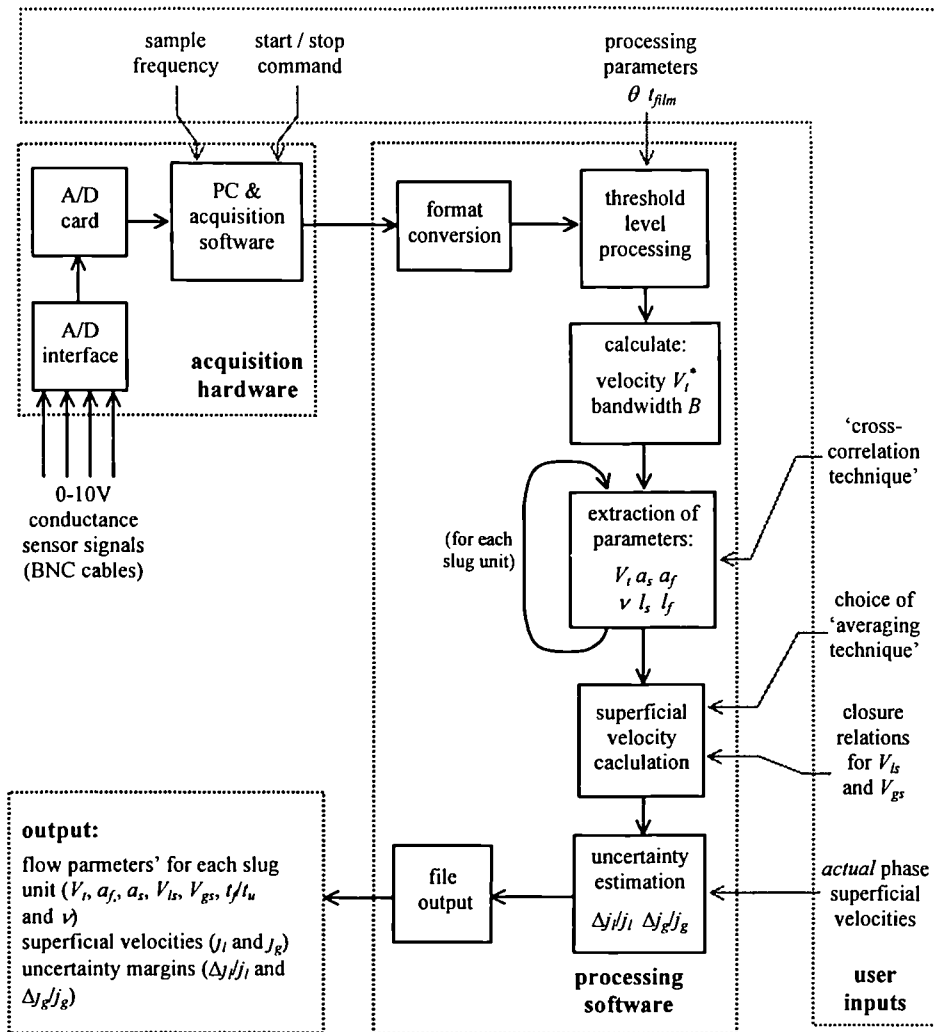


Figure 7.1: Data acquisition and processing software components (schematic diagram).

## 7.1 Hardware system

The raw data produced by the conductance sensors (described in Chapters 5 and 6) is captured and stored using the hardware system illustrated in figure 7.2. This contains the following components:

- A NI-SCB connector board (National Instruments). This board is interfaced to the output from the conductance instrumentation (chapter 6) by using BNC coaxial cables.
- A standard PC (100MHz Dell PC) with a 1GB hard disk and 32Mb RAM.

- An AT-M10 data acquisition (DAQ) card, which digitises the analogue data from each channel output. This card samples the input data to 16-bit accuracy, at a frequency up to 20kHz.

The hardware is controlled, by using the graphical programming language Labview (National Instruments). Since the duration of each test run can be considerable, this software continuously writes the incoming data to the computer hard disk. The hardware costs about £1500, so that the total development cost (sensor electrodes, electronics and hardware) is about £5000.

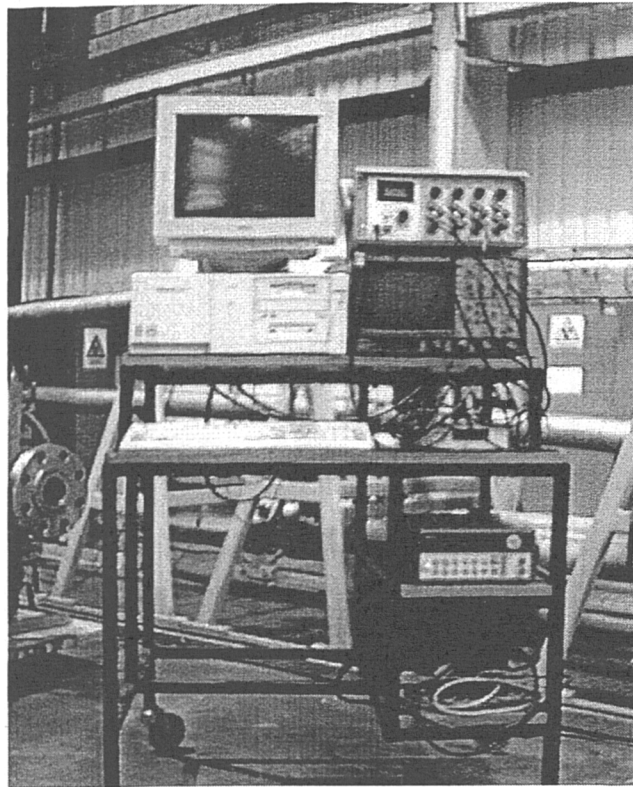


Figure 7.2: Computer system used to acquire data from the conductance sensors.

## 7.2 Parameter extraction

The processing software must analyse the raw sensor data, and extract the *measurement parameters* that are required by the stable slug flow model. As discussed in chapter 4, these parameters are the film duration  $t_f$ , the slug duration  $t_s$ , the corresponding phase fractions  $\alpha_f$  and  $\alpha_s$ , and the translation velocity  $V_r$ . The use of a ‘threshold level subroutine’ and a ‘cross-correlation’ subroutine to obtain these parameters will now be described.

### 7.2.1 Threshold level subroutine

A *threshold level* routine similar to that developed by Nydal *et al*<sup>88</sup> is first used, in order to locate the position of each ‘slug zone’ and each ‘film zone’ from the raw data. The subroutine `thrsh` (listed in appendix C) performs the following actions:

- The data from the holdup sensor are *normalised*, by comparing the measured conductance ( $G$ ) against the full-pipe conductance ( $G^*$ ). This process ensures that the holdup measurements lie within the range 0 to 1.
- The normalised data are compared in turn against the specified ‘threshold level’ parameter  $\theta$  (see figure 7.3a). Each position at which the sensor data crosses this threshold is recorded.
- The time delay between successive crossings is compared against a ‘film duration’ parameter  $t_{film}$  (see figure 7.3b). Only those data between sections of film at least  $t_{film}$  long are defined a slug. Therefore, holdup fluctuations that appear to be within the slug body are ignored.

The values that are chosen for  $\theta$  and  $t_{film}$  are dependent upon the *gas* and the *liquid phase flowrates*. The threshold level  $\theta$  should be lower than the slug holdup  $a_s$ , so it reduces with the gas flowrate, while the film duration  $t_{film}$  should be larger than  $t_s$ , so it reduces with the liquid flowrate. The exact values must be found by a trial and error process, but are expected to be of the order:

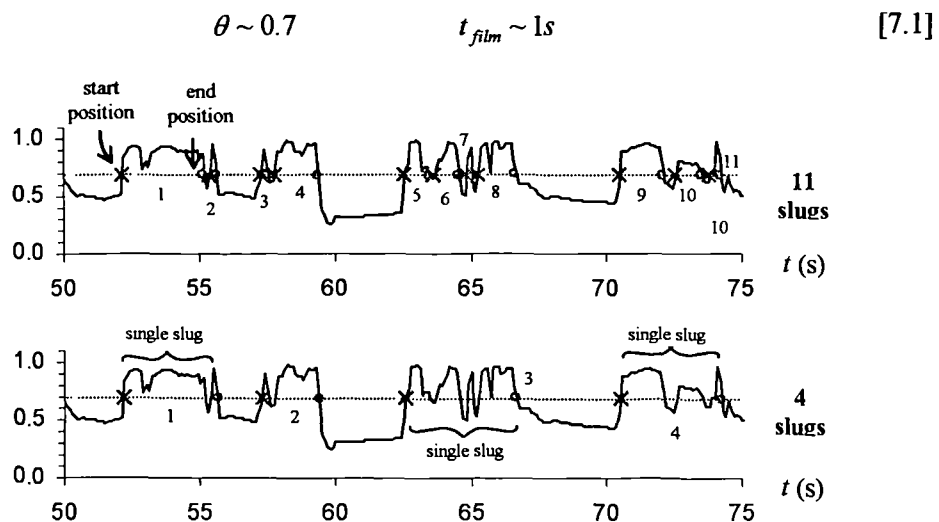


**Figure 7.3:** Use of the *threshold level subroutine* to process a section of experimental data. (a)  $\theta=0.7$  is used to identify the ‘slug’ and ‘film’ zones. (b)  $t_{film}=1s$  is used, to eliminate sections of data less than 1s long from the film zone.

The values used to process the data from the NEL facility (which is presented in Chapter 8 of this thesis) are summarised in table 8.1.

The output from the threshold level subroutine is used to compute the time measurements  $t_f$  and  $t_s$ , the phase fractions  $\alpha_f$  and  $\alpha_s$ , and the lengths  $l_u$ ,  $l_f$  and  $l_s$  (where  $l_f=V_l t_f$  and  $l_s=V_l t_s$ ). Therefore, any uncertainties in  $\theta$  and  $t_{film}$  will therefore cause an uncertainty in each of these parameters. This uncertainty effect is discussed further, in section 7.4 below. The error in the flowrates is expected to be most serious at large liquid flowrates, where the total duration of the slug unit ( $t_u$ ) is small.

### 7.2.2 Cross-correlation subroutine

The subroutine 'xcorrel' (listed in appendix C) is used to calculate the cross-correlation function  $\rho_{xy}(\tau)$ , the flow translation velocity  $V_t$ , and the signal bandwidth  $B$ . This is a computationally intensive process, and so to reduce the computer effort required the subroutine uses the 'fast' algorithm:

$$\rho_{xy}(\tau) = \frac{\text{ift}(X(\omega)Y^*(\omega)) - \mu_x\mu_y}{(R_{xx}(0) - \mu_x^2)^2 (R_{yy}(0) - \mu_y^2)^{1/2}} \quad [7.2]$$

where  $x(t)$  and  $y(t)$  are the input signals,  $\mu_x$  and  $\mu_y$  are the mean signal values,  $R_{xx}(0)$  and  $R_{yy}(0)$  are autocorrelation functions for the time delay  $\tau=0$ , and  $X(\omega)$  and  $Y(\omega)$  are the Fourier transforms of  $x(t)$  and  $y(t)$ .

The sensor data  $x(t)$  and  $y(t)$  should be *infinite*, in order to obtain a perfectly accurate result for the cross-correlation function  $\rho_{xy}$ . The use of a finite data sample means that an infinite and repeating data sequence is correlated, defined by:

$$\begin{aligned} x(t+nT) &= x(t) \\ y(t+nT) &= y(t) \end{aligned} \quad [7.3]$$

where  $n$  is an integer in the range  $-\infty < n < \infty$ . Therefore, the signals  $x(t)$  and  $y(t)$  should be as long as possible, and have good continuity at the point where the data wraps around, for an accurate result.

Two ways exist within the software, to correlate the data obtained from slug flow. Every slug and the surrounding film can be separately correlated (described here as the '*unit-by-unit*' method), or all of the available data can be correlated (the '*entire record*' method). Depending on this choice, two different types of task are performed:

- In the ‘unit-by-unit’ technique, a series of ‘start points’ and ‘end points’ are chosen to correspond to each slug unit. These start and end points are set in the *middle* of successive film zones to improve the continuity of the data, as shown in figure 7.4 below. This helps increase the level of correlation between the signals  $x(t)$  and  $y(t)$ , and hence reduce the measurement uncertainty.
- In the ‘entire record’ technique, the data are ‘chopped’ to the nearest  $2^n$  samples (where  $n$  is an integer). This means that a single, rapid, evaluation of the cross-correlation function takes place.

In what follows, the cross-correlation function and translation velocity obtained using the ‘entire record’ technique will be distinguished, by using the symbols  $\rho_{xy}^*$  and  $V_t^*$  respectively.

The ‘unit-by-unit’ and ‘entire record’ methods may have a significant effect upon the translation velocity and the phase flowrates. The ‘unit-by-unit’ technique results in a different velocity for each slug unit, but a large uncertainty ( $\Delta V_t/V_t$ ) while the ‘entire record’ method results in a single velocity for every slug unit, but a much reduced uncertainty. The effect of these options upon the measurement will be investigated, in Chapter 8 of the thesis.

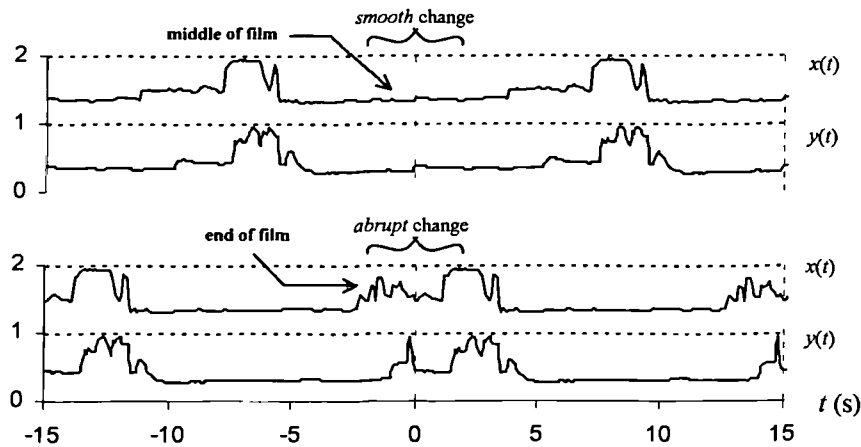


**Figure 7.4:** Cross-correlation of a 15s long ‘slug unit’. (a) Good continuity, between the beginning and end of each data section. (b) Poor continuity between the beginning and the end.

### 7.1.3 Signal bandwidth calculation

The signal bandwidth ( $B$ ) is required in order to calculate the translation velocity uncertainty  $\Delta V_t$  (see section 7.4 below). This bandwidth can be obtained by analysing the spectra of the signals  $x(t)$  and  $y(t)$ . However, it is quicker to obtain a *direct* estimate of  $B$  by using the

signals  $x(t)$  and  $y(t)$ . However, it is quicker to obtain a *direct* estimate of  $B$  by using the approximate model:

$$B \cong 1/\tau_{0.7} \quad [7.4]$$

(Beck & Plaskowski<sup>17</sup>), where  $\tau_{0.7}$  is the ‘peak width’ of the function  $\rho_{xy}^*(\tau)$  shown in figure 7.5 below. A reduction in the peak width thus corresponds to an increase in the signal bandwidth. In order to use equation [7.4] successfully, the sensor signals  $x(t)$  and  $y(t)$  must be reasonably coherent.

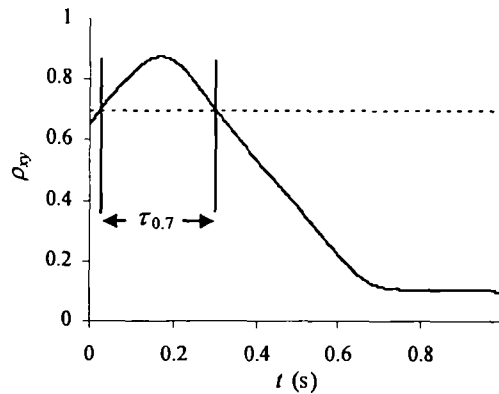


Figure 7.5: ‘Peak width’ method for calculating the cross-correlation signal bandwidth.

### 7.3 Flowrate prediction

The software calculates the phase flowrates using the *stable slug flow* model described in section 3.2. Each successive slug unit is assumed to be identical, so that the superficial velocities are given by:

$$j_l = V_{ls} a_s + V_{ls} (\bar{a}_f - a_s) \frac{l_f}{l_u} \quad j_g = V_{gs} (1 - a_s) - V_{ls} (\bar{a}_f - a_s) \frac{l_f}{l_u} \quad [7.5]$$

From which the mass flowrates are given by:

$$m_l = \rho_l j_l A \quad m_g = \rho_g j_g A \quad [7.6]$$

In order to evaluate equation [7.5], two pieces of information are required. First of all, *closure relationships* must be defined, in order to calculate the local slug velocities  $V_{ls}$  and  $V_{gs}$ . Secondly, the parameter data must be *averaged* in some way, so that mean flowrates can be calculated.

### 7.3.1 Closure relationships

Since the local velocities  $V_{ls}$  and  $V_{gs}$  cannot be measured directly, they must be estimated by using empirical closure relationships. Assuming that the flow in each slug unit is stable,  $V_{ls}$  and  $V_{gs}$  are defined by:

$$V_{ls} = \frac{j}{a_s + s(1 - a_s)} \quad V_{gs} = \frac{sj}{a_s + s(1 - a_s)} \quad [7.7]$$

where  $a_s$  is the holdup in the slug body,  $j$  is the total superficial velocity ( $j_l + j_g$ ), and  $s$  is the slip ratio in the slug body ( $V_{gs}/V_{ls}$ ).

The total superficial velocity  $j$  can be obtained, by making a correlation against the measurement of the *translation velocity*  $V_t$  (see table 3.1 in Chapter 3). Three different correlations will be used in this thesis, in order to assess the effect upon the predicted flowrates. These correlations are by Dukler & Hubbard<sup>30</sup>, Woods & Hanratty<sup>127</sup>, and from the experimental data taken from the NEL facility (see Chapter 8 which follows), and are respectively:

$$j = V_t / C \quad C = 0.021 \ln(Re_s) + 0.022 \quad [7.8]$$

$$j = \frac{V_t - V_o}{C_o} \quad \begin{cases} C_o = 1.10, & V_o = 0.54, & j(gD)^{-1/2} < 3 \\ C_o = 1.20, & V_o = 0, & j(gD)^{-1/2} > 3 \end{cases} \quad [7.9]$$

$$j = \frac{V_t - 1.09}{1.29} \quad [7.10]$$

The experimental data used to form the Woods & Hanratty and the NEL correlations are illustrated in figures 7.6 and 7.7.

The slip ratio  $s$  is a much more difficult parameter to correlate than the total superficial velocity. It is sometimes assumed that the phases in the slug body are a homogeneous mixture (see for example, Dukler & Hubbard<sup>30</sup> or Taitel & Bearna<sup>112</sup>), for all conditions of interest. In this case:

$$s = 1 \quad [7.11]$$

Woods & Hanratty<sup>123</sup> propose that the slip ratio should increase, as annular flow conditions are approached. By measuring the liquid shedding rate and using the model of Andritsos & Hanratty<sup>10</sup> to estimate the height of the incoming film layer, they were able to estimate the

slip ratio as a function of the superficial velocity  $j$  (figure 7.8). These data can be fitted by the approximate correlation:

$$s = \begin{cases} 1, & j < 3ms^{-1} \\ 1 + 0.125(j - 3), & 3 < j < 7ms^{-1} \\ 1.5, & j > 7ms^{-1} \end{cases} \quad [7.12]$$

An alternative correlation for the slip ratio was proposed by Malnes<sup>73</sup> but cannot be used as the original report is not available.

There are six possible ways to obtain predictions for the phase flowrates, by using equations [7.8] to [7.12] above. However, each of these methods will introduce an *uncertainty* and *systematic error* into the measurement, due to the following three factors:

- The translation velocity and the slip parameters are not unique functions of the total superficial velocity  $j$ .
- The slug flow may not be properly developed, i.e. there may be large numbers of growing and decaying slugs.
- The correlation data may have been obtained for different test conditions. Ideally, the data should be obtained for air-water slug flow in a 4-inch horizontal pipe, at atmospheric pressure.

In this thesis, three different sets of correlations will be used to define the local velocities, in order to determine the effect upon the predicted flowrates. These three models are summarised in table 7.1 below. The uncertainty that is caused due to these relationships is quantified, in section 7.4 that follows.

Model:	$j$ correlation	$s$ correlation
1	Dukler & Hubbard	No slip
2	Woods & Hanratty	Woods & Hanratty
3	NEL correlation	Woods & Hanratty

**Table 7.1.** Sets of closure relationships used to calculate the superficial velocities in Chapter 8 of the thesis.

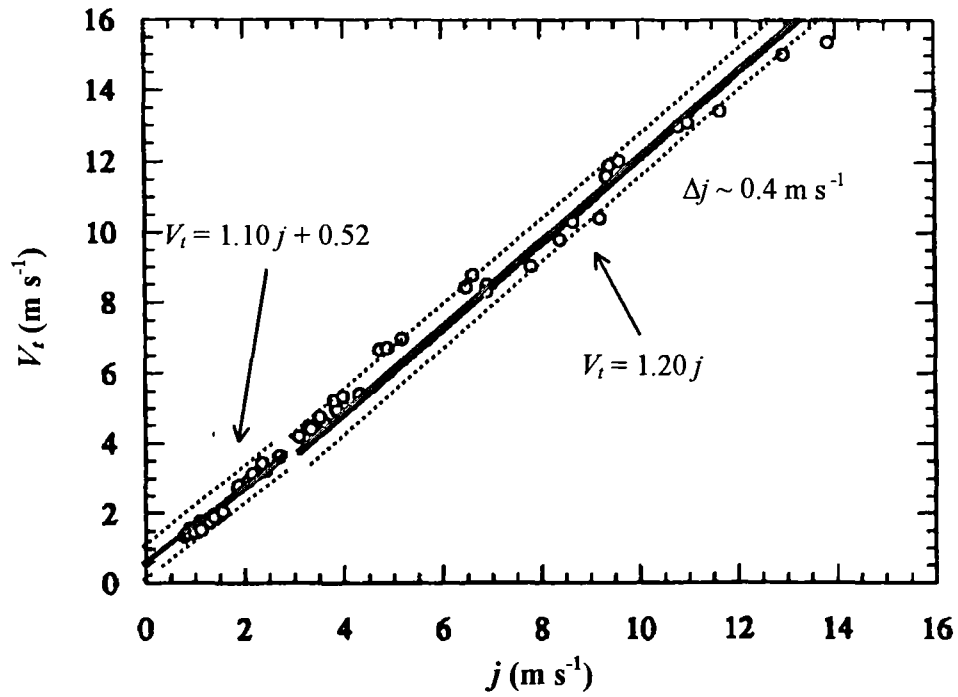


Figure 7.6: Total superficial velocity correlation of Woods & Hanratty<sup>127</sup>.

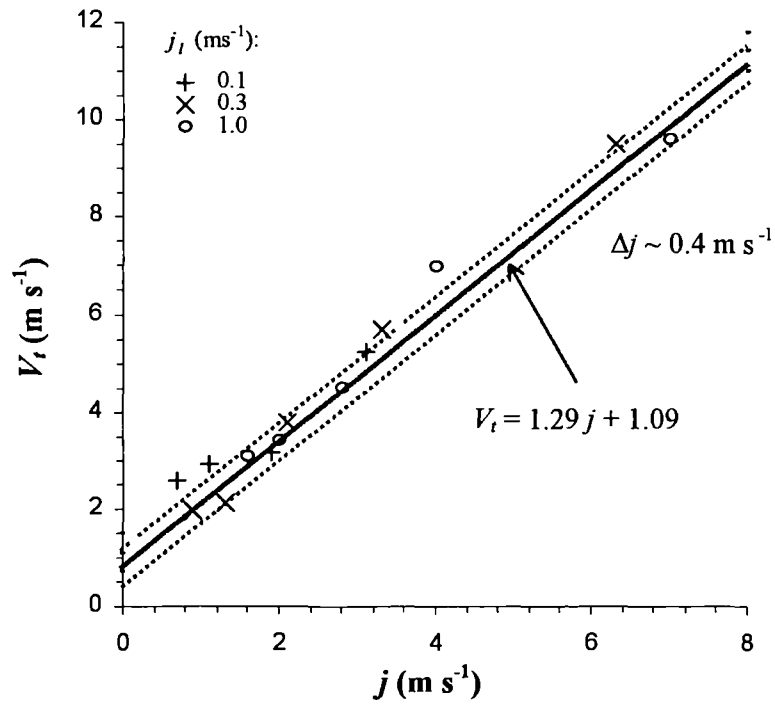


Figure 7.7: NEL correlation for the total superficial velocity  $j$ , developed using the experimental data from Chapter 8.

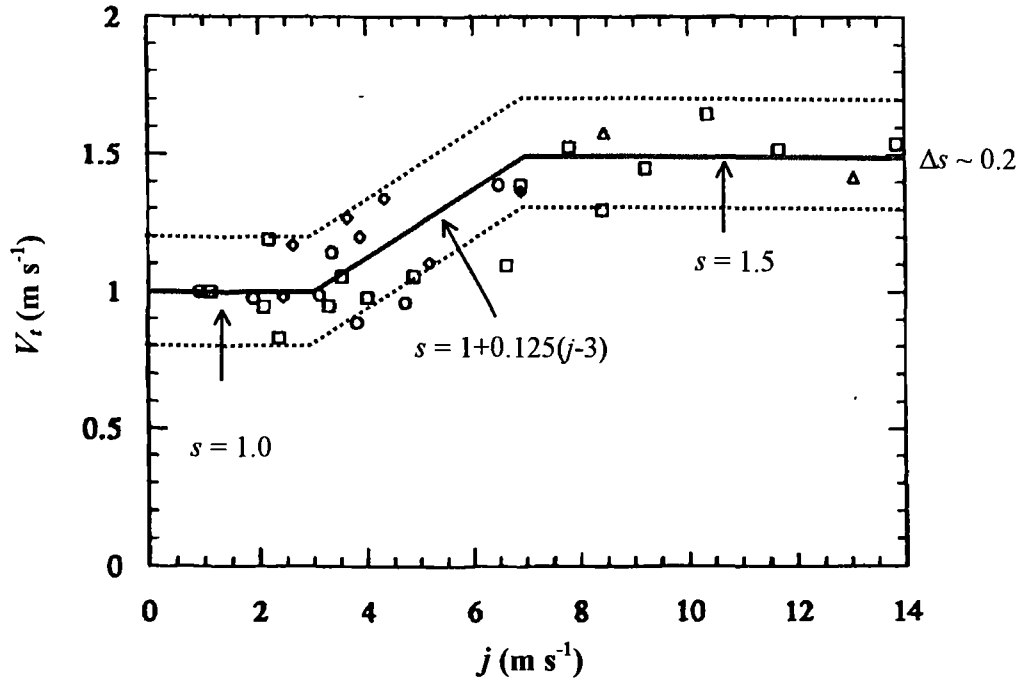


Figure 7.8: Correlation for the slip ratio  $s$ , using the experimental data of Woods & Hanratty<sup>127</sup>.

### 7.3.2 Averaging techniques

The stable slug flow model assumes that all successive slug units are identical, but the real flow data is 'quasi-stable'. That is, the length, velocity and holdup parameters will vary between slug units. To resolve this discrepancy, it is necessary to *average* the data in some way before the phase flowrates are calculated. The software offers two possible methods for averaging the data, which are as follows:

- 'Time-weighted' averaging. Here the total volumetric flowrate for each of the slug units is added together, and then divided by the total flow time. That is:

$$j_l = \frac{\sum V_{l_s}^i a_s^i + V_i^i (\bar{a}_f^i - a_s^i) (l_f^i / l_u^i)}{\sum 1 / v^i} \quad [7.13]$$

$$j_g = \frac{\sum V_{g_s}^i (1 - a_s^i) - V_i^i (\bar{a}_f^i - a_s^i) (l_f^i / l_u^i)}{\sum 1 / v^i} \quad [7.14]$$

- 'Parameter-weighted' averaging. Here the mean value of each measured parameter is used to calculate the flowrates, according to:

$$j_l = \overline{V_{ls}} \overline{a_s} + \overline{V_l} (\overline{a_f} - \overline{a_s}) (\overline{l_f/l_u}) \quad [7.15]$$

$$j_g = \overline{V_{gs}} (1 - \overline{a_s}) - \overline{V_l} (\overline{a_f} - \overline{a_s}) (\overline{l_f/l_u}) \quad [7.16]$$

Both these options make assumptions about the flow. In the ‘time-averaging’ technique it is assumed that each individual slug unit is stable. This model cannot be physically realised, since the fluxes that enter and exit successive slug units do not balance. On the other hand, to use the ‘parameter average’ technique, the flow must be approximated as a series of identical (and stable) slug units. This model is physically realistic, but it does not reflect the real data obtained from the sensors. However, as the limiting case of stable slug flow is approached, both methods give identical results.

#### 7.4 Uncertainty estimation

An important feature of the analysis system is its ability to estimate the *uncertainty margins* in the flowrate predictions. Since there are seven model parameters, there are a total of seven uncertainty components that are associated with the gas and liquid flowrates. Each of these components is derived by multiplying a sensitivity coefficient ( $S$ ) by the relative measurement uncertainty ( $\Delta X/X$ ), according to:

$$\left| \frac{\Delta j_l}{j_l} \right| = \left| S_{j_l}(X) \frac{\Delta X}{X} \right| \quad \left| \frac{\Delta j_g}{j_g} \right| = \left| S_{j_g}(X) \frac{\Delta X}{X} \right| \quad [7.17]$$

where  $X$  is a member of the set:

$$X \in \left\{ \overline{V_l}, \overline{a_f}, \overline{a_s}, \overline{V_{ls}}, \overline{V_{gs}}, \theta, t_{film} \right\} \quad [7.18]$$

In the following subsections, the expressions used to calculate the uncertainty in the translation velocity, holdup, local velocity and data processing parameters ( $\Delta V_l$ ,  $\Delta a_f$ ,  $\Delta a_s$ ,  $\Delta V_{ls}$ ,  $\Delta V_{gs}$ ,  $\Delta \theta$  and  $\Delta t_{film}$  respectively) will be defined, and the way that these are used to calculate the overall uncertainty will be discussed.

##### **7.4.1 The translation velocity uncertainty**

The translation velocity uncertainty ( $\Delta V_l$ ) is calculated using the model of Beck & Plaskowski<sup>17</sup>. This model assumes that the additive noise component  $n(t)$  (where  $n(t) =$

$y(t+\tau^*)-x(t)$  is *band-limited white noise*. The statistical uncertainty in the cross-correlation velocity is then given by:

$$\sigma_{V_i} = \frac{x}{\tau^{*2}} \cdot \frac{0.038^{1/2}}{T^{1/2} B^{3/2}} \left\{ \frac{1 - \rho_{xy}^2(\tau^*)}{\rho_{xy}^2(\tau^*)} \right\}^{1/2} \quad [7.19]$$

where  $x$  is the correlation sensor separation,  $\tau^*$  and  $\rho_{xy}(\tau^*)$  are the position and peak value of the normalised cross-correlation function  $\rho_{xy}$ , and  $T$  is the record duration. The signal bandwidth,  $B$ , is estimated using the equation:

$$B \cong 1/\tau_{0.7} \quad [7.20]$$

in which  $\tau_{0.7}$  is the ‘peak width’ of the correlation function  $\rho_{xy}(\tau^*)$  shown in figure 7.4. The statistical uncertainty predicted by equation [7.19] is converted to an absolute uncertainty (to within a 95% confidence limits), by using:

$$\Delta V_i \sim 2\sigma_{V_i} \quad [7.21]$$

#### 7.4.2 The phase fraction uncertainty

The phase fraction uncertainties ( $\Delta a_f$  and  $\Delta a_s$ ) are dependent upon the geometry of the sensor electrodes, described in Chapter 5. The use a *ring electrode* design meant that film zone uncertainty was expected to be of the order:

$$\overline{\Delta a_f} \sim 0.02 + \frac{0.3}{l_f} \quad [7.22]$$

while the ‘slug zone’ uncertainty was defined of the order:

$$\Delta a_s \sim 0.2(1 - a_s) \quad [7.23]$$

In equation [7.22], the right-hand term is the uncertainty due to the *transition region* between the ‘slug body’ and the film zone.

At low liquid flowrates, and at high gas flowrates, the estimates proposed above may be rather optimistic. This is because the theoretical models neglected the *liquid spray* above the film, and the *fine structure* in the slug body. However, it is not possible to quantify these effects without using local sensors to study the flow. The above expressions must be used, until more detail measurements can be obtained.

### 7.4.3 The local velocity uncertainty

The local velocity uncertainties ( $\Delta V_{ls}$  and  $\Delta V_{gs}$ ) are dependent upon the uncertainty in the slug body holdup ( $a_s$ ), the total superficial velocity ( $j$ ) and the slip parameter ( $s$ ). This is because differentiation of equation [7.7] results in the expressions:

$$\begin{aligned}\Delta V_{ls} &= \left| \frac{\partial V_{ls}}{\partial j} \Delta j \right| + \left| \frac{\partial V_{ls}}{\partial s} \Delta s \right| + \left| \frac{\partial V_{ls}}{\partial a_s} \Delta a_s \right| = \left| \frac{1}{\gamma} \Delta j \right| + \left| \frac{(a_s - 1)j}{\gamma^2} \Delta s \right| + \left| \frac{(s - 1)j}{\gamma^2} \Delta a_s \right| \\ \Delta V_{gs} &= \left| \frac{\partial V_{gs}}{\partial j} \Delta j \right| + \left| \frac{\partial V_{gs}}{\partial s} \Delta s \right| + \left| \frac{\partial V_{gs}}{\partial a_s} \Delta a_s \right| = \left| \frac{s}{\gamma} \Delta j \right| + \left| \frac{a_s j}{\gamma^2} \Delta s \right| + \left| \frac{s(s - 1)j}{\gamma^2} \Delta a_s \right|\end{aligned}\quad [7.24]$$

in which the parameter  $\gamma$  is defined as:

$$\gamma = a_s + s(1 - a_s) \quad [7.25]$$

The uncertainty in the slug holdup measurement ( $\Delta a_s$ ) has already been defined, in section 7.4.2 above.

The correlation uncertainties ( $\Delta j$  and  $\Delta s$ ) depend upon the amount of *scatter* that is present in the correlation data. By drawing boundary limits around the experimental data (shown in figure 7.5 to 7.7), these uncertainties are expected to be of the order:

$$\Delta j \sim 0.4 \text{ m s}^{-1} \quad [7.26]$$

$$\Delta s \sim 0.2 \quad [7.27]$$

These estimates are approximate, and are only valid for *air-water* slug flow in a horizontal pipe.

### 7.4.4 Data processing uncertainty

The uncertainties  $\Delta \theta$  and  $\Delta t_{film}$  depend upon the uncertainty in the ‘data processing’ parameters  $\theta$  and  $t_{film}$ . As there is no analytic method for setting  $\theta$  and  $t_{film}$  (see section 7.2.1 above) it is not possible to precisely define  $\Delta \theta$  and  $\Delta t_{film}$ , but it is suggested as a first approximation that:

$$\Delta \theta \sim 0.1 \quad [7.28]$$

$$\Delta t_{film} \sim 0.5 - t_{film} \quad [7.29]$$

As the values of  $\theta$  and  $t_{film}$  affect the measurement of  $t_f$  and  $t_s$ , the lengths  $l_f$  and  $l_s$  and the holdups  $a_f$  and  $a_s$ , the uncertainties  $\Delta\theta$  and  $\Delta t_{film}$  will cause uncertainties in *each* of these parameters. The effect upon the phase flowrates is discussed below.

#### 7.4.5 Flowrate uncertainty

Equation [7.17] is used, in order to convert the uncertainty into each of the model parameters ( $V_t$ ,  $\overline{a_f}$ ,  $a_s$ ,  $l_f$ ,  $l_s$ ,  $\theta$ , and  $t_{film}$ ) into a flowrate uncertainty. The sensitivity coefficients are derived by differentiation of the flowrate equations, as was described in Section 4.1 of this thesis. The resulting expressions for the coefficients  $S(V_t)$ ,  $S(a_f)$ ,  $S(a_s)$ ,  $S(V_{ls})$  and  $S(V_{gs})$  are re-stated in table 7.2 below.

	$V_t$	$V_{ls}$	$V_{gs}$	$a_f$	$a_s$
$S\{j_l\}$	$(\overline{a_f} - a_s) \frac{t_f V_t}{t_u j_l}$	$a_s \frac{V_{ls}}{j_l}$	-	$V_t \frac{t_f \overline{a_f}}{t_u j_l}$	$\left(V_{ls} - \frac{V_t t_f}{t_u}\right) \frac{a_s}{j_l}$
$S\{j_g\}$	$(a_s - \overline{a_f}) \frac{t_f V_t}{t_u j_g}$	-	$(1 - a_s) \frac{V_{gs}}{j_g}$	$-V_t \frac{t_f \overline{a_f}}{t_u j_g}$	$\left(\frac{V_t t_f}{t_u} - V_{gs}\right) \frac{a_s}{j_g}$

Table 7.2: Sensitivity parameters used to calculate the flowrate uncertainties.

The sensitivity coefficients  $S(\theta)$  and  $S(t_{film})$  depend upon the actual data acquired by the conductance sensors, and are not analytic expressions. In the software, these coefficients are calculated by adding two small perturbations ( $\delta\theta$  and  $\delta t_{film}$ ) to  $\theta$  and  $t_{film}$ , and re-calculating the flow velocities; from which it follows that:

$$S_{j_l}(\theta) \sim \frac{j_l(\theta + \delta\theta) - j_l(\theta)}{\delta\theta} \quad [7.32]$$

and:

$$S_{j_l}(t_{film}) \sim \frac{j_l(t_{film} + \delta t_{film}) - j_l(t_{film})}{\delta t_{film}} \quad [7.33]$$

(similar equations exist for  $S_{j_g}(\theta)$  and  $S_{j_g}(t_{film})$ ). This approach is time-consuming and also highly approximate, since the velocities  $j_l$  and  $j_g$  are generally not continuous functions of  $\theta$  and  $t_{film}$ .

Seven sets of uncertainty components can now be calculated, corresponding to each of the parameters  $V_l$ ,  $a_f$ ,  $a_s$ ,  $l_f$ ,  $l_s$ ,  $\theta$ , and  $t_{film}$ . These components are *absolute* errors, i.e. they represent the maximum uncertainty in the flowrates that can be caused due to each model parameter. In order to calculate a total uncertainty, it is assumed that the sources add statistically, so that:

$$\left| \frac{\Delta j_l}{j_l} \right|_{total}^2 = \sum \left| S_{j_l}(X) \frac{\Delta X}{X} \right|^2 \quad \left| \frac{\Delta j_g}{j_g} \right|_{total}^2 = \sum \left| S_{j_g}(X) \frac{\Delta X}{X} \right|^2 \quad [7.34]$$

While some of the uncertainties in equation [7.34] have constant values ( $\Delta V_l^*$ ,  $\Delta \theta$  and  $\Delta t_{film}$ ), others vary depending on the characteristics of each ‘slug unit’ ( $\Delta a_f$ ,  $\Delta a_s$ ,  $\Delta V_{ls}$ ,  $\Delta V_{gs}$  and  $\Delta V_l$ ). To resolve this discrepancy, those parameters that vary from unit-to-unit are *averaged* according to:

$$\Delta X = \frac{\sum_{i=1}^j \Delta X_i}{j} \quad X \in \{V_l, \overline{a_f}, a_s, V_{ls}, V_{gs}\} \quad [7.35]$$

Though equations [7.34] and [7.35] lack a theoretical basis, they mean that a *single* uncertainty can be calculated for each phase. As a result, the interpretation of the results (discussed in Chapter 8) is greatly simplified.

## 7.5 Summary

This chapter described the design of a system to collect the data from the conductance sensors, process this data, and then deliver the phase flowrates and the uncertainty margins. This system is the final component of the gas-water slug flow meter, which was specified in Chapter 4 of the thesis.

Section 7.1 briefly described the hardware and software used to acquire the data from the conductance sensors. These components took the overall cost of the meter development to around £5000.

Sections 7.2 to 7.4 then described the software used to process the data and deliver the phase flowrates:

- Section 7.2 described the routines used to extract the model parameters  $V_l$ ,  $a_f$  and  $a_s$ , and  $t_f$  and  $t_s$ , from the sensor data. A ‘threshold level’ routine was used to obtain the timing and the holdup measurements, and a ‘cross-correlation’ routine

was used to obtain the translation velocity  $V_t$ . There was more than one way to cross-correlate the data. Finally, a procedure for estimating the cross-correlation signal bandwidth ( $B$ ) was described.

- Section 7.3 defined the *closure relationships* and *averaging techniques* that are necessary for calculation of the phase flowrates. Three correlations for the total superficial velocity ( $j$ ) and two correlations for the slip ratio ( $s$ ) were defined, and used to form three models (illustrated in table 7.1). Two averaging techniques - ‘time-weighted’ averaging and ‘parameter’ averaging - were then defined. The influence of each of these methods upon the superficial velocity prediction will be assessed in Chapter 8.
- Section 7.4 described the routine used to calculate *uncertainty components* in the superficial velocities,  $\Delta j_l/j_l$  and  $\Delta j_g/j_g$ . In similar fashion to section 4.2, these uncertainties were the product of an measurement uncertainty and a sensitivity parameter. Expressions for the measurement uncertainties  $\Delta V_t$ ,  $\Delta a_f$ ,  $\Delta a_s$ ,  $\Delta V_{ls}$ ,  $\Delta V_{gs}$ ,  $\Delta \theta$  and  $\Delta t_{film}$  were defined. The estimation of the sensitivity parameters  $S(\theta)$  and  $S(t_{film})$  was considered. Finally, the way in which the *mean uncertainties* are calculated was described.

The completed slug flow meter - consisting of the sensor electrodes, the sensor electronics and the processing system - is now ready to be tested in horizontal slug flow, in the NEL flow facility. The following chapter will describe this assessment, and the interpretation of the results.

## 8. Performance assessment

In this chapter the metering system will be assessed, by using slug flow data generated by the NEL flow facility. The assessment is divided into three parts: to gather and analyse the raw data; to process this data using the software developed in the previous chapter; and, most importantly, to determine the effectiveness of the ‘stable slug flow’ model.

Section 8.1 will describe the NEL horizontal flow facility, the experimental apparatus, the bench-tests, and the raw data gathered from the conductance sensors. These data cover gas-water horizontal slug flow, in the range  $j_f=0.1 \text{ m s}^{-1}$  to  $1.0 \text{ m s}^{-1}$  and  $j_g=0.6 \text{ m s}^{-1}$  to  $6.0 \text{ m s}^{-1}$ .

Section 8.2, which is the major component of this chapter, will present the results obtained by processing the raw data. This section is divided into five sub-sections, in which the following are examined:

- The effect of the ‘cross-correlation method’ upon the translation velocity  $V_t$ , the signal bandwidth  $B$ , and the translation velocity uncertainty  $\Delta V_t$  (section 8.2.1).
- The agreement between the calculated values for the translation velocity  $V_t$ , the phase fractions  $\overline{\alpha}_f$  and  $\alpha_s$ , the lengths  $l_f$  and  $l_s$  and the slug frequency  $\nu$ , and the existing correlations (section 8.2.2).
- The predictions for the phase flowrates, obtained using the different ‘closure relationships’, ‘cross-correlation’ techniques and ‘averaging techniques’ (section 8.2.3).
- The *uncertainty* in the translation velocity  $V_t$ , the phase fractions  $\overline{\alpha}_f$  and  $\alpha_s$ , the local velocities  $V_{ls}$  and  $V_{gs}$  and the data processing parameters  $\theta$  and  $t_{film}$  (section 8.2.4).
- The uncertainty in the phase flowrates ( $\Delta j_l/j_l$  and  $\Delta j_g/j_g$ ) due to the uncertainty in the velocity  $V_t$ , the holdups  $\alpha_s$  and  $\overline{\alpha}_f$ , the local velocities  $V_{ls}$  and  $V_{gs}$  and the parameters  $\theta$  and  $t_{film}$  (section 8.2.5).

Finally, section 8.3 will interpret the experimental results. The performance of the meter and the uncertainty in the flowrate predictions will be summarised. The stable slug flow model does *not* do a good job at predicting the phase flowrates. The validity of the model will be assessed, by calculating the total uncertainty. Particular attention will be paid towards the *closure relationships*, which are used to define the local velocities within each slug unit.

## **8.1 Data acquisition**

The NEL facility has been used, to obtain raw data for a range of slug flows in a 4-inch horizontal pipe. In this section, the NEL test facility, the measurement system and the relevant bench-tests will be described, and then the ‘raw’ experimental data will be described.

### **8.1.1 The NEL facility**

Figure 8.1 is a schematic diagram of the NEL multiphase flow facility. This system uses nitrogen (density  $1.2 \text{ kg m}^{-3}$ ; viscosity  $1.8 \times 10^{-5} \text{ N s m}^{-2}$  at a.t.p), a  $50 \text{ g l}^{-1}$  magnesium sulphate water solution (density  $1000 \text{ kg m}^{-3}$ ; viscosity  $1.0 \times 10^{-3} \text{ N s m}^{-2}$  at a.t.p) and Forties field crude oil as the three test phases. The path taken by each of these phases through the facility is as follows:

- The individual phases pass through a set of pumps and a set of single-phase turbine meters. These turbine meters can measure a range of gas, water and oil flowrates between  $0.33$  to  $27.6 \text{ l s}^{-1}$ ;  $1.5$  to  $32.7 \text{ l s}^{-1}$ ; and  $0.8$  to  $41.2 \text{ l s}^{-1}$  respectively, to within 1% relative accuracy. Therefore, the reference superficial velocities are accurate to within 1%.
- The phases are injected into a 4-inch horizontal test section, parallel to the axis of flow. This parallel injection encourages *uniform flow* conditions at the entrance. The phases then pass along approximately 300 pipe diameters (30m) of straight pipe, before passing through a ‘U’ bend, and then along a return line.
- At the end of the return line, the gas phase is ejected, while the liquids are returned to the separator tank. An oil-in-water monitor is used to ensure that the liquid components are well separated during the operation.

A photograph of the facility, illustrating the separator tank, the horizontal test section and the return line is shown in figure 8.2.

The operation of the NEL multiphase facility is computer automated. The user sets the flowrates required at the point of metering, and then a control loop adjusts the actual flowrates until a match is obtained. This control loop uses measurements for the pressure and the temperature at the meter location, in order to correct for the expansion of the gas phase. Typically, the control loop takes a few minutes to stabilise the flow, before the experiments can commence.

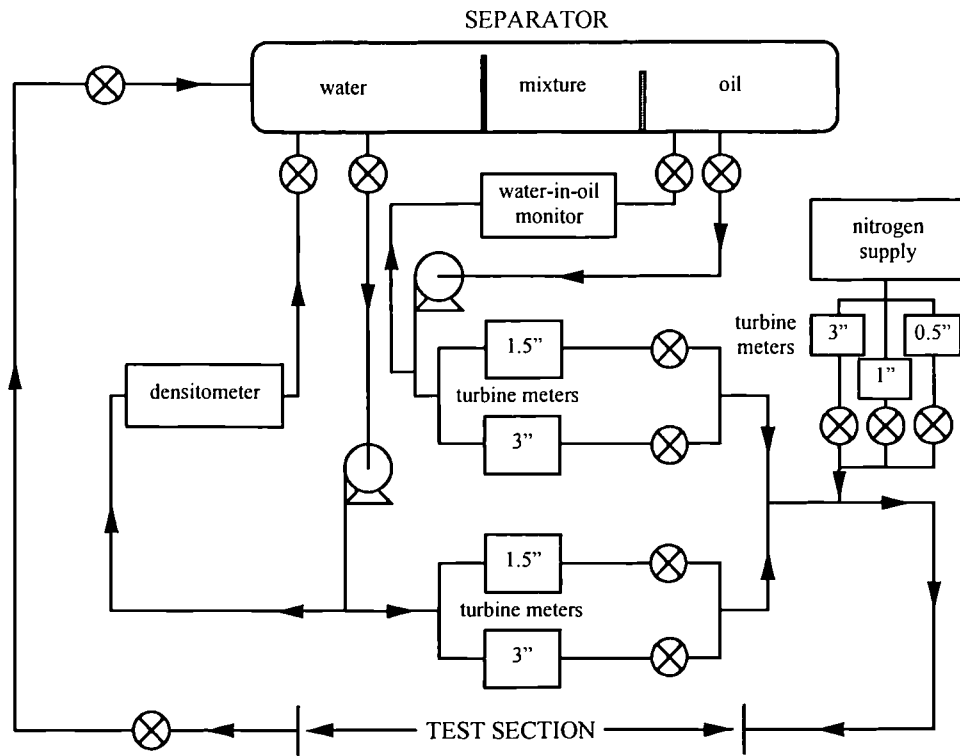


Figure 8.1: Schematic diagram of the NEL flow facility.

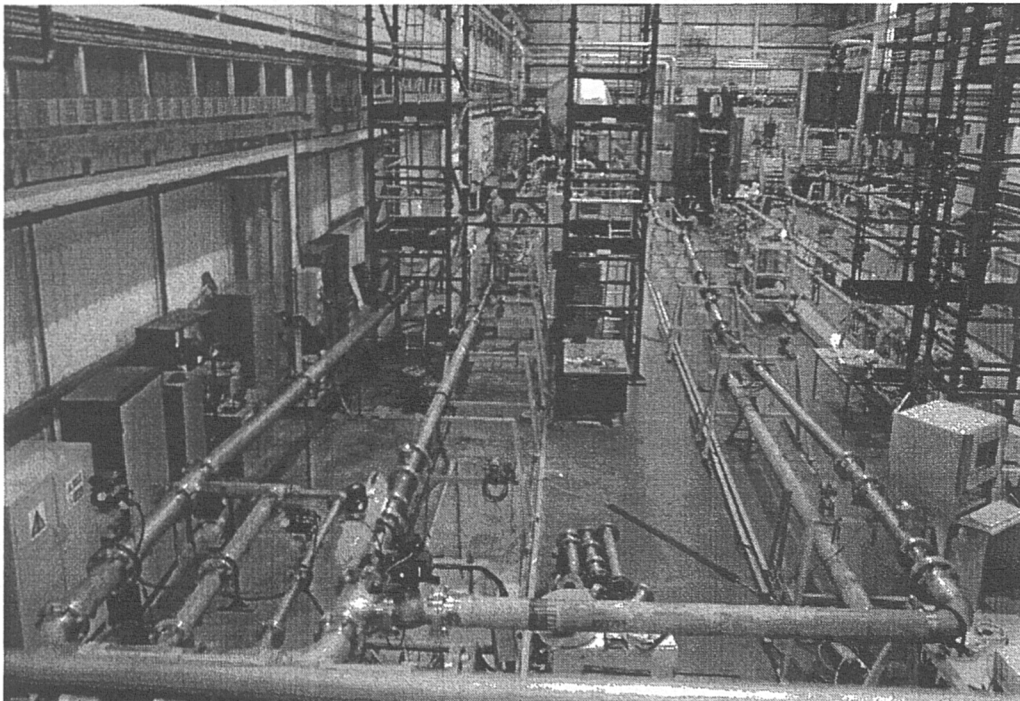


Figure 8.2: The NEL 4-inch test section.

### 8.1.2 Measurement system

The measurement system was developed in Chapters 5 to 7 of this thesis. A schematic diagram of the system components is shown in figure 4.1. To recap, the three main components are as follows:

- Three ring-electrode type conductance sensors, for measuring the holdup and the translation velocity of the slugs. The optimisation and the manufacture of these sensors was discussed in Chapter 5.
- Electronic instrumentation for activating the electrodes and measuring the cell conductance. This instrumentation, described in Chapter 6, has been designed to eliminate the measurement errors caused by a *high salt content* in the water phase.
- An A/D interface, for collecting the conductance data, and a set of software routines to process this data and deliver the phase flowrates. The acquisition system and the processing software were described, in Chapter 7.

The ring electrode sensors, which are illustrated in figure 8.3, are located approximately 200 pipe diameters (20 metres) downstream of the test section inlet. At this distance, the slugs will have had time to initiate and grow, so that the flow is reasonably ‘well-developed’. The intervening sections of pipe are grounded, to prevent any possibility of instrument crosstalk. The gas flowrate is corrected for expansion effects, by taking pressure and temperature measurements.

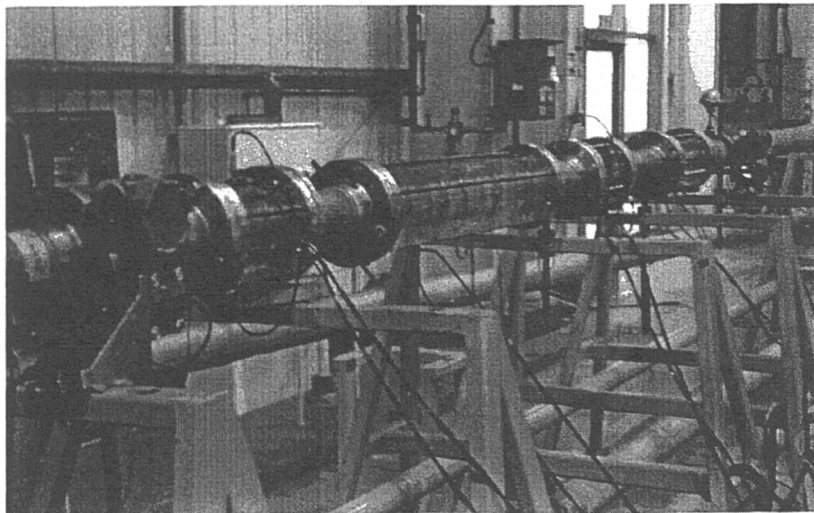


**Figure 8.3:** The conductance sensors and the NEL test section.

### 8.1.3 System bench tests

Three sets of bench tests must be carried out on the system prior to operation, in order to verify the pressure safety, the correct operating range for the instrumentation, and to test for the presence of sensor crosstalk. These bench tests are as follows:

- The holdup and cross-correlation sensor units must be pressure tested with water, to one-and-a-half times the maximum operating pressure (15 bar). This test is repeated several times.
- An appropriate operating range must be selected for each channel, in order to minimise the measurement error. The ‘full-pipe’ conductance for each pair of electrodes ( $G^*$ ) is measured. The full-pipe conductance is about  $0.05 \Omega^{-1}$  and  $0.5 \Omega^{-1}$ , for the holdup and the cross-correlation sensors respectively. Therefore, the operating ranges  $G_{FS}=80 \text{ m}\Omega^{-1}$  and  $G_{FS}=0.8 \Omega^{-1}$  are selected. It follows that conductivity of the water phase is approximately  $2.5 \Omega^{-1}\text{m}^{-1}$ .
- With one set of sensor electrodes activated, the change to the conductance output on the other channels must be monitored. During these tests, no change to the full-pipe conductance  $G^*$  was observed. This indicates that the crosstalk between adjacent sensors is negligible.

In addition to these tests, the full-pipe conductance  $G^*$  must be monitored *between* experimental runs. This monitoring is essential, to ensure that variations in the fluid conductivity (e.g. due to temperature fluctuations) do not affect the accuracy of the holdup measurement. The test section is flushed through with water, and then the full-pipe conductance is recorded for each sensor.  $G^*$  changes by less than 1% between successive tests, so the effect of *temperature drift* on the data is not significant.

### 8.1.4 The sensor data

Gas-water data are obtained using the NEL facility, for horizontal slug flow in a 4-inch test section at atmospheric pressure. A set of fifteen test points was investigated, defined by the superficial flow velocities:

$$\begin{aligned} j_l &\in \{0.1, 0.3, 1.0\} \text{ m s}^{-1} \\ j_g &\in \{0.6, 1.0, 1.8, 3.0, 6.0\} \text{ m s}^{-1} \end{aligned} \quad [8.1]$$

The ‘sample frequency’ and the ‘run time’ parameters for these tests are summarised in

table 8.1 below.

test point	$j_l$	$j_g$	sample rate (Hz)	record duration (s)	threshold level $\theta$	$t_{film}$ (s)
<i>a</i>	0.1	0.6	400	600	0.7	5
<i>b</i>	0.1	1.0	200	900	0.7	5
<i>c</i>	0.1	1.8	500	600	0.7	5
<i>d</i>	0.1	3.0	200	920	0.7	5
<i>e</i>	0.3	0.6	400	600	0.7	2
<i>f</i>	0.3	1.0	250	600	0.7	2
<i>g</i>	0.3	1.8	500	600	0.7	2
<i>h</i>	0.3	3.0	250	450	0.6	2
<i>i</i>	0.3	6.0	800	600	0.5	2
<i>j</i>	1.0	0.6	400	360	0.7	1
<i>k</i>	1.0	1.0	250	480	0.7	1
<i>l</i>	1.0	1.8	500	320	0.7	1
<i>m</i>	1.0	3.0	400	480	0.6	1
<i>n</i>	1.0	6.0	800	320	0.5	1

**Table 8.1:** Data acquisition and processing parameters for each test point

Figure 8.4 compares the test matrix against the gas-water flow map for the NEL facility developed by Hall<sup>44</sup>. The full range of slug flow conditions, from ‘plug flow’ to ‘bubbly slug’ and ‘slug-annular’ flow, is covered. All the data are used in the analysis, except those for the test point {0.1,0.6}. This point was too close to the stratified flow boundary to observe slugging during the run time.

Figure 8.5 illustrates sections of the normalised data obtained from the holdup and the cross-correlation sensors. As described in section 8.1.3 above, since the drift in the conductance  $G^*$  is about 1%, so the error introduced by this normalisation process should be no greater than 1%. Moving from the lowest to the highest flowrates, the following trends in the data are observed:

- At low gas flowrates (figures 8.5a, 8.5e and 8.5j), there is considerable *fine structure* within each ‘slug’ zone. This fine structure is illustrated in greater detail, in figure 8.6. There is also a large variation in the duration of each ‘slug unit’. In moving towards the boundary with bubble flow (e.g. figure 8.5j), it becomes very difficult to distinguish the ‘slug’ and the ‘film’.
- As the gas flowrate increases, the sequence of ‘slug’ and ‘film’ becomes much more periodic. The similarity between each slug unit, and its surrounding neighbours, will increase. The average duration of the slug unit remains approximately constant, but the holdup in the slug and the film zones tends to

reduce.

- At low liquid flowrates (figures 8.5a to 8.5d), the slug frequency is low, and the duration of each film zone is long (typically 100 seconds). The film zone will generally have a smooth, slowly changing profile. However, there are occasionally *large-amplitude waves* between the slugs. These waves are associated with the slug development process.
- As the liquid flowrate increases, there is a notable rise in the slug frequency, hence a notable fall in the film duration  $t_f$ . The ‘slug zone’ accounts for a much greater proportion of the slug unit than at lower flowrates. At the end of each slug zone (the beginning of the film) there is a much more pronounced curvature in the film zone profile.

The spectral content of the cross-correlation sensor data are illustrated in figure 8.7, for the set of test points {0.1,0.6}, {0.1,3.0}, {1.0,0.6} and {1.0,6.0}. In each spectrum, there are a set of prominent peaks between 0.1Hz and 1Hz that are associated with the slug frequency. There is then a rapid roll-off in the spectral content (as a first-to-second order effect) above 1Hz. This rapid roll-off indicates that there is a low signal bandwidth, and a negligible amount of aliasing. Similar spectra are obtained, for the other points within the test matrix.

In figure 8.5, the cross-correlation data and the holdup sensor data are generally very similar in appearance. However, there is a notable discrepancy between the upstream sensor  $x(t)$  and the downstream sensor  $y(t)$  just after a ‘slug’ passes, at large gas flowrates (for example, see figure 8.5i). This is because the first cross-correlation sensor was found to contain a small cavity behind one of its electrodes. This cavity will modify the electric field between the electrodes, and hence the measured conductance. The effect of this *unequal dynamic* upon the experimental results will be discussed, in section 8.3 below.

## **8.2 Data analysis**

The raw sensor data is processed, using the software developed in Chapter 7 of the thesis. This software requires the full-pipe conductance  $G^*$ , the processing parameters  $\theta$  and  $t_{film}$ , a ‘cross-correlation technique’, a ‘closure relationship’, and an ‘averaging technique’ as inputs. The resultant output for the *cross-correlation function*  $\rho_{xy}$ , the *model parameters*, the *phase superficial velocities* and the *superficial velocity uncertainty margins* will now be presented.

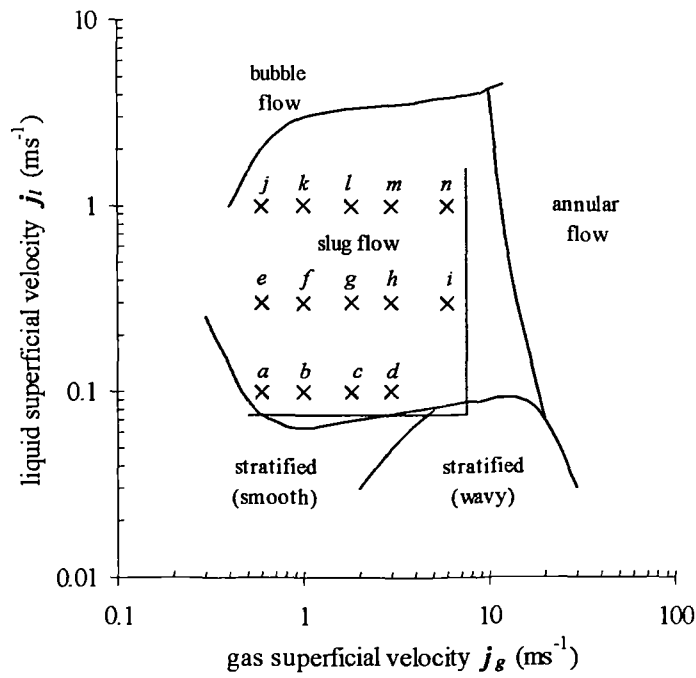


Figure 8.4: The experimental test matrix, and the gas-water flow map for the NEL facility developed by Hall<sup>44</sup>.

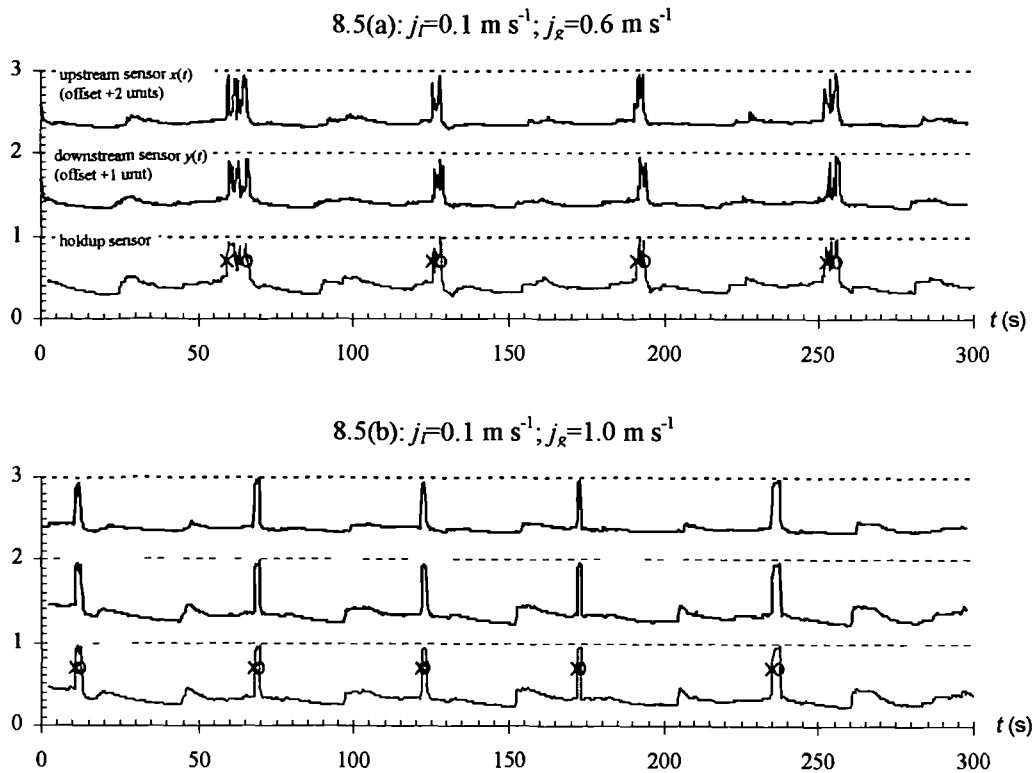
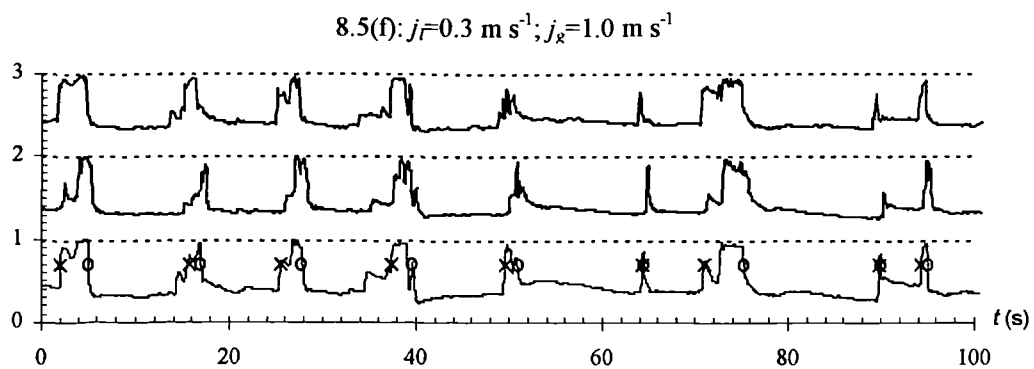
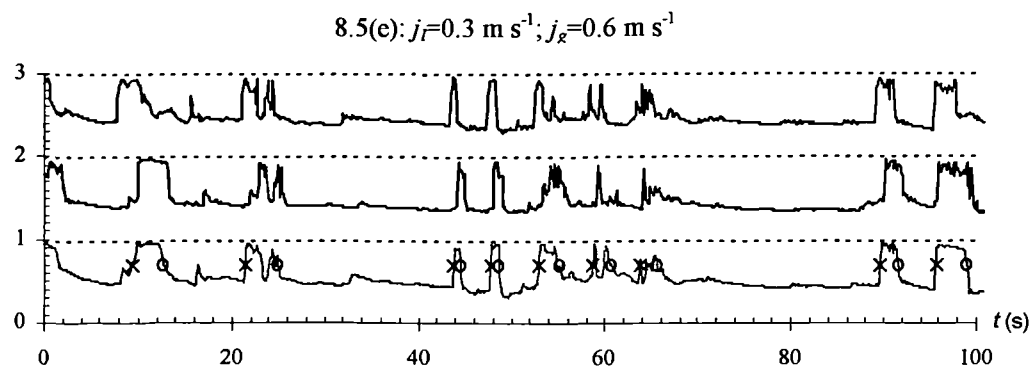
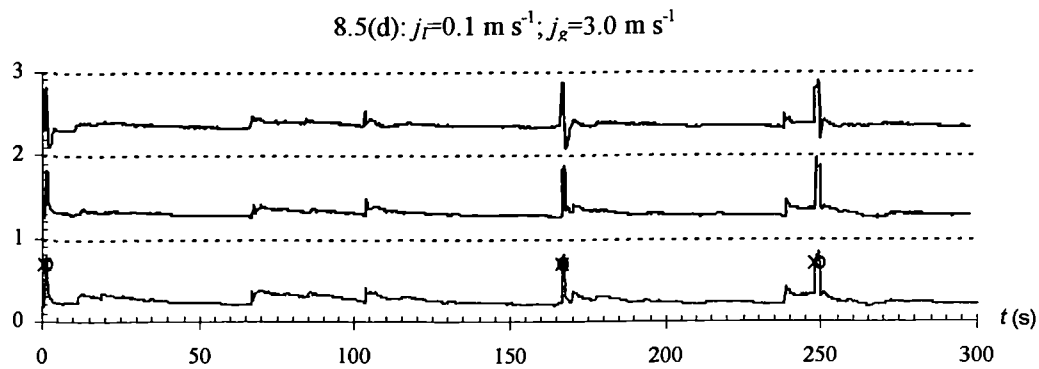
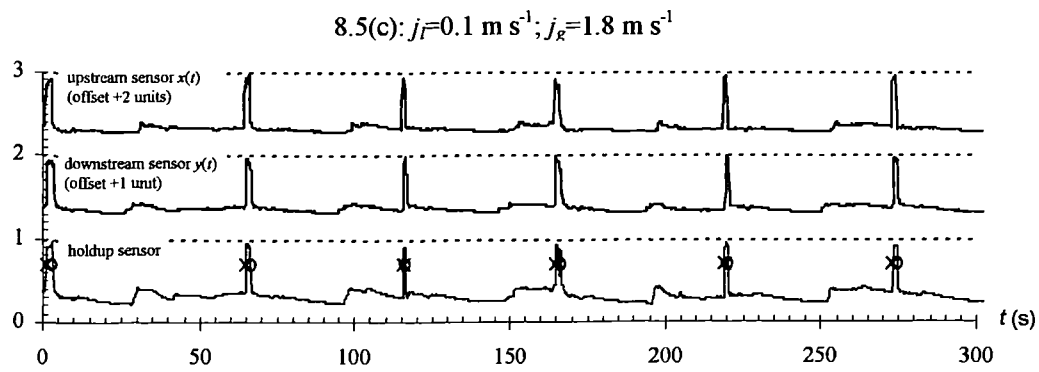


Figure 8.5: Normalised cross-correlation sensor and holdup sensor data, for the test points *a* and *b*. (The holdup data illustrates the position of the ‘slug’ and the ‘film’ zones).



**Figure 8.5 (continued):** Normalised cross-correlation sensor and holdup sensor data, for the test points *c*, *d*, *e* and *f*.

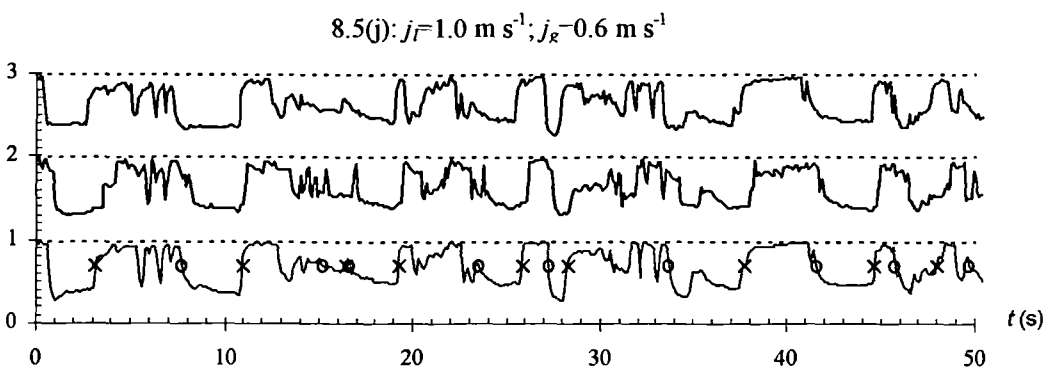
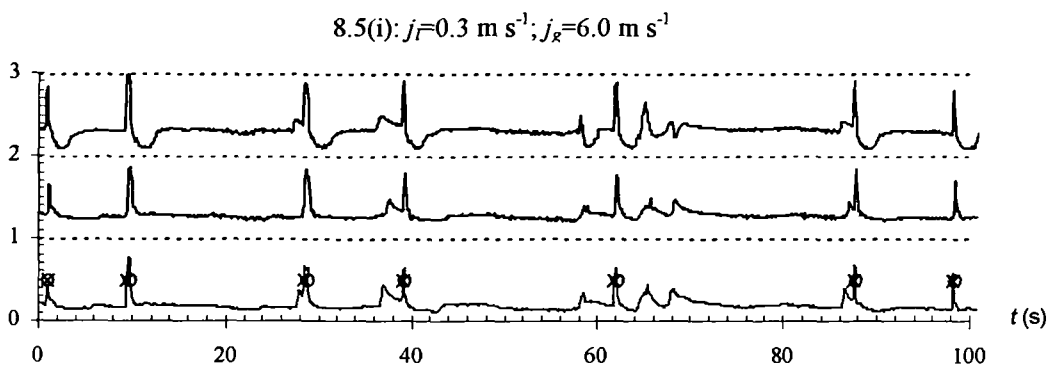
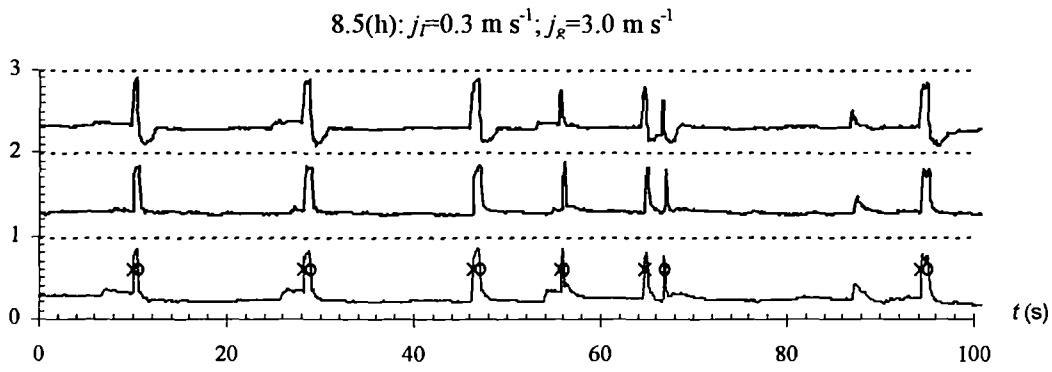
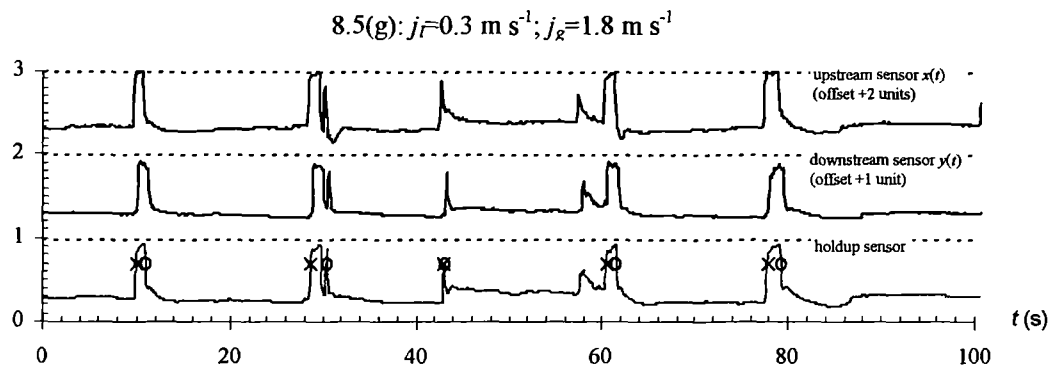


Figure 8.5 (continued): Normalised cross-correlation sensor and holdup sensor data, for the test points *g*, *h*, *i* and *j*.

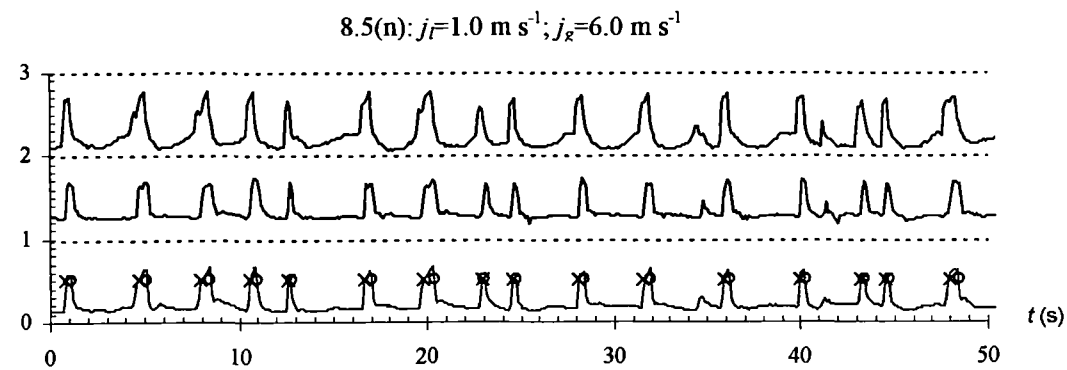
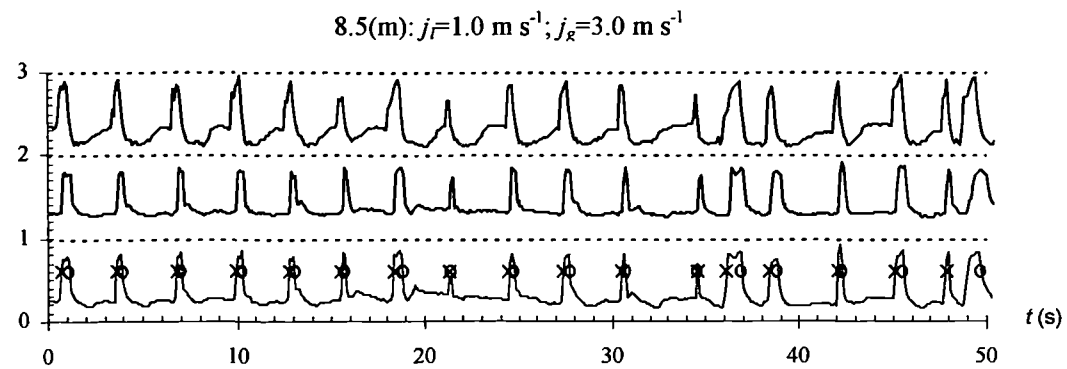
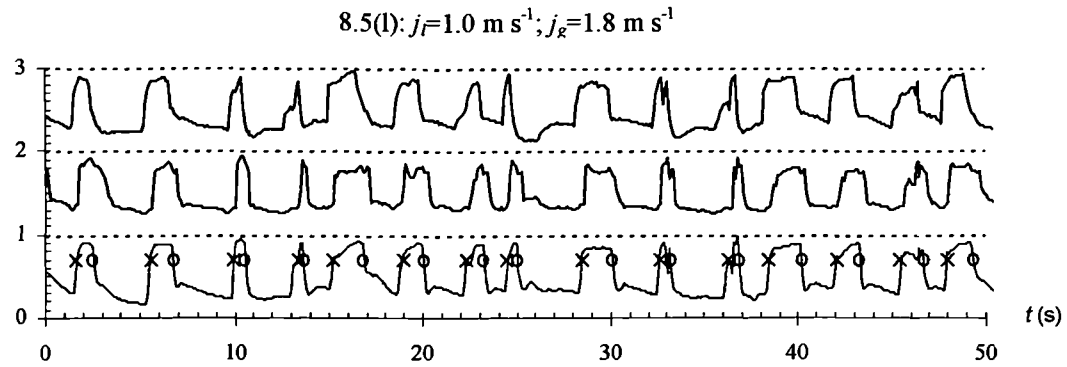
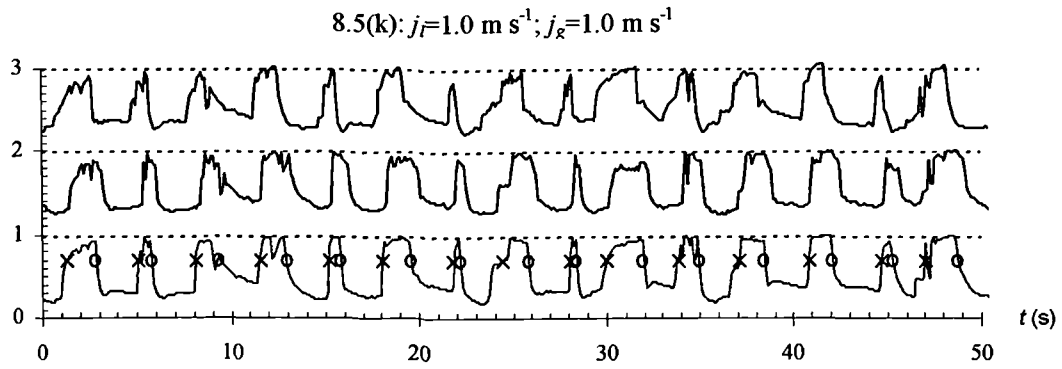
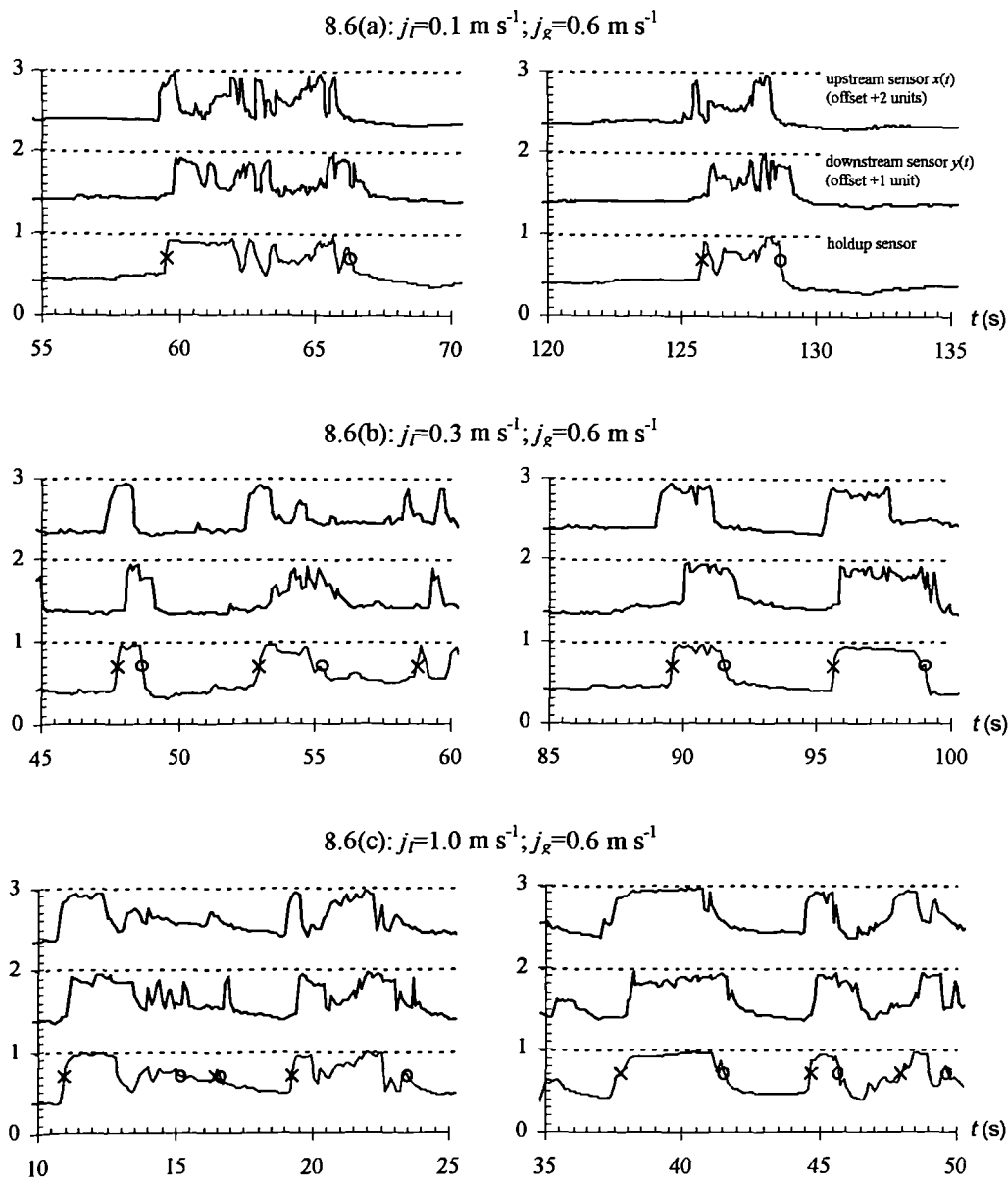


Figure 8.5 (continued): Normalised cross-correlation sensor and holdup sensor data, for the test points  $k$ ,  $l$ ,  $m$  and  $n$ .



**Figure 8.6:** Detailed structure within some selected slugs, for low total flowrate conditions.

### 8.2.1 The cross-correlation method

The sensor data can be cross-correlated using either the ‘unit-by-unit’ or the ‘entire record’ correlation techniques described in section 7.2.2. Figures 8.8a to 8.8d compares the effect of each technique upon the normalised cross-correlation function  $\rho_{xy}$ , for the set of four test points  $\{0.1,0.6\}$ ,  $\{0.1,3.0\}$ ,  $\{1.0,0.6\}$  and  $\{1.0,6.0\}$  respectively. The following observations are made:

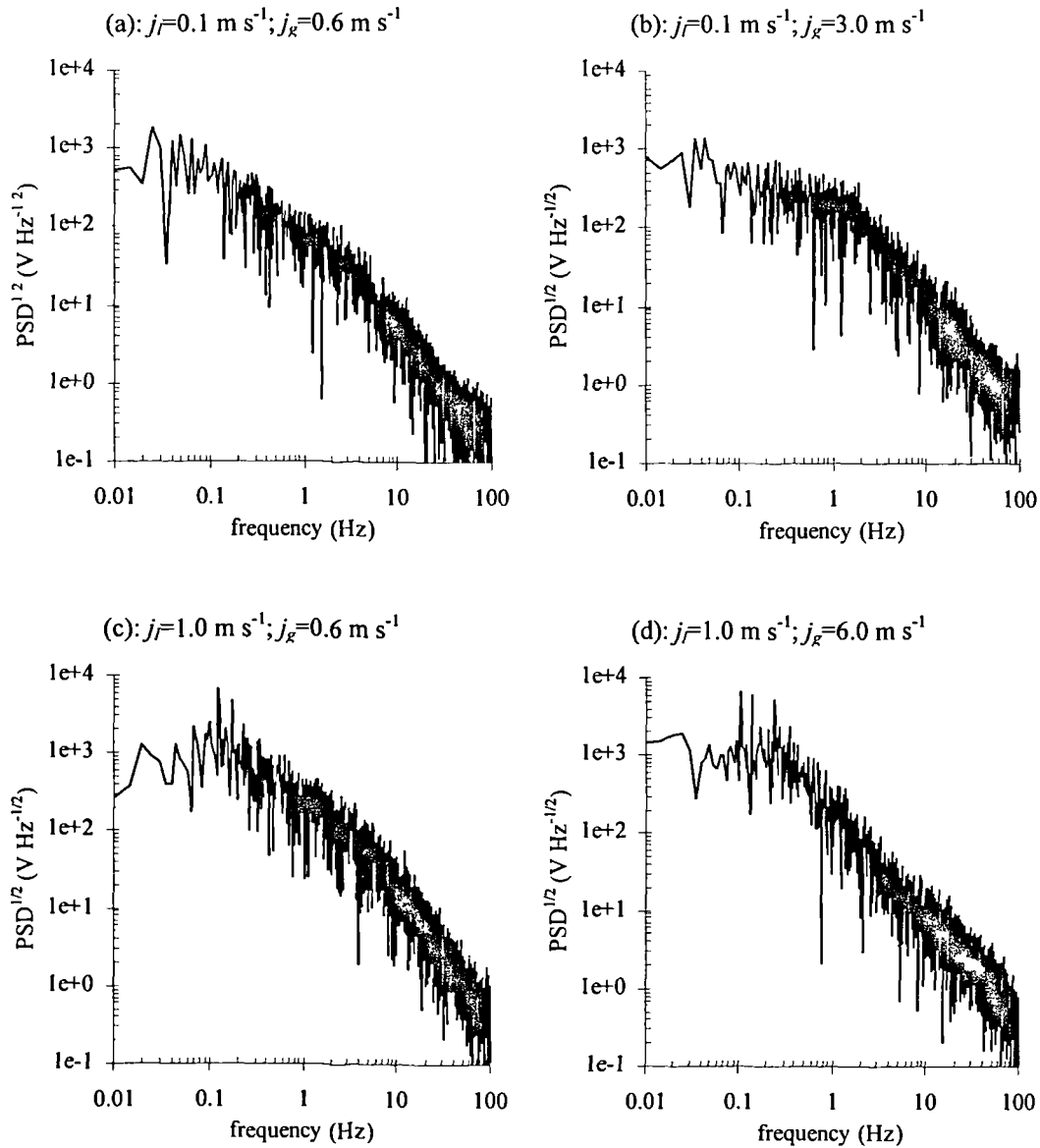


**Figure 8.7:** Spectral content of the cross-correlation sensor data, for the four test points *a*, *d*, *j* and *n* respectively.

- The ‘unit-by-unit’ technique produces a triangular peak, due to the ‘rectangular’ shape of the slug zone. The width of this peak reduces with the total superficial velocity  $j$ , but the peak height generally has a value around 0.8. The position of the maximum ( $\tau^*$ ) varies slightly, from unit to unit.
- The ‘entire record’ cross-correlation produces a triangular peak at a similar position and a similar height, though much smoother in appearance. Therefore, the effect of adding extra slug units to the correlation data is to *reinforce* the previous result.

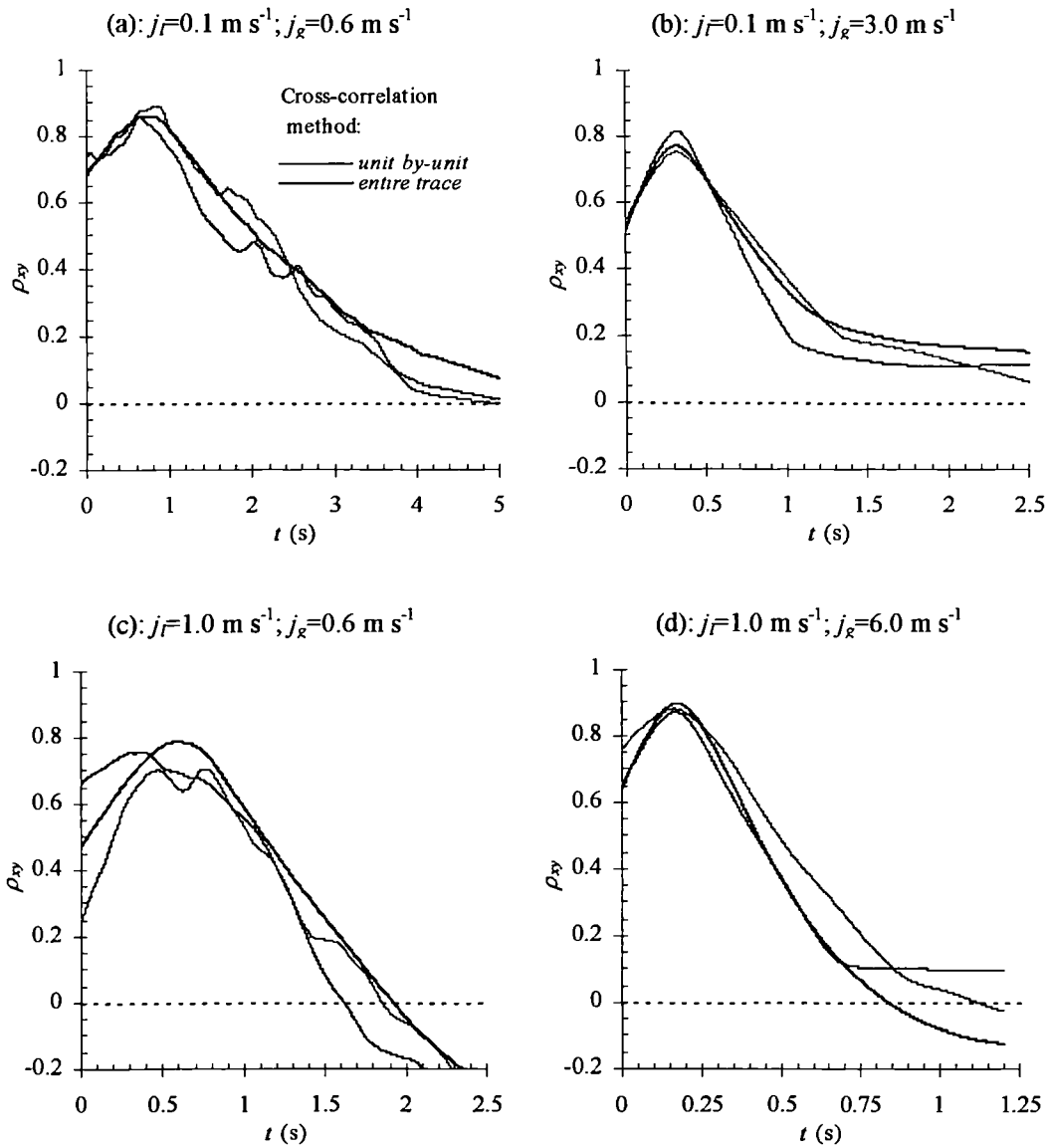


Figure 8.8: Comparison of 'individual slug' and 'entire trace' cross-correlation functions, for the four test points test points  $a$ ,  $d$ ,  $j$  and  $n$  respectively.

Similar cross-correlation functions are obtained, for the other ten points within in the experimental test matrix.

The choice of cross-correlation technique will affect the calculated values for the translation velocity ( $V_t$ ) and the velocity uncertainty ( $\Delta V_t/V_t$ ). Figure 8.9 compares the mean translation velocity and the mean uncertainty that are obtained by:

$$V_t = x/\tau^* \quad [8.2]$$

and the uncertainty model (Beck & Plaskowski<sup>17</sup>):

$$\frac{\Delta V_i}{V_i} = \frac{2x}{\tau^{\cdot 2}} \cdot \frac{0.038^{1/2}}{T^{1/2} B^{3/2}} \left\{ \frac{1 - \rho_{xy}^2(\tau^{\cdot})}{\rho_{xy}^2(\tau^{\cdot})} \right\}^{1/2} \quad [8.3]$$

in which  $x$  is the sensor separation,  $B$  is the signal bandwidth, and  $T$  is the cross-correlation record duration. The bandwidth  $B$ , which is illustrated figure 8.10, increases with the total superficial velocity  $j$  from about 0.2 Hz ( $j \sim 1 \text{ m s}^{-1}$ ) to 1 Hz ( $j = 8 \text{ m s}^{-1}$ ). The results indicate that:

- The mean ‘unit-by-unit’ velocity ( $\overline{V}_i$ ) and the ‘entire record’ velocity ( $V_i^*$ ) are very similar, for all conditions. The difference between the predicted values is almost always less than 10%.
- The ‘unit-by-unit’ uncertainty ( $\Delta \overline{V}_i / \overline{V}_i$ ) is much larger than the ‘entire record’ uncertainty ( $\Delta V_i^* / V_i^*$ ), especially at large flowrates (25% compared to 5%). This large uncertainty is due to the short duration of each slug unit.

Therefore (unless it is specifically stated otherwise), the ‘entire record’ cross-correlation technique will be used to calculate the translation velocity. This choice means that the relative measurement uncertainty  $\Delta V_i / V_i$  will be much reduced. However, it is assumed as a consequence that all the slug units translate with the same velocity.

An assumption of the uncertainty model was that the signals  $x(t)$  and  $y(t)$  were uncorrelated with the additive noise component  $n(t)$  (section 5.2.1). This noise component is defined by:

$$n(t) = y(t + \tau^{\cdot}) - x(t) \quad [8.4]$$

The signals  $x(t)$  and  $y(t)$  and  $n(t)$  for the test points {0.1,0.6}, {0.1,3.0}, {1.0,0.6} and {1.0,6.0} are compared in figure 8.11. The noise component is clearly localised around the ‘slug’ zone, rather than being random. This effect is most pronounced at low gas flowrates, near the stratified flow boundary. Therefore, equation [8.3] is probably inappropriate at low gas flowrates. The effect upon the calculated uncertainty values is unclear.

## 8.2.2 Flow parameters

The translation velocity  $V_i$ , the phase fractions  $\overline{a}_f$  and  $a_s$ , the slug frequency  $\nu$ , and the lengths  $l_s$  and  $l_f$  are calculated for each ‘slug unit’. These parameters are listed in table 8.2, and the mean values are plotted as a function of the superficial velocity  $j$  in figure 8.12. The

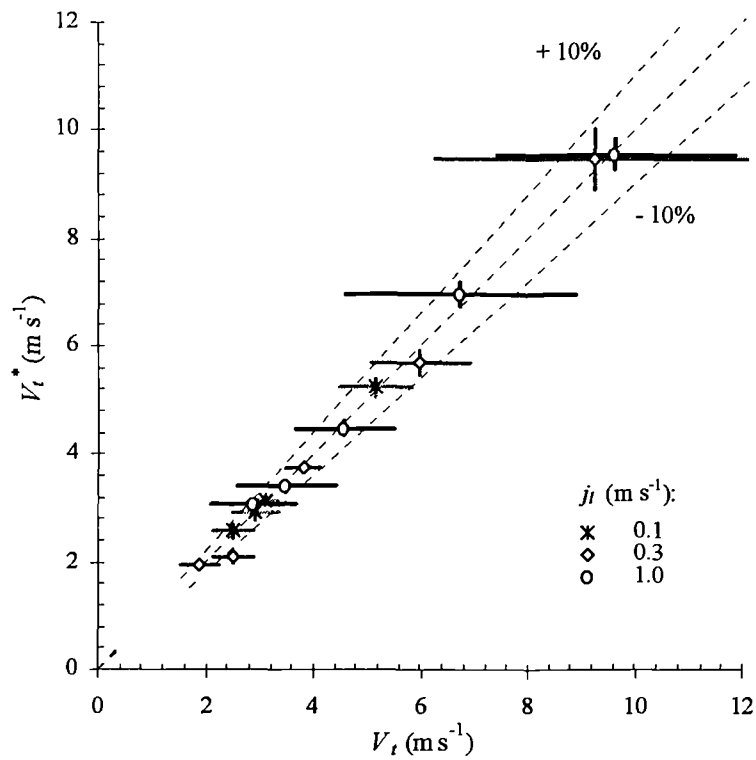


**Figure 8.9:** Comparison of the translation velocity  $V_t$  and the uncertainty  $\Delta V_t$  obtained using the ‘unit-by-unit’ cross-correlation and the ‘entire record’ cross-correlation techniques.

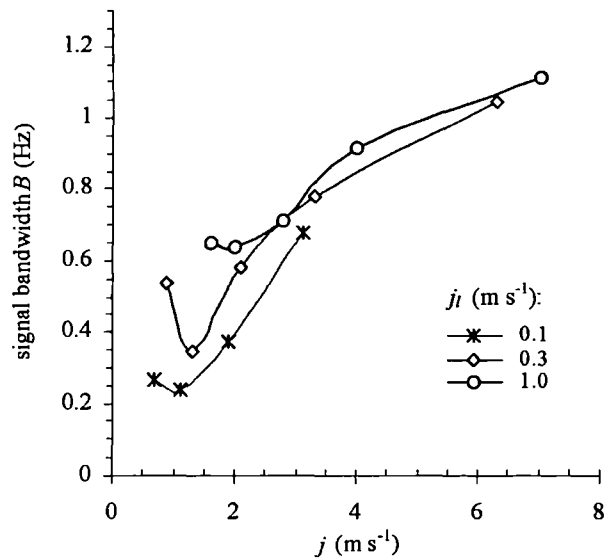


**Figure 8.10:** The signal bandwidth  $B$ , as a function of the total superficial velocity  $j$  (calculated using equation [7.4]).

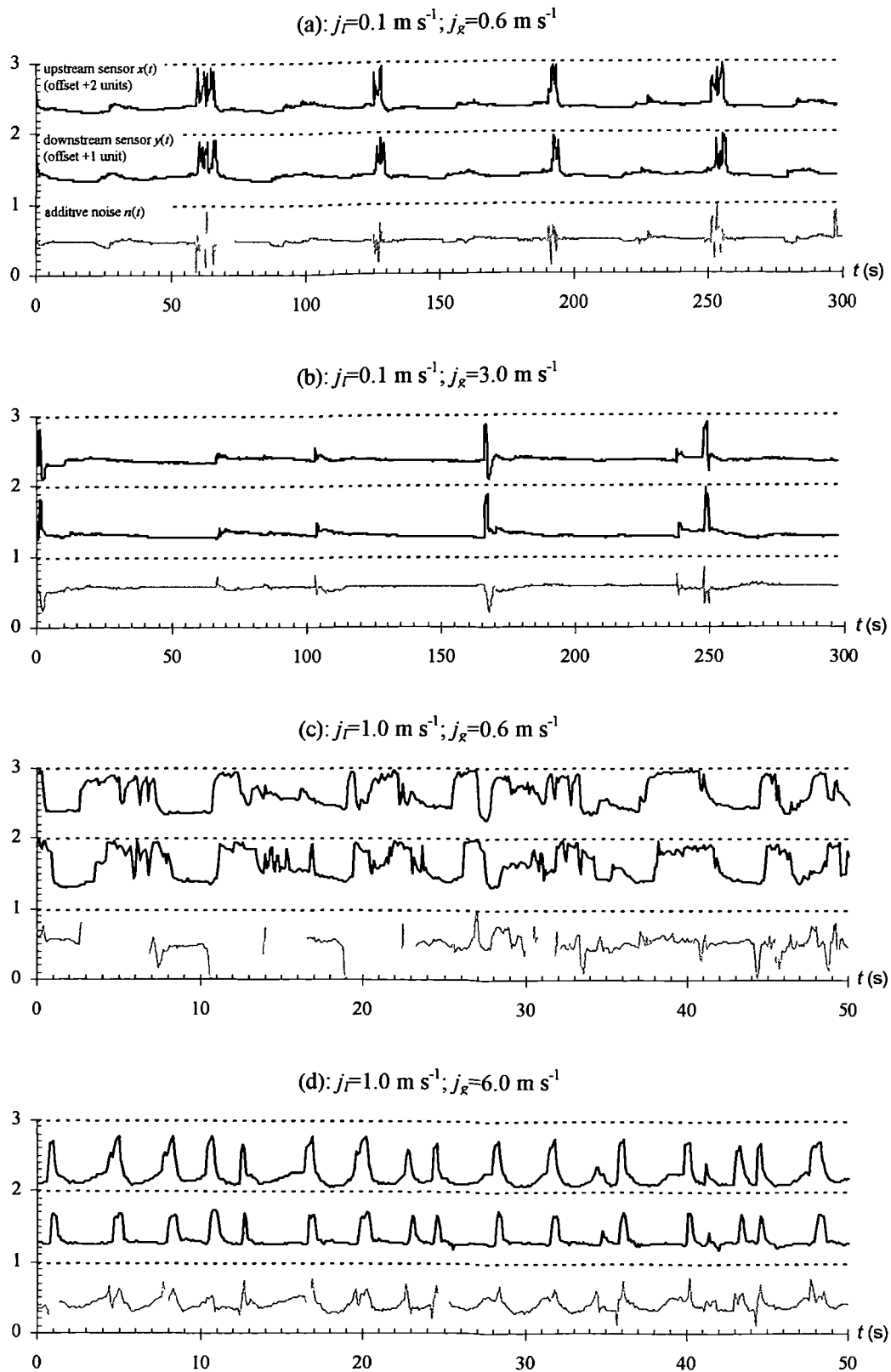


**Figure 8.11:** Comparison of the cross-correlation sensor data against the additive noise signal  $n(t)$ , for the test points  $a$ ,  $d$ ,  $j$  and  $n$  respectively.

standard distribution in these data is also shown, as a series of error bars. The following trends can be observed:

- The translation velocity  $V_t$  increases monotonously, with the total superficial velocity  $j$  (figure 8.12a). This increase occurs independently of the liquid superficial velocity,  $j_l$ .
- The slug holdup  $a_s$  and the film holdup  $\bar{a}_f$  both decrease, with the total superficial velocity  $j$  (figure 8.12b). The slug holdup is independent of the liquid velocity  $j_l$ , while the film holdup shows a weak dependency.
- The slug frequency  $\nu$  increases rapidly from 0.01 Hz to 1 Hz with the liquid velocity  $j_l$ , though it changes only modestly with the total velocity  $j$  (figure 8.12c).
- The film zone length  $l_f$  increases strongly with the liquid velocity  $j_l$ , while the slug length  $l_s$  remains approximately constant (figure 8.12d).

As shown, the standard distribution in the translation velocity and the holdup measurements are of the order  $\pm 1 \text{ m s}^{-1}$  and  $\pm 0.05$  respectively. However, the distribution in the slug frequency, the film length and the slug length are much larger (typically about a factor of 2). Therefore, the slug units translate with similar velocities and have similar phase fractions, but vary considerably in their length.

Figure 8.12 also displays the empirical correlations for the translation velocity, the phase fractions, the slug frequency and the slug lengths, used in Chapter 4 of the thesis. These were respectively:

$$V_t = C_o j - V_o \begin{cases} C_o = 1.10, & V_o = 0.54, & j(gD)^{-1/2} < 3 \\ C_o = 1.20, & V_o = 0, & j(gD)^{-1/2} > 3 \end{cases}$$

$$a_s = \begin{cases} 1, & j < 2.5 \text{ ms}^{-1} \\ 1.242 - 0.263 \ln j, & j > 2.5 \text{ ms}^{-1} \end{cases} \quad \bar{a}_f = (j_l - V_{ts} a_s) \frac{t_u}{V_t t_f} + a_s$$

$$\nu = 0.0037 \left( \frac{j_l}{gD} \cdot \frac{25 + j^2}{j} \right)^{18} \quad l_s = 15D \quad l_f = \frac{V_t}{\nu} - l_s \quad [8.5]$$

The correlations for the translation velocity (Woods & Hanratty<sup>127</sup>), the slug holdup and the film holdup agree reasonably well with the data, but cause some over-prediction (shown in figures 8.12a-b). The correlation of Manolis *et al*<sup>77</sup> predicts an upturn in the frequency at low velocities, which is not observed in practice (figure 8.12c). The film length  $l_f$  is

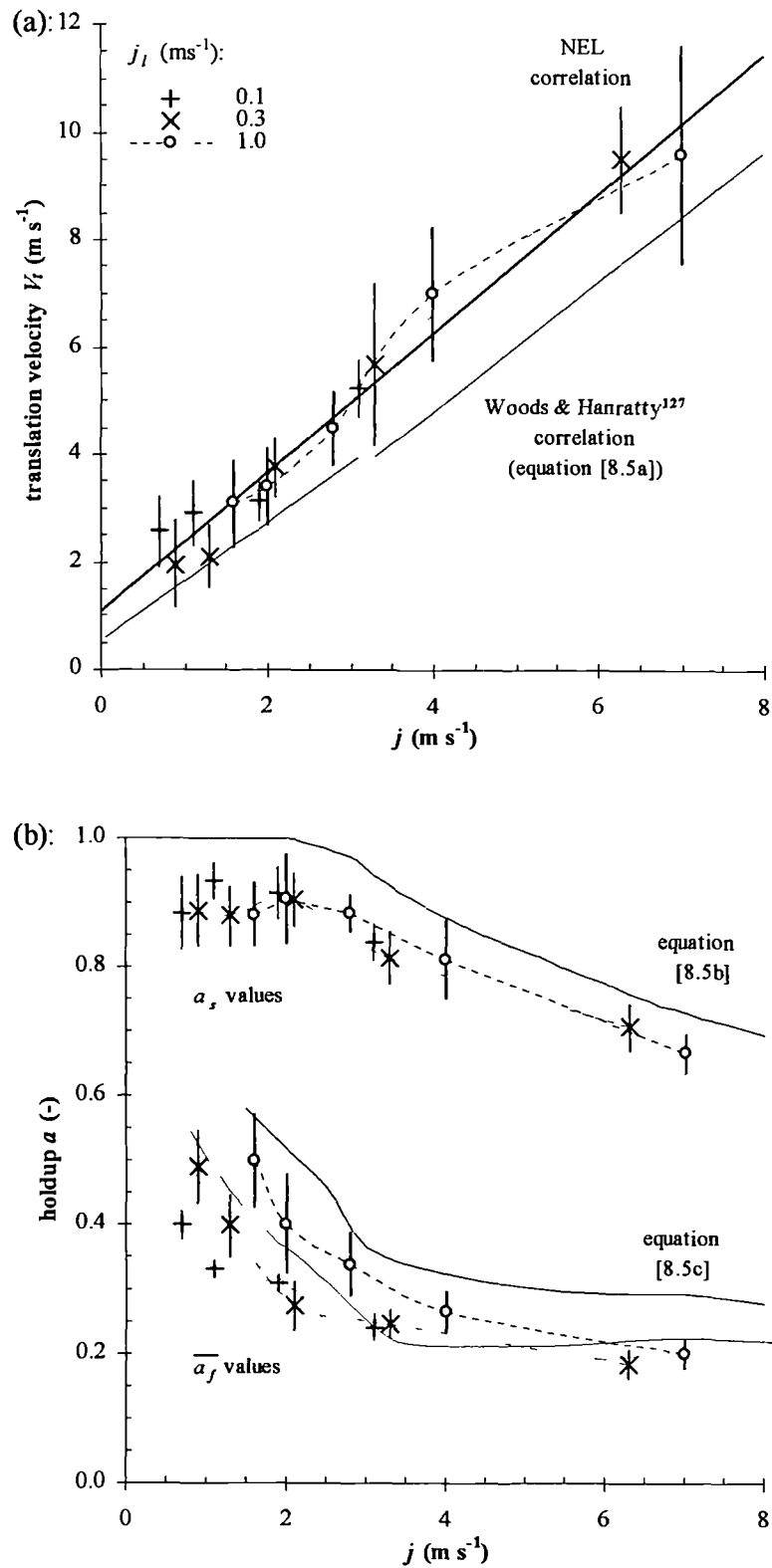


**Figure 8.12:** Mean parameter values, and the standard deviation, as a function of the total superficial velocity  $j$ : (a) the unit translation velocity  $V_t$ ; (b) the phase fractions  $\bar{a}_f$  and  $a_s$ .

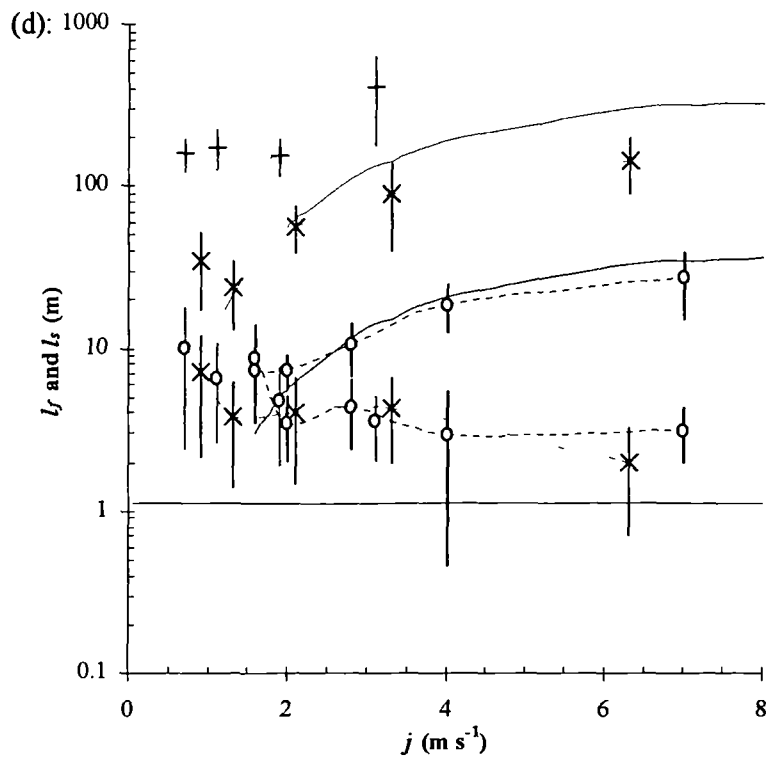
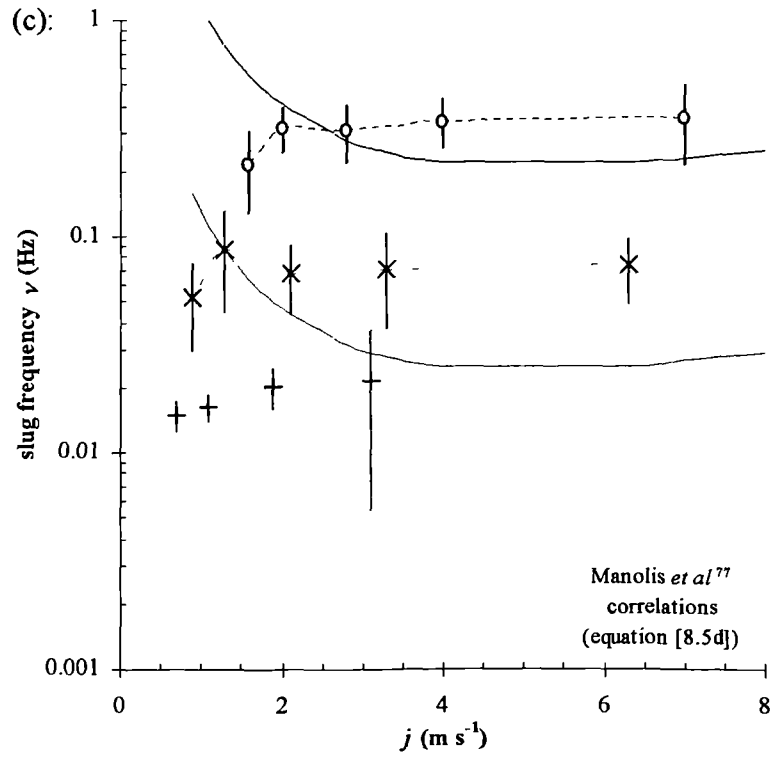


Figure 8.12 (continued): Mean parameter values, and the standard deviation, as a function of the total superficial velocity  $j$ : (c) the slug frequency  $\nu$ , (d) the film and slug lengths  $l_f$  and  $l_s$ .

test	$j_l$	$j_g$	$t$	$V_l$	$a_s$	$\bar{a}_f$	$l_f/l_u$	$\nu$			
a	0.1	0.6	60	3.80	0.84	0.39	0.90	0.015			
			126	2.69	0.84	0.38	0.96	0.015			
			191	2.01	0.83	0.39	0.95	0.016			
			252	2.19	0.83	0.40	0.95	0.013			
			331	2.56	0.94	0.40	0.96	0.015			
			396	1.68	0.92	0.41	0.99	0.013			
			471	2.56	0.94	0.44	0.97	0.013			
			547	3.08	0.95	0.39	0.89	0.020			
b	0.1	1.0	11	1.82	0.94	0.33	0.97	0.018			
			68	2.86	0.95	0.33	0.97	0.019			
			122	3.01	0.94	0.33	0.97	0.020			
			172	2.91	0.95	0.32	0.98	0.016			
			235	3.96	0.95	0.33	0.96	0.014			
			308	2.86	0.94	0.33	0.97	0.015			
			376	3.47	0.94	0.33	0.96	0.014			
			445	2.52	0.95	0.32	0.98	0.015			
			511	1.97	0.84	0.35	0.94	0.014			
			584	3.12	0.93	0.34	0.96	0.016			
			645	3.66	0.92	0.32	0.93	0.015			
			711	2.68	0.95	0.33	0.97	0.019			
			763	2.68	0.92	0.33	0.98	0.019			
			814	3.37	0.94	0.33	0.97	0.015			
c	0.1	1.8	1	3.57	0.94	0.31	0.96	0.016			
			65	2.82	0.94	0.31	0.97	0.020			
			116	2.92	0.92	0.32	0.98	0.020			
			165	3.26	0.89	0.28	0.96	0.018			
			219	2.84	0.93	0.31	0.98	0.019			
			273	3.08	0.92	0.30	0.97	0.025			
			313	3.27	0.92	0.30	0.98	0.016			
			376	3.12	0.94	0.31	0.94	0.019			
			429	3.04	0.92	0.30	0.98	0.031			
			461	2.63	0.80	0.32	1.00	0.022			
			507	4.03	0.92	0.31	0.97	0.019			
			d	0.1	3.0	166	5.32	0.84	0.25	0.99	0.012
						248	4.31	0.84	0.20	0.99	0.010
						369	5.08	0.89	0.27	0.99	0.012
449	5.08	0.85				0.23	0.99	0.016			
527	4.36	0.89				0.24	0.99	0.013			
606	5.32	0.83				0.26	0.99	0.008			
729	6.08	0.85				0.22	0.99	0.017			
787	5.58	0.83				0.23	0.99	0.012			
353	5.67	0.80				0.26	0.99	0.064			
512	5.40	0.82				0.23	0.98	0.067			
e	0.3	0.6				0	3.93	0.93	0.55	0.82	0.047
						9	0.77	0.94	0.54	0.73	0.029
			21	1.52	0.84	0.48	0.84	0.038			
			44	2.17	0.91	0.40	0.83	0.110			
			48	2.61	0.94	0.40	0.82	0.091			
			53	1.16	0.89	0.55	0.60	0.092			
			59	1.67	0.79	0.57	0.61	0.032			
			64	2.00	0.75	0.46	0.93	0.031			
			90	1.87	0.93	0.45	0.67	0.054			
			96	3.29	0.92	0.40	0.73	0.054			
			108	2.64	0.85	0.54	0.94	0.049			
			114	1.51	0.92	0.52	0.95	0.028			
			128	1.60	0.87	0.49	0.84	0.029			
			e			150	2.44	0.93	0.45	0.90	0.063
163	2.22	0.85				0.54	0.95	0.044			
f	0.3	1.0	2	2.43	0.93	0.36	0.78	0.074			
			16	1.50	0.86	0.41	0.86	0.101			
			26	2.05	0.87	0.43	0.81	0.085			
			37	2.69	0.86	0.32	0.82	0.082			
			50	1.47	0.86	0.44	0.91	0.068			
			64	1.84	0.87	0.38	0.97	0.148			
			71	2.00	0.84	0.34	0.77	0.053			
			90	1.64	0.86	0.49	0.96	0.220			
			94	2.43	0.93	0.38	0.96	0.063			
			110	2.87	0.93	0.34	0.93	0.066			
			125	2.44	0.82	0.37	0.80	0.069			
g	0.3	1.8	10	3.57	0.92	0.26	0.95	0.054			
			29	4.15	0.80	0.26	0.87	0.070			
			43	3.35	0.88	0.38	0.99	0.057			
			60	4.70	0.91	0.24	0.93	0.058			
			78	3.26	0.92	0.30	0.95	0.033			
			108	4.15	0.79	0.29	0.88	0.043			
			132	3.44	0.91	0.27	0.97	0.050			
			152	4.50	0.92	0.25	0.92	0.060			
			169	3.59	0.95	0.24	0.94	0.053			
			187	3.21	0.90	0.26	0.94	0.067			
			202	4.38	0.93	0.25	0.96	0.059			
h	0.3	3.0	10	6.75	0.85	0.24	0.97	0.055			
			28	7.21	0.85	0.23	0.96	0.055			
			46	5.91	0.86	0.26	0.92	0.105			
			56	3.76	0.86	0.28	0.97	0.114			
			65	4.67	0.47	0.25	0.92	0.034			
			94	7.88	0.81	0.26	0.97	0.030			
			127	6.44	0.86	0.29	0.83	0.161			
			134	1.54	0.88	0.26	0.94	0.034			
			163	6.54	0.81	0.24	0.96	0.055			
			181	6.25	0.83	0.24	0.95	0.069			
			195	5.06	0.85	0.23	0.96	0.056			
i	0.3	6.0	1	8.95	0.70	0.17	0.99	0.118			
			9	8.95	0.79	0.18	0.98	0.053			
			28	10.55	0.72	0.21	0.96	0.094			
			39	8.84	0.71	0.18	0.99	0.044			
			62	9.58	0.71	0.21	0.99	0.039			
			88	8.84	0.73	0.16	0.98	0.094			
			98	9.13	0.68	0.19	0.99	0.078			
			111	10.55	0.69	0.16	0.99	0.089			
			122	9.86	0.72	0.19	0.99	0.042			

**Table 8.2**—Data processing results. The start time  $t$ , the translation velocity  $V_l$ , the phase fractions  $a_f$  and  $a_s$ , the film length ratio  $l_f/l_u$  and the slug frequency  $\nu$ , for each slug unit. (First 15 slugs only, for east test point).

test	$j_l$	$j_g$	$t$	$V_l$	$a_s$	$\bar{a}_f$	$l_f/l_u$	$\nu$
			146	9.79	0.74	0.19	0.98	0.075
			159	10.16	0.72	0.15	0.98	0.110
			168	8.84	0.63	0.18	1.00	0.039
			194	8.15	0.72	0.23	0.99	0.080
			207	11.06	0.72	0.18	0.98	0.090
			218	8.61	0.70	0.18	0.99	0.056
$j$	1.0	0.6	3.1	2.54	0.88	0.42	0.41	0.128
			11.0	4.45	0.85	0.66	0.23	0.182
			16.5	2.73	0.84	0.54	0.95	0.357
			19.3	2.23	0.85	0.51	0.36	0.152
			25.8	3.64	0.97	0.39	0.42	0.412
			28.3	2.79	0.87	0.48	0.43	0.105
			37.8	2.71	0.94	0.49	0.45	0.145
			44.7	4.33	0.93	0.55	0.68	0.300
			48.0	2.09	0.84	0.53	0.59	0.239
			52.2	4.42	0.90	0.53	0.32	0.196
			57.3	2.95	0.91	0.34	0.60	0.188
			62.6	2.35	0.87	0.49	0.49	0.126
			70.5	4.20	0.85	0.50	0.41	0.158
			76.9	2.13	0.96	0.57	0.54	0.263
			80.7	3.09	0.81	0.50	0.56	0.327
$k$	1.0	1.0	1.3	3.08	0.88	0.33	0.59	0.262
			5.1	3.94	0.90	0.30	0.77	0.336
			8.1	2.56	0.88	0.51	0.63	0.293
			11.5	4.01	0.91	0.33	0.61	0.273
			15.2	3.15	0.96	0.30	0.78	0.343
			18.1	3.22	0.95	0.42	0.60	0.267
			21.9	4.43	0.92	0.39	0.87	0.382
			24.5	3.35	0.93	0.34	0.61	0.276
			28.1	3.94	0.94	0.36	0.82	0.522
			30.0	2.46	0.92	0.43	0.49	0.257
			33.9	4.05	0.91	0.33	0.66	0.312
			37.1	3.17	0.95	0.41	0.64	0.269
			40.8	4.01	0.97	0.39	0.67	0.260
			44.7	3.15	0.90	0.40	0.75	0.422
			47.1	2.50	0.92	0.34	0.59	0.235
$l$	1.0	1.8	1.7	4.43	0.90	0.28	0.77	0.257
			5.5	4.30	0.90	0.32	0.72	0.229
			9.9	5.22	0.93	0.31	0.82	0.287
			13.4	5.03	0.91	0.37	0.85	0.561
			15.2	5.15	0.88	0.45	0.56	0.266

test	$j_l$	$j_g$	$t$	$V_l$	$a_s$	$\bar{a}_f$	$l_f/l_u$	$\nu$
$l$			18.9	4.07	0.89	0.35	0.66	0.300
cont			22.3	4.09	0.85	0.36	0.55	0.464
			24.4	4.34	0.88	0.36	0.85	0.249
			28.5	4.75	0.88	0.35	0.61	0.240
			32.6	5.35	0.85	0.28	0.83	0.271
			36.3	5.09	0.83	0.29	0.74	0.474
			38.4	3.71	0.89	0.39	0.50	0.275
			42.1	3.32	0.87	0.36	0.63	0.296
			45.5	3.83	0.82	0.38	0.48	0.400
			48.0	4.83	0.89	0.37	0.65	0.251
$m$	1.0	3.0	0.7	7.48	0.80	0.25	0.85	0.337
			3.6	8.84	0.82	0.25	0.89	0.320
			6.8	7.01	0.84	0.28	0.92	0.320
			9.9	8.10	0.83	0.25	0.88	0.349
			12.8	6.87	0.79	0.26	0.90	0.360
			15.5	5.19	0.85	0.31	0.92	0.357
			18.3	7.56	0.86	0.34	0.84	0.337
			21.3	8.00	0.78	0.29	0.97	0.316
			24.5	8.61	0.83	0.27	0.92	0.341
			27.4	7.64	0.83	0.25	0.89	0.324
			30.5	8.61	0.83	0.26	0.95	0.246
			34.6	6.13	0.76	0.25	0.96	0.631
			36.2	8.20	0.85	0.26	0.64	0.446
			38.4	5.87	0.78	0.21	0.88	0.273
			42.1	5.62	0.89	0.27	0.92	0.329
$n$	1.0	6.0	0.8	10.55	0.66	0.19	0.92	0.261
			4.7	10.16	0.68	0.20	0.86	0.307
			7.9	7.36	0.67	0.23	0.79	0.388
			10.5	7.69	0.71	0.19	0.78	0.479
			12.6	12.04	0.65	0.17	0.96	0.250
			16.6	10.01	0.66	0.20	0.88	0.311
			19.8	8.35	0.69	0.21	0.82	0.325
			22.9	5.62	0.63	0.21	0.90	0.627
			24.5	11.15	0.62	0.18	0.94	0.277
			28.1	9.19	0.67	0.20	0.90	0.292
			31.5	10.01	0.66	0.20	0.91	0.231
			35.9	11.73	0.68	0.19	0.92	0.244
			40.0	10.39	0.70	0.22	0.91	0.310
			43.2	8.10	0.65	0.24	0.81	0.773
			44.5	12.15	0.63	0.19	0.94	0.291

Table 8.2: Continued.

reasonably well predicted, but the correlation of Nydal *et al*<sup>88</sup> under-predicts the slug length  $l_s$  by about a factor of two (figure 8.12d).

### 8.2.3 Flowrate predictions

In this thesis, the gas and liquid flowrates are inferred by calculating the phase superficial velocities ( $j_l$  and  $j_g$ ). These superficial velocities are equivalent the volumetric flowrates, per unit pipe cross-section area. The effect of the *closure relationships*, the *cross-correlation technique*, and the *averaging technique* upon the predicted flowrates is now assessed.

A variety of empirical correlations were presented in section 7.3, for calculating the local velocities within the slug body ( $V_{ls}$  and  $V_{gs}$ ). These correlations were organised into the following three groups:

$$j = \frac{V_t}{0.021 \ln(\text{Re}_s) + 0.022} \quad s = 1 \quad [8.6]$$

$$j = \frac{V_t - V_o}{C_o} \begin{cases} C_o = 1.10, & V_o = 0.54 \\ C_o = 1.20, & V_o = 0 \end{cases} \quad s = \begin{cases} 1, & j < 3 \text{ms}^{-1} \\ 1 + 0.125(j - 3), & 3 < j < 7 \text{ms}^{-1} \\ 1.5, & j > 7 \text{ms}^{-1} \end{cases} \quad [8.7]$$

$$j = \frac{V_t - 1.09}{1.29} \quad s = \begin{cases} 1, & j < 3 \text{ms}^{-1} \\ 1 + 0.125(j - 3), & 3 < j < 7 \text{ms}^{-1} \\ 1.5, & j > 7 \text{ms}^{-1} \end{cases} \quad [8.8]$$

(Equations [8.6a-b] are from Dukler & Hubbard<sup>30</sup>; [8.7a-b] from Woods & Hanratty<sup>127</sup>, and [8.8a] is obtained from the NEL facility). The effect of these different groups upon the predicted flowrates is shown in table 8.3 and figure 8.13. The results indicate that:

- The closure relationships strongly affect the prediction of the liquid phase flowrate. The first set (equations [8.6a]-[8.6b]) result in velocities that are approximately  $0.5 \text{ m s}^{-1}$  larger than those obtained with the second set (equations [8.7a]-[8.7b]), and about  $1.0 \text{ m s}^{-1}$  larger than those obtained with the third set (equations [8.8a]-[8.8b]).
- The closure relationships only affect the prediction for the gas phase flowrate, at high  $j_g$  values.

The differences in the predictions for the liquid phase flowrate are most apparent, at the largest velocities.

The effect of the ‘cross-correlation techniques’ and the ‘averaging techniques’ upon the predictions are summarised by figure 8.14. The ‘entire record’ and the ‘unit-by-unit’ cross-correlation techniques produce very similar results, for both the phase superficial velocities  $j_l$  and  $j_g$ . This is unsurprising, since the corresponding velocities  $\bar{V}_l$  and  $V_t^*$  are very similar (see section 8.2.1). Furthermore, the ‘parameter averaging’ and ‘ensemble averaging’ techniques also produce similar results for  $j_l$  and  $j_g$ . This implies that the measured flow is very close to ‘stable’ slug flow.

The *relative flowrate errors*  $\delta j_l/j_l$  and  $\delta j_g/j_g$  (i.e. the difference between the predicted and the

measured flowrates) are calculated, in order to assess the system performance. These results are listed in table 8.4, and are illustrated in figure 8.15. It emerges that:

- The errors in the phase flowrates rise substantially as the total flowrate reduces; from about 10% to 100% for the gas phase, and from about 50% to 500% for the liquid phase.
- The choice of closure relationships has little effect upon the prediction errors. The Woods & Hanratty<sup>127</sup> relationships generally give the best results, but the errors are still substantial.

In a commercial multiphase meter, it is necessary to measure the gas and liquid phase flowrates with at least a 5% relative accuracy (see section 2.5.3). The results presented in this section indicate that considerable improvement is necessary, to achieve this performance.

#### 8.2.4 Parameter uncertainties

Because the measurement process is imperfect, each of the model parameters suffers from some degree of uncertainty. This causes uncertainty in the superficial velocity predictions, which is defined by the equations:

$$\left| \frac{\Delta j_l}{j_l} \right| = \left| S_{j_l}(X) \frac{\Delta X}{X} \right| \quad \left| \frac{\Delta j_g}{j_g} \right| = \left| S_{j_g}(X) \frac{\Delta X}{X} \right| \quad [8.9]$$

where  $X \in \{V_t, \bar{a}_f, a_s, V_{ls}, V_{gs}, \theta, t_{film}\}$ , and  $S$  represents the *sensitivity* of each parameter within the stable slug flow model. The relative uncertainties  $\Delta \bar{V}_l / \bar{V}_l$ ,  $\Delta a_f / a_f$ ,  $\Delta a_s / a_s$ ,  $\Delta V_{ls} / V_{ls}$ ,  $\Delta V_{gs} / V_{gs}$ ,  $\Delta \theta / \theta$  and  $\Delta t_{film} / t_{film}$  (the ‘parameter uncertainties’) can be calculated, by using the equations presented in section 7.4. The results are shown in table 8.5, and can be summarised as follows:

- The uncertainty in the translation velocity ( $\Delta \bar{V}_l / \bar{V}_l$ ) is consistently between 5% and 10%, over the full range of test conditions.
- The uncertainty in the film holdup uncertainty ( $\Delta \bar{a}_f / \bar{a}_f$ ) and the slug holdup uncertainty ( $\Delta a_s / a_s$ ) are of the order of 5% at low  $j_g$ , but increase to about 10% as  $j_g$  rises.
- The uncertainty in the local liquid velocity ( $\Delta V_{ls} / V_{ls}$ ) and the local gas velocity

test	closure model:		superficial velocities					
	$j_l$	$j_g$	Type 1		Type 2		Type 3	
			$j_l$	$j_g$	$j_l$	$j_g$	$j_l$	$j_g$
<i>a</i>	0.1	0.6	0.70	1.39	0.42	1.35	-0.18	1.27
<i>b</i>	0.1	1.0	0.58	1.87	0.30	1.85	-0.37	1.80
<i>c</i>	0.1	1.8	0.54	2.04	0.28	2.02	-0.40	1.95
<i>d</i>	0.1	3.0	0.56	3.74	0.47	3.83	-0.41	3.56
<i>e</i>	0.3	0.6	0.79	0.78	0.48	0.74	-0.06	0.67
<i>f</i>	0.3	1.0	0.80	1.30	0.52	1.26	-0.08	1.18
<i>g</i>	0.3	1.8	0.63	2.53	0.42	2.51	-0.33	2.43
<i>h</i>	0.3	3.0	0.84	4.15	0.66	4.33	-0.19	3.99
<i>i</i>	0.3	6.0	0.68	7.03	-0.02	7.73	-0.78	7.11
<i>j</i>	1.0	0.6	1.57	0.83	1.57	0.83	0.68	0.71
<i>k</i>	1.0	1.0	1.43	1.48	1.20	1.45	0.48	1.38
<i>l</i>	1.0	1.8	1.64	2.17	1.44	2.18	0.65	2.05
<i>m</i>	1.0	3.0	1.38	4.24	1.12	4.50	0.26	4.12
<i>n</i>	1.0	6.0	1.40	6.64	0.64	7.41	-0.12	6.76

**Table 8.3:** Superficial velocity predictions, using the closure models 1, 2 and 3 listed in Table 7.1.

test	closure model:		absolute errors						relative errors					
	$j_l$	$j_g$	Type 1		Type 2		Type 3		Type 1		Type 2		Type 3	
			$\Delta j_l$	$\Delta j_g$	$\Delta j_l$	$\Delta j_g$	$\Delta j_l$	$\Delta j_g$	$\Delta j_l/j_l$	$\Delta j_g/j_g$	$\Delta j_l/j_l$	$\Delta j_g/j_g$	$\Delta j_l/j_l$	$\Delta j_g/j_g$
<i>a</i>	0.1	0.6	0.60	0.79	0.32	0.75	-0.26	0.67	600	131	321	125	-276	112
<i>b</i>	0.1	1.0	0.48	0.87	0.20	0.85	-0.47	0.80	475	87	205	85	-473	80
<i>c</i>	0.1	1.8	0.44	0.24	0.18	0.22	-0.50	0.15	436	13	179	12	-501	9
<i>d</i>	0.1	3.0	0.46	0.74	0.37	0.83	-0.51	0.56	457	25	366	28	-514	19
<i>e</i>	0.3	0.6	0.49	0.18	0.18	0.14	-0.36	0.07	163	30	59	24	-120	12
<i>f</i>	0.3	1.0	0.49	0.31	0.21	0.27	-0.38	0.19	166	30	74	26	-125	18
<i>g</i>	0.3	1.8	0.33	0.73	0.12	0.71	-0.63	0.63	110	41	38	39	-211	35
<i>h</i>	0.3	3.0	0.54	1.15	0.36	1.33	-0.49	0.99	179	38	120	44	-164	33
<i>i</i>	0.3	6.0	0.38	1.03	-0.32	1.73	-1.08	1.11	127	17	-105	29	-361	19
<i>j</i>	1.0	0.6	0.57	0.23	0.57	0.23	-0.32	0.11	57	39	57	39	-32	19
<i>k</i>	1.0	1.0	0.43	0.48	0.20	0.45	-0.52	0.38	43	48	20	45	-52	38
<i>l</i>	1.0	1.8	0.64	0.37	0.44	0.38	-0.35	0.25	64	21	44	21	-35	14
<i>m</i>	1.0	3.0	0.38	1.24	0.12	1.50	-0.74	1.12	38	41	12	50	-74	37
<i>n</i>	1.0	6.0	0.40	0.64	-0.36	1.41	-1.12	0.76	40	11	-36	23	-112	13

**Table 8.4:** The superficial velocities, absolute errors, and relative errors, expressed as percentages. These data are obtained using ‘entire record’ cross-correlation, ‘parameter-averaging’, and the closure models 1, 2 and 3.

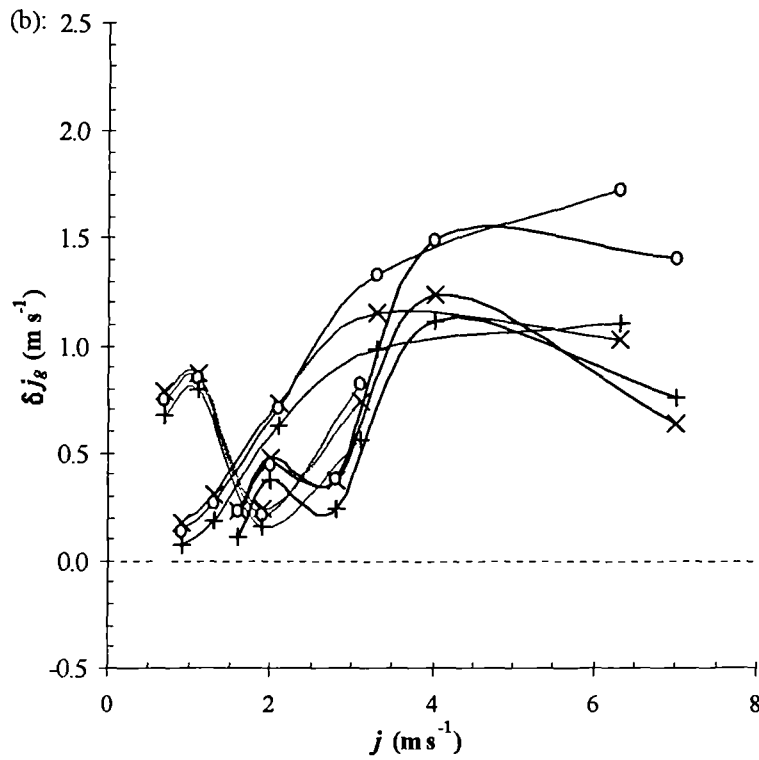
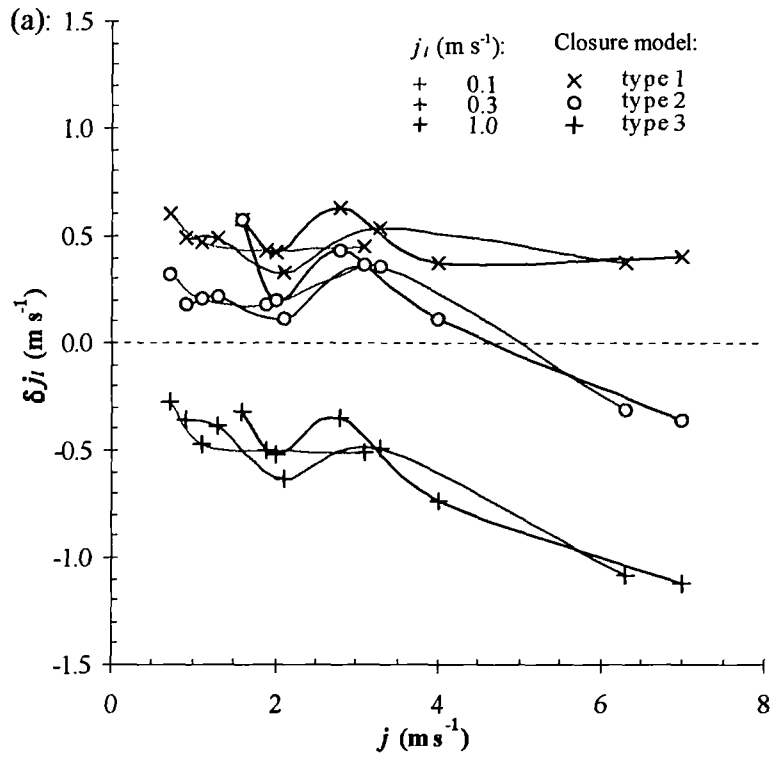


**Figure 8.13:** Superficial velocity predictions, calculated using the closure models 1, 2, and 3 (equations [8.6] to [8.8]). (a) liquid phase; (b) gas phase.

$(\Delta V_{gs}/V_{gs})$  are about 50% at low  $j_g$ , but reduce to about 10% as  $j_g$  rises.

- The ‘threshold level’ uncertainty ( $\Delta\theta/\theta$ ) is typically around 15%, while the ‘film duration’ uncertainty reduces from 90% to 50%, as  $j_l$  is increased.

In decreasing order of significance, uncertainties occur in the *data processing* parameters  $\theta$  and  $t_{film}$ , the *local velocities*  $V_{ls}$  and  $V_{gs}$ , then the translation velocity and the phase fraction parameters,  $V_t$ ,  $\bar{a}_f$  and  $a_s$ . These uncertainties are generally most substantial, at *low total flowrates*.

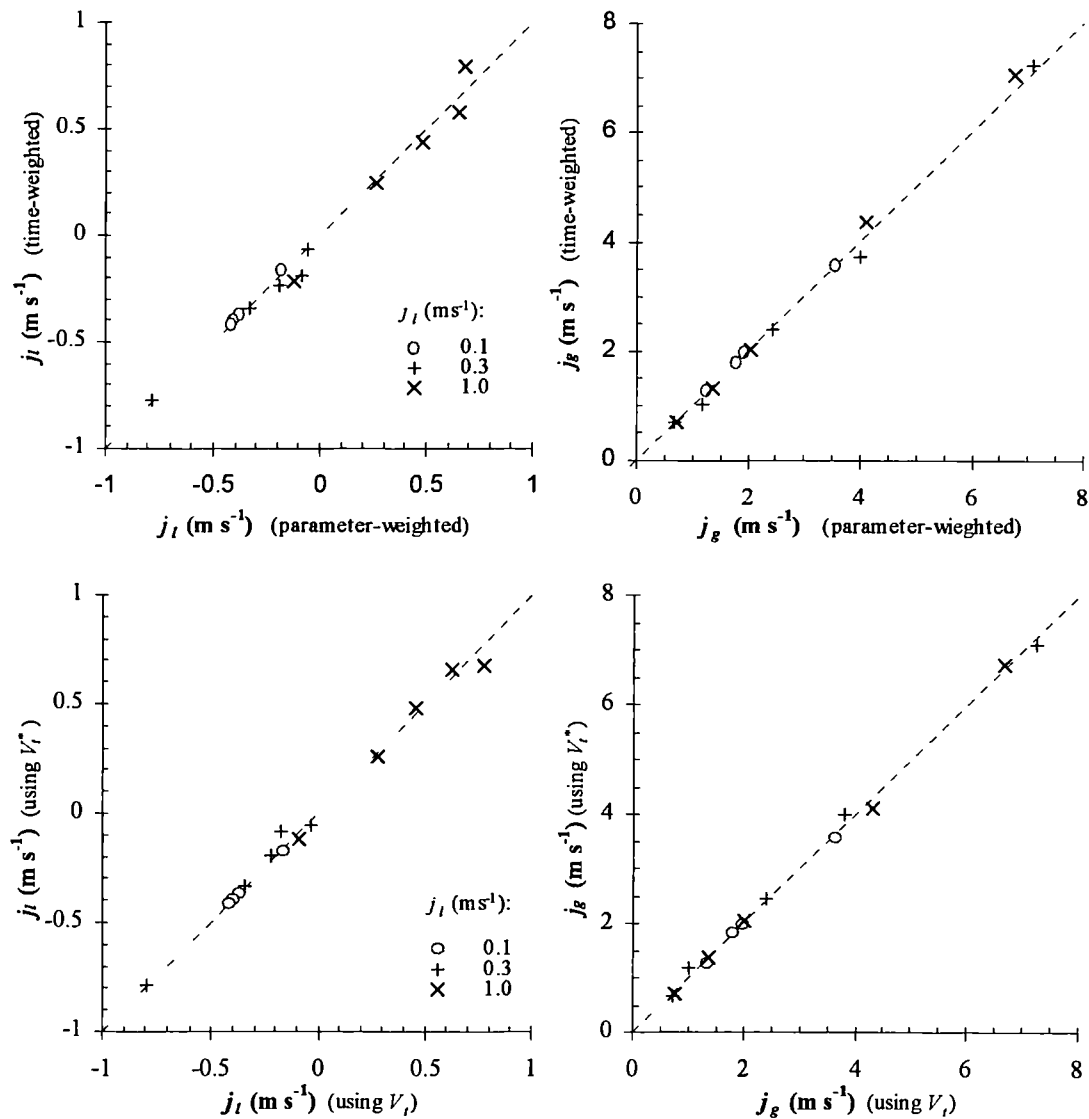


**Figure 8.14:** The effect of different techniques for *averaging* the sensor data and calculating the *translation velocity techniques* upon the superficial velocities  $j_l$  and  $j_g$ .

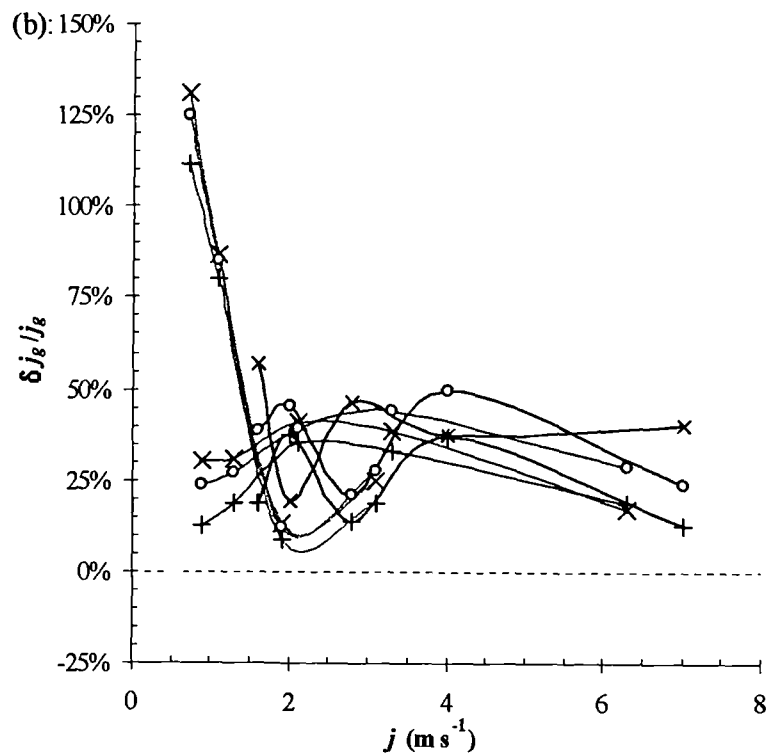
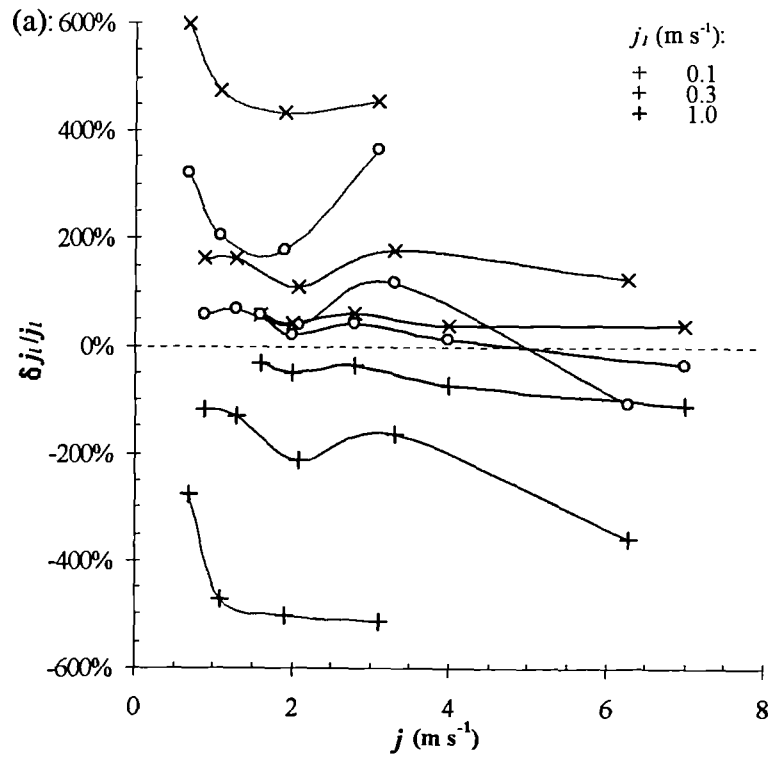


**Figure 8.15:** Relative errors in the superficial velocities, using closure models 1, 2, and 3 (equations [8.6] to [8.8]). (a) liquid phase; (b) gas phase.

test	$j_l$	$j_g$	measurement errors			slug velocity errors		data processing errors	
			$\Delta V_l/V_l$	$\Delta a_f/a_f$	$\Delta a_s/a_s$	$\Delta V_{ls}/V_{ls}$	$\Delta V_{gs}/V_{gs}$	$\Delta \theta/\theta$	$\Delta t_{film}/t_{film}$
a	0.1	0.6	11	5	3	44	60	14	90
b	0.1	1.0	10	7	2	34	51	14	90
c	0.1	1.8	5	7	2	28	44	14	90
d	0.1	3.0	7	9	4	16	29	14	90
e	0.3	0.6	4	6	3	62	73	14	75
f	0.3	1.0	8	8	3	56	72	14	75
g	0.3	1.8	4	9	2	22	40	14	75
h	0.3	3.0	7	9	4	16	27	17	75
i	0.3	6.0	10	12	8	14	17	20	75
j	1.0	0.6	5	12	3	33	47	14	50
k	1.0	1.0	5	15	2	28	43	14	50
l	1.0	1.8	6	14	3	20	35	14	50
m	1.0	3.0	6	14	5	15	25	17	50
n	1.0	6.0	6	15	10	14	17	20	50

**Table 8.5:** Relative uncertainties in the measurement of the parameters  $V_l$ ,  $a_f$  and  $a_s$ , and the estimates for  $V_{ls}$  and  $V_{gs}$ ,  $\theta$  and  $t_{film}$ , expressed as percentages. (Results obtained using ‘entire record’ cross-correlation, ‘parameter-averaging’ and ‘Closure model 3’).

### 8.2.5 Flowrate uncertainties

The phase flowrates (i.e. the superficial velocities  $j_l$  and  $j_g$ ) are subject a series of *uncertainty margins*, due to the uncertainty in the model parameters. In this thesis, these uncertainty margins are calculated by using equation [8.9], with the sensitivity coefficients defined by:

$$S_{j_l}(X) = \frac{\partial j_l}{\partial X} \cdot \frac{X}{j_l} \qquad S_{j_g}(X) = \frac{\partial j_g}{\partial X} \cdot \frac{X}{j_g} \qquad [8.10]$$

Table 8.6 summarises the resulting uncertainty components  $\Delta j_l/j_l$  and  $\Delta j_g/j_g$ , for each of the model parameters  $V_l$ ,  $\overline{a_f}$ ,  $a_s$ ,  $V_{ls}$ ,  $V_{gs}$ ,  $\theta$  and  $t_{film}$ . The relative sizes of these components are also compared for the two specific sets of flowrates  $j_l=0.1 \text{ m s}^{-1}$ ,  $j_g=1.0 \text{ m s}^{-1}$  and  $j_l=1.0 \text{ m s}^{-1}$ ,  $j_g=6.0 \text{ m s}^{-1}$ , in figure 8.16. From these results, the following trends are observed:

- The uncertainty in the liquid flowrate ( $\Delta j_l/j_l$ ) is at least an order of magnitude larger much than the uncertainty in the gas flowrate ( $\Delta j_g/j_g$ ), when  $j_l$  is small.
- The uncertainty in the liquid flowrate is dominated by the uncertainty in the *local liquid velocity* and the *translation velocity* measurements. These components are

about 50% and 20% respectively when  $j_l$  is large ( $1 \text{ m s}^{-1}$ ), but increase to about 400% and 100% respectively as  $j_l$  reduces.

- The contributions made by the mean film holdup  $\bar{a}_f$ , the gas holdup  $a_s$ , and the threshold level  $\theta$  to the liquid flowrate uncertainty ( $\Delta j_l/j_l$ ) increase in significance as  $j_g$  increases.
- The uncertainty in the gas flowrate ( $\Delta j_g/j_g$ ) is much smaller than the uncertainty in the liquid flowrate, and is not dominated by any one single component. At small values of  $j$ , the *translation velocity* component is relatively large (about 20%), but all components reduce to 10% as  $j$  increases.

The flowrate uncertainties in table 8.6 are clearly comparable with the flowrate errors presented in section 8.3, in particular for the *liquid phase*. The dominant sources of these uncertainties are the *local velocity* and the *translation velocity* measurements,  $V_{ls}$  and  $V_t$ . These uncertainties must be reduced significantly, if accurate metering of the flowrates is to be achieved.

test	$j_l$	$j_g$	Liquid flowrate ( $\Delta j_l/j_l$ ):						Gas flowrate( $\Delta j_g/j_g$ ):					
			$V_t$	$\bar{a}_f$	$a_s$	$V_{ls}$	$\theta$	$t_{film}$	$V_t$	$\bar{a}_f$	$a_s$	$V_{gs}$	$\theta$	$t_{film}$
<i>a</i>	0.1	0.6	125	48	29	377	7	44	21	8	0	11	1	11
<i>b</i>	0.1	1.0	167	58	19	390	17	6	17	6	0	4	2	1
<i>c</i>	0.1	1.8	95	61	25	389	5	14	5	3	0	3	5	4
<i>d</i>	0.1	3.0	207	103	63	425	0	18	7	3	0	5	0	5
<i>e</i>	0.3	0.6	9	10	7	123	16	25	4	5	0	8	9	24
<i>f</i>	0.3	1.0	29	16	8	125	13	13	9	5	0	6	4	14
<i>g</i>	0.3	1.8	29	25	9	132	6	4	5	4	0	3	1	2
<i>h</i>	0.3	3.0	81	40	24	144	5	26	8	4	0	6	0	2
<i>i</i>	0.3	6.0	188	63	68	182	30	0	9	3	1	7	1	0
<i>j</i>	1.0	0.6	3	3	0	38	16	0	5	5	0	13	6	3
<i>k</i>	1.0	1.0	7	6	1	39	7	7	7	6	0	7	6	2
<i>l</i>	1.0	1.8	10	8	1	40	5	0	6	4	0	6	3	0
<i>m</i>	1.0	3.0	21	14	6	44	8	8	7	5	0	7	1	1
<i>n</i>	1.0	6.0	23	20	19	56	19	2	4	3	1	8	1	0

**Table 8.6:** Relative uncertainty in the flowrates due to the uncertainties listed in Table 8.5: (a) liquid phase  $\Delta j_l/j_l$ ; (b) gas phase  $\Delta j_g/j_g$  (expressed as percentages).

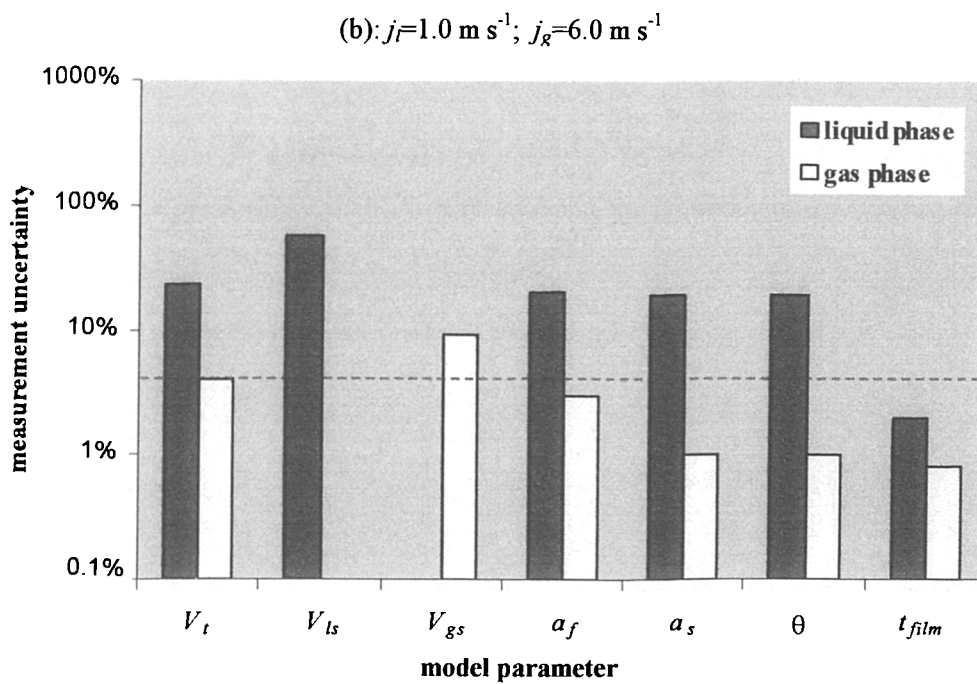
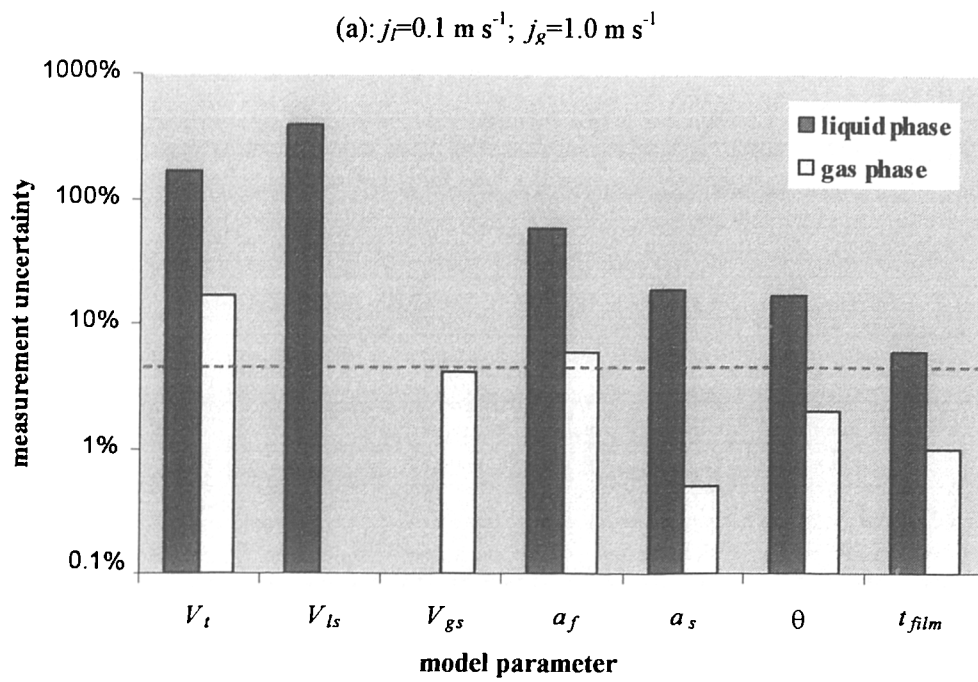


Figure 8.16: Comparison of the sensitivities for each model parameter, for the two conditions  $\{j_l=0.1 \text{ m s}^{-1}; j_g=1.0 \text{ m s}^{-1}\}$  and  $\{j_l=1.0 \text{ m s}^{-1}; j_g=6.0 \text{ m s}^{-1}\}$

### 8.3 Interpretation

The metering system has been tested in gas-water slug flow, with liquid superficial velocities from 0.1 to 1 m s<sup>-1</sup>, and gas superficial velocities from 0.6 to 6 m s<sup>-1</sup>. The data have been used to predict the superficial velocities, and obtain the errors and the uncertainty margins. The stable slug flow model does not do a good job at predicting the phase flowrates. The errors and the uncertainty are largest for the *liquid phase*, at low flowrates, with a strong dependency upon the choice of the *closure relationships*. These results will now be interpreted.

#### 8.3.1 Validity of the slug flow model

The validity of the stable slug flow model is assessed, by calculating the total measurement uncertainty. This calculation is based on the assumption that each of the seven uncertainty components is *statistical* in nature, such that:

$$\left| \frac{\Delta j_l}{j_l} \right|_{total}^2 = \sum \left| S_{j_l}(X) \frac{\Delta X}{X} \right|^2 \quad \left| \frac{\Delta j_g}{j_g} \right|_{total}^2 = \sum \left| S_{j_g}(X) \frac{\Delta X}{X} \right|^2 \quad [8.11]$$

where  $X$  is the set of parameters  $\{V_l, \alpha_f, \alpha_s, V_{ls}, V_{gs}, \theta, t_{film}\}$ . Strictly speaking, the components listed in table 8.6 are a mixture of statistical and absolute uncertainties, but this approach simplifies the interpretation.

The total measurement uncertainty is compared against the measurement error in figure 8.17 below. From these graphs, it is clear that:

- The liquid phase uncertainty is generally a similar size to the liquid phase error. Therefore, it is not possible to *disprove* the validity of the model, until a more accurate measurement for the liquid flowrate is obtained.
- The gas phase uncertainty is generally smaller than the gas phase error, with the discrepancy becoming substantial at low flowrates. Therefore, there are systematic measurement errors that have not been accounted for, or the predictive model is inappropriate.

To improve results, it may be necessary to modify the model for the gas flowrate at low velocities. However, a more pressing concern is to measure the model parameters with greater accuracy. In particular, this accuracy is necessary in the measurement of the local velocities  $V_{ls}$  and  $V_{gs}$ . The closure relationships that have been used to define the *total*

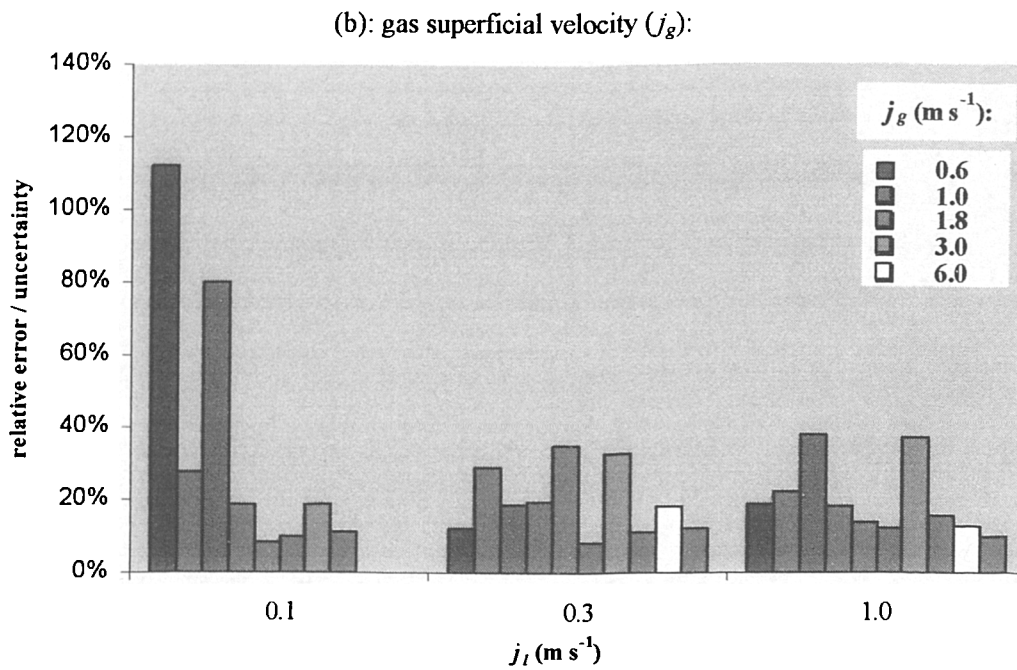
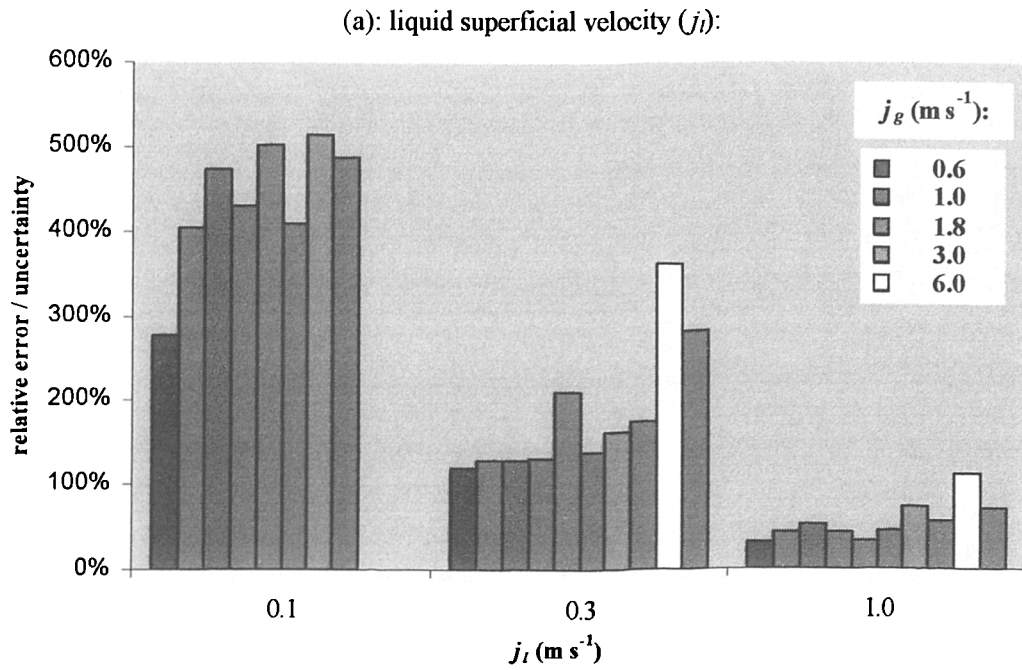


**Figure 8.17:** Comparison of the predictions errors  $\delta j_l/j_l$  and  $\delta j_g/j_g$  (shown in grey) against the cumulative uncertainty margins  $\Delta j_l/j_l$  and  $\Delta j_g/j_g$  (various colours). (a) liquid phase comparison; (b) gas phase comparison.

*superficial velocity* ( $j$ ) and the *slip parameter* ( $s$ ) are now discussed.

### 8.3.2 The total superficial velocity ( $j$ )

Three correlations were used to define the total superficial velocity  $j$ : equation [8.8a] (Dukler & Hubbard<sup>30</sup>); equation [8.9a] (Woods & Hanratty<sup>127</sup>); and equation [8.10a] (based on the NEL data). In general, the correlation of Woods & Hanratty<sup>127</sup> gave the most accurate results. This is surprising, considering that equation [8.10a] was specifically developed using data from the NEL facility. Two reasons are offered:

- The cross-correlation sensors have *unequal dynamics*, causing a systematic error in the measurement of the translation velocity  $V_t$ . The imperfections in the design of the upstream sensor (discussed in section 8.1.4 above) means that it responds to the flow in a slightly different way.
- Woods & Hanratty use two different linear correlations to fit their experimental data (for a total superficial velocity  $j < 3 \text{ m s}^{-1}$  and for  $j > 3 \text{ m s}^{-1}$ ). The correlation for the low velocity reflects the fact that there is a *drift velocity* component present in plug flow.

In order to reduce the measurement errors  $\delta j_t$  and  $\delta j_g$ , it is necessary to develop a better correlation for the total superficial velocity  $j$ . This can be done in two ways. First of all, the upstream cross-correlation sensor can be dismantled, and modified so that it is exactly identical to the downstream sensor. This will reduce systematic errors in the measured signal  $x(t)$ , and the additive noise signal  $n(t)$ . Secondly, a separate correlation between the translation velocity  $V_t$  and the total superficial velocity can be developed, for low flowrates.

### 8.3.3 The slip ratio ( $s$ )

Two correlations were used to define the slip ratio  $s$ : equation [8.8b] (the ‘no slip’ model of Dukler & Hubbard<sup>30</sup>) and equation [8.9b] (based on the data of Woods & Hanratty<sup>127</sup>). The effect of these correlations upon the flowrates was not specifically investigated. However, the predictions will only differ for superficial velocities above  $3 \text{ m s}^{-1}$ , and *neither* method is expected to give particularly accurate results. This is because the local velocities  $V_{ls}$  and  $V_{gs}$  are derived from the equations:

$$V_{ls} = \frac{j}{a_s + s(1 - a_s)} \quad V_{gs} = \frac{sj}{a_s + s(1 - a_s)} \quad [8.12]$$

Even if the slip parameter can be measured with perfect accuracy (i.e.  $\delta_s=0$ ), the dependency of  $V_{ls}$  and  $V_{gs}$  upon the slug holdup  $\alpha_s$  and the total velocity  $j$  can introduce substantial errors. Therefore, it is better to determine the velocities  $V_{ls}$  and  $V_{gs}$  by a different approach.

In stable slug flow, phase superficial velocities are much less sensitive to the measurement of film velocities  $V_{lf}$  and  $V_{gf}$  than the slug velocities  $V_{ls}$  and  $V_{gs}$ . This is demonstrated by writing the flowrate equations in the form:

$$j_l = V_{ls} \alpha_s \frac{l_s}{l_u} + \overline{V_{lf}} \alpha_f \frac{l_f}{l_u} \quad j_g = V_{gs} (1 - \alpha_s) \frac{l_s}{l_u} + \overline{V_{gf}} (1 - \alpha_f) \frac{l_f}{l_u} \quad [8.13]$$

Assuming that the film zone holdup rapidly approaches its equilibrium value  $\alpha_{fe}$  (such that  $\overline{V_{lf}} \alpha_f = \overline{V_{lf}} \alpha_{fe}$  and  $\overline{V_{gf}} (1 - \alpha_f) = \overline{V_{gf}} (1 - \alpha_{fe})$ ), partial differentiation of equation [8.13] results in the ratios:

$$\frac{S_{j_l}(V_{lf})}{S_{j_l}(V_{ls})} = \left\{ \frac{\overline{\alpha_f} \cdot l_f \cdot \overline{V_{lf}}}{\alpha_s \cdot l_s \cdot V_{ls}} \right\} \quad [8.14]$$

and:

$$\frac{S_{j_g}(V_{gf})}{S_{j_g}(V_{gs})} = \left\{ \frac{1 - \overline{\alpha_f} \cdot l_f \cdot \overline{V_{gf}}}{1 - \alpha_s \cdot l_s \cdot V_{gs}} \right\} \quad [8.15]$$

The sensitivity  $S_{j_l}(V_{lf})$  is normally much smaller than  $S_{j_g}(V_{lf})$ , since the film holdup  $\overline{\alpha_f}$  is smaller than  $\alpha_s$ ,  $V_{lf}$  is smaller than  $V_{ls}$  and  $l_f$  is smaller than  $l_s$  (especially at low liquid flowrates; see table 8.3). Similarly,  $S_{j_g}(V_{gf})$  is usually smaller than  $S_{j_g}(V_{gs})$ , since although  $1 - \alpha_f$  is larger than  $1 - \alpha_s$ ,  $V_{gf}$  is smaller than  $V_{gs}$  and  $l_f$  is smaller than  $l_s$  as before. Therefore, the measurement uncertainty will be significantly reduced by making a direct measurement of the film velocities. The difficulties with this measurement were highlighted in Chapter 4, and will be discussed further in Chapter 9 that follows.

#### **8.4 Summary**

In this chapter, the slug flow metering system was assessed, using slug flow data obtained from the NEL facility. The flow loop, the measurement system and the raw data were described; the raw data were processed and predictions for the phase flowrates were

presented; then, the results were interpreted by comparing the prediction errors and uncertainty margins.

Section 8.1 described the ‘raw’ data obtained using the NEL loop and the measurement system developed in Chapters 5 to 7. The data were obtained for the set of liquid superficial velocities  $j_l=0.1$  to  $1.0 \text{ m s}^{-1}$  and gas superficial velocities  $j_g=0.6$  to  $6.0 \text{ m s}^{-1}$ , and covered ‘plug flow’, ‘slug flow’ and ‘slug-annular’ flow conditions.

Section 8.2 described the analysis of the sensor data, using the software developed in Chapter 7. The results are summarised as follows:

- The ‘unit-by-unit’ and the ‘entire record’ cross-correlation techniques resulted in similar values for the cross-correlation function  $\rho_{xy}$  and the translation velocity  $V_t$  (section 8.2.1). However, the ‘entire record’ technique results in a much smaller uncertainty component,  $\Delta V_t/V_t$ .
- Measurements of the translation velocity  $V_t$ , the slug holdup  $a_s$ , and the mean film holdup  $\bar{a}_f$  agree well with the existing correlations, though there is discrepancy in measurements of the frequency  $\nu$ , the film length  $l_f$  and the slug length  $l_s$  (section 8.2.2). Generally, the slug units travel at the same velocity, but vary considerably in length.
- The predictions for the phase flowrates (i.e. the superficial velocities  $j_l$  and  $j_g$ ) show large errors, of up to 500% and 100% for the liquid and gas phases respectively (section 8.2.3). Therefore, the system is *ineffective* at metering the flow. The worst errors occur at low liquid flowrates, and are strongly dependent upon the choice of empirical closure relationships.
- The uncertainty in the local liquid velocity measurement ( $\Delta V_{ls}/V_{ls}$ ) and the translation velocity measurement are extremely large, particularly at low gas flowrates (section 8.2.4). This is due to the scatter in the correlations for the total velocity ( $j$ ) and the slip parameter ( $s$ ).
- The uncertainty in the liquid flowrate ( $\Delta j_l/j_l$ ) is much larger than the uncertainty in the gas flowrate ( $\Delta j_g/j_g$ ) (section 8.2.5). This uncertainty is largely due to inability to measure the local liquid velocity  $V_{ls}$  and the translation velocity  $V_t$  accurately, and exceeds the predicted values themselves at low liquid flowrates.

Section 8.3 provided an interpretation of the experimental results. The total flowrate uncertainties were computed using a statistical model, and were compared against the

flowrate errors. Except at very low gas flowrates, it was concluded that the *measurement accuracy* is insufficient as opposed to the stable slug flow being invalid. The empirical correlations for the total velocity  $j$  and the slip velocity  $s$  were then examined, to see how the measurement accuracy could be improved.

By analysing the experimental results, the last of the four objectives that was proposed in Chapter 1 has been completed. In the following (and final) chapter, the outcomes of each objective will be summarised and some further work will be proposed.

## 9. Conclusions

In this thesis, a new system for metering two-phase slug flow was developed. This system combined a slug flow model, non-intrusive instrumentation for measuring each of the model parameters, and a computer system for analysis of the data and delivery of the phase flowrates. Gas-water two-phase flow was studied in order to simplify the instrumentation and determine the overall success of the approach. There were four objectives presented in the introduction section, which were as follows:

- Review the background literature that describes sensing instrumentation within the multiphase flow meter, and methods for modelling slug flow.
- To assess the suitability of the approach by conducting a sensitivity analysis upon the slug flow model, and then proposing techniques for making each parameter measurement.
- To develop instrumentation (consisting of non-intrusive sensors and electronics) and processing software to enable calculation of the phase flowrates and the flowrate uncertainties.
- To assess the performance of the system, using the NEL 4-inch horizontal flow facility.

As the experimental work is now complete, these objectives will now be revisited in order to determine the overall level of success. A set of proposals for future work and a final summary of the thesis will then be presented.

### *Objective 1: Instrumentation and modelling review*

In Chapters 2 and 3 respectively, the literature concerning the multiphase metering system and the modelling of slug flow was reviewed.

Chapter 2 described the sensing instrumentation and the processing software contained within the multiphase flow meter. Various techniques for making the phase velocity, phase fraction and phase density measurements (and their limitations) were discussed. A division was made between systems that separated the flow, homogenised the flow, and were non-intrusive. Software for identifying the flow pattern, calculating the model parameters and

delivering the phase flowrates were then briefly summarised. Lastly, the accuracy requirements of the offshore oil industry and the performance of some commercial multiphase flow meters were discussed. It was noted that there was particularly poor performance when metering *slug flow*, because of the difficulty in making the local velocity measurements and the potential need for empirical closure relationships.

Chapter 3 reviewed the modelling of slug flow. The initiation and development processes, and the structure of the 'slug body' and the 'film zone' in a *two-phase* flow were described. A model for the phase flowrates was then presented, which consisted of a translation velocity, local velocities, local phase fractions and local lengths. Various correlations for closing this model were then discussed. This review concentrated upon the relationships between the 'translation' and 'local slug' velocities, the pressure drop profile, and the pickup and shedding processes at the front and rear of each 'slug zone'. Some empirical correlations for the slug frequency, the slug holdup, and the slug length were also presented. Finally, the two-phase model was developed in order to form a model for multiphase (oil-water-gas) slug flow.

Several gaps in the literature emerged while addressing the first objective. There was a particular lack of information concerning the processing software contained within the multiphase flow meter, how to measure the local phase velocities within a stable 'slug unit', and how to model a three-phase (oil-water-gas) slug flow.

#### *Objective 2: Assessment of metering approach*

In Chapter 4, the suitability of the slug flow model for metering the liquid and gas phase flowrates was assessed. This assessment consisted of a sensitivity analysis and the selection of suitable techniques for measuring the flow. There was a requirement that this sensing instrumentation was *non-intrusive* and *inexpensive*.

At the beginning of the chapter, the two equations for the liquid and gas phase flowrates were restated. As these equations contained nine unknown parameters, the assumption was immediately made that *stable slug flow* was being metered so that the number of unknowns could be reduced from *nine* to *seven*. A sensitivity analysis was then conducted, to establish the accuracy to which each model parameters needed to be measured. This analysis highlighted the particularly difficulty in metering the liquid phase flowrate, when the overall (total) flowrate was small. In order to sense the slug flow, it was proposed that a system of *conductance sensors* should be developed. These sensors could be *non-intrusive* and *inexpensive*, and were capable of measuring the translation velocity, the local phase

fractions, and the length of each slug unit.

While addressing the second objective, it became very clear that it would be very difficult to measure the *local velocities* within each slug unit. This meant that it would be necessary to use some of the empirical closure relationships that were defined in Chapter 3, in order to calculate the local velocities  $V_{ls}$  and  $V_{gs}$ .

### *Objective 3: Prototype meter development*

Chapters 5 to 7 addressed the third objective - the development of a prototype system for metering the slug flow. As in the offshore oil industry, it was important that this system was non-intrusive in order not to inhibit the flow, and that it could be developed at a minimal overall cost.

Chapter 5 described the design of two types of *ring electrode sensor*, for measurement of the local phase fractions ( $a_f$  and  $a_s$ ) and the translation velocity ( $V_t$ ). In each of these cases, the use of the ring electrode design (Andreussi *et al*<sup>8</sup>) was justified. A semi-theoretical approach was then used to select the optimum separation between the sensor electrodes. This separation was 0.3 metres (3 pipe diameters) for the holdup sensor, and about 0.006 metres (0.05 pipe diameters) for the cross-correlation sensors. The measurement *uncertainty* was then estimated by combining simple theoretical models of the flow, numerical simulations, and experimental measurements. The manufacture of the sensor units was then described, with the potential for *crossstalk* currents being eliminated by inserting of sections of grounded pipe between the adjacent units.

Chapter 6 discussed the development of instrumentation for measuring the conductance between the cell electrodes. The 4-inch diameter of the NEL facility and the presence of salt in the water phase (20g l<sup>-1</sup> Magnesium Sulphate) rendered the ‘classical’ solution to this problem (by Coney<sup>27</sup>) unusable. Therefore a new solution, which was comprised of an analog feedback loop that kept the cell voltage stable, was designed and built. This solution allowed the measurement of full-scale (i.e. full-pipe) conductance within the range  $0.002\Omega^{-1}$  to  $2\Omega^{-1}$ . The measurement precision was high (0.2%) and the measurement bandwidth was wide (at least 2kHz), to ensure that accurate measurements of the holdup and the translation velocity could always be made.

Chapter 7 described the computer system used to process the sensor data, and deliver the phase flowrates. In order to calculate the local holdup, translation velocity and length parameters, a *threshold level* and a *cross-correlation* algorithm were developed. There was

some uncertainty in each of these processes, due to the difficulty in defining the exact beginning and end of each ‘slug unit’. A choice of empirical correlations for the total superficial velocity ( $j$ ) and the slip parameter ( $s$ ) was then proposed, so that the local velocities  $V_{ls}$  and  $V_{gs}$  could be estimated. Two methods for *averaging* the input parameters so that average values for the phase flowrates could be calculated were then discussed. Finally and most significantly, equations for estimating the measurement uncertainty in each parameter ( $\Delta V_l$ ,  $\Delta \alpha_f$ ,  $\Delta \alpha_s$ ,  $\Delta V_{ls}$ ,  $\Delta V_{gs}$ ,  $\Delta \theta$  and  $\Delta t_{film}$ ) and the corresponding uncertainty in the phase flowrates ( $\Delta j_l/j_l$  and  $\Delta j_g/j_g$ ), were proposed.

The third objective was achieved at a total cost of £5000. This cost was divided equally between the manufacture of the sensor units, the sensor electronics, and the data analysis system.

#### *Objective 4: Performance assessment using the NEL facility*

Chapter 8 addressed the final objective - assessment of the system, using the NEL flow facility. This facility was used to generate slug flow in a 4-inch horizontal test section, and then the sensors were used to obtain data covering the range of liquid phase superficial velocities  $j_l=0.1$  to  $1.0 \text{ m s}^{-1}$ , and gas phase superficial velocities  $j_g=0.6$  to  $6.0 \text{ m s}^{-1}$ . These data were analysed, and then they were processed in order to obtain predictions for the phase flowrates (the superficial velocities  $j_l$  and  $j_g$ ), and a series of uncertainty components (denoted by  $\Delta j_l/j_l$  and  $\Delta j_g/j_g$ ). From these results it emerged that:

- The system was incapable of predicting the liquid phase flowrate, especially at low velocities. The relative error in the liquid flowrate ( $\delta j_l/j_l$ ) approached 500%, for the velocity  $j_l = 0.1 \text{ m s}^{-1}$ . However, the prediction for the gas phase flowrate was more reasonable. The relative error in the gas flowrate ( $\delta j_g/j_g$ ) was only about 10%, for  $j_g = 6 \text{ m s}^{-1}$ .
- The *uncertainty* in the flowrate predictions was often as large as the observed errors. These uncertainties came about, because of the inability to make accurate measurements for the local slug velocities  $V_{ls}$  and  $V_{gs}$  and (to a lesser extent) the translation velocity  $V_l$ , within each passing slug unit.

In addressing the final objective, some reasonable results were obtained for the gas flowrate prediction, but otherwise the performance was very poor. This appeared to be due to large uncertainties in the measurement of the model parameters, rather than any inherent

inaccuracy within the stable slug flow model. To improve the results, it was clear that better correlations for the total superficial velocity ( $j$ ) needed to be used, and that direct measurements for the local film velocities ( $V_{lf}$  and  $V_{lg}$ ) should be obtained if possible. These suggestions will be discussed in considerable detail, in the following section.

## **9.1 Future work**

The system developed in this thesis is incapable of metering slug flow very accurately, and is therefore *not* suitable to industrial applications where a 5% relative uncertainty in the gas and the liquid phase flowrates are required. The major limitation appears not to be the predictive model for slug flow, but rather the accurate measurement of the parameters that are used in this model. Four areas are identified, where improvements in the measurement system must be made:

- The uncertainty in the local velocities  $V_{ls}$  and  $V_{gs}$  must be reduced, by obtaining direct measurements of the film velocities.
- The uncertainty in the translation velocity  $V_t$  must also be reduced, by reconsidering the design of the cross-correlation sensors.
- The uncertainties in the phase fraction measurements  $a_f$  and  $a_s$  should be better characterised. The values for  $\Delta a_f$  and  $\Delta a_s$  were estimated using simple models.
- The system should be able to meter unstable slug flows. In general, if the meter is placed downstream of a pipe bend or a junction, the flow will neither be *developed* nor *stable*.

Each of these four proposals is discussed in greater detail, in sub-sections 9.1.1 to 9.1.4 below.

### **9.1.1 The local velocity measurement**

In this thesis, the local slug velocities  $V_{ls}$  and  $V_{gs}$  were obtained by measuring the translation velocity  $V_t$  and using empirical correlations to define the total superficial velocity  $j$  and the slip parameter  $s$ . However because these correlations are highly approximate, and also because there were some systematic errors in the measurement of  $V_t$ , there is both *systematic*

*error and uncertainty* in these velocity measurements.

To minimise the systematic errors in  $V_{ls}$  and  $V_{gs}$ , two actions were proposed in Section 8.3.1 of the thesis. These were as follows:

- Two straight lines should be used, to correlate the data for the total superficial velocity ( $j$ ) against the measured translation velocity  $V_t$ . The first straight line is used to fit the data at low velocities ( $j < 3 \text{ m s}^{-1}$ ), and reflects the fact there is a *drift velocity* component at low flowrates (i.e. plug flow conditions) due to the difference in the hydrostatic head between the ‘slug’ and ‘film’ regions (Section 3.3). The second straight line is used to fit the data at high velocities ( $j > 3 \text{ m s}^{-1}$ ), where the drift velocity component disappears (Bendiksen<sup>18</sup>).
- Removal of the first (upstream) cross-correlation sensor, and installation of a new ‘spacing block’ behind the electrodes. This block should be machined in such a way that it makes contact with the electrode surface, so that both the cross-correlation sensors are exactly identical in design. As a result, any systematic differences between the sensor signals  $x(t)$  and  $y(t)$  and any large components in the additive noise signal  $n(t)$  should be eliminated.

The measurement uncertainty arises, because the relationship between the total superficial velocity, the slip and the translation velocity parameters is unlikely to be *unique*. That is, there may be a dependency on other model parameters. For example, the translation velocity  $V_t$  may have some relationship to the holdup of individual slugs ( $a_s$ ), if there is a tendency for under-developed slugs to persist along the test section. Alternatively,  $V_t$  may depend upon the liquid heights around the slug body, since these affect the rates of fluid pickup and shedding in each slug unit (Fan *et al*<sup>33</sup>, Woods & Hanratty<sup>127</sup>). Nevertheless, a significant amount of the uncertainty must be due to the fact that slug flow is a *stochastic* process. Unpredictable changes occur in the translation velocity, due to the chaotic nature of the flow.

Another way to reduce the local velocity uncertainty is to try and directly measure the local film velocities  $V_{lf}$  and  $V_{gf}$ . As was discussed in Section 8.3, it is much better to measure these local velocities than the slug velocities  $V_{ls}$  and  $V_{gs}$ , since the predictive model is much less sensitive to errors in the former at *low flowrates*. The following techniques are proposed for making this measurement:

- The *actual* superficial velocities (taken from the rig) can be combined with the mean film holdup measurement in order to obtain:

$$V_{lf} \sim \frac{j_l}{\bar{a}_f} \qquad V_{gf} \sim \frac{j_g}{(1-\bar{a}_f)} \qquad [9.1]$$

As the velocities  $j_l$  and  $j_g$  are generally not known, however, some form of empirical correlation to relate  $V_{lf}$  and  $V_{gf}$  must be developed.

- Measure the total pressure drop along the film zone  $\Delta P_{film}$ , by installing a pressure transducer near the existing sensors. The mean pressure gradient can be combined with the measurement of the film holdup, in order to solve the ‘constant film’ equations:

$$a_f \frac{dP}{dx} = \frac{\tau_l S_l}{A} - \frac{\tau_i S_i}{A} \qquad (1-a_f) \frac{dP}{dx} = \frac{\tau_g S_g}{A} + \frac{\tau_i S_i}{A} \qquad [9.2]$$

$V_{lf}$  and  $V_{gf}$  are functions of the shear stresses, and must be obtained using the iterative solution procedure illustrated in figure 3.9. In this model, empirical friction factors for the gas-wall, liquid-wall and liquid-liquid interfaces must be defined.

Equations [9.1] and [9.2] above are strictly only applicable to stratified flow, which occurs in the limit as the slug frequency approaches zero (i.e.  $l_f/l_u \rightarrow 1$ ). For other flow conditions, the above techniques may not give very accurate results. However, it for conditions where the *slug zone is short* and the *film zone is long* where these measurements are most required.

### 9.1.2 The translation velocity measurement

There is a substantial uncertainty in the prediction at low flowrates, due to the uncertainty in the translation velocity measurement. This uncertainty is due to *evolution of the flow* between the cross-correlation sensors, and also the *low bandwidth* of the slug flow signals.

Beck & Plaskowski<sup>17</sup> propose that the measurement uncertainty  $\Delta V_t$  is minimised in single-phase flow, when the sensor separation ( $x$ ) is of the order of the pipe diameter (see Section 5.2). To investigate whether this is true for slug flow, the guard electrodes between neighbouring sensors must be removed. This will make the system vulnerable to crosstalk, which must be eliminated by using one of the following techniques:

- Float each pair of electrodes by using transformers, as described and implemented by Coney<sup>27</sup>.
- Activate each sensor with a different frequency, and then use narrowband filters to reject the a.c. current from neighbouring sensors. This might be achieved by using a ‘lock-in’ amplifier design (Meade<sup>80</sup>).

The measurement uncertainty can also be reduced, by redesigning the sensor electrodes. The results in Chapter 8 suggested that although the sensor bandwidth  $B_S$  was wide (of the order of kHz), the signal bandwidth  $B$  was much smaller (approximately 1Hz) because of the insensitivity of the electrodes to the *fine structure* in the flow. To increase the bandwidth, more localised (and possibly intrusive) electrodes must be manufactured. Either a pair of ‘thin-wire’ electrodes (Manolis<sup>77</sup>) or a pair of local impedance probes (Teyssedou & Tapicu<sup>116</sup>) should be developed and substituted for the existing sensors, to study this problem further.

### 9.2.3 The phase fraction measurement

The uncertainties in the film zone and the slug body measurements,  $\Delta a_f$  and  $\Delta a_s$ , were estimated by assuming simple geometries for the flow (Section 5.1). In order to determine whether these assumptions are realistic, the following experiments are required:

- An investigation of the liquid spray carried in the gas bubble between the slug regions, by inserting either a local optical sensor (e.g. Andreussi *et al*<sup>6</sup>) or a local impedance sensor (Teyssedou & Tapicu<sup>116</sup>) into the flow.
- An investigation into the effect of the bubble *distribution* in the slug body upon the measured conductance, at large void fractions. Some progress has already been made in this direction, by Gillanders<sup>38</sup>.

Non-intrusive electrode were used to measure the parameters  $a_f$  and  $a_s$  in this thesis, on account of there relative simplicity (Section 5.2). However, there is a fundamental limit to the accuracy that can be achieved with a non-intrusive impedance sensor, because the field in the centre of the pipe cannot be carefully controlled. For accurate non-intrusive measurements, reliance on a ‘hard-field’ technique - that is, X-ray or gamma-ray attenuation - is probably necessary.

### 9.2.4 Unstable slug flow

Like a single-phase flowmeter, the multiphase flowmeter should be installed well downstream of a pipe bend or a junction to optimise its performance. However, since the development distance for slug flow is far greater than for single-phase flow (several hundreds as opposed to several tens of pipe diameters), this is not always possible, and the flow may be unstable. In the general case, the system will need to meter flows where there are growing and decaying slugs are where there are large-amplitude waves within the film zone.

In an unstable slug flow, the rates of pickup and shedding from each slug unit do not necessarily match. Therefore, equation [7.5] is not longer valid and the superficial velocities must be defined by:

$$j_l = V_b a_s \frac{l_s}{l_u} + \frac{1}{l_u} \int_0^{l_f} a_f V_f dx \quad j_g = V_g (1 - a_s) \frac{l_s}{l_u} + \frac{1}{l_u} \int_0^{l_f} (1 - a_f) V_g dx \quad [9.3]$$

The volume of liquid in the slug body is not constant, so the mass conservation equation must include the extra term:

$$(V_i - V_b) a_s = (V_i - V_{fe}) a_{fe} - \frac{dV}{dt} \quad [9.4]$$

The rate of change of liquid in the slug body ( $dV/dt$ ) can be approximately measured, by installing a second holdup sensor in the pipeline. This process is described by Woods & Hanratty<sup>127</sup>.

The presence of *large waves* between the slugs may be a particular problem, at low liquid flowrates. Though these waves are clearly evident in the experimental data (see, for example, figure 8.5b) they are not separately considered by the software. It is unlikely that the local velocity remains unchanged on either side of a large wave, so that there will be an effect upon the measured flowrates. Separate measurements of the local velocity should be made if possible, before and after the wave front.

### 9.3 Final Summary

This thesis has examined the use of a model-based approach, for the metering of gas-water slug flows. To achieve this aim:

- The stable slug flow model was examined. For each model parameter, the sensitivity of the flowrates to the measurement, and a suitable measurement technique were proposed.
- A prototype system was developed, consisting of ring electrodes (for making local holdup and translation velocity measurements), sensing instrumentation (for accurate measurement of the conductance between the electrodes), and software for analysis of the sensor data.

An important feature of the analysis system was its ability to estimate the uncertainty in the measurement of the model parameters.

The system was assessed in horizontal gas-water flow at atmospheric pressure, using the NEL flow facility. The results were generally unsatisfactory, and the performance needs to be improved by obtaining better measurements for the translation velocity and the liquid film velocity in each slug unit.

The recommended ways to improve the performance are to redesign the cross-correlation sensors and reduce their separation distance, and to introduce pressure transducers to measure the film zone pressure drop. However, the electronic instrumentation may need to be improved to prevent any crosstalk between the sensors, and suitable friction factor relationships may need to be selected to allow good measurement of the film velocities.

The work in this thesis is of great importance, in understanding how to meter multiphase slug flow. It is anticipated that the above proposals will dramatically reduce the error in the liquid and gas phase flowrates, so that the accuracy required by the oil industry can be achieved.

(blank page)

## References

1. Abouelwafa, M.S.A. & Kendall, E.J.M. 1980. The use of capacitance sensors for phase percentage determination in multiphase pipelines. *IEEE Transactions on Instrumentation & Measurement*. Vol. IM-29, p.24-27.
2. Abro, E. & Johansen, G.A. 1999. Improved void fraction determination by means of multibeam gamma-ray attenuation measurements. *Flow Measurement & Instrumentation* **10**, p.99-108.
3. Açıkgöz, M., Franca, F. & Lahey, R.T. 1992. An experimental study of three-phase flow regimes. *Int. J. Multiphase Flow* **18**, p.327-336.
4. Agrawal, S.S, Gregory, G.A. & Govier, G.W. 1973. An analysis of horizontal stratified two-phase flow in pipes. *Canadian J. Chem. Engng.* **51**, p.280-286.
5. Andreussi, P. & Bendiksen, K. 1989. An investigation of void fraction in liquid slugs for horizontal and inclined gas-liquid pipe flow. *Int. J. Multiphase Flow* **6**, p.937-946.
6. Andreussi, P., Bendiksen, K.H. & Nydal, O.J. 1993. Void distribution in slug flow. *Int. J. Multiphase Flow* **19**, p.817-828.
7. Andreussi, P., Ciandri, P., Talarico, C., Giuliani, F., Loh, W.H. & Mazzoni, A. 1993. Development of a multiphase flowmeter for subsea well testing. *Proc. 6<sup>th</sup> Intl. Conference of Multiphase Production* (Cannes, France).
8. Andreussi, P., Di Donfrancesco, A. & Messia, M. 1988. An impedance method for the measurement of liquid holdup in two-phase flow. *Int. J. Multiphase Flow* **14**, p.777-787.
9. Andreussi, P., Minervini, A. & Paglianti, A. 1993. A mechanistic model of slug flow in near-horizontal pipes. *AIChE Jnl.* **39**, p.1281-1291.
10. Andritsos, N. & Hanratty, T.J. 1987. Influence of interfacial waves in stratified gas-liquid flows. *AIChE Jnl.* **33** p.444-454.
11. Annuziatio. 1987. Horizontal two phase flow: a statistical method for pattern recognition. Paper F1, *BHRA 3<sup>rd</sup> International conference on Multiphase Flow* (the Hague, Netherlands).
12. Arirachakaran, S., Oglesby, K.D., Malinowsky, M.S., Shoham, O. & Brill, P. 1989. An analysis of oil/water flow phenomena in horizontal pipes. SPE Paper 18836, *SPE Production Operations Symposium* (Oklahoma, USA).
13. Ashton, S.L., Cutmore, N.G., Roach, G.L., Watt J.S., Zastawny, H.W. & McEwan, A.J. 1994. Development of a multiphase flowmeter for subsea well testing. *6<sup>th</sup> International Conference on Multiphase Production* (Cannes, France).

14. Barber, D.C., & Brown B.H. 1984. Applied potential tomography. *J. Phys. E: Scient. Instrum.* **17**, p.723-733.
15. Barnea, D. & Taitel, Y. 1993. A model for slug length distribution in gas-liquid slug flow. *Int. J. Multiphase Flow* **19**, p. 829-838.
16. Beams, D.M. 1999. Modulation. Chapter 81 in: *The measurement, instrumentation and sensors handbook*. J.G. Webster (ed.), CRC Press / Springer-Verlag / IEEE Press.
17. Beck, M.S. & Plaskowski, A. c1987. *Cross-correlation flowmeters: their design and application*. p.144-160. Bristol: Hilger.
18. Bendiksen, K.H. 1984. An experimental investigation of the motion of long bubbles in inclined tubes. *Int. J. Multiphase Flow* **6**, p.797-812.
19. Benjamin, T.B. 1968. Gravity currents and related phenomena. *J. Fluid Mech.* **31**, p.209-248.
20. Bissell, C.C. 1994. *Control Engineering (Tutorial guides in Electronic Engineering)*. 2<sup>nd</sup> ed, Nelson-Thornes.
21. Brill, J.P., Schmidt, Z., Coberly, W.A., Herring, J.D. & Moore, D.W. 1981. Analysis of two-phase tests in large-diameter flow lines in Prudhoe Bay Field. *SPE Jnl.* **1981**, p.363-377.
22. Brinkman, H.C. 1952. The viscosity of concentrated suspensions and solutions. *J. Chemical Physics* **20**, p.571.
23. Brown, R.C, Andreussi, P. & Zanelli, S. 1978. The use of wire probes for the measurement of liquid film thickness in annular gas-liquid flows. *Canadian J. Chem. Engng.* **56**, p.754-757.
24. Bruggeman, D.A.G. 1935. Calculation of different physical constants of heterogeneous substances. *Annln Phys.* **24**, p.636-679.
25. Ceccio, S.L. & George, D.L. 1996. A review of electrical impedance techniques for the measurement of multiphase flows. *J. Fluids Engng.* **118**, p.391-399.
26. Chisholm, D. 1967. A theoretical basis for the Lockhart-Martinelli correlation for two-phase flows. *Int. J. Heat & Mass Transfer* **10**, p.1767-1778.
27. Coney, M.W.E. 1973. The theory and application of conductance probes for the measurement of liquid film thickness in annular gas-liquid flows. *J. Phys. E: Scient. Instrum.* **6**, p.903-910.
28. Cook M., & Behina, M. 1997. Film profiles behind liquid slugs in gas-liquid pipe flow. *AIChE Jnl.* **43**, p.2180-2186.
29. Donnelly, G.F. 1997. An analytical evaluation of horizontal multiphase flow. *PhD*.

*Thesis*. University of Belfast.

30. Dukler, A.E. & Hubbard, M.G. 1975. A model for gas-liquid slug flow in horizontals and near-horizontal pipes. *Ind. Engng. Chem. Fundamentals* **14**, p.337-347.
31. Dykesteen, E., Hallanger, A., Hammer, E., Samnoy, E. & Thorn, R. 1985. Non-intrusive three component ratio measurement using an impedance sensor. *J. Phys. E: Scient Instrum.* **18**, p.540-544.
32. Dykesteen, E., & Midttveidt, O. 1992. A flow regime independent multiphase flowrate meter. *Proc. 10<sup>th</sup> North Sea Flow Measurement Workshop* (Peebles, Scotland).
33. Fan, Z., Jepson, W.P. & Hanratty, R.J. 1992. A model for stationary slugs. *Int. J. Multiphase Flow* **18**, p.477-494.
34. Fan, Z., Ruder, Z. & Hanratty, T.J. 1993. Pressure profiles for slugs in horizontal pipelines. *Int. J. Multiphase Flow* **19**, p.421-437.
35. Franca, F. & Lahey, R.T. 1992. The use of drift-flux techniques for the analysis of horizontal two-phase flows. *Int. J. Multiphase Flow* **18**, p.787-801.
36. Fossa, M. 1998. Design and performance of a conductance probe for measuring the liquid fraction in two-phase gas-liquid flows. *Flow Measurement & Instrumentation* **9**, p.103-109.
37. Geraets J.J.M. & Borst, J.C. 1988. A capacitance sensor for two-phase void fraction measurement and flow pattern identification. *Int. J. Multiphase Flow* **14**, p.305-320.
38. Gillanders, S.R. 2001. Characterisation of multiphase flow by measurement of electrical impedance. *Final year MEng project*, Department of Electrical & Mechanical Engineering, University of Strathclyde, Glasgow.
39. Gopal, M., & Jepson, W.P. 1997. Development of digital image analysis techniques for the study of velocity and void profiles in slug flow. *Int. J. Multiphase Flow* **23**, p.945-965.
40. Gregory, G.A., Nicholson, M.K. & Aziz, K. 1978. Correlation of the liquid volume fraction in the slug for horizontal gas-liquid slug flow. *Int. J. Multiphase Flow* **4**, p.33-39.
41. Gregory, G.A. & Scott, D.S. 1969. Correlation of liquid slug velocity and frequency in horizontal co-current gas-liquid slug flow. *Ind. Eng. Chem. Proc. Design Dev.* **11**, p.317-
42. Greskovich, E.J. & Shrier, A.L. 1972. Slug frequency in horizontal gas-liquid slug flow. *Ind. Eng. Chem. Proc. Design Dev.* **11**, p.317-318.
43. Hale, C.P. 2001. Slug formation, growth and decay in gas-liquid flows. *PhD Thesis*. Imperial College, London.

44. Hall, A.R.W. 1992. Multiphase flow of oil, water and gas in horizontal pipes. *PhD Thesis*. Imperial College, London.
45. Hall, A.R.W. 1995. Flow patterns in horizontal three-phase flows of oil, water and gas. *NEL Report No. 335/95*.
46. Hammer, E.A., Tollefsen, J. & Cimpan, E. 1996. The importance of calculating the resulting permittivity and conductivity in mixtures of two liquids. *Proc. 14<sup>th</sup> North Sea Flow Measurement Workshop* (Peebles, Scotland).
47. Hanssen, B.V. & Torkildsen, B.H. 1995. Status of the Framo subsea multiphase flowmeter. *Proc. 13<sup>th</sup> North Sea Flow Measurement Workshop* (Lillehammer, Norway).
48. Hart, J., Hamersma, P.J., & Fortuin, J.M.H. 1989. Correlations predicting frictional pressure drop and liquid holdup during horizontal gas-liquid pipe flow with a small liquid holdup. *Int. J. Multiphase Flow* **15**, p. 947-964.
49. Hatlo, A. & Sten-Halvorsen, V. 1995. The KOS MCF 351 multiphase flowmeter – field experience and test results. *Proc. 13<sup>th</sup> North Sea Flow Measurement Workshop* (Lillehammer, Norway).
50. Hatscheck, E. 1928. *The viscosity of liquids*. Bell & Sons Ltd, London.
51. Hewitt, G.F. 1978. *Measurement of two-phase flow parameters*. London: Academic Press.
52. Hewitt, G.F., Harrison, P.S., Parry, S.J., & Shires, G.L. 1995. Development and testing of the 'Mixmeter' multiphase flowmeter. *Proc. 13<sup>th</sup> North Sea Flow Measurement Workshop* (Lillehammer, Norway).
53. Heywood, N.I. & Richardson, J.F. 1979. Slug flow of air-water mixtures in a horizontal pipe: determination of liquid holdup by  $\gamma$ -ray absorption. *Chem. Engng. Science* **34**, p. 17-30.
54. Hinze, J.O. 1955. Fundamentals of the hydrodynamic mechanism of splitting in dispersion processes. *AIChE Jnl.* **1**, p.289-295.
55. Horowitz, P., & Hill, W. 1989. *The Art of Electronics*. 2<sup>nd</sup> ed., Cambridge University Press, Cambridge.
56. van Hout, R., Shemer, L. & Barnea, D. 1992. Spatial distribution of void fraction within a liquid slug and some other related slug parameters. *Int. J. Multiphase Flow* **18**, p. 831-845.
57. Jepson, W.P. 1987. The flow characteristics in horizontal slug flow. Paper F2, *BHRA 3<sup>rd</sup> International Conference on Multiphase Flow* (the Hague, Netherlands).
58. Johansen G.A., Frøystein, T., Hjertaker, B.T., Isaksen, Ø., Olsen, Ø., Strandos, S.K., Skoglund, T.O., Åbro, E. & Hammer, E.A. 1995. The development of a dual mode

- tomograph for three-component flow imaging. *Chemical Engineering Jnl.* **56**, p. 175-182.
59. Kak, A.C. & Slaney, M. 1988. *Principles of Computerized Tomographic Imaging*. IEEE Press.
60. Kjolberg & Berentsen. 1997. The Porsgrunn 2 test programme of multiphase flowmeters: general results and examples of different meter performance. *Proc. 15<sup>th</sup> North Sea Measurement Workshop*.
61. Kordyban, E.S., & Ranov, T. 1970. Mechanism of slug formation in horizontal two-phase flow. *J. Basic Eng.* **92**, p.857-864.
62. Kruger, G.L, Birke, A. & Weiss, R. 1996. Nuclear magnetic resonance (NMR) for two-phase mass flow measurement. *Flow Measurement & Instrumentation* **7**, p.25-37.
63. Lahey, R.T., Acikgoz, M. & Franca, F. 1992. Global volumetric phase fractions in horizontal three-phase flows. *AIChE Jnl* **38** p.1049-1058.
64. Lee, H.A., Sun, J.Y. & Jepson, W.P. 1993. Study of flow regime transitions of oil-water-gas mixtures in horizontal pipes. *ISOPE 3<sup>rd</sup> International Offshore and Polar Engng. Conference* (Singapore).
65. Lemmonier, H, Nakach, R., Favreau, C. & Selmer-Olsen, S. 1991. Sensitivity analysis of an impedance void meter to the void distribution in annular flow: a theoretical study. *Nuclear Engng. & Design* **126**, p.105-112.
66. Lin, P.Y. & Hanratty, T.J. 1986. Prediction of the initiation of slugs with linear stability theory. *Int. J. Multiphase Flow* **12**, p.79-98.
67. Lin, P.Y. & Hanratty, T.J. 1987. Detection of slug flow from pressure measurements. *Int. J. Multiphase Flow* **13**, p.13-21.
68. Lockhart, R.W. & Martinelli, R.C. 1949. Proposed correlation of data for isothermal two-phase, two-component flow in pipes. *Chem. Engng. Progr.*, **45**, p.39-48.
69. Lucas, G.P. & Albasaidi, K.H. 1996. Measurement of multiple velocities in multiphase flow. *IEE Colloquium on Advances in Sensors for Fluid Flow Measurement*. IEE, London, UK.
70. Lucas, G.P., Cory J.C., & Waterfall, R.C. 2000. A six-electrode local probe for measuring solids velocity and volume fraction profiles in solids-water flows. *Meas. Science & Technology* **11**, p.1498-1509.
71. Lucas, G.P., Cory J.C., Waterfall, R.C., Loh, W.W., & Dickin F.J. 1999. Measurement of the solids fraction and velocity distributions in solids-liquid flows using dual-plane electrical resistance tomography. *Flow Measurement & Instrumentation* **10**, p.249-258.

72. Lucas, G.P. & Walton, I.C. 1997. Flow rate measurement by kinematic wave detection in vertically upward, bubbly two-phase flows. *Flow Measurement & Instrumentation* **8**, p.133-143.
73. Malnes, D. 1983. Slug flow in vertical, horizontal and inclined pipes. *IFE Report KR/E-83/002*, Kjeller, Norway.
74. Mandhane, J.M., Gregory, G.A. & Aziz, K. 1974. A flow pattern map for gas-liquid flow in horizontal pipes. *Int. J. Multiphase Flow* **1**, p.537-553.
75. Manfield, P. 2000. Experimental, computational and analytical studies of slug flow. *PhD Thesis*. Imperial College, London.
76. Manolis, I.G. 1995. High pressure gas-liquid slug flow. *PhD Thesis*. Imperial College, London.
77. Manolis, I.G., Mendes-Tatsis, M.A. & Hewitt, G.F. 1995. The effect of pressure on slug frequency in two-phase horizontal flow. *2<sup>nd</sup> International Conference on Multiphase Flow* (Amsterdam, Netherlands) xiii+805, p.347-354.
78. Maron, D.M., Yacoub, N. & Brauner, N. 1982. New thoughts on the mechanism of gas-liquid slug flow. *Letters in Heat and Mass Transfer* **9**, p.333-341.
79. Maxwell, J.C. 1881. *A treatise on Electricity and Magnetism*. Clarendon Press, Oxford.
80. Meade, M.L. 1983. *Lock-in amplifiers: Principle and applications*. London : Peregrinus (on behalf of IEEE).
81. Merilo M., Dechene, R.L. & Cichowlas W.M. 1977. Void fraction measurement with a rotating electric field conductance gauge. *ASME J. Heat Transfer* **99**, p.330-332.
82. Mi, Y., Ishii, M. & Tsoukalas, L.H. 2001. Flow regime identification methodology with neural networks and two-phase flow models. *Nuclear Engng. & Design* **204**, p.87-100.
83. Mishima, K. & Ishii, M. 1980. Theoretical prediction of the onset of slug flow. *J. Fluids Eng.* **102**, p.441-445.
84. Moissis, R. & Griffith, P. 1962. Entrance effects in a two-phase slug flow. *J. Heat Transfer* **84**, p.29-39.
85. Monson, L.T. 1938. Viscosity of petroleum emulsions. *Industrial & Engng. Chem.* **30**, p.287-1291.
86. Nadler, M. & Mewes, D. 1995. Effects of the liquid viscosity on the phase distribution in horizontal gas-liquid slug flow. *Int. J. Multiphase Flow* **21**, p.253-266.
87. Neogi, S., Lee, H.A., & Jepson W.P. 1994. A model for multiphase (gas-water-oil) stratified flow in horizontal pipelines. SPE Paper 28799, *SPE Asia Pacific Oil & Gas*

*Conference* (Melbourne, Australia).

88. Nydal, O.J., Pintus S. & Andreussi, P. 1992. Statistical characterisation of slug flow in horizontal pipes. *Int. J. Multiphase Flow* **16**, p.1117-1129.
89. Nydal, O.J. & Andreussi, P. 1991. Gas entrainment in a long liquid slug advancing in a near horizontal pipe. *Int. J. Multiphase Flow* **17**, p.179-189.
90. Økland, O. & Berentsen, H. 1994. Using the MFI multiphase flow meter for well testing at Gullfaks B. *Proc. 12<sup>th</sup> North Sea Flow Measurement Workshop* (Peebles, Scotland).
91. Odozi, U.A. 2000. Three phase gas-liquid-liquid slug flow. *PhD Thesis*. Imperial College, London.
92. Olsvik, K., Marshall, M. & Whitaker, T. 1995. Fluent multiphase flowmeter, tested and marinised. *Proc. 13<sup>th</sup> North Sea Flow Measurement Workshop* (Lillehammer, Norway).
93. Ong, K.H. 1975. Hydraulic flow measurement using ultrasonic transducers and correlation techniques. *PhD thesis*. University of Bradford.
94. Ong, K.H. & Beck, M.S. 1975. Slurry flow concentration and particle size measurement using flow noise and correlation techniques. *Meas. Control* **8**, p.453-460.
95. Pal, R. 1993. Flow of oil-in-water emulsions through orifice and venturi meters. *Ind. Eng. Chem. Res.* **32**, p.1212-1217.
96. Pan, L. 1996. High pressure three-phase (gas-liquid-liquid) flow. *PhD Thesis*. Imperial College, London.
97. Plaskowski, A., Beck, M.S., Thorn, R. & Dyakowski, T. 1995. *Imaging Industrial Flows*. Bristol, IOP.
98. Priddy, W.J. 1994. BP Multiphase meter test experience. *Proc. 12<sup>th</sup> North Sea Measurement Workshop* (Peebles, Scotland).
99. Rafael, R. & Woods, R. 1992. Chapter 8, *Digital Image Processing*. Massachusetts: Addison Wesley.
100. Ramu, T.S. & Rao, N.Y. 1973. On the evaluation of conductivity of mixtures of liquid dielectrics. *IEEE Trans Electrical Insulation*, Vol E1-8, 2, p.55-60.
101. Richardson, E.G. 1933. On the viscosity of emulsions. *Colloid Zeitschrift* **65**, p.32-37.
102. Roach, G.J & Watt, J.S. 1996. Current status of development of the CSIRO gamma-ray multiphase flow meter. *Proc. 14<sup>th</sup> North Sea Flow Measurement Workshop* (Peebles, Scotland).
103. Ruder, Z., Hanratty, P.H. & Hanratty, T.J. 1989 Necessary conditions for the existence

of stable slugs. *Int. J. Multiphase Flow* **15**, p.209-226.

104. Saether, G., Bendiksen, K., Muller, J. & Frøland, E. 1990. The fractal statistics of liquid slug lengths. *Int. J. Multiphase Flow* **16**, p.1117-1126.

105. Scheers, A.M. & Letton, W. 1996. An oil-water-gas composition meter based on multiple energy gamma ray absorption (MEGRA) measurement. *Proc. 14<sup>th</sup> North Sea Flow Measurement Workshop* (Peebles, Scotland).

106. Schmidt, Z., Brill, J.P., & Beggs, H.D. 1981. Experimental study of two-phase normal slug flow in a pipeline-riser pipe system. *Jnl. Energy Resources Technology*, vol. 103/67.

107. Scott S.L., Shoham, O. & Brill, J.P. 1987. Modelling slug growth in large diameter pipes. Paper B2, *BHRA 3<sup>rd</sup> International conference on Multiphase Flow* (the Hague, Netherlands).

108. Slijkerman, W.F.J., Jamieson, A.W., Priddy, W.J., Økland, O., & Moestue, H. 1995. Oil companies needs in multiphase flow metering. *Proc. 13<sup>th</sup> North Sea Flow Measurement Workshop* (Lillehammer, Norway).

109. Snell, C.C., Dechene, R.L. & Newton, R.E. 1978. Two-phase relative volume fraction measurement with a rotating field conductance gauge. *Measurements in Polyphase flows*, ASME, San Francisco, p.21-24.

110. Stapelberg, H.H. & Mewes, D. 1994. The pressure drop and slug frequency of liquid-liquid-gas slug flow in horizontal pipes. *Int. J. Multiphase Flow* **20**, p.285-303.

111. Taitel, Y. 1986. Stability of severe slugging. *Int. J. Multiphase Flow* **12**, p.203-217.

112. Taitel, Y. & Barnea, D. 1990. A consistent approach for calculating pressure drop in inclined slug flow. *Chem. Engng. Science* **45**, p.1199-1206.

113. Taitel, Y., Barnea, D. & Brill, J.P. 1995. Stratified three-phase flow in pipes. *Int. J. Multiphase Flow* **21**, p.53-60.

114. Taitel, Y., Barnea, D. & Dukler, A.E. 1980. Modelling flow pattern transitions for steady upward gas-liquid flow in vertical tubes. *AIChE Jnl.* **26**, p.345-354.

115. Taitel, Y. & Dukler, A.E. 1976. A model for predicting flow regime transitions in horizontal and near-horizontal gas-liquid flow. *AIChE Jnl.* **22**, p.47-55.

116. Teyssedou, A. & Tapucu, A. 1988. Impedance probe to measure local void fraction profiles. *Review of Scientific Instruments* **59**, p. 631-638.

117. Thorn, R., Johansen, G.A., & Hammer, E.A. 1997. Recent developments in three-phase flow measurement. *Meas. Science & Technology* **8**, p.691-701.

118. Tournaire, A. 1986. Dependence of the instantaneous response of impedance probes on

- the local disturbance of the void fraction in a pipe. *Int. J. Multiphase Flow* **12**, p.1019-1024.
119. Tronconi, E. 1990. Prediction of slug frequency in horizontal two-phase slug flow. *AIChE Jnl.* **36**, p.701-709.
120. Tuss, B., Perry, D., & Shoup, G. 1996. Field tests of the high gas volume fraction multiphase meter. *Proc. SPE Annual Technical Conf* (Denver, USA).
121. Vlachos, N.A., Paras, S.V., & Karabelas, A.J. 1997. Liquid-to-wall shear stress distribution in stratified/atomisation flow. *Int. J. Multiphase Flow* **23**, p.845-863.
122. Wallis, G.B. 1969. *One-dimensional two-phase flow*. New York: Maidenhead; McGraw-Hill.
123. Williams R.A., Mann, R., Dickin, F.J., Llyas, O.M., Ying, P., Edwards, R.B. & Rushton, A. 1993. Application of electrical impedance tomography to mixing in a stirred vessel. *Part 2, AIChE Symposium series*, **89**, p.8-15.
124. Whalley, P.B. 1996. *Two-phase flow and heat transfer*. Oxford University Press.
125. Whitaker, T. 1996. Assessment of multiphase flowmeter performance. *Proc. 14<sup>th</sup> North Sea Flow Measurement Workshop* (Peebles, Scotland).
126. Wolff, C.J.M. 1997. Comparing performance of multiphase meters. *Proc. 15<sup>th</sup> North Sea Flow Measurement Workshop*.
127. Woods, B.D. & Hanratty, T.J. 1996. Relation of slug stability to shedding rate. *Int. J. Multiphase Flow* **22**, p. 809-828.
128. Wright, C.P. 1995. *Applied Measurement Engineering*. p.227-241. Prentice Hall.
129. Wu, H., Zhou, F. & Wu, Y. 2001. Intelligent identification system of flow regime of oil-water-gas multiphase flow. *Int. J. Multiphase Flow* **27**, p. 459-475.
130. Xie, C.G., Stott, A.L., Plaskowski, A., & Beck, M.S. 1990. Design of capacitance electrodes for concentration measurement of two-phase flow. *Meas. Science & Technology* **1**, p.65-78.
131. Xu, L.-A., Green, R.G., Beck, M.S., & Plaskowski, A. 1986. A pulsed ultrasound cross-correlation system for velocity measurement in two-component fluids. *Proc. NEL Conference on Flow Measurement in the Mid 1980's*.
132. Yang, W.Q. & Liu, S. 2000. Role of tomography in gas/solids flow measurement. *Flow Measurement & Instrumentation* **11**, p.237-244.
133. Yeh, G.C., Haynie, F.H. & Moses, R.A. 1964. Phase-volume relationship at the point of phase inversion in liquid dispersions. *AIChE Jnl.* **10**, p.260-265.

134. Yorkey, T.J., Webster, J.G. & Tompkins, W.J. 1987. Comparing reconstruction methods for electrical impedance tomography. *IEEE Trans. on Biomedical Engineering* **11**, p. 83-85.
135. Zuber, N. & Findlay, J.A. 1965. Average volumetric concentration in two-phase flow systems. *Jnl. Heat Transfer A.S.M.W. Ser. C.* **87**, p.453-468.
136. Zwiens, H. 1999. Development of tomographic algorithms. *Kleine Studienarbeit Report*, Department of Chemical Engineering, Imperial College.

(blank page)

## APPENDIX A: ANSYS modelling

This appendix presents the software used to simulate the field between the ring electrode sensors, described in Chapter 5. For all simulations, the finite-element modelling package ANSYS was used.

The four instances where a numerical simulation was required were as follows:

- **Section 5.1.2:** Prediction of the conductance between ring electrodes for an annular flow geometry, and a relative separation  $D_e/D=3.0$ . These results are used, to determine the accuracy of the model proposed by Andreussi<sup>8</sup>.
- **Section 5.1.4:** Prediction of the cell conductance as a step change in annular film thickness passes between the electrodes. These results are used to assess the *spatial filtering* ability of the holdup sensor.
- **Section 5.3.5:** Prediction of the ratio between the crosstalk current and the measured current ( $I_X/I_{cell}$ ) in the presence of a section of grounded pipework. These results are used, to determine the length of the guard electrode ( $X$ ) between adjacent sensors.
- **Section 5.4.1:** Prediction of the conductance between ring electrodes, for a 2D geometry, with the effective liquid height derived using equation [5.4] (Coney<sup>27</sup>). The influence of nearby guard electrodes is included in this simulation, so that the results can be compared with experimental measurements.

Each set of simulations is performed using the ANSYS command code 'relsims', which is listed in full in figure A1, and the two-dimensional geometric model that is illustrated in figure A2. The creation of the model and the solution of the field equations proceed as follows:

- Simulation keypoints are defined according to figure A2. The electrode separation  $D_e$ , insulation lengths  $z_{1a}$ ,  $z_{1b}$  and  $z_{2a}$ , guard electrode lengths  $X$  and  $X_I$ , film heights  $h_1$  and  $h_2$ , and the step position  $x$  set by the user. Optional rotational symmetry can be applied around the line  $y=0$ .
- Keypoints are joined to create lines and areas, which are then meshed to create a network of elements. It is easiest to automate this process by using the ANSYS solver 'smart' meshing. Additional refinement to the mesh is made along the line

$y=h$ , where the electric field is expected to be strongest and most divergent.

- The model is loaded with the constant voltage boundary conditions listed in table A1. (The symbol ‘-’ denotes that no loading is applied). The ANSYS solver is then activated, which transforms the problem into a set of iteratively solved linear equations.
- The current flowing between the live and sink electrodes (as well as leakage and crosstalk currents) is calculated by summing the contributions at each of the surface elements.

To test the accuracy of the simulation, a ‘flat liquid layer’ model (corresponding to figure 5.1a) was initially generated and solved. The predictions were compared against the analytical solution of Coney<sup>27</sup> (equations [5.1] to [5.3]); the simulated conductance ( $G^*$ ) and the relative simulation error ( $\Delta G/G$ ) illustrated in figure A4. The simulation error is smallest (0.1%) for a *wide electrode separation* ( $D_e/D = 3.0$ ) and a *thick liquid layer*. The simulation error increases (to about 2%) as the dimensionless electrode separation is reduced to a value  $D_e/D = 0.05$ .

The accuracy of the simulation might be improved, by developing a more sophisticated mesh, and possibly by using a three-dimensional model. However, because of the demands upon the computer system and the lengths of solution time required, these proposals were not implemented in this thesis.

```

/BATCHJ
/input,menust,tmp,,,,,,,,,,,,,1J
/GRA,POWERJ
/GST,ONJ
! General simulation of 2D axially
! symmetric ring electrode field, including
! optional effect of guard electrodes; step
! change in film height from h1 to h2;
! adjacent crosstalk sensor conductance
! prediction, including guard

! Thermo-electric element type
/prep7J ET,1,67J MP,rsvx,1,1J

! Activate rotational symmetry
KEYOPT,1,3,1J KEYOPT,1,4,0J

! Principal distances
zbl 0.1J zcl 0.3J De=0.3J
z1 0.3J X 0.3J z2=0.1J
s 0.006J x 0.1J
! 4-inch pipe diameter
h 0.0508J h1 0.00508J h2=0.0254J

! Define geometry
/GOPRJ
K,1,h,0,,, J
K,2,h-h1,0,,, J
K,3,h,zbl,,, J
K,4,h-h1,zbl,,, J
K,5,h,zbl+z2,0,,, J
K,6,h,zbl+z2+s,,, J
K,7,h,zbl+z2+s+De,,, J
K,8,h,zbl+z2+s+De+s,,, J
K,9,h,zbl+z2+s+De+s+z1,,, J
K,10,h,zbl+z2+s+De+s+z1+X,,, J
K,11,h-h2,zbl+z2+s+De+s+z1+X,,, J
K,12,h h2,zbl+z2+s+De+s+z1,,, J
K,13,h-h2,zbl+z2+x,,, J
*IF,h2,NE,h1,THENJ
K,14,h-h1,zbl+z2+x,,, J
*ENDIFJ
K,15,h,zbl+z2+x,,,J
K,16,h,zbl+z2+s+De+s+z1+X+za2,,,J
K,17,h,zbl+z2+s+De+s+z1+X+za2+s,,,J
K,18,h,zbl+z2+s+De+s+z1+X+za2+s+0.1,,,J
K,19,h-h2,zbl+z2+s+De+s+z1+X+za2+s+0.1,,,J

! create lines and areas
/NOPRJ
LSTR,1,3J LSTR,3,5J LSTR,5,6J
LSTR,6,7J LSTR,7,8J LSTR,8,9J
LSTR,9,10J LSTR,1,2J LSTR,3,4J
LSTR,9,12J LSTR,10,11J LSTR,2,4J
LSTR,11,12J LSTR,10,16J LSTR,16,17J
LSTR,17,18J LSTR,18,19J LSTR,19,11J
*IF,h2,GT,h1,THENJ
LSTR,15,14J LSTR,4,14J
LSTR,12,13J LSTR,13,14J
*ELSEIF,h2,LT,h1,THENJ
LSTR,15,13J LSTR,4,14J
LSTR,12,13J LSTR,13,14J
*ELSEJ
LSTR,15,13J LSTR,4,13J LSTR,12,13J
*ENDIFJ
FLST,2,4,4J
FITEM,2,8J FITEM,2,1J
FITEM,2,9J FITEM,2,12J A,P51XJ
FLST,2,4,4
FITEM,2,7J FITEM,2,11J
FITEM,2,13J FITEM,2,10J A,P51XJ
*IF,h2,NE,h1,THENJ

```

```

FLST,2,10,4J
FITEM,2,2J FITEM,2,3J FITEM,2,4J
FITEM,2,5J FITEM,2,6J FITEM,2,10J
FITEM,2,21J FITEM,2,22J FITEM,2,20J
FITEM,2,9J A,P51XJ
*ELSEJ
FLST,2,9,4J
FITEM,2,2J FITEM,2,3J FITEM,2,4J
FITEM,2,5J FITEM,2,6J FITEM,2,10J
FITEM,2,21J FITEM,2,20J FITEM,2,9J
A,P51XJ
*ENDIFJ
ADIV,3,14J
FLST,2,6,4J
FITEM,2,14J FITEM,2,15J FITEM,2,16J
FITEM,2,17J FITEM,2,18J FITEM,2,11J
A,P51XJ

! Initial 'smart' meshing of areas
SMRT,1J MSHAPE,0,2DJ MSHKEY,0J
FLST,5,5,5,ORDE,4J
FITEM,5,1J FITEM,5,-2J
FITEM,5,4J FITEM,5,-6J
CM,_Y,AREAJ ASEL,,,P51XJ
CM,_Y1,AREAJ
CHKMESH,'AREA'J CMSEL,S,_YJ
AMESH,_Y1J CMDEL,_YJ
CMDEL,_Y1J CMDEL,_Y2J
! refine bottom line
FLST,5,10,4,ORDE,4J
FITEM,5,1J FITEM,5,-7J
FITEM,5,14J FITEM,5,-16J
CM,_Y,LINEJ LSEL,,,P51XJ
CM,_Y1,LINEJ CMSEL,S,_YJ
CMDEL,_YJ LREF,_Y1,,,1,1,1,1J
CMDEL,_Y1J
! refine all areas
FLST,5,5,5,ORDE,4J
FITEM,5,1J FITEM,5,-2J
FITEM,5,4J FITEM,5,-6J
CM,_Y,AREAJ ASEL,,,P51XJ
CM,_Y1,AREAJ CMSEL,S,_YJ
CMDEL,_YJ AREF,_Y1,,,1,0,1,1J
CMDEL,_Y1J
! refine all areas again
FLST,5,5,5,ORDE,4J
FITEM,5,1J FITEM,5,-2J
FITEM,5,4J FITEM,5,-6J
CM,_Y,AREAJ ASEL,,,P51XJ
CM,_Y1,AREAJ CMSEL,S,_YJ
CMDEL,_YJ AREF,_Y1,,,1,0,1,1J
CMDEL,_Y1J
FLST,5,5,5,ORDE,4

! load guard electrode surfaces
FLST,2,2,4,ORDE,2J
FITEM,2,1J FITEM,2,7J
DL,P51X,Blank,VOLT,0J
! load sensor electrodes
FLST,2,1,4,ORDE,1J
FITEM,2,3J DL,P51X,Blank,VOLT,1,J
FLST,2,1,4,ORDE,1J
FITEM,2,5J DL,P51X,Blank,VOLT,0,J
! load crosstalk electrode
FLST,2,1,4,ORDE,1J
FITEM,2,15J DL,P51X,Blank,VOLT,10J

! solve geometry
/SOLUJ
/STAT,SOLUJ
SOLVEJ FINISHJ

```

```

/POST1
/REP
! current to collector electrode
LSEL,S,,,5 NSLL,S,1 ESLN,S FSUM
! leakage current to nearby guard
LSEL,S,,,1 NSLL,S,1 ESLN,S FSUM
! leakage current to distant guard
LSEL,S,,,7 NSLL,S,1 ESLN,S FSUM
ALLSEL,ALL FINISH

! Delete mesh and keypoints
/PREP7
FLST,5,5,5,ORDE,4
FITEM,5,1 FITEM,5,-2
FITEM,5,4 FITEM,5,-6
ACLEAR,P51X
FLST,2,5,5,ORDE,4
FITEM,2,1 FITEM,2,-2
FITEM,2,4 FITEM,2,-6
ADELE,P51X
FLST,2,22,4,ORDE,2
FITEM,2,1 FITEM,2,-22
LDELE,P51X
/CLEAR

```

**Figure A1:** The ANSYS command code 'relsim', used for obtaining conductance predictions between electrode pairs.

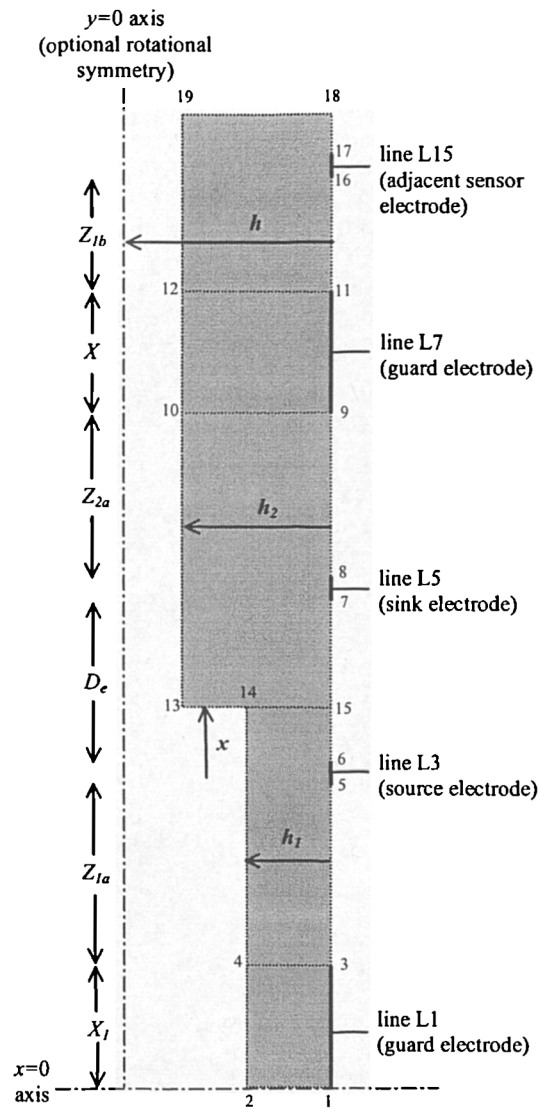


**Figure A2:** The simulation geometry used by the command code 'relsim'. (Illustrating the keypoint numbers, the line numbers, and the user-defined distances  $X_1$ ,  $Z_{1a}$ ,  $D_e$ ,  $Z_{2a}$ ,  $X$ ,  $Z_{1b}$ ,  $h$ ,  $h_1$ ,  $h_2$ , and  $x$ ).

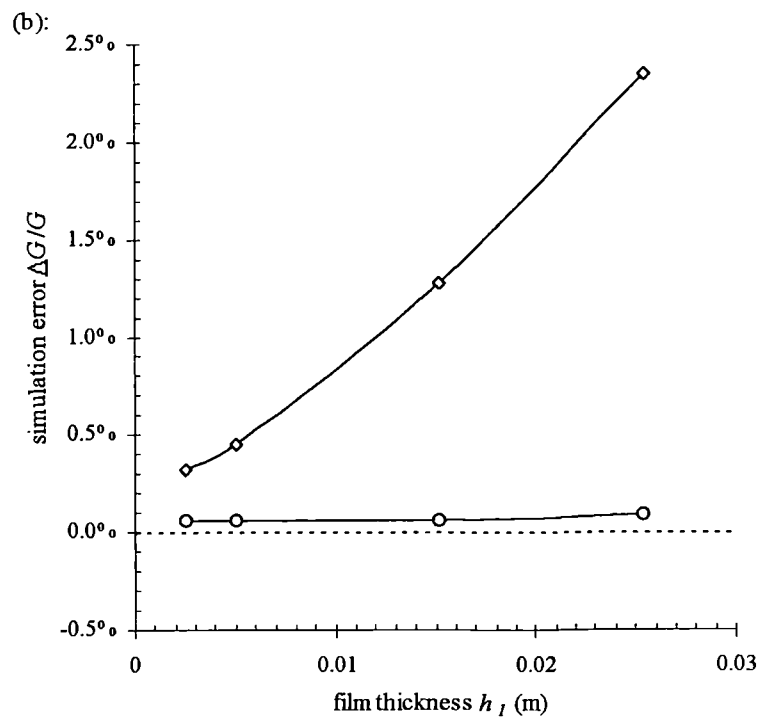
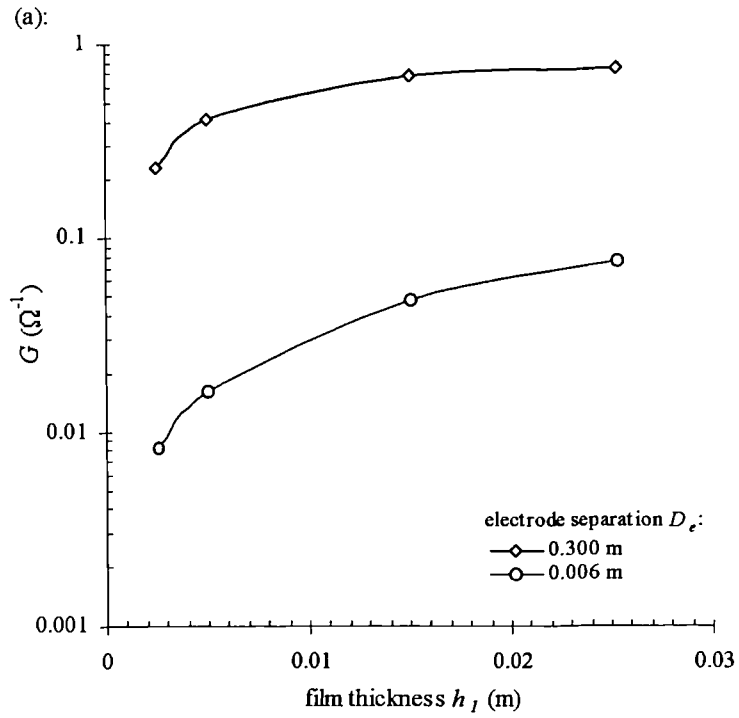


**Figure A3:** Calibration experiments: simulation of a 2D ‘flat liquid layer’ geometry for a range of film thickness. (a) Calculated conductance  $G^*$ ; (b) Relative simulation error  $\Delta G/G$ , obtained by comparing the results against the analytic solution (Coney<sup>27</sup>).

Test number	axial symmetry?	Distances in mm:				Line voltages (V):				
		$z_{1a}$	$D_e$	$z_{2a}$	$X$	L1	L3	L5	L7	L11
1	yes	300	300	300	100	-	0	1	-	-
2	yes	300	300	300	100	-	0	1	-	-
3	no	300	300	300	20; 30; 40; 50; 100	0	0	1	0	0.1
4a	no	300	300	300	100	0	0	1	0	-
4b	no	100	6	100	100	0	0	1	0	-

Test number	$i$ (mm)	$x, h_1$ and $h_2$ values (mm)
1	50.80	$x=0; h_1 \in \{2.61; 5.36; 8.30; 11.45; 14.88; 18.67; 22.97; 28.08; 34.74; 50.80\}; h_2=h_1$
2	50.80	$x \in \{-50; 0; 75; 150; 200; 250; 280; 300; 306; 356\}; h_1 \in \{2.61; 5.36; 14.88\}; h_2=50.80$
3	50.80	$x=0; h_1=50.80; h_2=h_1$
4a	50.80	$x=0; h_1 \in \{6.29; 9.81; 12.66; 15.11; 17.27; 19.22; 20.99; 22.60; 24.07; 25.40; 26.61; 27.69; 28.64; 29.46; 30.21; 30.62; 30.89; 30.85; 30.24; 25.40\}; h_2=h_1;$
4b	50.80	$x=0; h_1 \in \{6.29; 9.81; 12.66; 15.11; 17.27; 19.22; 20.99; 22.60; 24.07; 25.40; 26.61; 27.69; 28.64; 29.46; 30.21; 30.62; 30.89; 30.85; 30.24; 25.40\}; h_2=h_1$

**Table A1:** Summary table of the parameter values used for each simulation in Chapter 5. ( $X_I=100\text{mm}$ , and  $z_{Ib}=100\text{mm}$ , for all experiments).

## **APPENDIX B: Instrumentation design details**

This appendix contains the design drawings (generated using ORCAD), used in the manufacture of the measurement instrumentation described in Chapter 6. As described in section 6.1, the system consists of four identical ‘measurement channels’, which activate the electrodes and measure the cell conductance, and a separate ‘display module’, which holds the digital display and local output functions.

The contents of this appendix is organised as follows:

- Figures B1 to B6 are the *schematic designs* (showing the connections between different electronic components). The signals common to both these channels are shared through the backplane connector, shown in figures B1a and B1e.
- Figures B7 and B8 show the corresponding *PCB layout drawings* (which illustrate the copper pour tracks) to near actual scale. The tracks on both the front of the board and on the rear of the board have been superimposed.
- Tables B1 to B3 are the *bills of materials* required for the PCB manufacture, and the miscellaneous parts required for the instrument caseframe. The component reference, supplier, and approximate cost of each part are given where possible. As described in section 6.4.5, the overall manufacturing cost is approximately £1500.

Three possible improvements to the system design can be suggested. To cope with the long-term variations in the water conductivity, an *auto-ranging function* would be useful. To improve the rejection of external interference, improved *bandpass filters* could be added before demodulation. By driving each measurement channel with a *different operating frequency*, the crosstalk between the different system channels would be automatically rejected. Modifications to the schematic and layout diagrams should be made in future, to accommodate these improvements.

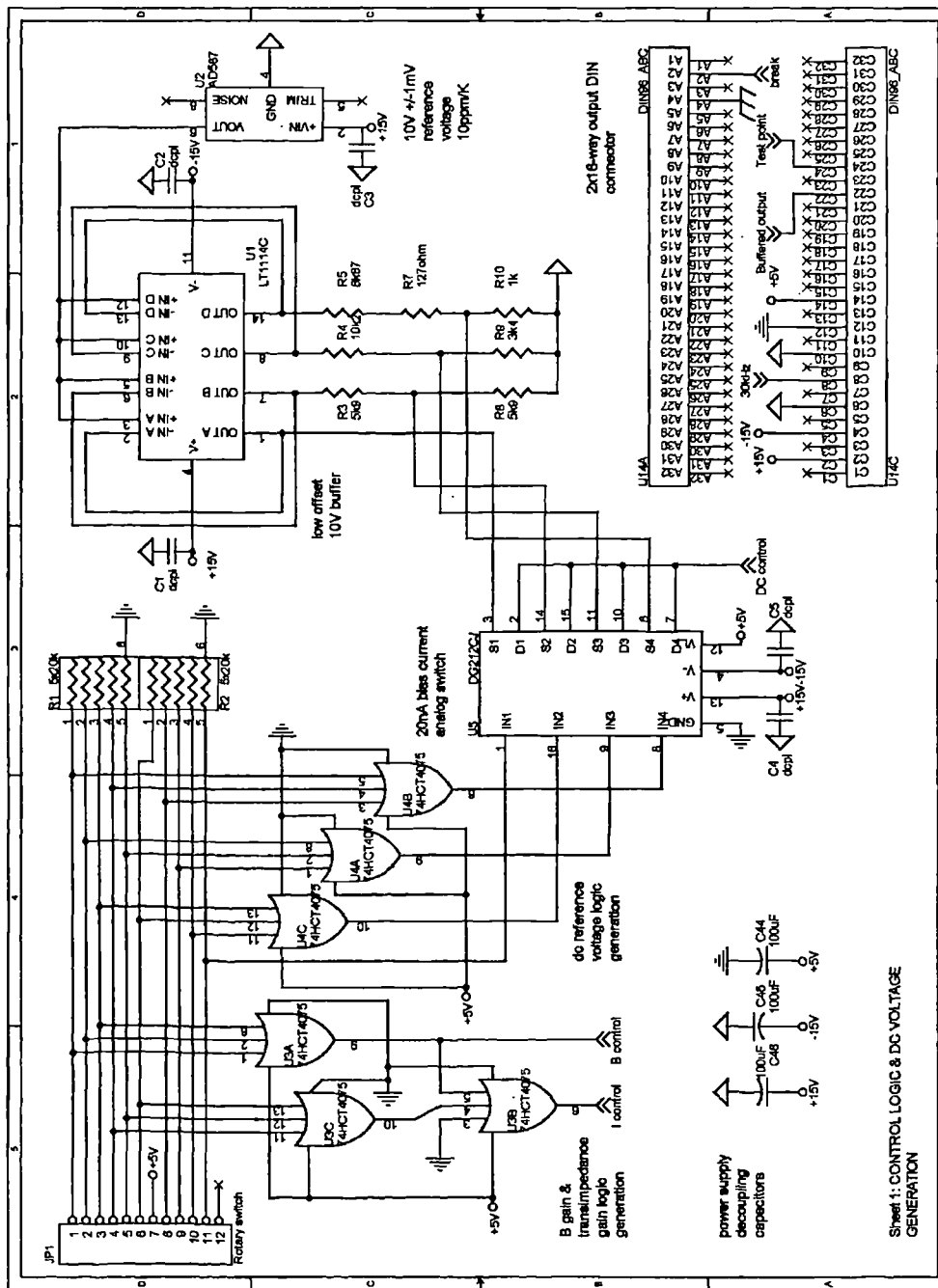


Figure B1: Measurement board schematic diagram: generation of the control voltage  $V_{ref}$  and the control logic for setting system gains  $A$ ,  $\beta$  and  $C$ .

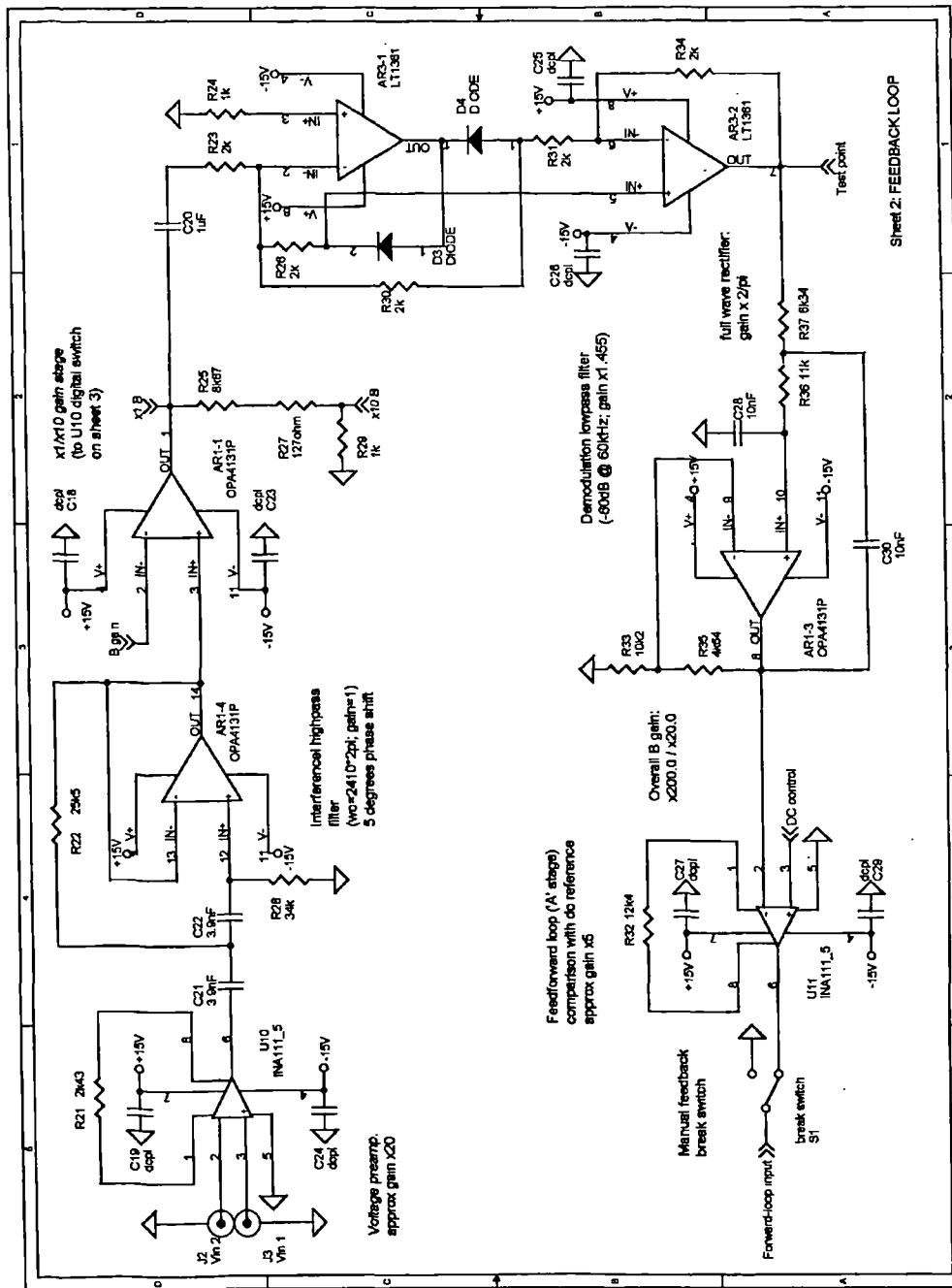


Figure B2: Measurement board schematic diagram: feedback loop ( $\beta$ ) components.



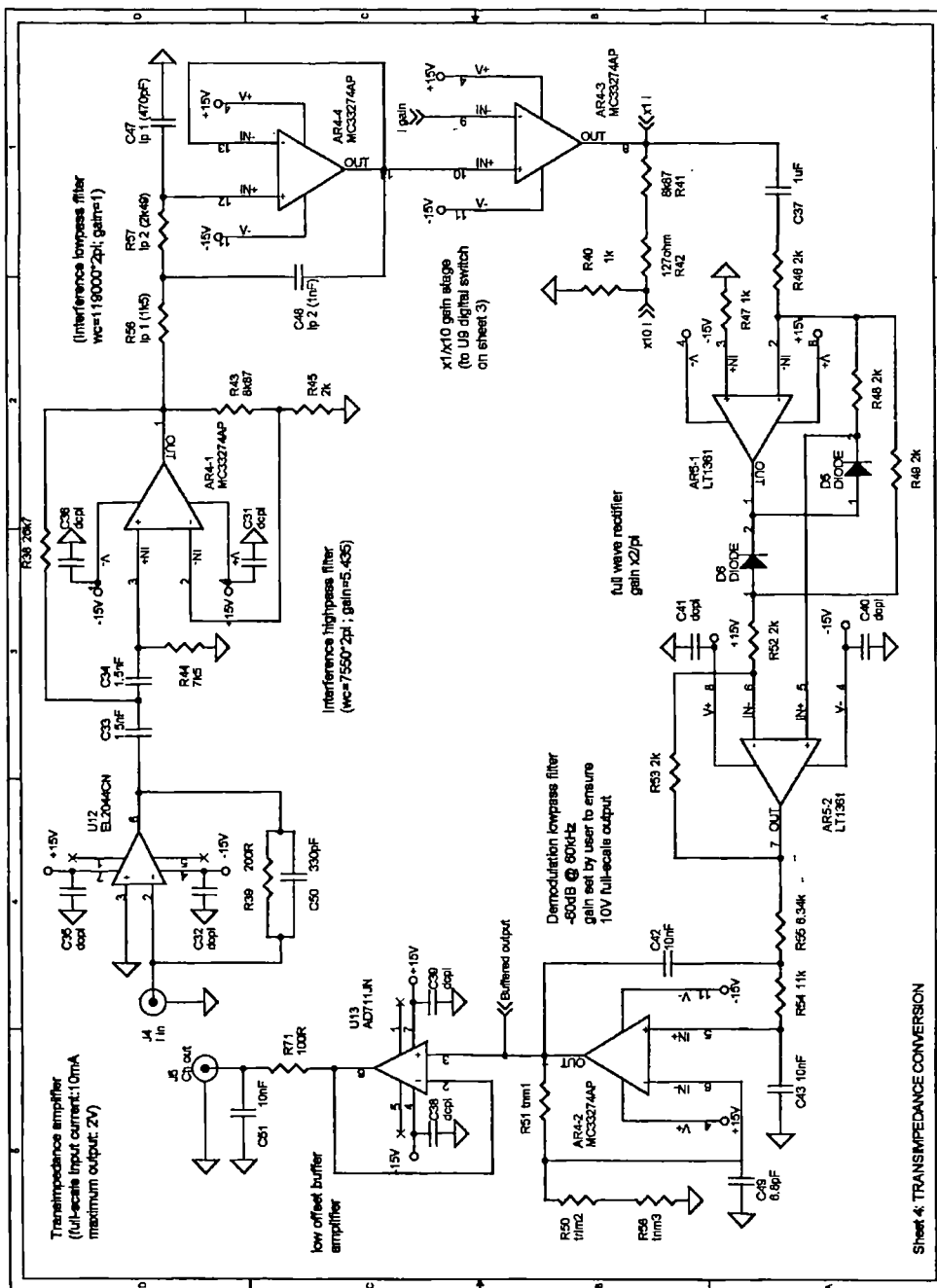


Figure B4: Measurement board schematic diagram: transimpedance stage (C) and channel output components

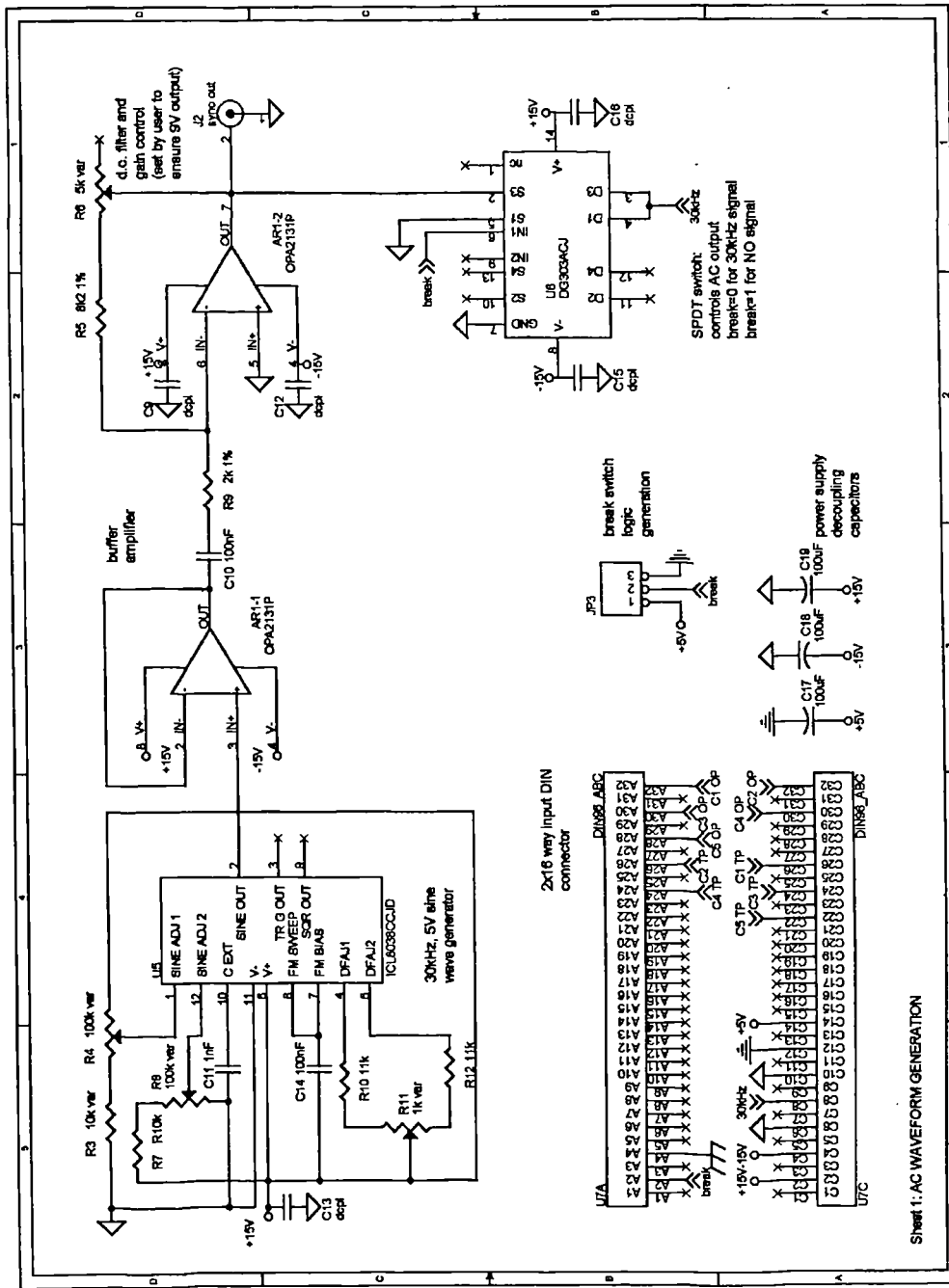
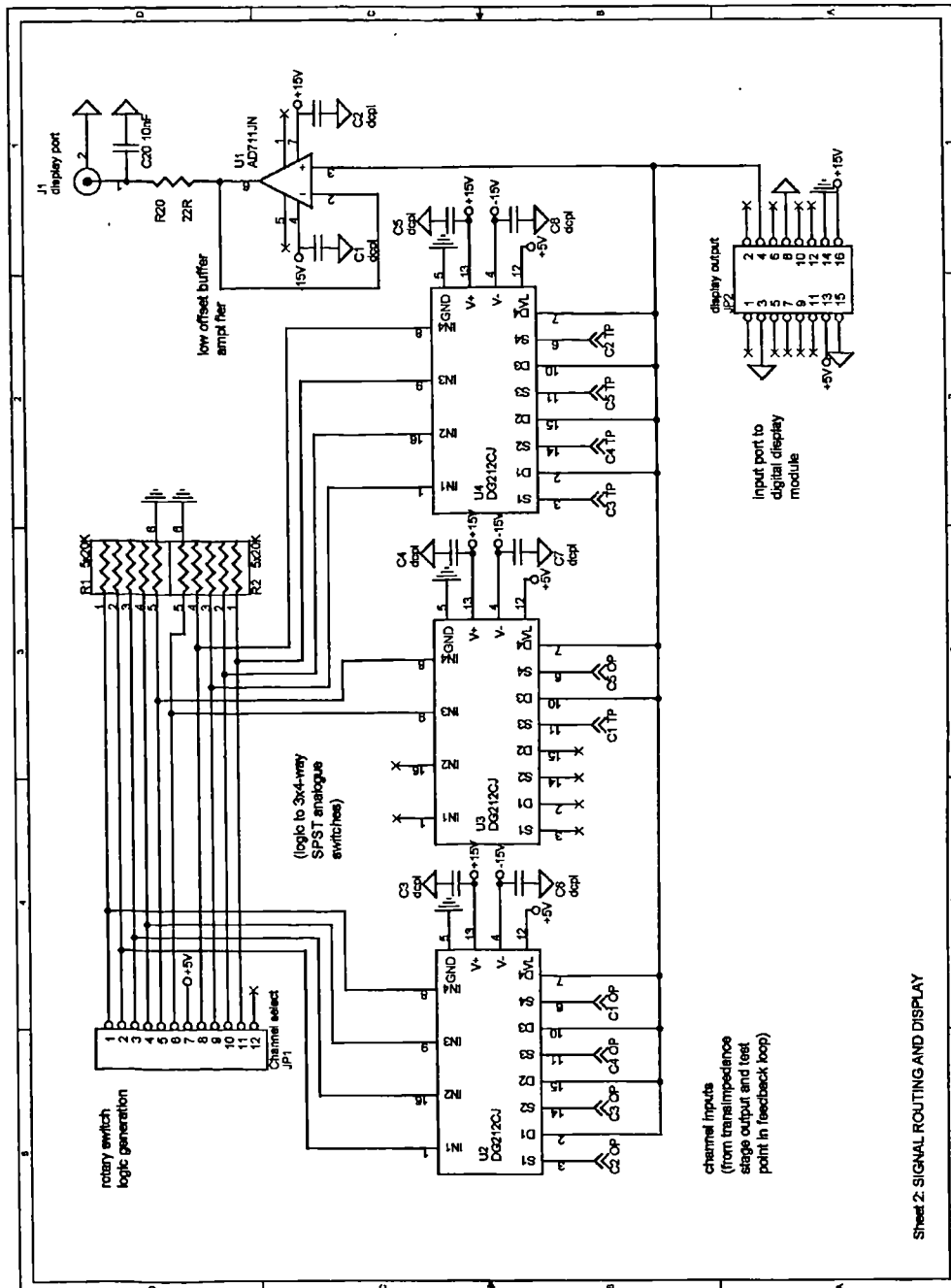


Figure B5: Display module schematic diagram: Generation of the 30kHz carrier signal waveform, and system backplane connections.



Sheet 2: SIGNAL ROUTING AND DISPLAY

Figure B6: Display module schematic diagram: routing of signals to the local output port and digital display

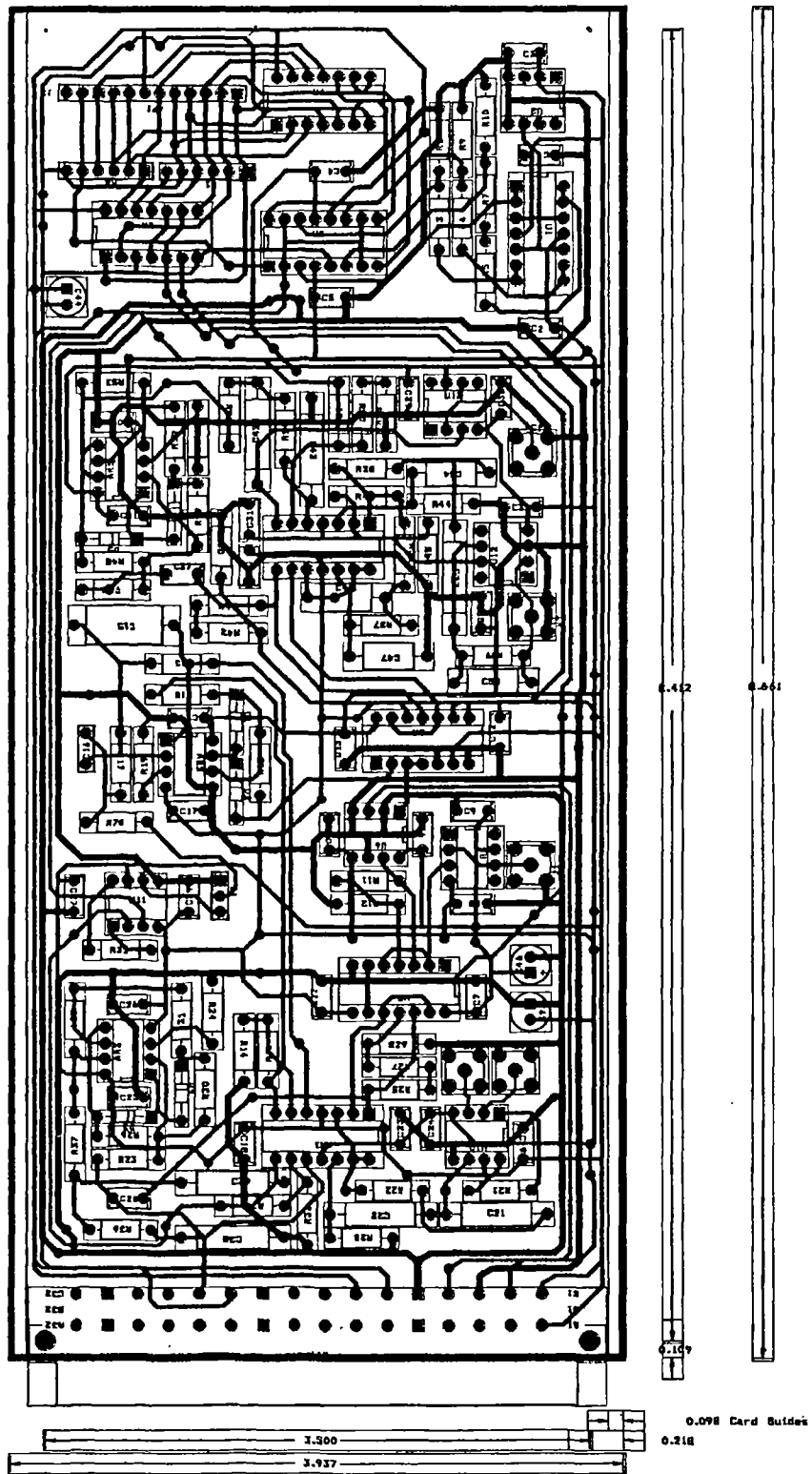


Figure B7: PCB layout diagram (individual measurement channel)

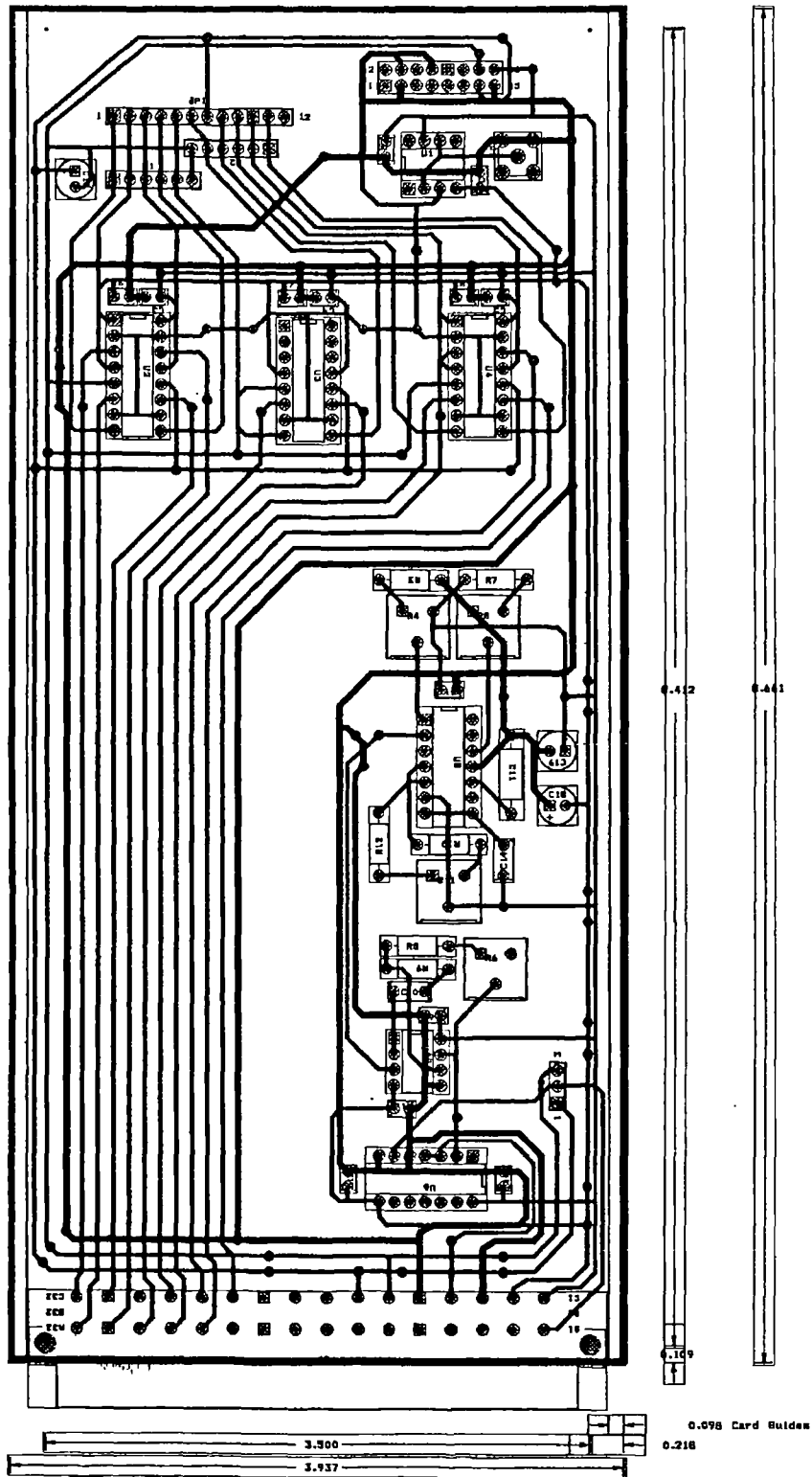


Figure B8: PCB layout diagram: display channel.

Qty	Component reference	Schematic name	Manufacturer	Description	Cost
2	AR1,AR4	OPA4131P	Burr-Brown	general purpose quad amplifier	8.20
1	AR2	EL2244CN	Elantec	60MHz video amplifier	4.98
2	AR3,AR5	LT1361CN8	Linear	dual 50MHz high slew rate amplifier	9.20
1	U1	LT1114CN	Linear	quad, low offset buffer amplifier	6.20
1	U2	AD587KN	Analog	±5mV, 100ppm/°C 10V reference	4.10
2	U3,U4	74HCT4075	Philips Semiconductor	3-way triple input NOR gate	0.40
1	U5	DG212CJ	Siliconix	4-way SPST analog switch	1.80
2	U7,U9	DG303ACJ	Siliconix	2-way SPDT analog switch	6.40
1	U6	AD633JN	Analog	4-quadrant analog multiplier	6.15
1	U8	OPA604AP	Burr-Brown	20mA driving amplifier	1.05
2	U10,U11	INA111	Burr-Brown	2MHz, high CMRR instrumentation amplifier	11.50
1	U12	EL2044CN	Elantech	transimpedance amplifier	3.00
2	U13	AD711JN	Linear	low offset output buffer	1.36
1	U14	DIN96_ABC	Harting	32-way type D PCB socket	6.00
31	C1-C14; C17-C19; C23-C27;C29,C31,C3 2,C35,C36; C38-C41	dcpl	Kemet Electronics	10nF decoupling capacitors	1.80
1	C15	22nF	Philips Components	22nF ±1% capacitor 424 series	0.59
4	C28,C30,C42,C43	10nF		10nF ±1% 424 series	1.76
2	C21,C22	3.9nF		3.9nF ±1% 424 series	0.88
2	C33,C34	1.5nF		1.5nF ±1% 424 series	0.88
1	C48	1p 2 (1nF)		1nF ±1% 426 series	0.30
1	C47	1p 1 (470pF)		470pF ±1% 426 series	0.30
1	C16	2u2	Evov-Rifa	2.2µF ±10% MMK series	0.42
2	C20,C37	1uF	Kemet Electronics	1µF ±20% Z5U series (demodulator)	0.80
1	C49	6.8pF	Philips Components	6.8pF ±0.25pF miniature 481 series	0.08
1	C50	330pF	Evov-Rifa	330 pF ±5% metallised polypropylene	0.21
3	C44-C46	100uF	Rubycon	100µF 25V radial dielectric capacitor	0.18
1	S1	break switch	RS Components	2-way SIP changeover switch	0.65
1	JPI	Rotary switch	AMP	12-way single row straight header	0.40
5	J1-J5	I out, V in 2, V in 1, I in, Ch Out	Transradio	MCX 50Ω straight PCB socket	10.10
3	R7,R27,R42	127ohm	Welwyn	0.25W 0.1% ±15ppm resistors	0.90
1	R39	200ohm			0.30
5	R10,R24,R29,R40, R47	1k			1.50
1	R56	1p 1 (1k5)			0.30
13	R13,R18,R23,R26, R30,R31,R34,R45, R46,R48,R49,R52, R53	2k	"	" "	3.90
1	R21	2k43			0.30
1	R57	1p 2 (2k49)	"	" "	0.30
1	R9	3k4			0.30
1	R51	trim1 (4k53)			0.30
1	R35	4k64			0.30
2	R3,R8	5k9	"	" "	0.60
2	R37,R55	6k34			0.60
1	R44	7k5			0.30
4	R5,R25,R41,R43	8k87			1.20
1	R17	9k09			0.30
2	R33,R4	10k2	"	" "	0.60
2	R54,R36	11k			0.60
1	R32	12k4			0.30
1	R22	25k5			0.30
1	R38	26k7			0.30
1	R28	34k	"	" "	0.30
1	R15	90k9			0.30
1	R50	trim2		calibration resistor (chosen by user during assembly process)	0.30
1	R58	trim3		calibration resistor	0.30
2	R1,R2	5x20k	BI Technologies	L06-1S 5x22k bussed resistors	0.90
2	R16,R11	9k1 1%	NEOHM	0.25W 1% ±100ppm resistors	0.05
2	R12,R14	1k 1%		0.25W 1% ±100ppm resistors	0.05
6	D1-D6	DIODE	Siliconix	1N5711 Schottky diodes	3.00
TOTAL (per board):					108.39

Table B1: Bill of materials: Measurement board components.

Qty	Component reference	Schematic name	Manufacturer	Description	Cost
1	AR1	OPA2131P	Burr-Brown	general purpose dual amplifier	3.70
1	U1	AD711JN	Linear	low offset output buffer	1.36
3	U2-U4	DG212CJ	Siliconix	4-way SPST analog switch	5.60
1	U5	ICL8038CCJD	Harris Semiconductor	0.001Hz-100kHz waveform generator	4.90
1	U6	DG303ACJ	Siliconix	2-way SPDT analog switch	6.40
1	U7	DIN96_ABC	Harting	32-way type D PCB socket	6.00
13	C1-C9; C12-C16	depl	Kemet Electronics	10nF decoupling capacitors	0.78
2	C14,C10	100nF	Kemet Electronics	100nF 50V ±20% X7R series	0.20
1	C11	1nF	Philips Components	1nF ±1% 426 series	0.30
3	C17-C19	100uF	Rubycon	100µF 25V radial dielectric capacitor	0.18
1	JP1	Channel select display output	AMP	12-way single row straight header	0.40
1	JP2	display output	Thomas & Betts	16-way low profile header	2.39
1	JP3	Break switch	RS Components	3-way single row straight header	0.40
1	J1	display port	Transradio	MCX 50Ω straight PCB socket	2.05
2	R1,R2	5x20k	BI Technologies	L06-1S 5x22k bussed resistors	0.90
1	R11	1k var	Spectrol	10mm 500mV 63M potentiometer	0.49
1	R6	5k var		10mm 500mV 63M potentiometer	0.49
1	R3	10k var		10mm 500mV 63M potentiometer	0.49
2	R4,R8	100k var		10mm 500mV 63M potentiometer	0.98
1	R9	2k 1%	NEOHM	0.25W 1% ±100ppm resistors	0.03
1	R5	8k2 1%		0.25W 1% ±100ppm resistors	0.03
1	R7	10k	Welwyn	0.25W 0.1% ±15ppm resistor	0.30
2	R10,R12	11k		0.25W 0.1% ±15ppm resistors	0.60
<b>TOTAL:</b>					<b>38.97</b>

**Table B2: Bill of materials: Display board components**

	Qty	Manufacturer	Description	Cost
Caseframe materials	1	VERO electronics	3U×60HP caseframe 718-604'06L	100.00
	4		9HP blank front panel	16.20
	1		21HP blank front panel	4.92
	1		3HP blank front panel	2.74
	10		card guides (*mm x *mm)	4.75
	1	Electrospeed	DIN41612 connector frame	12.80
	2		front tie bars (60HP)	3.80
	2		rear tie bars (60HP)	3.80
	1		set of tapped strips	5.20
	5	Harting	32-way type D PCB plug	19.38
Power supply	1		(Special unit built at Strathclyde University)	60.00
Lower board display	20	AMP	RG174 clamp bulkhead jacks	29.80
	4		1-pole 12-way rotary switch	11.80
(connections)	20		RG174 crimp plugs	19.00
	1	Thomas & Betts	12-way single row IDT socket	1.06
Upper board display	1	Lascar Electronics	DMM939 digital multimeter module	48.20
	1	AMP	RG174 clamp bulkhead jack	1.49
	1	RS Components	double-pole on-on miniature toggle switch	3.02
	2	Thomas & Betts	16-way IDC socket	4.84
(connectors)	1		1-pole 12-way rotary switch	2.95
	1		RG174 crimp plug	0.95
	1	Thomas & Betts	12-way single row IDT socket	1.06
	1		3-way single row IDT socket	0.33
Miscellaneous	100		8-way d.i.p. sockets	10.82
	56		14-way d.i.p. sockets	10.62
	28		16-way d.i.p. sockets	5.41
	1		100m reel RG58 cable	25.50
	1		25m reel RG174 cable	9.80
PCB manufacture	1	European Circuits Ltd	Upper board PCB manufacture	230.60
	5		Lower board PCB manufacture	309.08
<b>TOTAL:</b>				<b>1103.72</b>

**Table B3: Bill of materials: Casing, power supplies and miscellaneous parts not listed above.**

## Appendix C: Processing software

This appendix contains the Matlab code, which is used to analyse the raw data presented in Chapter 8. This code calculates the flow parameters for each slug unit, and delivers predictions for the phase flowrates, relative uncertainties in the model parameters, and a series of relative uncertainty components. It is assumed that the phase superficial velocities  $j_l$  and  $j_g$  (which are the parameters that are actually returned) are proportional to the mass flowrates.

As summarised by figure 7.1 in Chapter 7, the analysis software performs the following functions:

- Input of the raw data from Labview (one phase fraction signal and two cross-correlation signals) and conversion to Matlab data format.
- Calculation of the entire-record cross correlation function (see section 7.2.2) and the signal bandwidth  $B$ ;
- Calculation of the parameters  $V_t$ ,  $\bar{a}_f$ ,  $a_s$ ,  $\nu$ ,  $l_f$  and  $l_s$  for each successive slug unit, by using the ‘threshold level’ and the ‘cross-correlation’ routines `thrsh` and `xcorrel`.
- Calculation of the local velocities  $V_{ls}$  and  $V_{gs}$ , using the appropriate *closure relationships* (the subroutine `closrel`), and subsequent prediction of superficial velocities  $j_l$  and  $j_g$ .
- Calculation of the uncertainty components  $\Delta V_t/V_t$ ,  $\Delta \bar{a}_f/\bar{a}_f$ ,  $\Delta a_s/a_s$ ,  $\Delta V_{ls}/V_{ls}$ ,  $\Delta V_{gs}/V_{gs}$ ,  $\Delta \theta/\theta$  and  $\Delta t_{film}/\Delta t_{film}$ , and the corresponding flowrate uncertainties. In this calculation, it is necessary to loop through the previous steps two times, in order to obtain the sensitivity parameters  $S(\theta)$  and  $S(t_{film})$ .

The user inputs are the raw sensor data (in Labview binary file format), sampling frequency and sample duration parameters, the full-pipe conductance  $G^*$  (for normalising the holdup data); the processing parameters  $\theta$  and  $t_{film}$ , and the actual phase velocities  $j_l$  and  $j_g$  (taken from the NEL control system). The user must also specify the *cross-correlation technique*, the *closure relationships* for the local velocities  $V_{ls}$  and  $V_{gs}$ , and an *averaging technique* for calculating the velocities  $j_l$  and  $j_g$ .

```

function[JL, JG, VT, VLS, VGS, VLF, VGF, AS, AF, ...
    FREQ, LS, LF, uVT, uAS, uAF, uVLS, uVGS, ...
    uTHETA, uTFILM]=flvxtr(FILE, FREQ, ...
    NORM, THETA, TFILM, X, T, j1, jg, ivcalc, ...
    iclos, iavg)
% FLVXTR [JL, JG, VT, VLS, VGS, VLF, VGF, AS, AF, ...
    FREQ, LS, LF, uVT, uAS, uAF, uVLS, uVGS, ...
    uTHETA, uTFILM]=flvxtr(FILE, FREQ, ...
    NORM, THETA, TFILM, X, T, j1, jg, ivcalc, ...
    iclos, iavg)
%
% Processes the raw holdup and cross-
% correlation sensor for the flow variables,
% the phase superficial velocity predictions,
% and the prediction uncertainties, given:
%
% FILE      input filename
% FREQ      sample frequency (Hz)
% NORM      holdup normalisation constant
% THETA     threshold level height (sect. 7.2.1)
% TFILM     minimum film duration (sect. 7.2.1)
% X         sensor separation
% T         processing duration
% j1        liquid superficial velocity
% jg        gas superficial velocity
% ivcalc    velocity selection:
%           1 for unit-by-unit x-correlation
%           2 for entire trace x-correlation
% iclos     closure relationship selection:
%           -1 for equations [7.7] & [7.10]
%           -2 for equations [7.8] & [7.11]
%           -3 for equations [7.9] & [7.11]
% iavg      averaging technique selection:
%           1 'time weighted' averaging
%           -2 'parameter weighted' averaging
%
% The utputs are as follows:
%
% JL        gas superficial velocity
% JG        liquid superficial velocity
% VT        slug translation velocity
% VLS       local slug liquid velocity
% VGS       local slug gas velocity
% VLF       mean liquid film velocity
% VGF       mean gas film velocity
% AF        mean film zone holdup vector
% AS        slug body holdup vector
% FREQ      slug frequency vector
% LS        slug zone length vector
% LF        film zone length vector
%
% and the uncertainties caused by:
%
% uVT       translation velocity VT
% uAS       slug holdup uncertainty
% uAF       film holdup uncertainty
% uVLS      slug velocity uncertainty (liquid)
% uVGS      slug velocity uncertainty (gas)
% uTHETA    threshold level uncertainty
% uTFILM    minimum film duration uncertainty
%
% Main program
%
% input and convert raw data Labview file
fid=fopen(FILE, 'r', 'b');
A=fread(fid, 'float');
b=length(a); clear A;
fid=fopen(FILE, 'r', 'b');
A=fread(fid, [4,b/4], 'float');

% Use the first T seconds for processing only
L=fix(T*FREQ); A=A(:,1:L);

% calculate the entire record correlation
% velocity VT* and the signal bandwidth BW
n=nextpow2(length(A(1,:))/2); n=2^n;
[VT, SIGVT]=xcorrel(A, 1, n, BW, FREQ, X, TRUE);

if ivcalc=2
    for i=1:nslugs;
        VT(i)=VT; SIGVT(i)=SIGVT;
    end
end

% Main program loop
for loop=1,3
    if loop=1
        Dtheta=0.1;
        THETA=THETA+Dtheta;
    else if loop=2
        THETA=THETA;
        Dtfilm=mean(0.5-LF./(LF+LS));
        TFILM1=TFILM+Dtfilm;
    else
        TFILM1=TFILM;
    end

% threshold level data processing
    id=thrsh(A(2:1, L)/NORM, THETA1, TFILM1*FREQ);
    nslugs=length(id(1,:));

% calculate the unit-by-unit correlation
% velocity
    if ivcalc=1
        [NST, NFIN]=slugid(id);
        [VT, SIGVT]=xcorrel(A, NST, NFIN, BW, ...
            FREQ, X, FALSE);
    end

% evaluate flow variables
    for i=1, nslugs
        AF(i)=mean(A(2, id(2,i):id(3,i)))/NORM;
        AS(i)=mean(A(2, id(1,i):id(2,i)))/NORM;
        SFREQ(i)=1/(id(3,i)-id(1,i));
        LS(i)=VT(i)*(Z2(2,i)-Z2(1,i))/FREQ;
        LF(i)=VT(i)*(Z2(3,i)-Z2(2,i))/FREQ;
        LU(i)=LS(i)+LF(i);
        % closure relationships for VLS and VGS
        [J(i), S(i), VLS(i), VGS(i)]=closrel(...
            iclos, VT(i), AS(i), 9.81, 0.1016);
        VLF(i)=VT(i)-((VT(i)-VLS(i))*AS(i)/AF(i));
        VGF(i)=VT(i)-((VT(i)-VGS(i))*(1-AS(i)) ...
            /(1-AF(i)));
    end

% evaluate parameter mean values
        VTm=mean(VT); VLSm=mean(VLS);
        VGSm=mean(VGS); ASm=mean(AS);
        ASm=mean(AS); LFm=mean(LF);
        LUm=LFm+LSm;

% calculate the superficial velocities
        if iavg=1
            [JL, JG]=Jcalc(VTm, VLSm, VGSm, ASm, AFm, LFm, ...
                LUm);
        else
            [JL, JG]=Jcalc(VT, VLS, VGS, AS, AF, LF, LU);
        end

        if loop=1
            [JLth, JGth]=[JL, JG]
        else if loop=2
            [JGtf, JGtf]=[JL, JG]
        end
    end

% Calculate the relative prediction errors
% (Dj1/j1 and Djg/jg)
    DVt=(2*SIGVT);
    DaF=(0.02+(0.3/.LF));
    DaS=(0.2*(1-AS));
end

```

```

gam=AS + S*(1-AS); gam2=gam*.gam;
Dj=0.4; Ds=0.2;
DVls abs(Dj/.gam)+abs(Ds*J*(AS-1)/.gam2)+ ...
    abs(Das*(S-1)*J/.gam2)
DVgs=abs(Dj*S/.gam)+abs(Ds*AS*J/.gam2)+ ...
    abs(Das*S*(S-1)*J/.gam2)

uAF [mean((VT*.LF/.LU) *. Daf)/j1, ...
    mean((VT*.LF/.LU) *. Daf)/jg];
uAS [mean((VLS-(VT*.LF/.LU)) *. Das)/j1, ...
    mean((VT*.LF/.LU)-VGS) *. Das)/jg];
uVT=[mean(((AF-AS)*.LF/.LU) *. DVT)/j1, ...
    mean((AS-AF)*.LF/.LU) *. DVT)/jg];
uVLS=mean(AS*.DVls)/j1;
uVGS=mean((1-AS)*.DVgs)/jg;
uTHETA [(JLth-j1)/Dtheta, (JGth-jg)/Dtheta];
uTFILM-[(JLtf-j1)/Dtfilm, (JGtf-jg)/Dtfilm];

```

```

% End of main program

```

```

end

```

```

function ID=thrsh(A,THETA,NFILM)
% THRS ID=thrsh(A,THETA,NFILM)
% Identify the positions of start & finish
% of slug zones on vector A according to
% THETA. NFILM is the number of required
% data points below THETA, to indicate a
% film zone between slugs. NSLUG is the
% number of data points each slug unit
% should contain. Entries are returned in
% the vector 'id', format: slug start;
% slug finish; film finish.

```

```

ID [];

```

```

% set first point to ensure first slug is
% picked up

```

```

A(1 THETA+0.001;

```

```

% identify p ints above the threshold

```

```

i find A>THETA;
diff i 2:length(i):-i(1:length(i)-1);
i2 find diff>NFILM ;

```

```

% always include the first slug

```

```

if (i2(1 >1)
    i2 [1 i2];
end

```

```

% store the slug finish & start indices

```

```

sf i(i2 ; ss-i(i2+1);
nslugs=length(sf);

```

```

% eliminate short slugs; store in a 'slug
% start'/'finish'/'film finish' format

```

```

if nslugs>1
    k 1;
    for j=1:nslugs-1;
        if (sf(j+1)-ss(j)>NSLUG)
            ID(1,k) ss(j); ID(2,k)=sf(j+1);
            ID(3,k)=ss(j+1)-1;
            k=k+1;
        end
    end
end
end

```

```

function [NST,NFIN]=slugid(id)
% SLUGID [NST,NFIN]=slugid(id)
% obtain the position of the start

```

```

% and finish indices, for the cross-
% correlation process.

```

```

for i=1:length(id(1,:)),
    if i==1
        nst=1;
    else
        if (id(3,i-1)==id(1,i)-1)
            NST=(id(2,i-1)+id(1,i))/2;
        else
            NST=(id(3,i-1)+id(1,i))/2;
        end
    end
    end
    NFIN=(id(3,i)+id(2,i))/2;
end

```

```

function[VT,SIGVT]=xcorrel(A,nst,nfin, ...
    BW,FREQ,X,flag)
% XCORREL[VT,SIGVT]=xcorrel(A,nst,nfin, ...
    BW,FREQ,X,flag)
% Performs the covariance cross-
% correlation of A, given vector of
% correlation indices NST and NFIN,
% bandwidth estimate BW, sample frequency
% FREQ, sensor separation X, using Fourier
% transform technique. Returns vector of
% velocity values VT and statistical
% measurement uncertainty SIGVT.

```

```

nslugs=length(nst)
for i=1:nslugs,
    RT=[];
    nlength=nfin(i)-nst(i)+1;

```

```

% Covariance factors (required for
% normalisation)

```

```

ave1=mean(A(1,nst(i):nfin(i)));
ave3=mean(A(3,nst(i):nfin(i)));
aut1=A(1,nst(i):nfin(i))*A(1,nst(i): ...
    nfin(i)')/nlength;
aut3=A(3,nst(i):nfin(i))*A(3,nst(i): ...
    nfin(i)')/nlength;
norm=sqrt((aut1-ave1^2)*(aut3-ave3^2));

```

```

% Evaluate normalised correlation function

```

```

RT=(abs(iff(fft(A(3,nst(i):nfin(i))) .* ...
    conj(fft(A(1,nst(i):nfin(i))))/nlength)- ...
    ave1*ave3)/norm;

```

```

% Evaluate velocity VT and uncertainty SIGVT

```

```

j=min(5*FREQ,length(RT)); RT=RT(1:j);

```

```

% find first peak in RT
T=find(RT==max(RT)); T=T(1);
t=T/FREQ;

```

```

% estimate the bandwidth BW using peak
% width, if requested

```

```

if flag==TRUE,
    T2=find(RT<0.7); T2=T2(1);
    BW=0.5/(ABS(T2-T)/FREQ);
end
sig=sqrt(0.038*((1/RT(T))^2)-1) ...
    *(FREQ/nlength)/(BW^3);
VT(i)=X/t; SIGVT(i)=VT(i)*sig/t;
% plot((1:i)/FREQ,RT);
end
end

```

```

function [JL,JG]=Jcalc(VT,VLS,VGS,AF,AS,LS,LU)
% JCALC [JL,JG]=Jcalc(VT,VLS,VGS,AF,AS,LS,LU)

```

```

% calculates time weighted phase superficial
% velocities, given unit-by-unit vectors for
% velocity VT, the local slug velocities VLS
% and VLS, the holdups AF and AS, the slug
% length LS, and the total length LU.

for i 1:length(VT),
    JL1(i)=VLS*.AS + (VT*(AF-AS)*.LF/.LU);
    JG1(i)=VGS*(1-AS) + (VT*(AF-AS)*.LF/.LU);
    T1(i)=LU(i)/VT(i);
end
JL JL1*.T1'/sum(T1);
JG-JG1*.T1'/sum(T1);
end

function [JL,JG,VLS,VGS]=closrel( ...
    iclos,VT,AS,G,D)
% CLOSREL [JL,JG,VLS,VGS]=closrel( ...
    iclos,VT,AS,G,D)
% selects the closure relationships for J
% and S, depending on the parameter iclos:
% iclos 1: equations [7.7] and [7.10]
% iclos 2: equations [7.8] and [7.11]
% iclos 3: equations [7.9] and [7.11]

if icl s 1,
% Dukler & Hubbard correlations
    RL 1000; RG 1.2;
    ML 0.001; MG-0.000018;
    VLS VT*0.8; Z-1;
% iterative solution for VLS
    while abs(Z)<1.e-5,
        ReS= RL*AS+ RG*(1-AS)*VLS*D/ ...
            (ML*AS+MG*(1-AS));
        C-0.021ln(ReS)+0.022;
        Z = VT/(1+C) - VLS
        if Z<0
            VLS=VLS*0.99;
        else
            VLS=VLS/0.98;
        end
        J=VLS; S=1;
    else if iclos>1,
        if iclos=2,
% Woods & Hanratty correlations
            J1=(VT-0.54)/1.10; J2=VT/1.20;
            if (3-J1/sqrt(G*D))-(J2/sqrt(G*D)-3)>0,
                J=J1;
            else
                J=J2;
            end
        else if iclos=3,
% correlation based upon equation [8.2]
            J=(VT-1.09)/1.29
        end
        if J<3,
            S=1;
        else if J<7,
            S=1+0.125*(J-3);
        else
            S=1.5;
        end
    end
    VLS=J/(AS+S*(1-AS)); VGS=S*VLS;
end

```

**Figure C1:** Computer code 'flvxt r', used for processing the raw data and calculation of the flow parameters ( $V_t$ ,  $a_r$ ,  $\bar{a}_f$ ,  $l_f$ ,  $l_u$  and  $\nu$ ), the phase superficial velocities ( $j_i$  and  $j_g$ ), and the superficial velocity uncertainty components ( $\Delta j_i/j_i$  and  $\Delta j_g/j_g$ )

(blank page)